creative commons
COMMONS DEED

저작자표시-비영리-변경금지 2.0 대한민국

이용자는 아래의 조건을 따르는 경우에 한하여 자유롭게

- 이 저작물을 복제, 배포, 전송, 전시, 공연 및 방송할 수 있습니다.

다음과 같은 조건을 따라야 합니다:

저작자표시. 귀하는 원저작자를 표시하여야 합니다.

비영리. 귀하는 이 저작물을 영리 목적으로 이용할 수 없습니다.

변경금지. 귀하는 이 저작물을 개작, 변형 또는 가공할 수 없습니다.

- 귀하는, 이 저작물의 재이용이나 배포의 경우, 이 저작물에 적용된 이용허락조건을 명확하게 나타내어야 합니다.
- 저작권자로부터 별도의 허가를 받으면 이러한 조건들은 적용되지 않습니다.

저작권법에 따른 이용자의 권리는 위의 내용에 의하여 영향을 받지 않습니다.

이것은 이용허락규약(Legal Code)을 이해하기 쉽게 요약한 것입니다.

Disclaimer

dCollection

Ph.D. Dissertation of Engineering

Effects of Earthquake Loading Rate and Prestressing on Shear Strength of Cylindrical Squat Walls

지진하중 변형률 속도 및 프리스트레싱이 원형 저형 벽체 전단 강도에 미치는 영향

February 2023

Graduate School of Engineering

Seoul National University

Architecture and Architectural Engineering

Hyeon-Keun Yang

Effects of Earthquake Loading Rate and Prestressing on Shear Strength of Cylindrical Squat Walls

Advisor: Hong-Gun Park

Submitting a Ph.D. Dissertation of
Architecture and Architectural Engineering

February 2023

Graduate School of Engineering
Seoul National University
Architecture and Architectural Engineering

Hyeon-Keun Yang

Confirming the Ph.D. Dissertation written by
Hyeon-Keun Yang

February 2023

Chair	**Sung-Gul Hong**	**(인)**
Vice Chair	**Hong-Gun Park**	**(인)**
Examiner	**Cheol-Ho Lee**	**(인)**
Examiner	**Thomas Kang**	**(인)**
Examiner	**Min-Kyu Kim**	**(인)**

Abstract

Effects of Earthquake Loading Rate and Prestressing on Shear Strength of Cylindrical Squat Walls

Hyeon-Keun Yang

Department of Architecture and Architectural Engineering

College of Engineering

Seoul National University

In recent years, Gyeong-ju and Po-hang, two earthquakes were occurred. Because of these two earthquakes, which occurred near the nuclear power plant site, the concern in seismic safety of nuclear power plants was increased. In addition, the importance of identifying the exact seismic performance of nuclear power plants has been emphasized as the number and risk of earthquakes increased. In addition, it was confirmed that the characteristic of Korea earthquake includes high frequency components.

Nuclear power plants are the building that controls radioactive materials and requires high seismic performance to minimize leakage of radioactive materials

in the event of an accident. Therefore, the thickness of auxiliary and containment buildings is about 1.2 m. In addition, high reinforcement ratios exceeding the current design criteria are used. In particular, the post-tensioning is applied in containment buildings to withstand internal pressure that may occur in the event of an emergency accident. However, due to the post-tensioning and massive scale of containment buildings, structural experiments have been rarely conducted. In the case of existing experiments, panel experiments with the same details or small-scaled model were conducted. In addition, experiments of cylindrical walls with post-tensioning were rarely conducted.

Unlike planar walls, cylindrical walls do not transfer the shear force directly. The shear force is transmitted along the cross-sectional shape. Because of these characteristics of cylindrical section, confining force is required. However, the confining force of horizontal reinforcing bars cannot be applied, if the proposed expression through existing planar wall experiments is used. Thus, it is necessary to develop a shear strength model for cylindrical walls. In particular, it is necessary to research the characteristics of structure behavior characteristic of the structure against the earthquakes with high-frequency components.

In this dissertation, dynamic loading tests were performed to investigate the effect of high-frequency earthquakes, and shaking table tests were performed for verification. In addition, to investigate the seismic performance of the containment building, a cylindrical wall was prepared and cyclic loading tests were conducted. Based on the experimental results, the failure mode change was not occurred and the seismic performance of reinforced concrete wall was

confirmed. In addition, the greater strength of structure was observed under high loading rate.

In the results of the comparison experiment between cylindrical and planar walls, the effect of post-tensioning on maximum shear strength was low in the case of planar wall. However, in the case of cylindrical wall with post-tensioning and crosstie, the maximum strength was increased. On the other hand, in the case of post-tensioned cylindrical walls without cross ties, the delamination cracks were observed. Due to the internal cracks, the maximum shear strengths were decreased. Based on the experimental results, the shear strength equation of the cylindrical wall was proposed.

In the conclusion of this dissertation, based on the test and analysis results, the shear strength equation for cylindrical wall was proposed to predict the seismic capacity of wall. In addition, design recommendations were proposed to prevent premature failure of structure and improve the structural safety of nuclear power plants from seismic loads.

Keywords : high-frequency earthquake, post-tensioning concrete, deviation force, cylindrical wall, evaluation of nuclear power plant

Student Number : 2017-23892

Contents

List of Tables

List of Figures

List of Symbols

A_{cv} : gross area of concrete section

A_{eff} : effective cylindrical wall area

A_{sh} : area of reinforcing bars in horizontal direction

A_{sv} : area of reinforcing bars in vertical direction

A_{web} : web area of concrete wall

c : maximal strength reduction factor

d_0 : outside diameter of the cylindrical wall

E_D : cumulative dissipated energy

E_c : elastic modulus of concrete

E_s : elastic modulus of reinforcing bar

E_{So} : elastic strain energy

e : a vertical component of the tangent unit vector

F_{Ax} : Resistance force at segment A

F_{Bx} : Resistance force at segment B

F_{Cx} : Resistance force at segment C

F_{hw} : forces carried by horizontal reinforcement

F_{vbe} : forces carried by boundary element

F_{vw} : forces carried by vertical reinforcement

F_x : tensile force of reinforcing bar

f_{Ay} : axial stress in the concrete at the bottom of segment A

f_c' : compressive strength of concrete.

$f_{c,max}$: maximum compressive strength considered principal tensile strain

f_{dc}' : dynamic compressive strength of concrete

f_{dy} : dynamic yield stress of reinforcing bar

f_{py} : yield stress of prestressing steel

f_t : tensile strength of concrete

f_v : yield stress of reinforcing bar

G_f : fracture energy coefficient

h_w : height of wall

K : elastic stiffness

K_s : effective stiffness

l_w : length of wall

l_{eff} : effective wall length

N_h : membrane force in horizontal direction

N_{hl} : membrane force in horizontal direction from external load

P : axial force in wall

p_c : confining pressure

R : radius of cylindrical wall

T_b : Tensile force for binding force

t_c : thickness of concrete strut

t_{cover} : thickness of concrete cover

t_w : thickness of wall

w : width of cross-section

α : a factor according to moment shear ratios (EPRI)

β : a factor of the ratio of tensile stress to yield stress of vertical reinforcing bar

γ : a factor related to aspect ratio

ε_1 : strain of principal tensile direction

ε_2 : strain of principal compressive direction

ε_c : concrete cylinder strain corresponding to the cylinder strength f_c'

ε_d : plastic strain of concrete

ε_h and ε_v :average strains in the horizontal and vertical directions

ε_R : additional strain due to binding force

$\acute{\varepsilon}_s$: actual strain rate of reinforcing bars

$\acute{\varepsilon}_c$: actual strain rate of concrete

θ_{AB} : bottom central angle of segment A

θ_{AT} : top central angle of segment A

θ_B : central angle of segment B

θ_{BR} : rotational angle of segment B;

θ_c : cracked angle

θ_{CB} : bottom central angle of segment C

θ_{CT} : top central angle of segment C

λ : light-weight concrete modification factor

μ : shear-friction coefficient

ξ_{eq} : equivalent viscous damping ratio

ρ_h and ρ_v : ratio of reinforcing bar in horizontal and vertical directions

ρ_{ph} and ρ_{pv} : ratio of post-tensioning tendon in horizontal and vertical directions

σ_c : compressive stress of concrete strut

σ_h and σ_v : horizontal and vertical stresses resulting from dead load, internal pressures and lateral load (tension positive)

σ_{ph} and σ_{pv} : horizontal and vertical compressive stresses due to post-tensioning

φ : a factor for proposed equation to applying EPRI form

Chapter 1. Introduction

1.1 General

In 2016, an earthquake with high-frequency contents in Gyeong-Ju was occurred. The response spectrum of the earthquake was greater than the design spectrum in high-frequency range, as shown in Figure 1-1. Due to this reason, wol-sung nuclear power plant was paused by manually. In addition, as the frequency and risk of earthquake in Korea increase, the seismic performance of nuclear power plant building was emphasized.

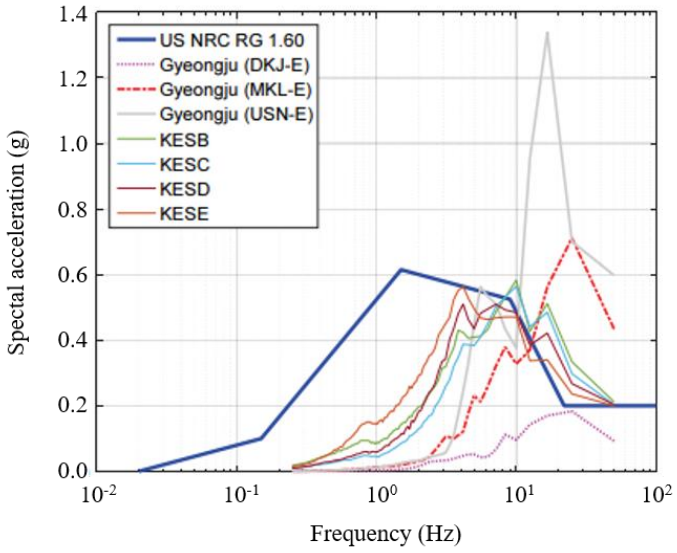

Figure 1-1 Comparison of response spectrum of the RG1.60, the 2016 Gyeong-ju earthquake motions and artificial motions of Korea (Park and Lee)

Chapter 1. Introduction

The nuclear power plant is an infrastructure that deals with radioactive materials. If the radioactive materials are leaked, huge economic and environmental damages are expected. To prevent leakage of radioactive materials, nuclear power plant structures were designed to have high performance against various accidents. The earthquake loading is a large proportion in calculating the accident scenario of the nuclear power plant. Therefore, nuclear power plants were required high seismic performance, and the buildings were designed with the maximum reinforcing bar ratio and 1.2 m of thickness. As the thickness of wall and stiffness increase, the natural frequency of the building is increased, and the natural frequency of nuclear power plant is expected over 4 Hz. Therefore, nuclear power plant buildings have greater resonance with the earthquake with high-frequency contents, such as a characteristic of earthquakes in Korea. Especially, in the case of containment buildings with low aspect ratio and the post-tensioning force in the vertical and horizontal directions, the natural frequency of the structure is close to 5 Hz and 12 Hz for the horizontal and vertical directions, respectively. Therefore, the containment buildings are also expected to be vulnerable to high-frequency earthquakes.

In the case of nuclear power plants safety assessment, the earthquake with beyond design earthquake is assumed and the scenarios are reported to identify the extreme performance. This procedure is called “Seismic Probabilistic Risk Assessment (SPRA, Figure 1-2)”. Therefore, an accurate method of seismic evaluation for beyond design earthquakes is required

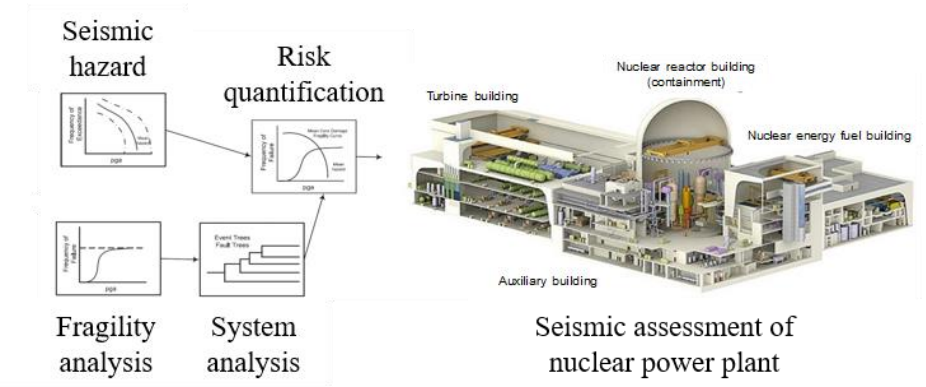

Figure 1-2 SPRA methodology (Grant, Hardy and Short (2018))

Nuclear power plant building consists of various wall types. Figure 1-3 shows the summary of wall types of the nuclear power plant. The behavior of characteristics of the structure is different according to each building. A seismic evaluation procedure shall be performed by applying the properties of these walls. Therefore, in this dissertation, the problem of the existing evaluation is identified and the improved method is proposed based on the characteristic of the containment building.

Containment building in NPP

Geometry: S**quat cylindrical wall**

: wall thickness: 1,200 mm, height: 55,000 mm, diameter: 50,000mm

High reinforcing bar ratio: the maximum ratio is close to 1.7 %

High post-tensioning bar ratio:

0.6 % and 1.0 % for vertical and horizontal directions

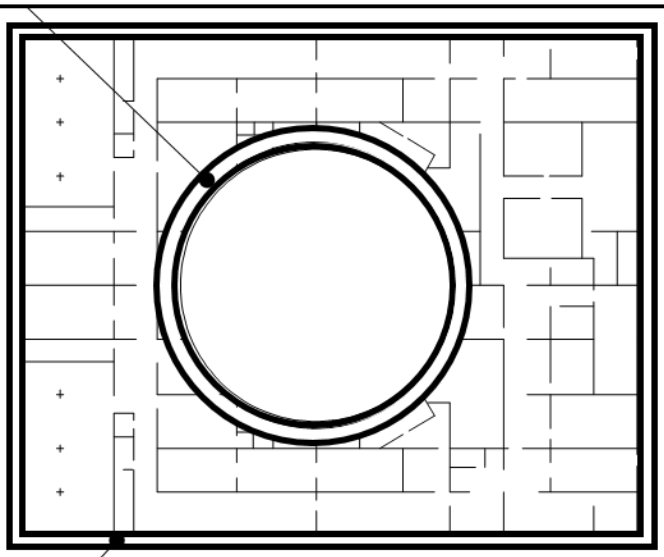

Auxiliary building in NPP

Geometry: **Squat walls with flanges (intersecting walls)**

: wall thickness: 1,200 mm, height: 5,000 – 7,000 mm

High reinforcing bar ratio: the maximum ratio is close to 1.0 %

With 4 layers of large diameters bars (ex. #14bars, diameter of 43 mm)

Figure 1-3 Section of nuclear power plant and summary of wall characteristics

For the improvement of seismic assessment of nuclear power plant, especially containment, the followings were considered.

First, because of cylindrical shape of containment building, the experimental and analytical researches for cylindrical wall is required. In the most case of previous researches of squat wall, the target building had rectangular, barbell, or planar shape. In the case of cylindrical shape, few experimental researches were conducted. In the case of most hollow cylindrical section test, the aspect ratios of cylindrical specimens were greater than 3, because the test purpose was to investigate the shear capacity of piers. However, in the case of cylindrical squat wall, the hollow section is expected to effect on the shear strength (i.e. the diagonal strut action and the increment of shear strength). Thus, based on the experimental and analytical methods, the characteristic of cylindrical squat wall is required.

Second, the effect of post-tensioning on shear strength or capacity of containment building is required. Currently, through previous researches and investigation, the tensile cracking in the concrete wall caused by curved post-tensioning was reported. Figure 1-4 shows the delamination cracks in the actual nuclear power plant building at Crystal River (USNRC (2010)). The most delamination cracks were occurred at the dome area with double-curvature post-tension. Therefore, in the case of the standard published prior to 2013, the additional analysis and reinforcement was required if the structures were designed using the post-tensioning with double curvature. In recent years, the standard had been supplemented to perform additional analysis on post-tensioning walls with single curvature or double-curvature. However, the effect

of curved post-tensioning and internal cracks on shear strength of cylindrical wall was not reported.

Figure 1-4 Delamination of containment wall at Crystal River (Nuclear Regulatory Commission, (2010))

Last, in the case of earthquake, the structures deforms with high strain rate. Previous researches about strain rate had mainly been conducted on high strain rate load such as impact and impulse. On the other hand, in the case of earthquake load, the effect of strain rate was not considered, because the effect is expected to be small. However, to apply the characteristics of earthquakes for evaluation of structures, the effect of strain rate must be considered.

For improvement of seismic evaluation of containment building, which is the final object of this dissertation, it is important to be able to accurately predict the actual behavior of cylindrical squat wall. Particularly, peak strength of cylindrical wall is the primary index to be captured. However, existing web-crushing equation provided by design or evaluation codes proposed by other studies for cylindrical walls does not reflect the effect of post-tensioning. Thus, it is necessary to develop an alternative way to predict the web-crushing strength of cylindrical squat wall.

1.2 Scope and Objectives

The primary objective of this dissertation is to contribute to a better understanding of shear behavior of nuclear power plant building. To achieve the objective, cyclic loading test, shaking table test for planar and cylindrical concrete walls with low aspect ratios ($0.5 \leq h_w/l_w \leq 1.0$) were performed. The tested maximum strength were compared with the predictions by current design codes. Based on the results, the effect of loading rate and delamination on shear strength was discussed. The dynamic-loading tests were directly compared with those of static-loading tests. The improved shear strength model of cylindrical wall was proposed and the accuracy was verified through test results and analysis. Finally, the recommendations were proposed for the design and evaluation of nuclear power plant. Each objective was summarized as follows:

1) Experimental studies on low aspect ratio walls were performed. The shape of test specimens were planar and cylindrical for auxiliary and containment building of nuclear power plant, respectively. In consideration of the high seismic demand of nuclear power plant, the specimens with high reinforcing bar and prestressing bar ratio were used. Based on the literature review on shear strength modes, the plan of experiments were focused on the shear strength contribution of the cylindrical shape, loading rate and delamination. The results were compared with the existing strength equations to verify the applicability of the equations in seismic performance evaluation.

2) The shear strength model based on force equilibrium for cylindrical wall with better accuracy was proposed. The availability and accuracy of the proposed models were verified statistically based on existing cylindrical concrete wall test data.

3) To improve the accuracy of evaluation of nuclear power plant, recommendations were proposed. The proposed shear strength model, method of applying loading rate, effect of delamination on shear strength, and additional moment due to horizontal post-tensioning.

1.3 Outline of the Ph.D. dissertation

This dissertation consists of eight chapters: Introduction, Literature Review, Structural test for loading rate, Structural test for cylindrical Walls, Nonlinear finite element analysis, Effect of design parameters on shear strength of cylindrical wall, Shear strength model of cylindrical walls, and Conclusion. Figure 1-5 shows the flow chart of this dissertation.

In chapter 2, current design codes and previous researches were reviewed. The scope of the current design codes was codes for the shear strength of squat and cylindrical wall. The previous researches regarded shear strength of walls, delamination, and loading rate effect. The list of design variables in existing models were investigated and compared.

In chapter 3, structural experiment researches were performed to verify the effect of high-frequency earthquakes on reinforced concrete walls using planar walls. The fast-loading test and shaking table test were conducted. Based on the literature reviews and design plan, the test specimens were designed to verify the seismic capacity of auxiliary building of nuclear power plant.

In chapter 4, structural experiment researches were performed to evaluate seismic capacity of cylindrical walls. The target building was the containment building of nuclear power plant. The test specimens were designed with prestressing and high-reinforcing bar ratio.

In chapter 5, finite element analysis was conducted to investigate the effect

of aspect ratio, vertical and horizontal post-tensioning forces and the ratio of diameter to thickness of wall. The analysis results were used to simplify the proposed shear strength equation and verify of that.

In chapter 6, the effect of various design parameters on shear strength and characteristic of cylindrical section were discussed based on the test results of the present study. The major design parameters affecting the shear strength of the walls are the loading rate, post-tensioning force and shape of wall (cylindrical).

In chapter 7, shear strength model for cylindrical wall was proposed based on the force equilibrium. Simplified procedure was developed to predict shear strength based on the proposed equation.

Finally, in chapter 8, summary and conclusions of the dissertation were presented. Design and evaluation recommendations for nuclear power plant buildings were proposed. Loading rate effect, delamination, and additional moment due to horizontal prestressing were described.

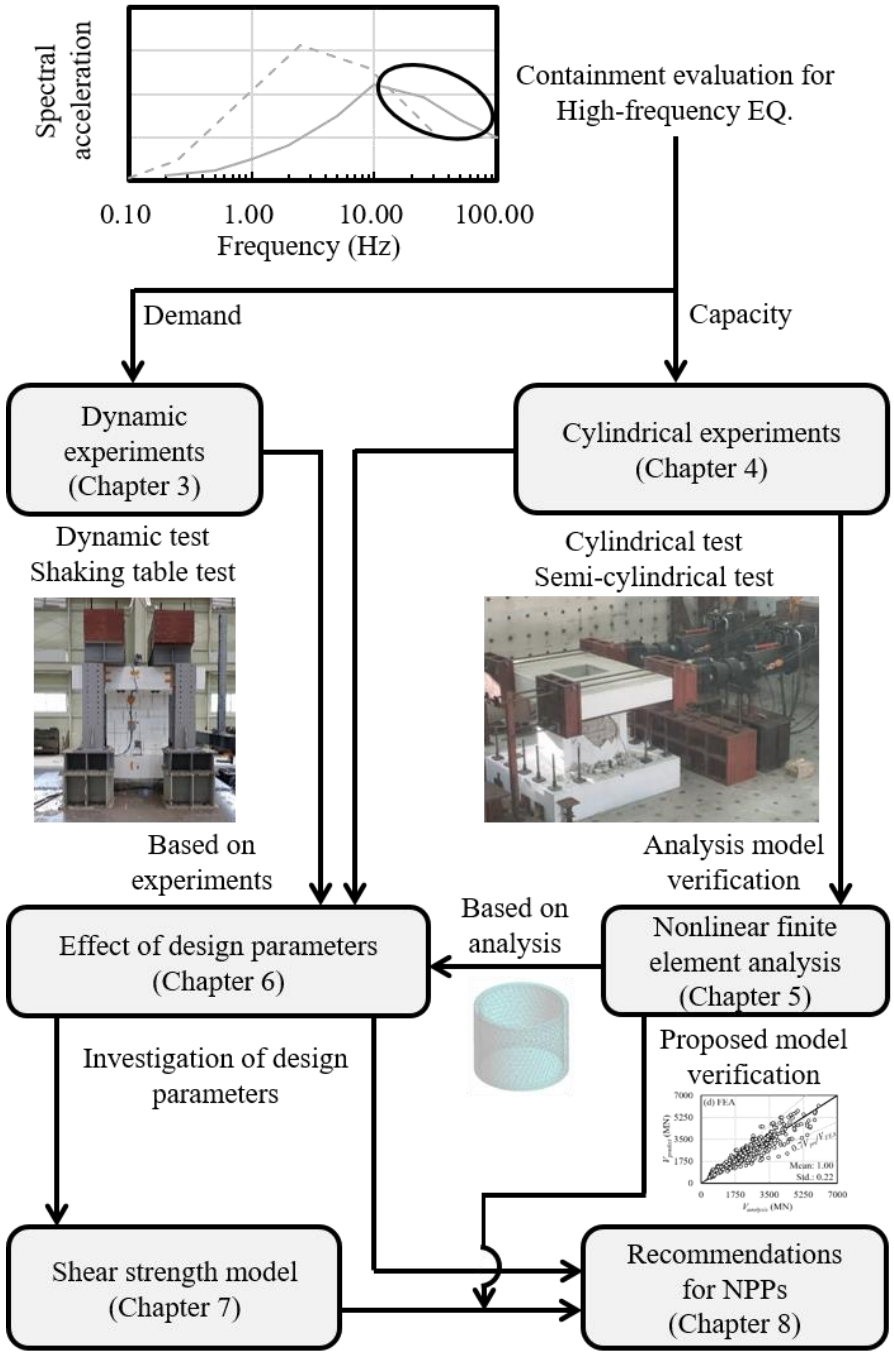

Figure 1-5 Flow chart of dissertation

Chapter 2. Literature Review

This section provides reviews of current design codes and the literatures on experimental studies for planar and cylindrical concrete walls. Section 2.1 reviews the shear strength equations that are currently used in seismic design and evaluation procedure. Section 2.2 and Section 2.3 review previous studies for squat and cylindrical walls, respectively.

2.1 Current Design Codes

Primary provisions in the current design codes are summarized in this section. The majority of the current design codes covers the provisions for nuclear power plant building structures.

2.1.1 ACI 349

ACI 349 is a code for nuclear power safety-related concrete structures. In sections 11.5, and 18.10, the code presents the design requirements for ordinary structural planar walls subject to non-seismic lateral loadings, and seismic design of special structural walls, respectively.

The shear strength equation of ACI 349-13 is identical to the equation of ACI 318-19 (Section 18.10.4.1). Eq. (2-1) presents the shear strength equation specified in ACI 318-19.

$$V_n = (\alpha_c \lambda \sqrt{f_c'} + \rho_h f_y) A_{CV} \leq 0.67 \sqrt{f_c'} A_{CV} \tag{2-1}$$

where α_c is a factor 0.25 for walls with aspect ratio less than 1.5 and 0.17 for walls with aspect ratio greater than 2.0, while linearly varying between the aspect ratios between 1.5 and 2.0; λ is a modification factor to reflect the reduced mechanical properties of lightweight concrete relative to normal weight concrete of the same compressive strength; f_c' is a compressive strength of concrete; ρ_t is a transverse (horizontal) reinforcement ratio; and A_{cv} = gross

area of concrete section bounded by web thickness and length of section in the direction of shear force, respectively. The maximum shear strength of $0.67\sqrt{f_c'}$ is to prevent brittle web-crushing failure before re-bar yielding.

2.1.2 ACI 359 (or ASME BPVC.III.2)

ACI 359 is a code for concrete containments of boiler and pressure vessel. In sections CC-3521, the code provides the design requirements for reinforced and prestressed cylindrical walls subject to seismic load. The maximum tangential shear flow calculated from elastic theory for cylindrical wall is used with considering shear force distribution along the wall length.

The shear flow strength $\dot{V}_n$ of the reinforced or prestressed concrete containment wall is defined as the sum of the contributions of concrete $\dot{V}_c$ and shear reinforcement $\dot{V}_s$. However, in the case of the reinforced concrete wall, the contribution of concrete is neglected ($\dot{V}_c = 0$). In the case of the prestressed concrete wall, when $\dot{V}_u$ exceeds $0.85\dot{V}_c$, the entire tangential shear should be resisted by shear reinforcement$\dot{V}_s$, the shear flow strength $\dot{V}_n$ is equal to $\dot{V}_s$.

1) Tangential shear and membrane force

The required area of orthogonal reinforcement, with and without inclined reinforcement, provided for combined tangential shear and membrane strength shall be as Eq (2-2).

$$A_{sh} + A_{si} = \frac{N_h + \left(N_{hl}^2 + V_u^2\right)^{1/2}}{0.9 f_y} \quad (2\text{-}2)$$

where f_y is a yield stress of reinforcing bars; A_{sh} is a area of bonded reinforcement in the hoop direction (mm^2/m); A_{si} is a area of bonded reinforcement in one direction of inclined bars at 45 degree to horizontal (mm^2/m); N_h is a membrane force in the hoop direction due to pressure, prestress, and dead load; and N_{hl} is a membrane force in the hoop direction from lateral load such as earthquake wind or tornado loading (the values are positive when tension and negative when compression).

2) Radial tension reinforcement

In ACI 359 CC-3545, the requirement of reinforcing bar to radial direction is mentioned to resist radial tensile forces for portions of prestressed containments with single curvature. In the requirements, the detail analysis shall include consideration for curvature, location size, etc.

The spacing of radial reinforcement shall not be greater than half the shell thickness or 600 mm. The radial reinforcement shall be developed no either side of the centroid of the curved tendons.

2.1.3 EPRI

The technical report-3002012994 (EPRI (2018)) deals with seismic fragility and seismic margin of nuclear power plant building. In the report, the failure modes of the walls in nuclear power plants are diagonal shear cracking, flexure, and shear friction. The typical governing failure mode considered for cylindrical concrete walls such as containment building is tangential shear failure. Shear failure equations for planar walls and cylindrical walls that were currently used in seismic fragility analysis were summarized in this section.

1) Shear strength equation for planar walls

The type of planar shear walls is classified as walls with boundary elements and without boundary elements. For walls without boundary elements and aspect ratios greater than 1.0, the shear strength equation should be determined the shear strength of ACI 349 without strength reduction factor. For squat walls with aspect ratio less than 1.0, the shear strength of walls can be estimated using following equation (2-3).

$$V_n = \frac{1.29\sqrt{f_c'}A_{web} + 0.26F_{vw} + 0.04F_{hw} + 0.2F_{vbe} + 0.39P}{(h_w / l_w)^{0.58}} \quad (2\text{-}3)$$

where A_{web} is a wall area; 0.25, F_{vw}, F_{hw} are forces carried by vertical, and horizontal reinforcement in the area of web; F_{vbe} is a force carried by vertical reinforcement in the area of boundary; and P is a axial force in wall.

2) Shear strength equation for cylindrical walls

In the report, the overall shear strength is considered. The overall horizontal shear strength of cylindrical concrete wall is calculated using the effective shear area.

$$A_{eff} = \frac{A_{cv}}{\alpha} \tag{2-4}$$

where A_{cv} is the gross section area of the cylindrical walls; α is a factor according to moment-shear ratios (2.0 for walls with M/Vd_0 less than 0.5 and 2.5 for M/Vd_0 greater than 1.25, while linearly varying between the moment-shear ratios between 0.5 and 1.25); and d_0 is the outside diameter of the cylindrical wall.

The shear strength of cylindrical wall is determined based on Ogaki et al. (1981) and Aoyagi, et al (1981).

$$V_{n,EPRI} / A_{eff} = 0.8\sqrt{f_c'} + (\rho f_y)_{AVER} \tag{2-5}$$

$$\left(\rho f_y\right)_{AVER} = \frac{\rho_h + \rho_v}{2} f_y - \frac{\sigma_h + \sigma_v}{2} \tag{2-6}$$

$$V_{n,EPRI} \le 1.75\sqrt{f_c'} \tag{2-7}$$

where ρ_h and ρ_v are the hoop and meridional reinforcement ratios, respectively; f_c' is the concrete compressive strength; f_y is the yield stress capacity of the reinforcing steel; and σ_h and σ_v are the horizontal and vertical

stresses resulting from dead load, internal pressures, and lateral load (tension positive). The maximum shear strength of $1.75\sqrt{f_c'}$ is to prevent brittle web-crushing failure before re-bar yielding

2.2 Review of previous research for squat walls

2.2.1 Barda et al. (1977)

Barda et al. (1977) proposed a shear strength equation for squat walls based on the test results with boundary or barbell elements. The range of horizontal and vertical reinforcing bar ratios were 0.0 – 0.5 % and 1.8 – 6.4%, respectively. The equation showed as followed Eq. (2-8).

$$V_{n,barda} = \left(0.69\sqrt{f_c'} - 0.28\sqrt{f_c'}\left(\frac{h_w}{l_w} - \frac{1}{2}\right) + \rho_h f_y + \frac{P}{4 l_w h_w} \right) t_w d \quad (2\text{-}8)$$

The equation was independent with vertical and horizontal reinforcing bar ratio. The equation is applicable for squat walls with aspect ratio lower than 2.0 and with boundary elements. The equation proposed by Barda et al. (1977) was adopted by ASCE/SEI 43-05 and EPRI with modification.

2.2.2 Gulec and Whittaker (2011)

Gulec and Whittaker proposed an empirical shear strength equation to predict peak shear strength of rectangular walls, and flanged walls, respectively. The equations were for squat walls with aspect ratio lower than 1.0. For statistical analysis, the 277 test data were used to derive the equations (74 for rectangular walls, 79 for barbell walls, and 74 for flanged walls). The equations were consisted with seven optimized variables and six parameters: compressive strength of concrete, vertical, and horizontal reinforcing bar ratios in the area of web, vertical reinforcing bar ratio in the area of flange, axial load, and aspect ratio. The equation was presented as below Eq (2-9)

$$V_n = \frac{\beta_1 f_c{}'^{\beta_2} A_{web} + \beta_3 F_{vw} + \beta_4 F_{hw} + \beta_5 F_{vbe} + \beta_6 P}{(h_w / l_w)^{\beta_7}} \quad (2\text{-}9)$$

The optimized variables were found based on the nonlinear regression analysis. Table 2-1 shows the best estimated variables according to shear strength model.

Table 2-1 Coefficients for models to predict shear strength (Gulec and Whittaker, 2011)

Model ID	β_1	β_2	β_3	β_4	β_5	β_6	β_7
Wall without boudnary							
V_{1a}	1.29	0.5	0.26	0.04	0.20	0.39	0.58
V_{1b}	0.014	1.0	0.28	0.05	0.22	0.40	0.64
Wall with boudnary							
V_{2a} ($b_{eff}=b_f$)	0.04	1.0	0.30	0.12	0.12	0.37	0.51
V_{2b} ($b_{eff}=b_f$)	2.08	0.5	0.29	0.18	0.11	0.39	0.57
V_{3a} ($b_{eff}=h_w$)	0.04	1.0	0.34	0.05	0.13	0.35	0.49
V_{3b} ($b_{eff}=h_w$)	2.49	0.5	0.33	0.09	0.11	0.36	0.53
V_{4a} ($b_{eff}= h_w/2$)	0.04	1.0	0.43	-0.09	0.14	0.34	0.48
V_{4b} ($b_{eff}= h_w/2$)	2.91	0.5	0.43	-0.06	0.11	0.35	0.51
V_{5a} ($b_{eff}= h_w/4$)	0.05	1.0	0.52	-0.12	0.13	0.32	0.48
V_{5b} ($b_{eff}= h_w/4$)	3.21	0.5	0.52	-0.09	0.09	0.33	0.51

The first under subscript relation indicates the type of walls according to effective flange width. The second under subscript “a” and “b” indicates the β_2 is equal 0.5 and 1.0, respectively.

Form those two equations, Gulec and Whittaker selected two type of model for the walls with and without flanges and simplified the equation. The selected models were based on the best performance in shear predictions. For two equations, the contribution of horizontal reinforcing bars was not included. The two equations were simplified as in Eqs (2-10) and (2-11)

For walls without flange area

$$V_{REG,Gulec} = \frac{0.125\sqrt{f_c'}A_{web} + 0.25F_{vw} + 0.20F_{vbe} + 0.40P}{\sqrt{h_w / l_w}} \leq 0.83\sqrt{f_c'}A_{web} \quad (2\text{-}10)$$

For walls with flange area

$$V_{Flange,Gulec} = \frac{0.04 f_c' A_{web} + 0.40F_{vw} + 0.15F_{vbe} + 0.35P}{\sqrt{h_w / l_w}} \leq 1.25\sqrt{f_c'}A_{web} \quad (2\text{-}11)$$

The maximum shear strength limitation was proposed for walls with and without flanges, respectively, to prevent web-crushing failure. The shear strength predictions for wall were presented in Fig 2-1.

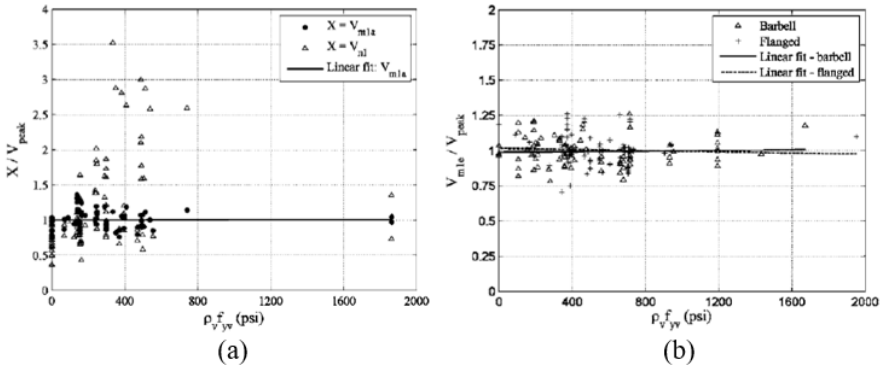

Figure 2-1 Variation of the predicted shear strength with respect to effective vertical reinforcing bar ratio in web (a) for walls without flange area, and (b) for with flange area. (Gulec and Whittaker 2011)

In addition, the shear strength equation based on ACI (Eq 2-12) and ASCE (Eq 2-13) equations were proposed with best-estimated coefficient.

$$V_{ACI,Gulec} = \left(\beta_1\sqrt{f_c'} + \beta_2\rho_h f_y\right)A_{web} \tag{2-12}$$

$$V_{ASCE,Gulec} = \left(\beta_1\sqrt{f_c'} - \beta_2\sqrt{f_c'}\frac{h_w}{l_w} + \beta_3\rho_{se}f_y + \beta_4\frac{P}{A_{web}}\right)dt_w \tag{2-13}$$

The optimized variables were summarized in the table 2-2.

Table 2-2 Coefficients for ACI and ASCE equations (Gulec and Whittaker, 2011)

Model ID	β_1	β_2	β_3	β_4
Wall without boundary				
$V_{ACI,Gulec}$	5.72	0.0		
$V_{ASCE,Gulec}$	6.79	0.91	0.20	0.64
Wall with boundary				
$V_{ACI,Gulec}$	10.70	0.22		
$V_{ASCE,Gulec}$	17.42	14.77	0.93	0.56

2.2.3 Hwang, et al. (2001)

Hwang, et al (2001) proposed a softened strut tie model based shear strength equation for squat walls. The proposed model originates from the strut-and-tie concept and satisfies equilibrium, compatibility, and constitutive laws of cracked reinforced concrete. The loading transferring mechanism of squat walls showed in Fig 2-2. The maximum shear strength was derived as following procedure.

1) From the force equilibrium, the compressive stress $\sigma_{d,max}$ resulting from the summation of the compressive forces from diagonal, flat, and steep struts (Fig 2-2 (d)) on the nodal zone can be calculated as Eq (2-13)

$$\sigma_{d,\max} = \frac{1}{A_{str}}\left\{ D - \frac{\cos\left(\theta - \tan^{-1}\left(\frac{h_w}{2l_w}\right)\right)}{\cos\left(\tan^{-1}\left(\frac{h_w}{2l_w}\right)\right)} F_h - \frac{\cos\left(\tan^{-1}\left(\frac{h_w}{2l_w}\right) - \theta\right)}{\sin\left(\tan^{-1}\left(\frac{h_w}{2l_w}\right)\right)} F_v \right\} \tag{2-13}$$

2) From constitutive laws, the maximum concrete strength was determined. The cracked concrete model of Zhang and Hsu (1998) was used. The stress-strain curve was presented as follows (Eq 2-14)

$$\sigma_d = -\xi f_c' \left[2\left(-\frac{\varepsilon_d}{\xi\varepsilon_0}\right) - \left(\frac{\varepsilon_d}{\xi\varepsilon_0}\right)^2 \right] \ldots for - \frac{\varepsilon_d}{\xi\varepsilon_0} \le 1 \tag{2-14}$$

3) From compatibility condition, the strains were calculated.

To verify the proposed strength prediction, a total of 62 test specimens and their available results in the technical literature were used and compared ACI 318-95 model (Fig 2-3). The average strength ratio ($V_{test}/V_{predict}$) in this approach is 1.18 with a coefficient of variation (COV) of 0.17.

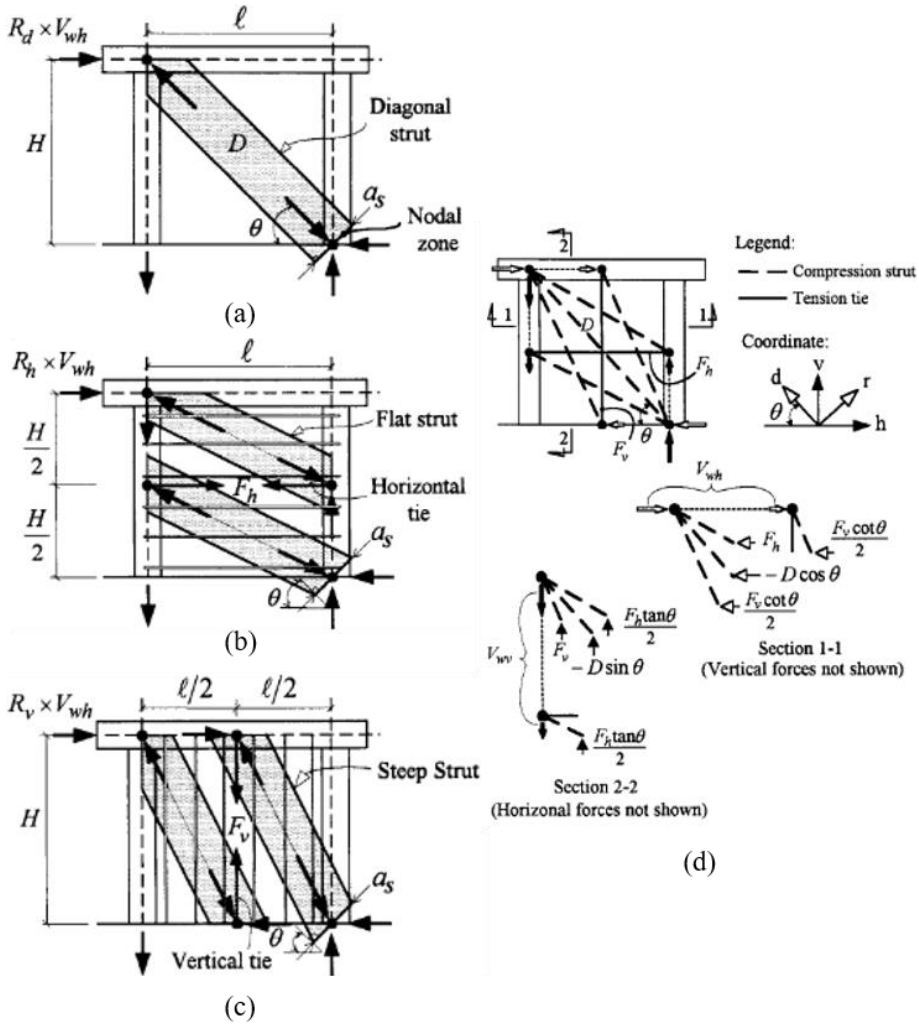

Figure 2-2 Wall shear resisting mechanisms: (a) Diagonal; (b) Horizontal reinforcing bars; and (c) Vertical reinforcing bars and (d) strut-tie model for squat wall (Hwang, et al (2001))

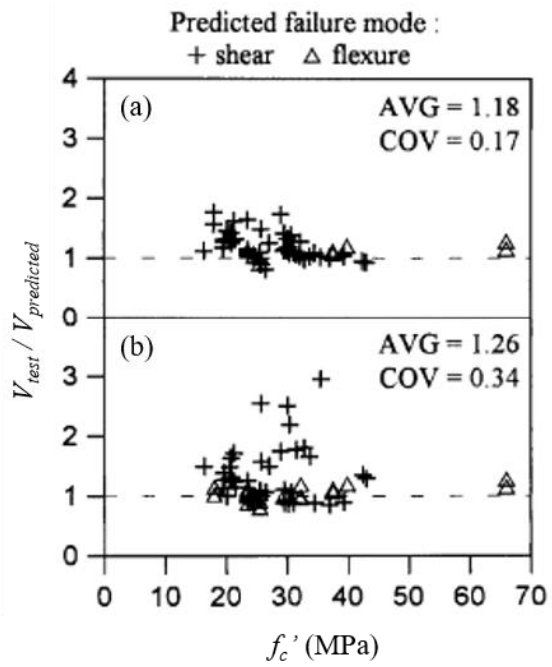

Figure 2-3 Correlation of experimental and predicted wall shear strength: (a) Proposed method; and (b) ACI 318-95

2.2.4 Luna and Whittaker (2019)

Luna and Whittaker (2019) were proposed an empirical shear strength equation for reinforced concrete walls with and without boundary element and low aspect ratio based on the twelve squat wall tests. The proposed equation was assumed idealized crack pattern and derived shear strength equation satisfying the force equilibrium condition (Fig 2-4). A wall was divided into three segments: Compression zone; diagonal strut zone; and tensile zone. Eqs (2-15) and (2-16) shows the proposed equation for with and without boundary elements, respectively.

1) Walls without boundary elements

$$V_{n,Luna} = V_{na} + V_{nb} + V_{nc} \rightarrow \begin{cases} V_{na} = \mu\left[\left(\rho_h t_w f_y + p\right)\left(\dfrac{h_w}{\tan\theta}\right) + pc\right] \\ V_{nb} = \left(\rho_h t_w f_y + p\right)\left(l_w - \dfrac{h_w}{\tan\theta} - c\right)\dfrac{1}{\tan\theta} \\ V_{nc} = \rho_v h_w t_w \left(0.25 f_y\right) \end{cases} \quad (2\text{-}15)$$

2) Walls with boundary elements

$$V_{n,Luna} = V_{na} + V_{nb} + V_{nc}$$

$$\rightarrow \begin{cases} V_{na} = \mu\left[\left(\rho_h t_w f_y + p\right)\left(\dfrac{h_w}{\tan\theta}\right) + pl_{be} + P\right] \\ V_{nb} = \left[\left(\rho_h t_w f_y + p\right)\left(l_w - \dfrac{h_w}{\tan\theta} - c\right) + \left(\rho_{be} t_w f_y + p\right)\left(l_{be}\right) + P\right]\dfrac{1}{\tan\theta} \\ V_{nc} = \rho_v h_w t_w \left(0.25 f_y\right) \end{cases} \quad \text{(2-16)}$$

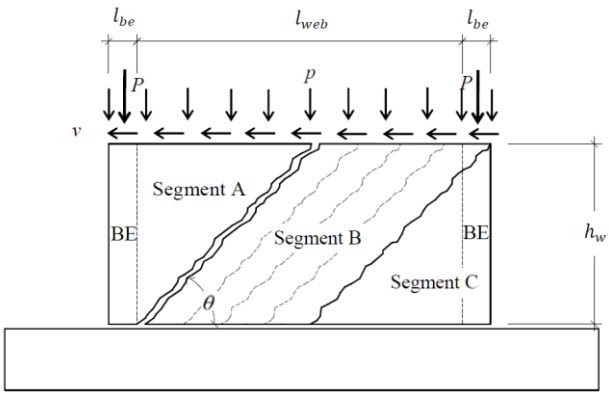

Figure 2-4 Idealized crack patterns of low aspect ratio RC wall (Luna and Whittaker, 2019)

where μ is a shear-friction coefficient. The equation about segment A V_{na} is presented as a shear-friction mechanism. The shear strength provided by segment B V_{nb} is derived from the force equilibrium condition of the diagonal strut. The V_{nc} which is provided by segment C is the contribution of horizontal reinforcement.

To simplify the equation, crack angle of 40° and shear-friction coefficient of 0.5 were assumed. Based on 74 shear-critical walls and using nonlinear regression analysis, optimized empirical shear strength equation for walls without boundary elements was proposed as Eq (2-17).

$$V_{n,Luna} = \frac{0.09\sqrt{f_c'}A_{eff} + 0.25F_{vw} + 0.08F_{hw} + 0.21P}{h_w / l_w^{0.81}} \quad (2\text{-}17)$$

2.3 Review of previous research for cylindrical walls

2.3.1 Ogaki, et al. (1981)

Ogaki, et al (1981) presents the results of experiments on shear strengths of prestressed concrete containment vessels subjected to lateral and torsional forces during earthquakes. The experiments consist of two kinds of static load tests with torsional and horizontal force, using 16 cylindrical concrete specimens (11 for torsional and 6 for horizontal loading). Ogaki, et al (1981) proposed a shear strength equation for cylindrical concrete walls in two methods.

1) The ultimate shear stress was set as follows Eqs 2-18 and 2-19.

$$\tau_u = \frac{\left[\left(\rho_w \sigma_y\right)_v + \left(\rho_w \sigma_y\right)_h\right]}{2} \tag{2-18}$$

$$\left(\rho_w \sigma_y\right)_x = \rho_{rx} f_y + \rho_{px} f_{py} - \sigma_x \tag{2-19}$$

where, ρ_{rx} and ρ_{px} are reinforcing bar and prestressing steel ratio in direction x, f_y and f_{py} are yield point stresses of reinforcing bar and prestressing steel, and σ_x is membrane stress in direction x due to applied load.

2) The ultimate shear stress of concrete considering redistribution of stress due to restringing force of steel was obtained by the failure envelope of concrete reported by Kupfer et al. (1969).

$$\tau_u = k\tau_{cu} \tag{2-20}$$

$$\tau_{cu} / f_c' = \begin{cases} -\left[e' + (1-0.8e')\sigma_A^*\right] \Big/ (1+0.8e') & \text{for } \left(\rho_w\sigma_y\right)_\theta = \left(\rho_w\sigma_y\right)_z \\ \sigma_B^* \tan(2\alpha) & \text{for } \left(\rho_w\sigma_y\right)_\theta \neq \left(\rho_w\sigma_y\right)_z \end{cases}$$

(2-21)

$$\sigma_A^* = \left[\left(\rho_w\sigma_y\right)_\theta + \left(\rho_w\sigma_y\right)_z\right] / 2f_c' \tag{2-22}$$

$$\sigma_B^* = \left[\left(\rho_w\sigma_y\right)_\theta - \left(\rho_w\sigma_y\right)_z\right] / 2f_c' \tag{2-23}$$

$$e' = \left|f_t / f_c\right|, \cos(2\alpha) = -(1+0.8e')\sigma_B^* \Big/ \left[e' + (1-0.8e')\sigma_A^*\right] \tag{2-24}$$

where, f_t and f_c are tensile and compressive strengths of concrete, respectively. The maximum shear strength of $1.75\sqrt{f_c'}$ (psi units) is to prevent brittle web-crushing failure before re-bar yielding.

The proposed prediction method was applied to evaluate the horizontal loading test results, and the results were shown together with the torsional loading tests in Fig (2-5). The equation proposed by Ogaki et al. (1981) was adopted by EPRI with modification.

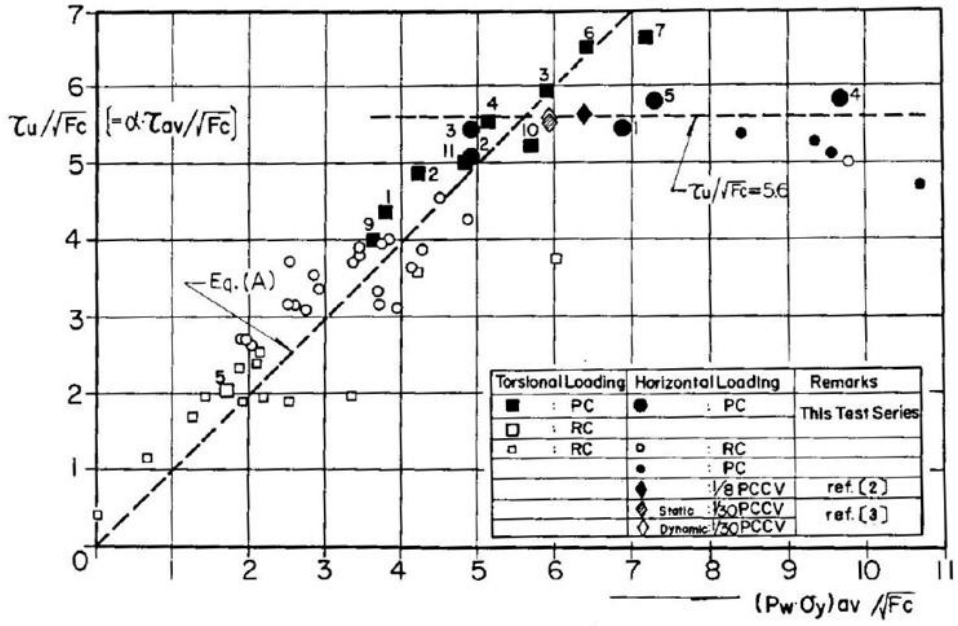

Figure 2-5 Relationship of shear strength and $(\rho_y \sigma_y)_{aver}$ (Ogaki, et al (1981))

2.3.2 Cho et al (2007)

Cho et al (2007) was conducted cyclic test using a cylindrical concrete wall. Before test, numerical analysis using MIDAS program was conducted. The type of element was 3-D shell element, and combination of plate bending and plane stress model was used. The 1/16 scale of containment building was designed. The vertical and horizontal reinforcing bar ratios were 0.8 % and 0.4 %, respectively. The dimensions of specimen were 2.15 m, 75 mm, and 1,400 mm for height of gravity center, thickness of wall, and exterior diameter of specimen, respectively. To prevent local failure at the top of specimens, steel struts were installed.

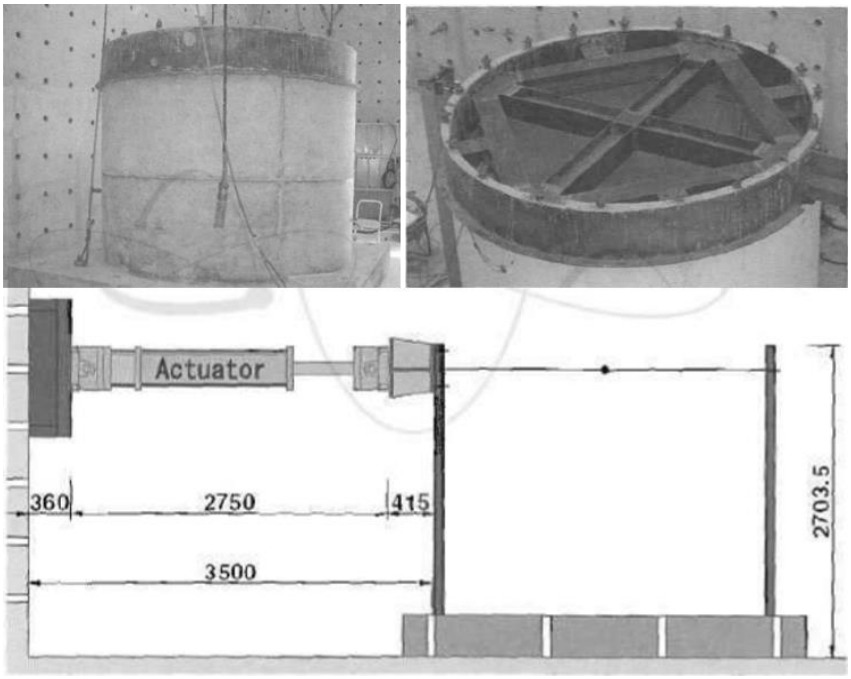

Figure 2-6 Test specimens and set-up (Cho et al (2007))

The test results were summarized as follows: the stiffness was decreased with cracking propagation; after reinforcing bar yielding, the stiffness degradation was occurred; the failure mode of specimen was shear failure at the bottom of wall and flexural failure, the maximum shear strength stress was 0.02 (kg/cm^2) (Fig 2-7); and the failure area was about 1/4 of total height (Fig 2-8). Especially, the failure area was as same as Ogaki et al (1981).

The results could be used as base data for evaluation or predictions of the shear failure behavior. In addition, the results could be used in evaluating the structural integrity of containment. The compatibility of existing failure scenarios could be checked. The local failure modes for each structural elements could be evaluated to effectively expect the aspects of failure behavior of the containment.

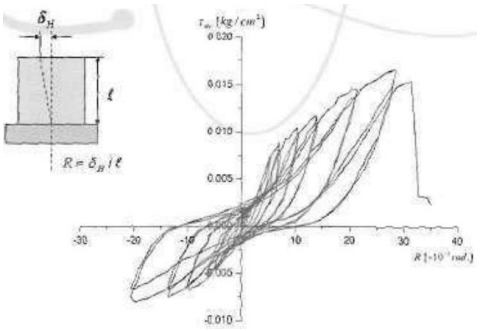

Figure 2-7 Relationship of shear stress and displacement (Cho et al (2007))

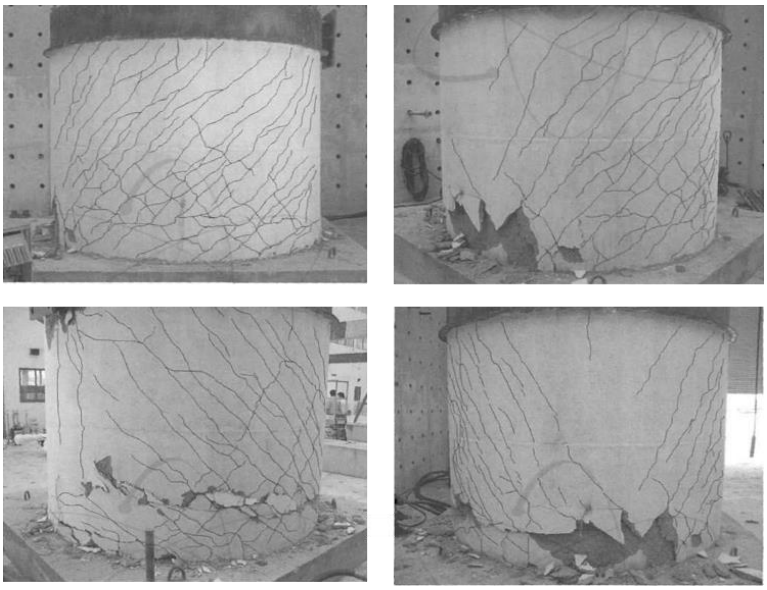

Figure 2-8 Failure mode of cylindrical wall (Cho et al (2007))

2.3.3 Völgyi et al (2014)

Völgyi et al tested reinforcing members with thick-walled hollow circular cross-sections to study their behavior under combined bending and shear. The test results were used to verify a proposed shear prediction model.

The basic equation of proposed mechanical model is the sum of the contribution of the compression zone and the contribution of the transverse reinforcement crossing the shear crack part. The contribution of the transverse reinforcement was calculated using Eq (2-25)

$$V_{s,Volgyi} = \sum A_s f_y e \tag{2-25}$$

where e is a vertical component of the tangent unit vector along the helical bars.

The contribution of the compression zone was similar to that of sliding surfaces from soil mechanics. The contribution was calculated follows Eqs 2-26 and 2-27

$$V_{s,Volgyi}{}^{*} = V_c \left(1+\rho_v \eta_s\right) \frac{E_s}{E_c} \tag{2-26}$$

$$\eta_s = 1 - 0.3\frac{R-v}{R} \tag{2-27}$$

where v is a validity of the proposed composite action factors which is the range from D/6 to D/3.

This model took into account how the amount of longitudinal and transverse reinforcement, the wall thickness of the cross-section, the strengths of concrete and reinforcing bars, the load-to-support distance and the simultaneity of bending moment and axial force with shear force influence the resistance of the member.

2.3.4 Wu, et al (2017)

In the Wu et al (2017), the structural behavior of cylindrical concrete containment specimens subjected to reversed cyclic loadings. Two specimens with an exterior diameter 2.5 m, interior diameter of 2.2 m and a height 2.25 m. The reinforcing bar ratio was 2.0 %. Figure 2-9 shows the test set up. To prevent flexural failure, vertical actuators and zigs were used.

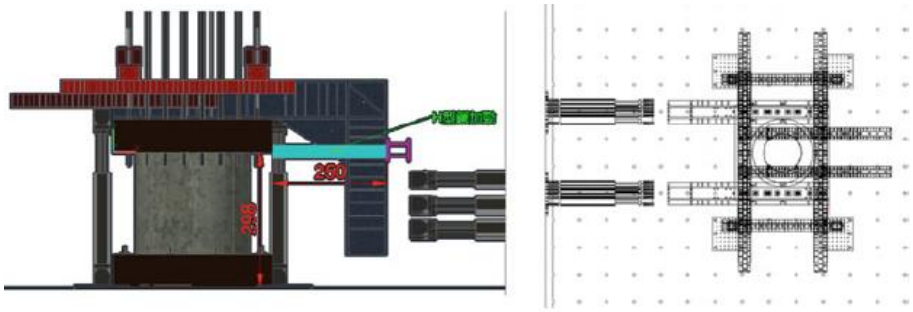

Figure 2-9 Test set up (Yang, et al (2017))

The failure modes of specimen were sliding shear and web crushing failure. Figure 2-10 shows the failure mode of specimens. The maximum shear strength were 5580 kN and 6113 kN at the sliding and web-crushing failure specimens, respectively. The other reactions at important state were summarized in the Table 2-3.

Table 2-3 Critical states of engineering importance (Yang, et al (2017))

Model ID	Horizontal force		Interstorey drift (%)	
	Sliding	Shear	Sliding	Shear
Initial crack of concrete	1,993	2,095	0.077	0.073
Peak strength	5,580	6,113	0.743	0.899
Drift ratio at 1%	2,227	4,245	1.002	1.000
First yield of horizontal rebar	3,634	3,338	0.35	0.276
First yield of vertical rebar (Top and bottom)	2,144	1,660	0.156	0.099
First tield of vertical rebar (Middle)	-	4,426	-	0.427

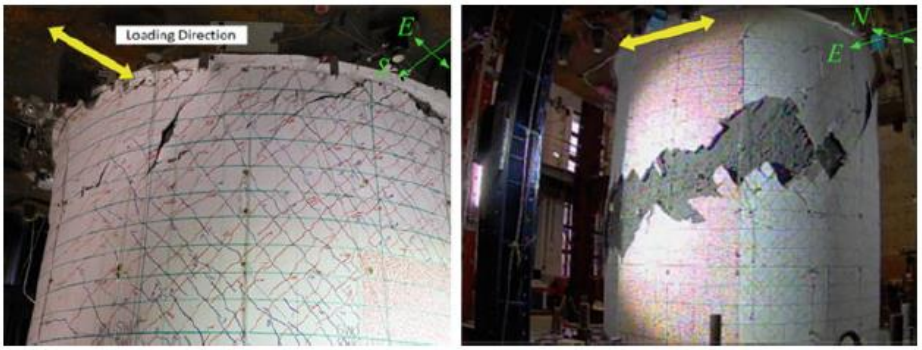

(a) Specimen 1: Sliding shear (b) Specimen 2: Web shear

Figure 2-10 Photographical view of specimen failure modes at the peak strengths (Yang, et al (2017))

2.3.5 Previous literatures about delamination failure at containment

The delamination cracks were observed at dome and walls of containment building due to curved post-tensioned forces. In this section, dome and wall delamination failures, and previous researches which were related to delamination failure are summarized.

2.3.5.1) Dome delamination failure

In 1970, dome delamination of Turkey Point Nuclear power plant Unit 3 was discovered. Concrete surface cracking and sheathing filler leakage was observed at various locations on the dome surface after post-tensioning operation. Design details of the delamination dome was found to be not adequate for structural performance, so a repair plan was proposed. The top layer of delaminated concrete was removed from the dome, radial reinforcement was anchored, and new concrete was placed against the inner layer of concrete. (Florida Power and Light Company (1970))

After the investigation at the Turkey Point Nuclear Power Plant Unit-3, several provisions were incorporated in the ACI 359: Provide sufficient allowable compressive stress criteria to prevent concrete delamination; requirement about radial tensile reinforcement in the double curved section.

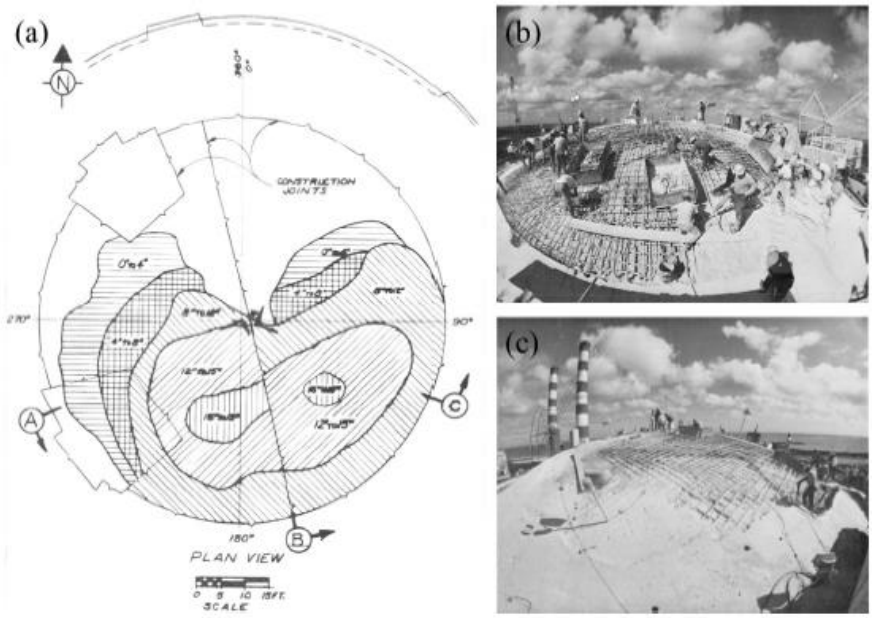

Figure 2-11 Dome delamination of Turkey Point Nuclear Power Plant (Florida Power and Light Company (1970))

In 1976, the dome delamination of Crystal River Nuclear Power Plant Unit - 3 was observed (Florida Power Corporation (1976)), and in 1994, the other dome delamination was observed at Kaiga Atomic Power Project Unit-1 (Basu and Cupchup (2001).

2.3.5.2) Wall delamination failure

In October 2009, wall delamination was discovered in nuclear containment of Crystal River Nuclear Power Plant Unit-3 using the construction of an access opening in the containment wall for the steam generator replacement (Nuclear Regulatory Commission (2010)).

Figure 2-12 Wall delamination at the Crystal River Nuclear Power Plant Unit-3 (Nuclear Regulatory Commission (2010))

After this incident, an extensive investigation about delamination was promptly performed to identify the possible causes of the delamination. Based on the investigation, it was found that the primary cause of the wall delamination is sequence of de-tensioning of tendons. The repair plan of wall delamination as follows: additional tendons were de-tensioned; delaminated concrete removed; reinforcement was installed to resist radial tensile stress; new concrete was placed; and tendons were re-tensioned.

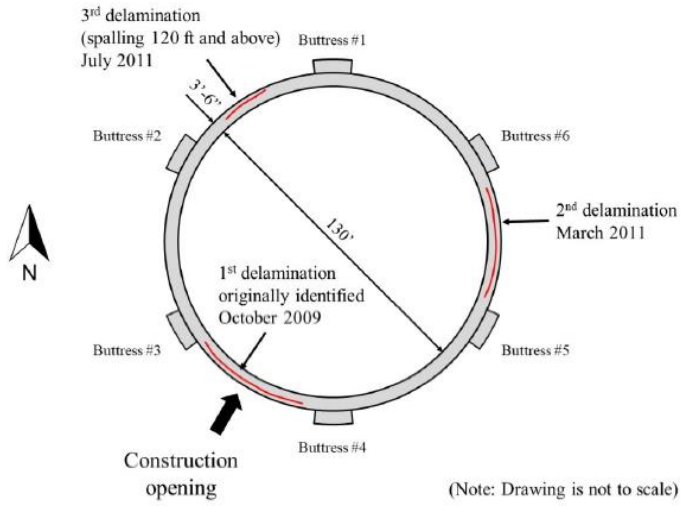

Figure 2-13 Location of the construction opening and wall delamination (Lehman et al. 2011)

2.3.5.3) Choi et al (2018)

Choi et al (2018) prepared three curved post-tensioned concrete walls and tested to delamination failure under monotonically increasing prestressing loads.

The delamination cracking initiated near the ducts and propagated away from the ducts. At approximately circumferential compressive stress levels about 0.09 ~ 0.24 f_c', the delamination crack were observed. This level of stress was considerably less than the service stress limit of 0.35 f_c' provided by the provisions of ACI-359.

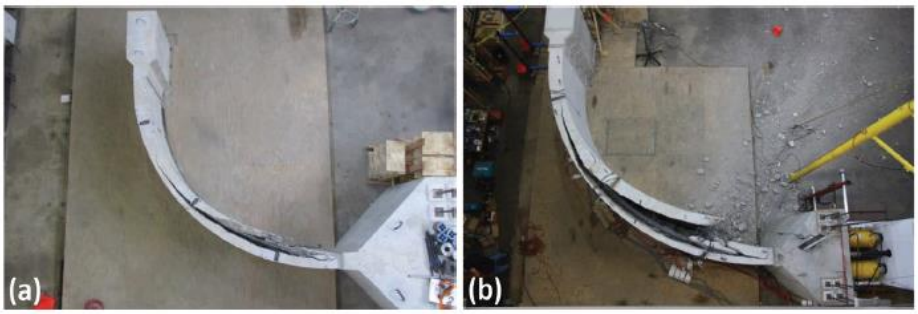

Figure 2-14 Specimens after delamination failure (Choi et al (2017))

Choi proposed that for design recommendations of a concrete containment structures. Lower bound estimates for the tensile strength of concrete could be used as a conservative assumption in designing to prevent delamination failures.

2.3.5.4) Bae (2013).

Bae (2013) reported the radial tension due to curved tendons and introduced a classical theory on a curved beam and provides the relationship between radial stress and moment acting in a curved section. The radial pressure due to curved tendons generates radial tension in an outer concrete section and radial compression in an inner section. The stress distribution of tension can be calculated using the following Eqs 2-28 - 30 (Acharya and Menon, (2003))

$$p = \frac{P}{R_{ps} w} \tag{2-28}$$

$$\sigma_{r,out} = \alpha p \tag{2-29}$$

$$\sigma_{r,\text{in}} = \left(1-\alpha\right) p \tag{2-30}$$

where p is a radial pressure, P is a prestressing force in tendon, R_{ps} is a radius of prestressing tendon, w is a width of cross-section, and $\alpha = \frac{b - R_{ps}}{b - a}$.

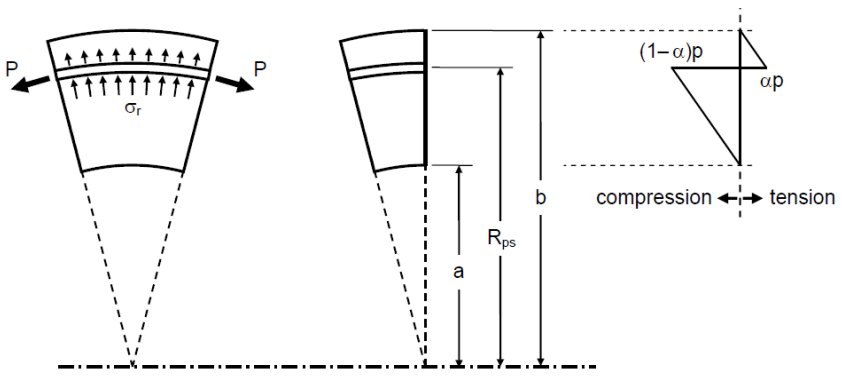

Figure 2-15 Radial stress due to curved tendon (Bae (2013))

From the radial stress due to moment in a curved beam can be expressed as Eq (2-31)

$$\sigma_r = \frac{R_C - e}{wAer} M \left(\int_a^r d \frac{A_1}{r_1} - \frac{A_r}{R_c - e} \right) \tag{2-31}$$

where R_c is a centerline radius, t is depth of cross section, A is a cross-sectional area, A_r is $\int_a^r dA_1$, and e is $\frac{l_c}{R_c A}$ for $\frac{R_c}{t} > 8$.

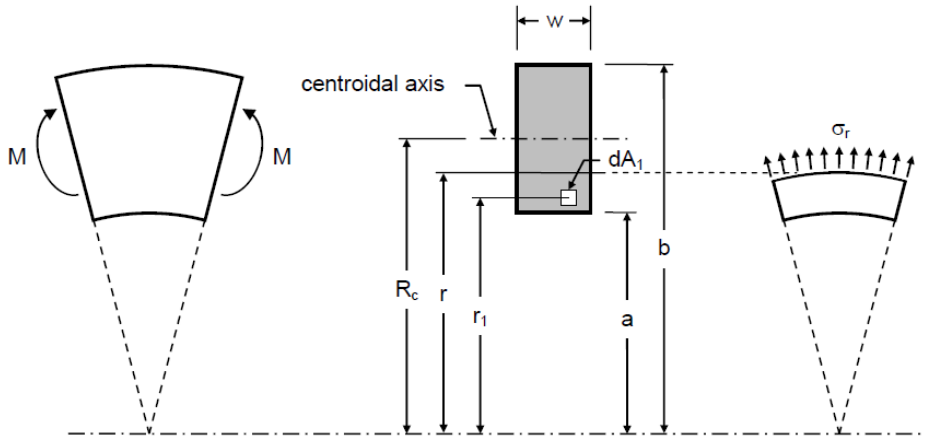

Figure 2-16 Radial stress in a curved beam due to moment (Bae (2013))

Bae (2013) reported prestressing force and moment on radial stress in containment structures and compared the theoretical results and FE analysis showing that the maximum radial stress can be better estimated by theoretic equations.

Chapter 3. Structural Test for Effect of High Frequency Earthquakes

In this chapter 3, to investigate the effect of high-frequency earthquakes on reinforced concrete wall, the dynamic loading test and shaking table test were conducted. The two tests were conducted to verify additional or side effects that may occur in high-frequency earthquakes.

3.1 Experiment I: Dynamic loading test

This chapter is modified version of the published paper of Baek, et al (2020) and has been reproduced here.

3.1.1 General

In 2016, due to the high magnitude of earthquakes, the nuclear power plants were stopped according to the manual for the safety of nuclear power plants. Due to the high seismic capacity of the nuclear power plant, structural damage was not observed. The concern about the seismic safety of nuclear power plants was increased. In the current seismic evaluation, the safety of nuclear power plants has been evaluated under a static strain rate. Thus, the current design codes for the earthquake design of reinforced concrete ACI 318 or ACI 349 are based on the experimental results of the quasi-static test. In fib Model Code 2010, to address the effect of strain rate, dynamic increase factors (DIFs) for yield strength (f_{dy}/f_y) and tensile strength (f_{du}/f_u) of steels, and for ultimate concrete strength (f_{dc}'/f_c') were specified for the design of reinforced concrete elements under high strain rates.

Since recent large-scale earthquakes, the ground acceleration demand has increased even for seismic evaluation of existing nuclear power plants. In the case of high-magnitude of earthquakes, the velocity of ground acceleration or floor response is increased as the peak ground acceleration increases. Because

the strain rate of a reinforced concrete member is related to the velocity of loading, the effect of the loading rate is increased. For this reason, the seismic margin analysis requires to be re-evaluated considering the strain rate effect. As a part of such re-evaluation research, the effect of the loading rate on the reinforced concrete walls needs to be studied.

Such high loading rate may change the failure mode, and strength of the structure. Loading rate can be categorized into static (lower than 10^{-5} s^{-1}), intermediate (from 10^{-5} s^{-1} to 10 s^{-1}), and high level (over 10 s^{-1}). Especially, the range of intermediate requires consideration of inertia forces (i.e. earthquake loading). In the case of earthquake loading, the loading rate of structure is higher than static state. For plain concrete, a logarithmic increase occurred in the compressive strength as the loading rate increased.

Such characteristics of material properties under different strain rate can change the capacity and failure modes of reinforced concrete wall. Most researches of loading rate on reinforced concrete member were for the beam member. Mutsuyoshi and Machida (1984) reported the failure mode change of beams. The failure mode was changed from flexural yielding to shear failure as the strain rate increased. On the other hand, in the research of Kulkarni and Shah (1998), the test result reported that the failure mode was changed from shear to flexural yielding with high loading rate. These results indicate that the capacity and failure mode of reinforced concrete member are changed according to loading rate.

In the previous research of Chung and Shah (1989), beam-column joint specimens were tested under different rates (0.0025 Hz and 0.5 Hz). The results

of research were as follows: 1) Low ductility was occurred under high loading rate. 2) In the case of high-loading rate, the width of cracks was increased, and the number of crack were decreased. The damages were concentrated at the interface between in the beam and column. 3) Due to the concentration of damage, the shear strength of the specimen was decreased under high loading rate. However, the effect of high loading rate was not significant at the specimens with a high reinforcing bar ratios.

In the case of reinforced concrete columns, the specimens were tested under different loading rates (Ghannoum et al (2012)). The research reported that the lateral peak strengths of columns were increased under high loading rate, but significant post-peak shear strength degradation was occurred.

Previous researches reported the effect of loading rate on reinforced concrete members. However, the only few experimental researches on squat wall as nuclear power plant was conducted. Furthermore, most existing tests under high loading rates were focused on the impact of blast loading which are higher strain rate than seismic loading. In addition, most of design or evaluation equations were derived from static experiments or data. To increase the accuracy of seismic margins for nuclear power plant, the effect of loading rate on capacity is considered. In the case of shaking table test, due to the complexity of test results, the test results were mixed the various parameters and effect of loading rate.

In this chapter, to investigate the effect of loading rate on shear strength, reinforced concrete wall specimens were tested under low and high loading rates. The major parameters of test were the loading rates, failure modes of

reinforced concrete wall, aspect ratio, and reinforcing bar ratio. Based on the test results, the effect of loading rate on peak strength, stiffness, and strain distribution was studied.

3.1.2 Test Plan

3.1.2.1) Loading rate

To investigate the effect of high frequency earthquakes, dynamic loading test was conducted. The test method was summarized as follows: 1) Use the same loading protocol. 2) In the case of high loading rate, the loading rate was increased. 3) Stop for 0.2 seconds at the maximum drift ratio of each cycle to exclude other dynamic effects except for loading rate.

The loading rate 100 (mm/s) was calculated based on the maximum velocity of walls estimated from an elastic time history analysis of an auxiliary building of nuclear power plant subjected to 0.3g ground accelerations. The target building of time history analysis was auxiliary building. The natural frequency of analysis model was 5.6 and 6.2 Hz for x- and y-axis and 5% of damping ratio was used.

3.1.2.2) Major Test parameters

The test specimens were designed considering characteristics of the nuclear power plant buildings. Because of high seismic requirement, the reinforcing bar ratios were very high. Total eight number of specimens were prepared: Three specimens were for static loading; and five specimens were for dynamic loading. The aspect ratio (h_w/l_w) of specimens were 1.0 and 0.5, three specimens with h_w/l_w = 0.5, and five specimens with h_w/l_w = 1.0. The main test parameters are

summarized in Table 3-1 and Figs 3-1 and 3-2: aspect ratio, design failure mode, sectional shape, compressive strength of concrete, reinforcing bar ratios, and loading rate.

The specimen names indicate the design parameters used for the specimens. The first letter ‘P’ refers to a planar shape of specimen. Although not refer in this chapter, the first letters ‘C’, and ‘B’ are used for a cylindrical shape of specimen and a barbell shaped wall, respectively. The second letter ‘R’ refers to a reinforced concrete wall without prestressing. The other second letter ‘P’ to be mentioned in chapter 4 refers to a prestressed concrete wall. The third letters ‘S’ and ‘D’ refer to static and dynamic test, respectively. To simulate the `static and dynamic loading effects, loading rates of 1 and 100 (mm/s) were respectively applied. The fourth letters ‘F’, ‘M’, and ‘S’ indicate the design failure modes: F, M, S refer to Flexural yielding, Shear-friction, and Shear failure mode, respectively. The failure mode was controlled by the vertical reinforcing bar ratio of flanges. The numbers ‘1.0’ and ‘0.5’ refer the aspect ratio (h_w/l_w) of specimens. The last letters ‘H’ and ‘M’ indicate the horizontal reinforcing bar ratio: H and M refer to 0.5% and 1.0%, respectively.

Three pairs of identical twin specimens were directly compared to investigate the effect of loading rate on failure mode and strength. The pairs which were (PRSF1.0H and PRDF1.0H), (PRSM0.5H and PRDM0.5H), and (PRSS1.0H and PRDS1.0H) were for flexural yielding, shear-friction, and shear failure modes, respectively. For shear-friction failure specimens, an aspect ratio of 0.5 was used to induce a higher shear demand force with lower flexural moment.

Table 3-1 Major test parameters of dynamic loading test for planar walls

Specimens	f_c' ,MPa	Aspect ratio	Design failure mode	Loading rate, (mm/s)	μ_{ACI}	Reinforcing bar ratios			Design strength prediction		
						ρ_h, %	ρ_v, %	ρ_f, %	V_f, kN	V_n, kN	V_{sf}, kN
PRSF1.0H	35.8	1.0	Flexural	1	0.6	0.51	0.47	4.05	823	836	1,332
PRDF1.0H	35.8			100	0.6	0.51	0.47	4.05	823	836	1,332
PRDF1.0M	35			100	0.6	0.93	1.19	5.75	1,128	1306	1,650
PRDF0.5H	41	0.5		100	1.4	0.51	0.47	1.94	851	848	1,942
PRSM0.5H	41		Shear-friction	1	0.6	0.51	0.47	1.94	851	848	832
PRDM0.5H	41			100	0.6	0.51	0.47	1.94	851	848	832
PRSS1.0H	36	1.0	Shear	1	0.6	0.51	0.47	11.5	1,960	848	1,650
PRDS1.0H	36			100	0.6	0.51	0.47	11.5	1,960	848	1,650

Note: f_c' is a concrete compressive strength; aspect ratio is h_w/l_w; μ_{aci} is a coefficient of shear-friction of ACI-349; ρ_h, ρ_h, and ρ_h, are reinforcing bar ratios of horizontal, vertical in the web area, and vertical in the flange area, respectively; V_f is a flexural strength prediction; V_n is a shear strength prediction; and V_{sf} is a shear-friction strength prediction.

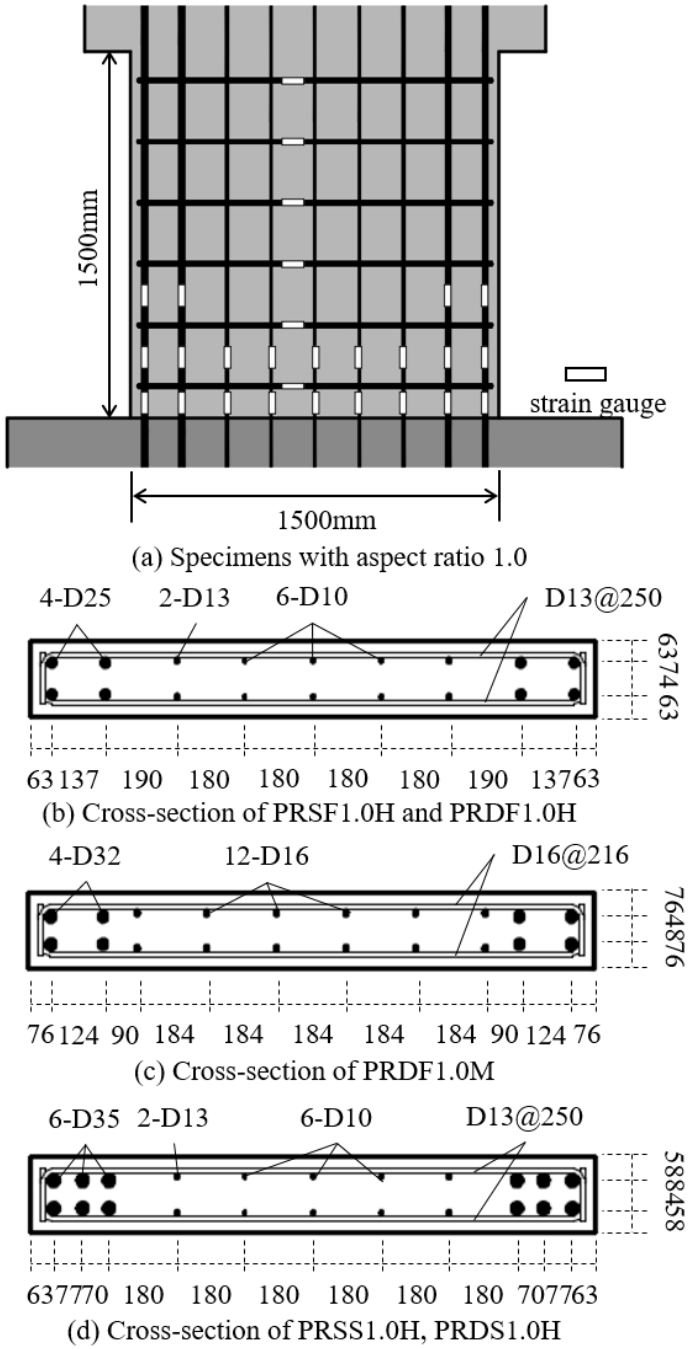

Figure 3-1Dimensions and reinforcement details of specimens with aspect ratio 1.0

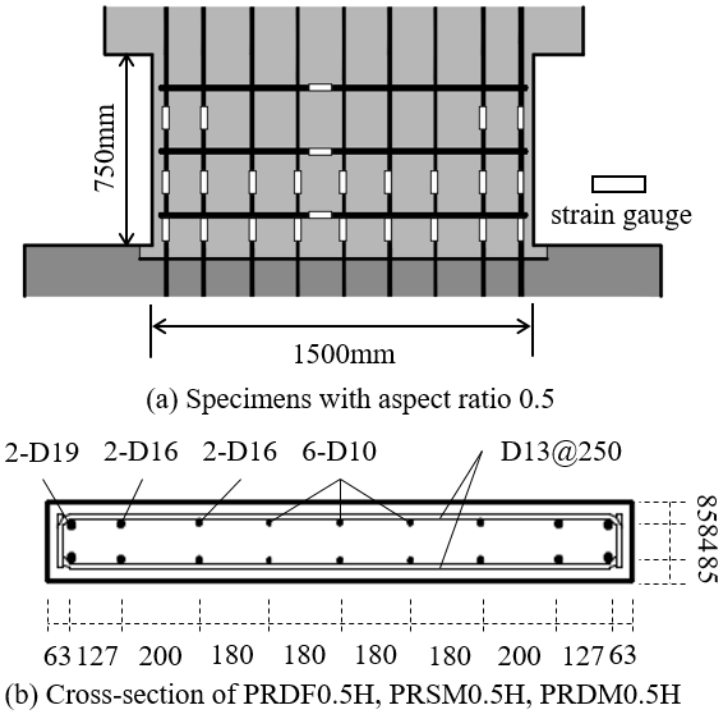

Figure 3-2 Dimensions and reinforcement details of specimens with aspect ratio 0.5

3.1.2.3) Design of test specimens

The dimension of walls with aspect ratio of 1.0 and 0.5 were 1500 mm (length) × 1500 (height) × 200 mm (thickness), and 750 mm × 1500 mm × 200 mm, respectively (Table 3-1 and Figs 3-1 and 3-2). Due to high seismic demand, the shear reinforcement ratio s close to the maximum value permitted by current design codes: in the case of ACI 349[2]. The maximum horizontal reinforcing bar ρ_{max} is closed to 0.9% for Grade 420 MPa. Due to limitation of capacity of the dynamic actuator (maximum force 2,000 kN and maximum velocity 150 mm/s), approximately half of the maximum horizontal reinforcing bar ratio was used for majority of specimens (Table 3-1).

In flexural yielding failure specimens PRSF1.0H and PRDF1.0H, Grade 420 MPa, D13 (No. 4) reinforcing bars with a spacing of 250 mm were used for shear reinforcement; the ratio of shear reinforcement ρ_h was 0.51 % which is half of the permissible maximum shear reinforcement ratio specified by ACI 349. The nominal flexural strength V_f = 823 kN estimated by sectional analysis (using the linear strain distribution assumption and the stress-strain relationships of concrete and reinforcing bars, MacGregor et al (1997)). The nominal shear strength V_n predicted by ACI 349 was 836 kN. Due to conservative nature of the ACI design shear equation, flexural yielding was generally expected before shear failure, even if the nominal flexural and shear strength was close. Meanwhile, using a shear-friction coefficient of 0.6, the shear-friction strength V_{sf} was estimated to be 1,332 kN which was much larger than nominal flexural or nominal shear strength. The friction coefficient was

0.6, specified as ‘not intentionally roughened. The table 3-2 shows the friction coefficient of ACI 349. The vertical reinforcing bar ratios in the web ρ_v and in the flange ρ_f were 0.47 % and 4.05 %, respectively. The flange area was defined as the area including all boundary bars and cover concrete. The cross section of the web was defined as the wall area excluding the boundary area.

To investigate the strain rate effect on walls with high reinforcing bar ratio, the maximum shear reinforcing bar ratio (ρ_h = 0.91) was used for specimen PRDF1.0M. D16 (No. 5), Grade 420 MPa reinforcing bars were used for horizontal reinforcing bars with spacing 215 mm. Due to increment of reinforcing bar ratio, the nominal shear strength (V_n) was increased to 1,306 kN. To ensure flexural yielding failure before shear sliding or shear failure, the ratios of vertical reinforcement in the web (ρ_v) and flange (ρ_f) were increased to 1.19% and 5.75%, respectively. Thus, the nominal flexural (V_f) and shear-friction (V_{sf}) strength were increased to 1,228 kN and 1,650 kN, respectively. The other details were the same as those of PRDF1.0H.

The other flexural yielding specimen PRDF0.5H with aspect ratio 0.5 was prepared to investigate the effect of loading rate on aspect ratio. To prevent premature shear-friction failure, the interface between wall and basement was intentionally moved down 50 mm into the inside of the foundation. Thus, the wall-slab interface can be regarded as a monolithic joint. In the walls, ρ_f and ρ_v were 1.94 % and 0.47%, respectively, while ρ_h was 0.51 %. Based on ACI 349, the shear-friction strength was significantly increased to V_{sf} = 1,942 kN, which was greater than the flexural strength (V_f = 851 kN). The shear strength V_n was 848 kN.

In the shear-friction failure specimens (PRSM0.5H and PRDM0.5H), the aspect ratio was 0.5 to induce shear-friction failure. In the walls, the details of reinforcing bar were the same as that of the flexural yielding failure specimens with aspect ratio 0.5 (PRDF0.5H). The only different variable was the interface of wall and slab because of separated placement of concrete. The shear-friction coefficient should be used to 0.6. Thus, the shear-friction strength V_{sf} was calculated as 832 kN. The other nominal strengths (V_f and V_n) were the same as those of PRSF0.5H.

In the case of shear failure specimens (PRSS1.0H and PRDS1.0H), the flexural reinforcing bars in the flange area, were intentionally increased to induce shear failure before flexural yielding. Grade 420 MPa 12-D35 reinforcing bars were used for flexural reinforcement in the flange area. Thus, the nominal flexural yielding strength V_f was 1,960 kN and the shear-friction strength V_{sf} was 1,650 kN. The nominal shear strength V_n which is related to the horizontal reinforcing bar ratio was 836 kN. The other details were the same as those of specimens with aspect ratio 1.0.

Table 3-2 Shear-friction coefficient specified in ACI 349

Surface condition	μ
Concrete placed monolithically	1.4
Concrete placed against hardened concrete that is clean, free of laitance, and intentionally roughened to a full amplitude of approximately 1/4 in.	1.0
Concrete placed against hardened concrete that is clean, free of laitance, and not intentionally roughened	0.6
Concrete placed against as-rolled structural steel that is clean, free of paint, and with shear transferred across the contact surface by headed studs or by welded deformed bars or wires	0.7

3.1.2.4) Test procedure and instrumentation

A cyclic lateral loading was applied using the test set-up shown in fig 3-3. The lateral loading was applied with an increasing drift ratio according to ACI 374.2 with and cyclic loading was repeated three times.at each drift ratio. The drift ratio increased 1.25 to 1.5 times the previous drift ratio (fig 3-4). In nuclear power plant walls, the axial force load ratio is typically low, ranging from approximately 0.05 to 0.20 $A_c f_c'$. Thus, the effect of axial force does not significant. The test proceeded in this test until the specimen's load-carrying capacity decreased to 50 % of the maximum strength.

In high loading rate tests, the inertial force of the specimen and mechanical supports may affect the behavior of the wall. Due to inertia force, at the maximum drift, unexpected additional drift might be occurred. Thus, the loading was paused for 0.2 seconds at the maximum drift ratio at each loading step.

Figure 3-3 shows the linear variable displacement transducers (LVDTs) for the measurements of lateral displacement (L1), flexural deformations (L3 to L8), shear deformations (L9 to L12) and sliding at the base (L13). Figure 3-1 shows the locations of the strain gauges for the reinforcing bars.

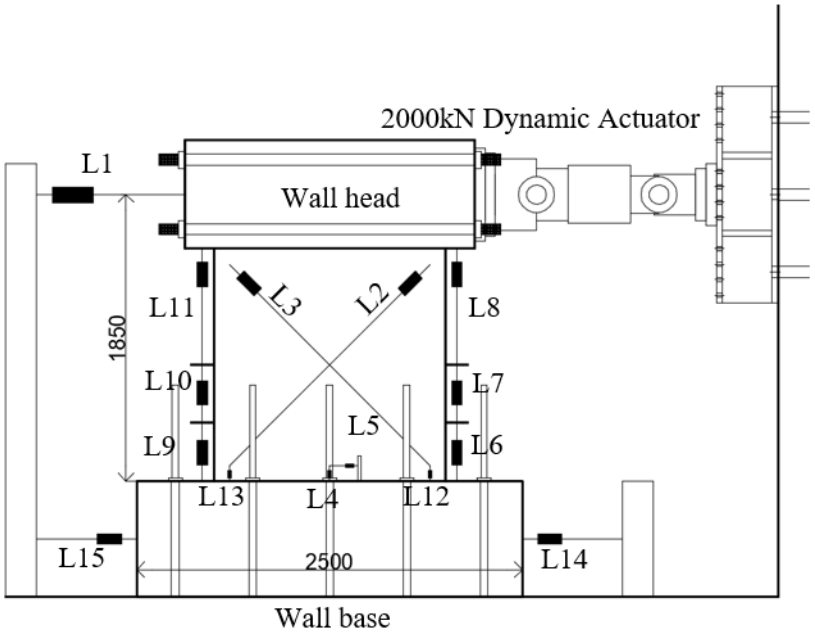

(a) Aspect ratio 1.0 specimen

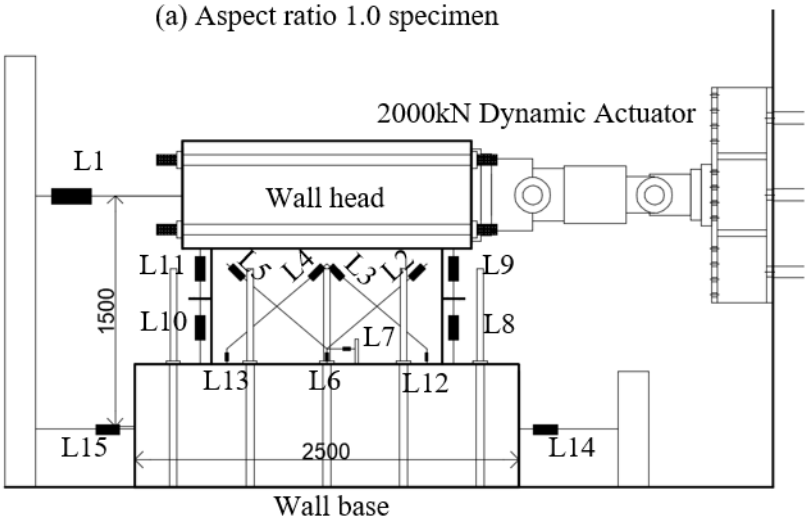

(b) Aspect ratio 0.5 specimen

Figure 3-3 Test set-up

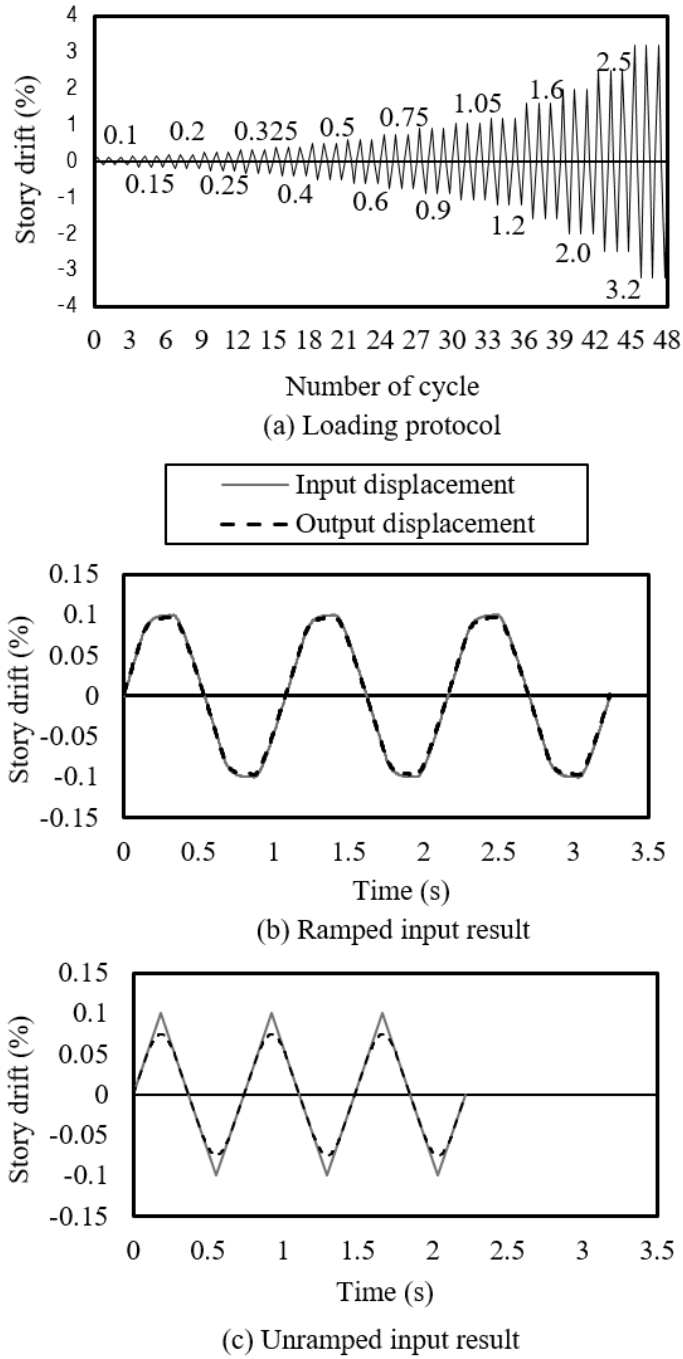

Figure 3-4 Loading protocol and ramped input

3.1.3 Test results

3.1.3.1) Material test results

In the Table 3-3, the material test results obtained under static loading and dynamic loading. Three pairs test coupons were tested for the reinforcing bars, and the average values are presented in Table 3-3. The strain-stress curve are shown in Fig 3-5. Dynamic loading tests were conducted for only D13 and D25 reinforcing bars. According to increasing the strain rate 100 times, the yielding strengths of reinforcing bars were increased from f_y = 479 MPa and f_y = 445 MPa to f_y = 519 MPa and f_y = 460 MPa for D 13 and D25, respectively. The increases in yield strength were 3.3 % to 8.3 %.

In the case of the concrete, the compressive strength f_{ck}' tests were conducted on the same day as the structural experiments. The compressive strength under the high loading rate was in the range of 0.96 f_{ck}' to 1.008 f_{ck}', where f_{ck}' is the compressive strength under static loading rate.

Table 3-3 Properties of reinforcement

Type	D10	D13	D16	D19	D25	D29	D32	D35
Grade	420 MPa							
Bar diameter	9.53 mm (No. 3)	12.7 mm (No. 4)	15.9 mm (No. 5)	19.1 mm (No. 6)	25.4 mm (No. 8)	28.6 mm (No. 9)	31.8 mm (No. 10)	34.9 mm (No. 11)
Yield strength under static loading rate (5.4×10^{4} s^{-1})	534	479	475	490	445	462	503	544
Yield strength under dynamic loading rate (5.4×10^{2} s^{-1})	-	519	-	-	460	-	-	-

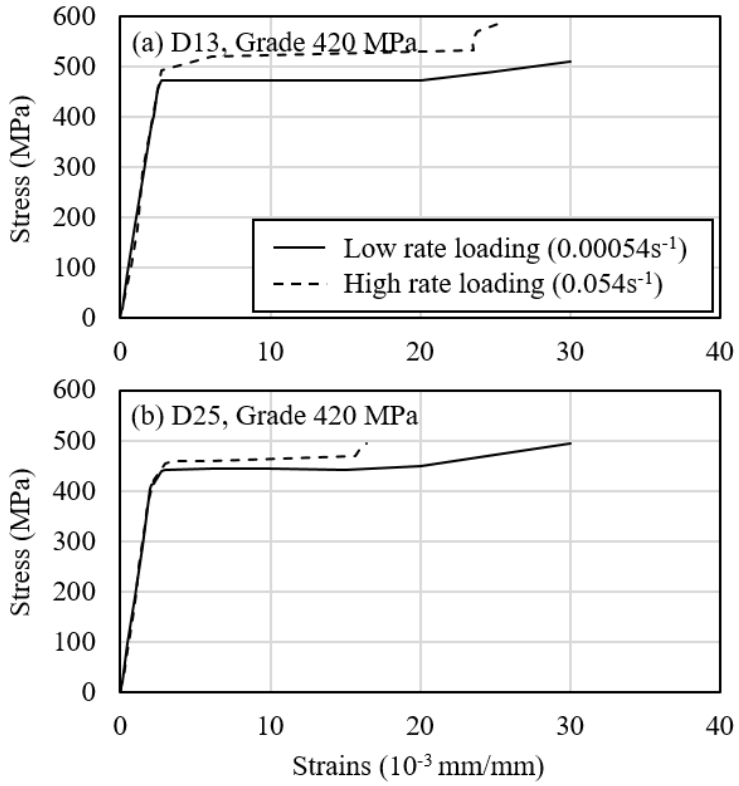

Figure 3-5 Comparison of stress-strain relationships of reinforcing bars under static and dynamic loading

3.1.3.2) Damage modes of wall specimens

Test results are summarized in Table 3-4. Figure 3-6 shows the comparison of crack propagation of the specimens PRSF1.0H and PRDF1.0H (low loading rate and high loading rate specimens with flexural yielding failure) at drift ratios of 0.2, 0.32, 0.5, and 0.75 %. The properties of PRSF1.0F and PRDF1.0H were identical same except for the loading rate. In both specimens, at a drift ratio 0.2 %, the first horizontal cracks occurred at the boundary area of walls (Figs 3-6 (a) and (b)). The horizontal cracks propagated to diagonal shear cracks (Figs 3-6 (c) and (d)) at a drift ratio 0.32 %. As the drift ratio increased further, the diagonal cracks occurred (Figs 3-6 (e) and (f)). In case of the dynamic loading rate specimen PRDF1.0H, at the maximum load, the number of flexural cracks was 20 % less than that of the static loading specimen (PRSF1.0H). On the other hand, the number of diagonal cracks was the same in static and dynamic test.

Figure 3-7 shows the flexural failure modes of the specimens at the end of testing (PRSF1.0H, PRDF1.0H, PRDF1.0M. and PRDF0.5H). At a drift ratio of 2.0 %, due to concrete crushing at the wall end, PRSF1.0H failed, followed by vertical reinforcing bars buckling (Fig 3-7 (a)). On the other case of dynamic specimen PRDF1.0H (Fig 3-7 (b)), similar damages with PRSF1.0H occurred at the wall boundary at the drift ratio of 2.0 %. However, shear sliding occurred after flexural yielding. The test proceeded up to a drift ratio of 3.2 %.

In the case of the maximum horizontal reinforcing bar ratio specimen (PRDF1.0M, Fig 3-7 (c)) with high loading rate, concrete crushing occurred at the wall boundary, and the damages was more severe than that of PRDF0.5H (Fig 3-7 (b)) with half of the maximum permissible horizontal reinforcing bar ratio. However, shear-slip displacement at interface of the wall-slab was limited due to the high vertical reinforcing bar ratio.

In the case of PRDF0.5H (Fig 3-7 (d))with low aspect ratio of 0.5, high loading rate and the slab-wall interface moved down to prevent shear-friction failure, shear-slip displacement at the interface was limited in contrast with PRDF1.0H (Fig 3-7 (C)). The failure was occurred with concrete crushing at the wall boundary. Figure 3-8 shows the shear-friction and shear failure modes of specimens at the end of test.

Table 3-4 Summary of test results

Specimens	Loading rate, (mm/s)	Test results													V_{sf}, kN
		$V_{test,+}$ (kN)	$V_{test,-}$ (kN)	$V_{test,+}$ (kN)	Drift ratio at V_{test} (%)	Failure mode	K_y, kN/mm		δ_y, %		δ_u, %		δ_y/δ_u		
							+	-	+	-	+	-	+	-	
PRSF1.0H	1	867	716	792	0.71 / 0.79	Flexural	80	61	0.59	0.64	1.60	2.01	2.7	3.2	0.96
PRDF1.0H	100	953	803	878	0.68 / 0.72	Flexural	92	76	0.56	0.57	1.60	1.60	2.8	2.8	1.07
PRDF1.0M	100	1415	1187	1301	1.46 / 1.02	Flexural	106	77	0.72	0.83	2.00	2.00	2.8	2.4	1.06
PRDF0.5H	100	976	747	862	0.64 / 0.69	Flexural	203	113	0.44	0.60	2.51	2.51	5.7	4.2	1.01
PRSM0.5H	1	849	606	728	0.59 / 0.50	Friction	183	126	0.25	0.26	0.54	1.20	2.1	4.6	0.88
PRDM0.5H	100	891	640	766	0.71 / 0.59	Friction	171	119	0.28	0.29	0.63	0.96	2.3	3.3	0.92
PRSS1.0H	1	1544	1302	1423	1.04 / 1.05	Shear	93	75	1.51	1.57	1.77	2.03	1.2	1.3	1.70
PRDS1.0H	100	1605	1530	1568	1.14 / 1.44	Shear	120	78	1.22	1.78	2.57	2.56	2.1	1.4	1.88

Note: $V_{test,+}$, $V_{test,-}$, and V_{test} are the measured maximum loads in the positive, negative and average loading directions, respectively; and V_p is predicted strength corresponding to the failure mode of specimen (= min[Vf, Vn, Vsf]).

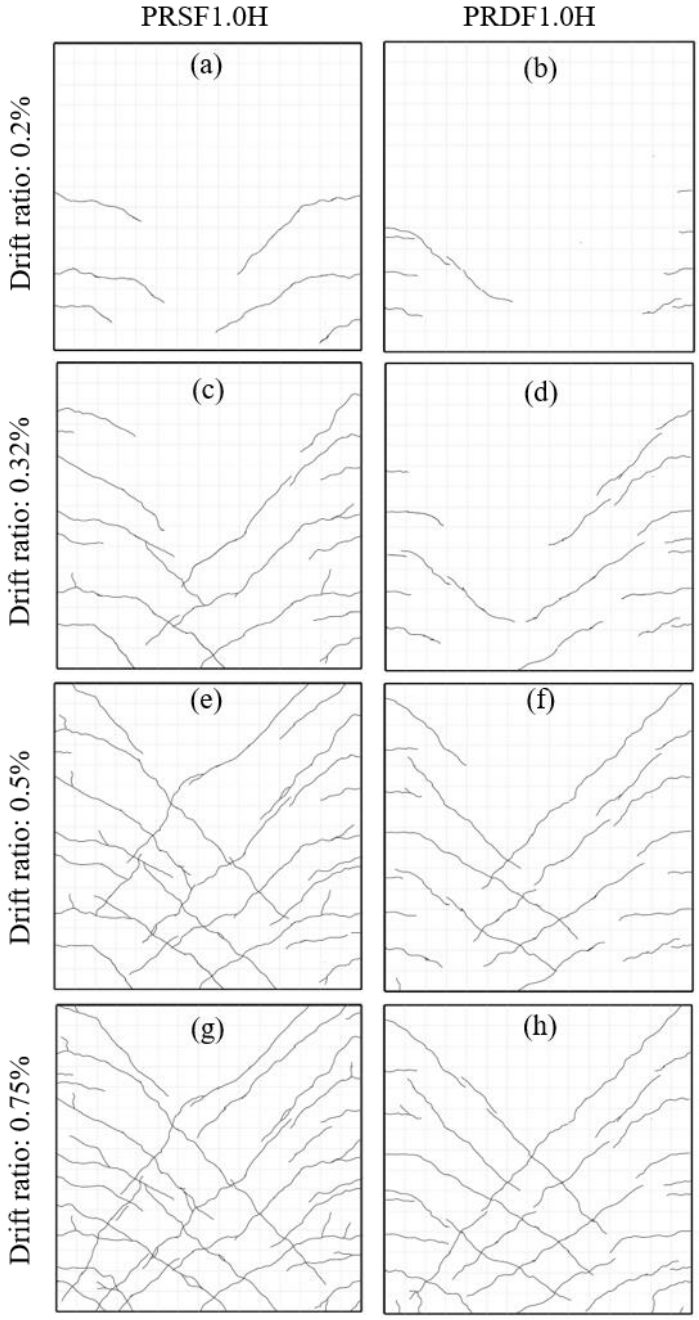

Figure 3-6 Crack propagation of PRSF1.0H and PRDF1.0H

(a) PRSF1.0H

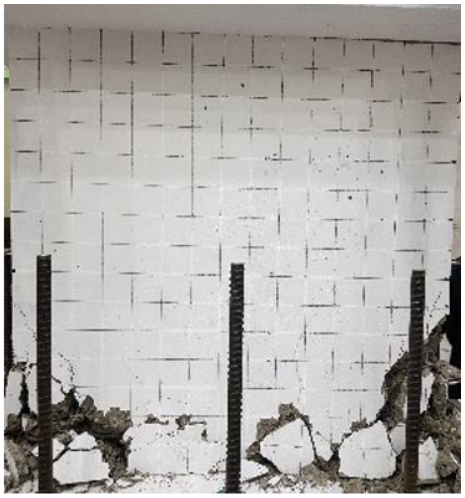

(b) PRDF1.0H

(c) PRDF1.0M

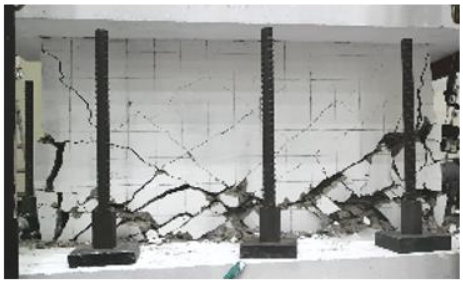

(d) PRDF0.5H

Figure 3-7 Failure modes of specimens with flexrual fialure at end of test

In the case of shear-friction mode specimens PRSM0.5H and PRDM0.5H (Figs 3-8 (a) and (b)), with a construction joint at the wall-slab interface, the crack patterns were similar to each other. During initial loading horizontal cracks occurred at the wall ends as similar as flexural specimen with same aspect ratio of 0.5 (PRDF0.5H, Fig 3-7 (d)). Then, as the drift ratio increased, the cracks propagated to diagonal cracks at the web area. At a drift ratio of 0.4 %, vertical cracks occurred at the wall boundary, which were attributed to shear sliding at the interface. At the drift ratio 0.75 %, shear-friction failure occurred at the interface of wall-slab. The number of cracks in PRDM0.5H (Fig 3-8 (a)) with high loading rate was smaller than that of static loading condition (PRSM0.5H, Fig 3-8 (b)).

In the case of shear failure specimens PRSS1.0H and PRDS1.0H (Figs 3-8 (c) and (d)), first diagonal shear cracks were occurred at a drift ratio of 0.25 %. Then, as the drift ratio increased, the number of diagonal cracks increased. At a drift ratio of 0.9 %, the width of diagonal shear crack was significantly increased. Ultimately, concrete crushing occurred in the web area.

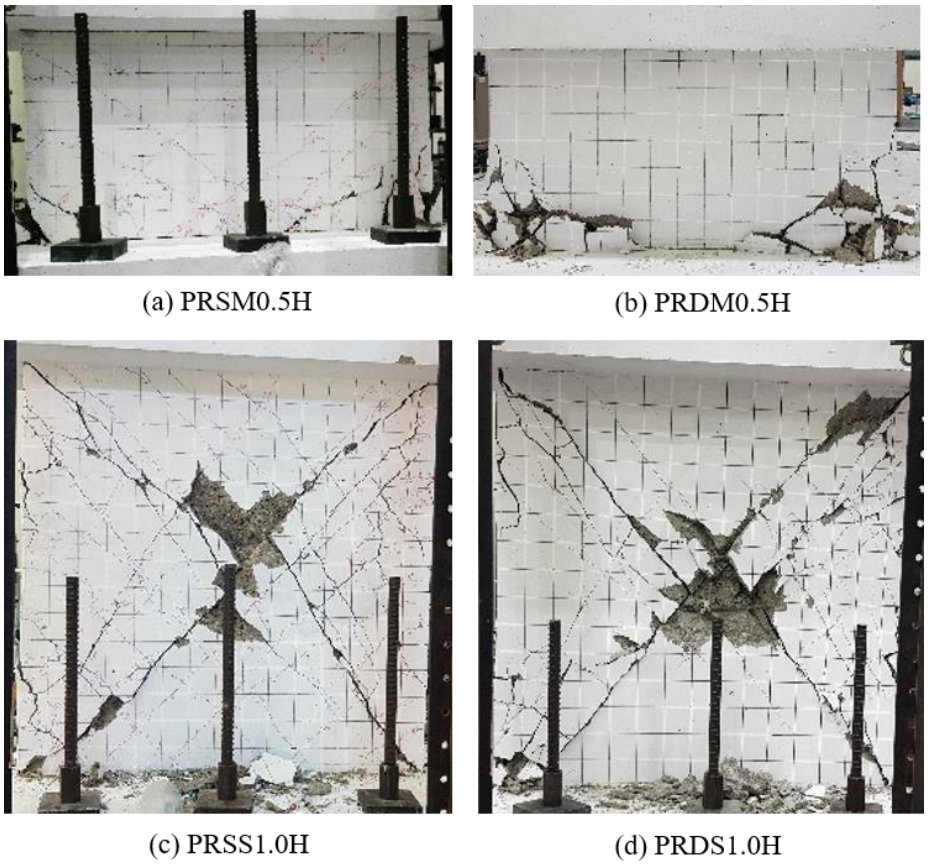

Figure 3-8 Failure modes of specimens with shear-friction and shear filature at end of test

3.1.3.3) Load-displacement relationships

Figures 3-9 and 3-10 show the lateral load-displacement (lateral drift ratio) relationships of the specimens. The displacement shown in the figures indicates displacement of the actuator. The lateral displacement in Figs 3-9 and 3-10 indicates the net displacement excluding slip displacement at the bottom slab. For comparison, each figures show the flexural strength V_f, the nominal shear strength V_n, and the nominal shear-friction strength V_{sf} predicted by ACI 349. In all specimens, the maximum strength in the positive direction (push) was greater than that in the negative direction (pull).

In the flexural yielding specimen PRSF1.0H with static loading rate (fig 3-9 (a)), at a drift ratio of 0.75 %, the maximum strengths were + 867 and -716 kN, which were 5 % greater and 13 % smaller than the nominal flexural strength V_f, in the positive and negative loading directions, respectively (Fig 3-9 (a)). After flexural yielding, the load-carrying capacity gradually decreased. The load-carrying capacity decreased below 80 % of the maximum tested strength after a drift ratio of 2.0 %.

In the case of counterpart specimen PRDF1.0H with dynamic loading rate (fig 3-9 (b)), at a drift ratio of 0.7 %, the maximum tested strength were measured (+953 and -803 kN, in the positive and negative loading directions, respectively). The maximum strengths were 9.9 % and 12.2 % higher than those of static specimen PRSF1.0H (fig 3-9 (a)). The load-carrying capacity decreased to 0.8 V_{test} at a drift ratio of 1.6 %. The displacement at 0.8 V_{test} was

smaller than that of PRSF1.0H. However, due to the high loading rate, shear sliding was occurred after flexural yielding failure. For this reason, the displacement at 0.5 V_{test} increased up to a drift ratio of 3.2 %, and the extent of pinching was occurred.

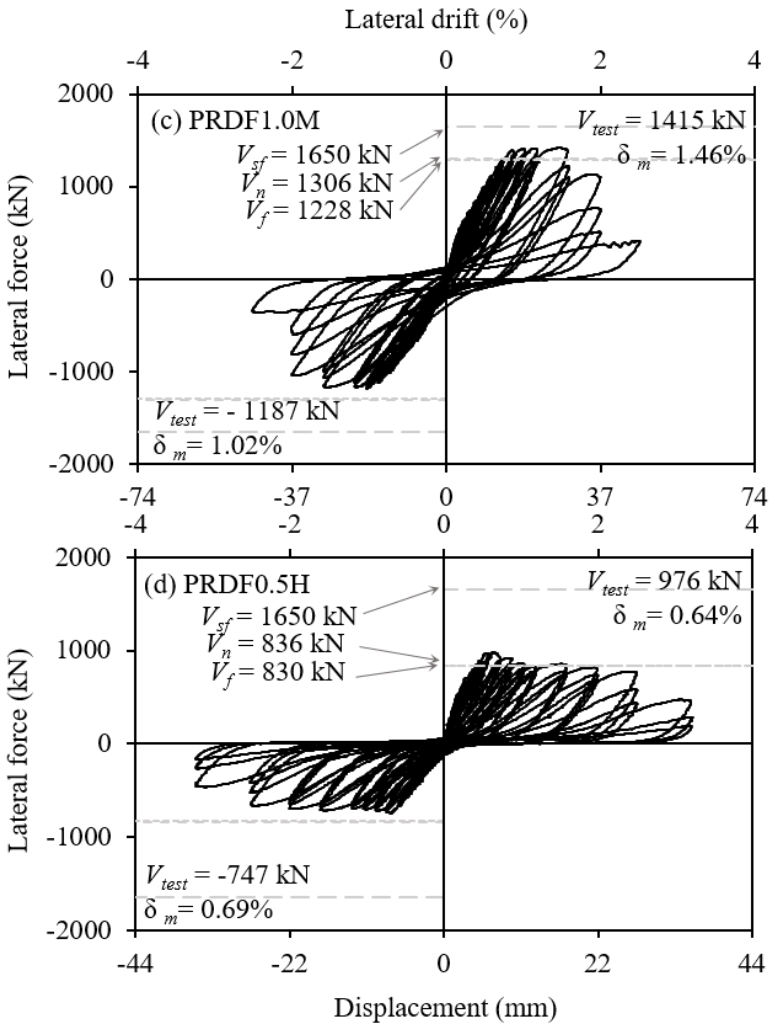

Figure 3-9 Lateral load-displacement relationships of flexural yielding failure specimens

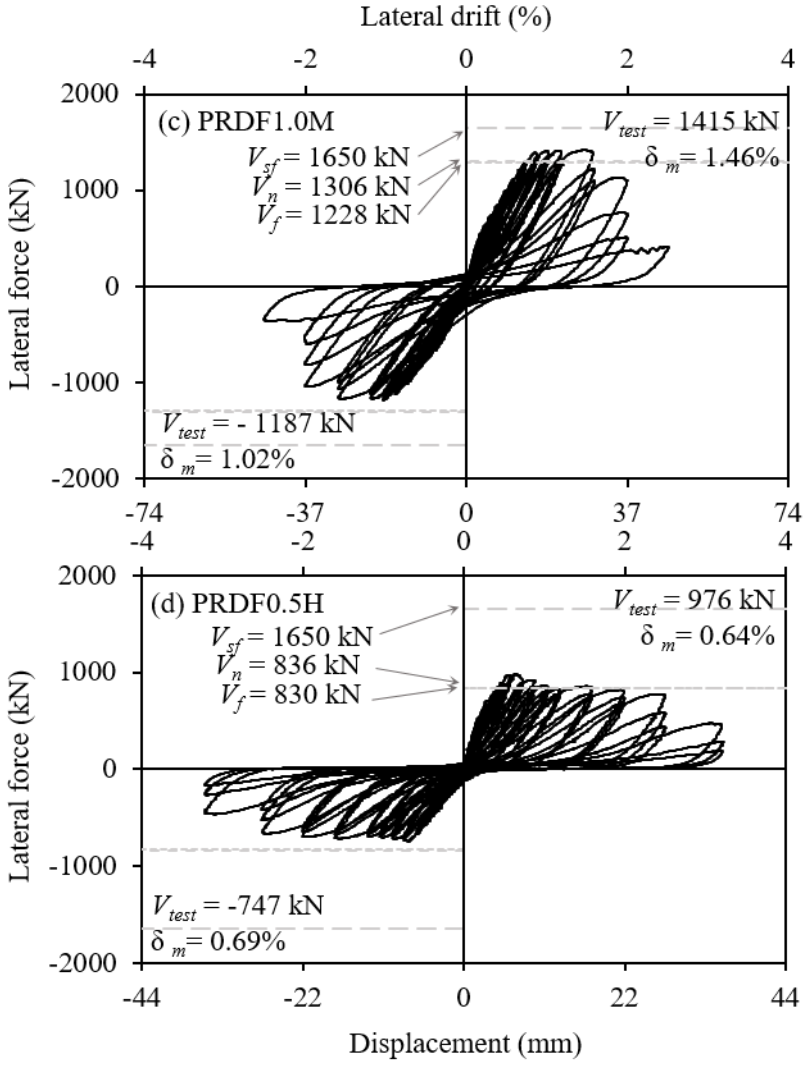

Figure 3-9 Lateral load-displacement relationships of flexural yielding failure specimens

In the case of maximum horizontal reinforcing bar ratio specimen (PRSF1.0M) with high loading rate, flexural yielding occurred at a drift ratio of 0.75 %. Until a drift ratio of 1.6 %, the load-carrying capacity was maintained. Due to the high reinforcing bar ratio, the maximum tested strength were increased to +1,415 kN and -1,187 kN, which were 15 % greater and 3% smaller than the nominal flexural strength V_f, respectively. At a drift ratio of 1.46 % and 1.02 %, the maximum tested strengths were occurred in the positive and negative loading directions, respectively. At a drift ratio of 2.0 % the load-carrying capacity decreased below 25 % of the maximum tested strength.

In the case of specimen with low aspect ratio of 0.5 and high loading rate (PRDF0.5H), the maximum tested strengths were +976 kN and -747 kN in positive and negative loading directions, respectively, at a drift ratio of 0.75 %. The maximum strengths were 1.15 and 0.88 times of the nominal flexural strength in the positive and negative loading directions, respectively. After flexural yielding, the load-carrying capacity was maintained up to a drift ratio of 2.5 %.

In the shear-friction failure specimen PRSM0.5H (fig 3-10 (a)) with static loading rate, at a drift ratio of 0.6 %, the maximum tested strengths were observed (+849 kN and -606 kN for positive and negative loading directions, respectively). The maximum strengths were 2 % greater and 27 % smaller than nominal shear-friction strength. On the counterpart specimen (PRDM0.5H, fig 3-10(b)) with dynamic loading rate, the maximum tested strength were +891 kN and -640 kN, which were 4.9 % and 5.6 % greater than those of PRSM0.5H with low loading rate.

In the case of shear failure specimen with low loading rate (PRSS1.0H), at a drift ratio of 1.05 %, the maximum tested strength of +1,544 and -1,320 kN, which were 85% and 56 % greater than the nominal shear strength V_n for postivie and negative loading directions, respectively. On the other hand, in the counterpart specimen with high loading rate (PRDS1.0H, fig 3-10(d)), the maximum tested strength was occurred at a drift ratio of 1.2 %. The maximum tested strengths were +1,605 and -1,530 kN in positive and negative loading direction, respectively. These values were 4.0 % and 17.5 % greater than those of low loading rate specimen (PRSS1.0H).

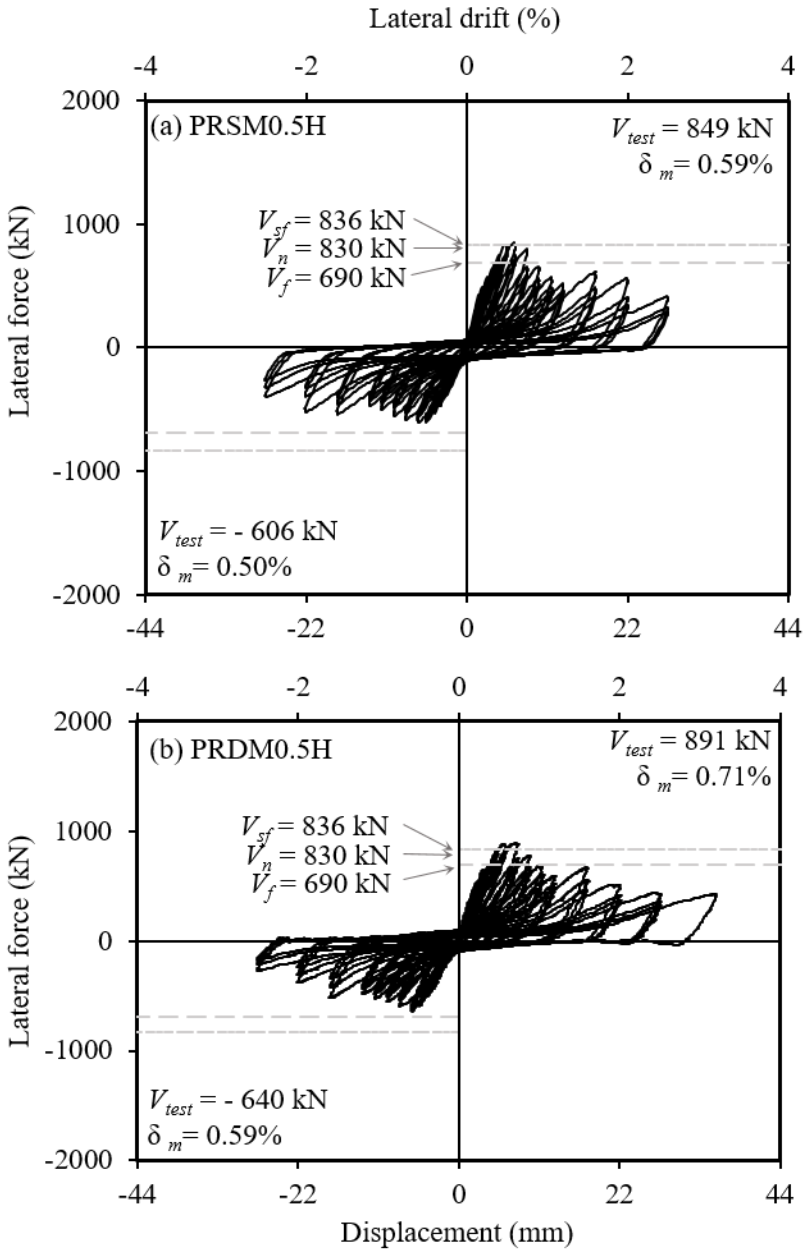

Figure 3-10 Lateral load-displacement relationships of shear-friction and shear failure specimens

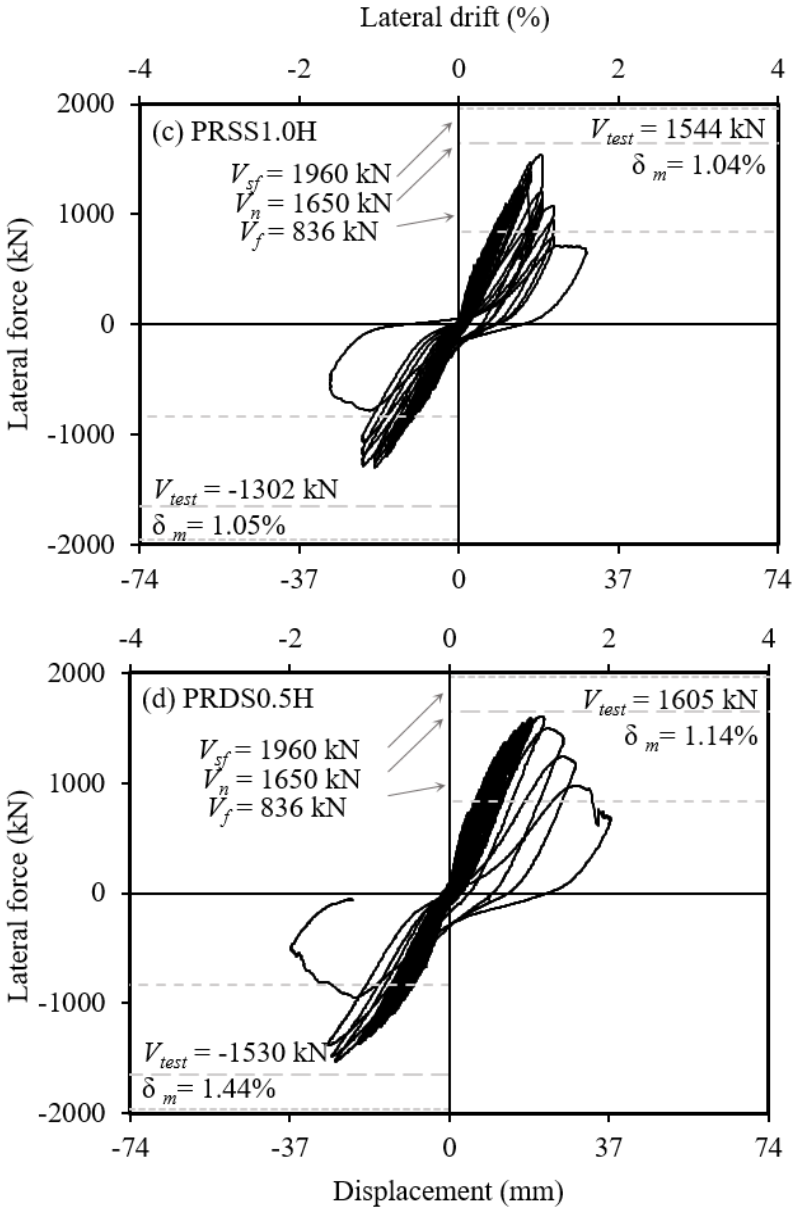

Figure 3-10 Lateral load-displacement relationships of shear-friction and shear failure specimens

In the flexural failure specimens PRSF1.0H, PRDF1.0H, PRDF1.0M, and PRDF0.5H (fig 3-9), the tested strengths reached at the nominal strength V_f with ductile behavior. Particular in the high loading rate specimens, the maximum displacement that load-carrying capacity after maximum tested strength is maintained increased due to shear sliding, which was caused by the large crack width.

In the shear-friction failure mode specimens PRSM0.5H, and PRDM0.5H (figs 3-10 (a) and (b)), the measured strength decreased after shear-friction failure. However, the displacement increased due to the shear slip.

In the shear failure mode specimens (PRSS1.0H and PRDS1.0H), the load-carrying capacities decreased immediately after the maximum tested strength, showing a typical shear failure mode. In the case of high loading rate, the displacement at the maximum tested strength was clearly increased.

3.1.3.4) Strians of reinforcing bars

Figure 3-11 shows the strain distributions of the vertical reinforcement at 0.5 V_{test}, 0.75 V_{test}, and 1.0 V_{test}, where V_{test} indicates the maximum tested strength. The strain rate of reinforcing bars was almost constant under constant loading velocity. Because the strain itself increased as the lateral displacement increased. The average strain rates of the reinforcing bars were 3.0×10^{-4} s^{-1} and 5.0×10^{-2} s^{-1} in the case of the specimens under static and dynamic loading rate, respectively. The strain rate of the reinforcing bars in dynamic loading specimens belong to the intermediate range, corresponding to an earthquake loading case.

In the cases of flexural specimens PRSF1.0H, PRDF1.0H, PRDF1.0M, and PRDF0.5H (figs 3-11 (a), (b), (c), and (d)), vertical reinforcing bars at the wall boundary were yield at the maximum tested strength (V_{test}).

On the other hand, in the shear-friction failure specimens PRSM0.5H and PRDM0.5H (figs 3-11 (e), and (f)), the strains of vertical reinforcing bars were smaller than those of flexural yielding failure specimen (PRDF0.5M, fig 3-11 (d)). In addition, no vertical reinforcing bars were yield at maximum tested strength.

In the shear failure specimens (PRSS1.0H and PRDS1.0H, figs 3-11 (g) and (h)), the strains of the vertical reinforcement were significantly smaller than those of other specimens.

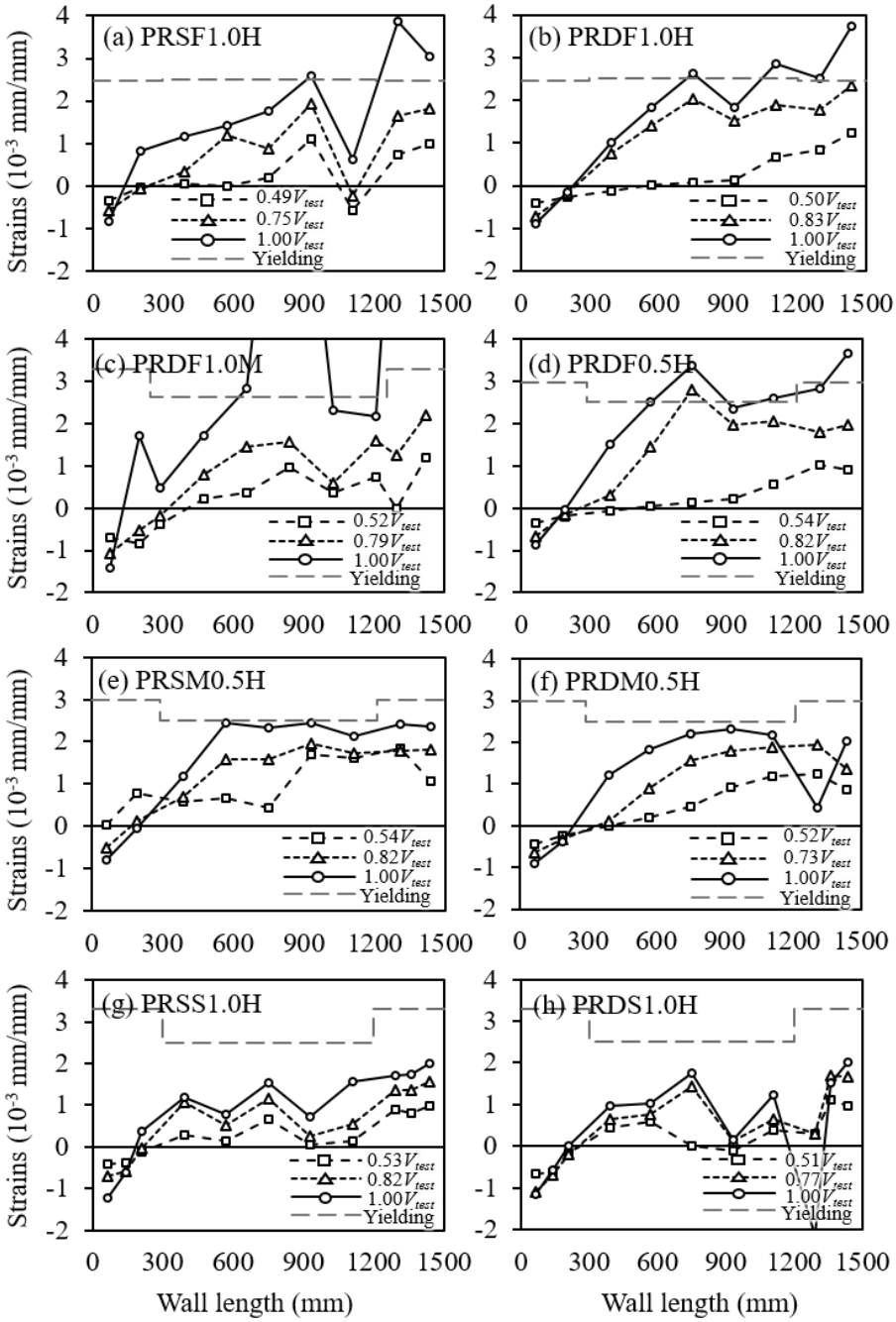

Figure 3-11 Measured strains of vertical reinforcing bars in specimens

Figure 3-12 shows the strain distributions of the horizontal reinforcing bars. In the case of flexural yielding and shear-friction failure specimens, the horizontal reinforcing bars were not yield (figs .3-12 (a) and (b)). However, in the case of shear failure specimens (PRSS1.0H and PRDS1.0H), at 0.75 V_{test} and 1.0 V_{test}, the horizontal reinforcing bars were yield.

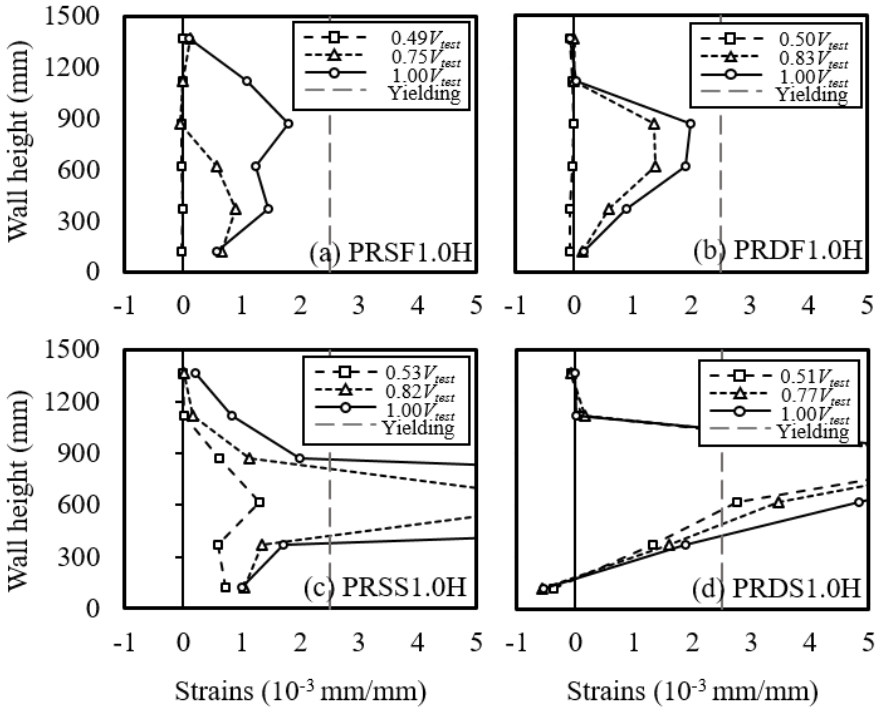

Figure 3-12 Measured strains of horizontal reinforcing bars in specimens

3.1.3.5) Displacement contributions

The overall lateral displacement of a wall consist of shear, flexural and sliding contributions. The contribution of each displacement component was measured using the instrumentation shown if fig 3-3, and the measurement values are shown in fig 3-14. Using the diagonal length changes in the wall panel, shear deformation was estimated. The average shear deformation can be obtained from Eq 3-1 and fig 3-13. Sliding displacement was measured form the horizontal displacement at the interface of-bottom slab. Flexural deformation was estimated using L3 to L8.

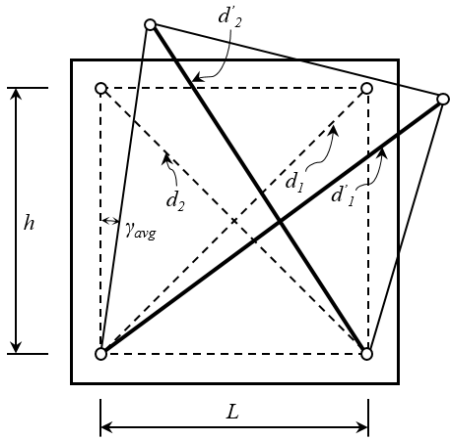

Figure 3-13 Calculation of average shear distortion of wall

$$\gamma_{avg} = \frac{(d_1' - d_1)d_1 - (d_2' - d_2)d_2}{2hL} \quad (2\text{-}1)$$

In the flexural yielding failure specimens PRSF1.0H, and PRDF1.0H (figs 3-14 (a) and (b)), the contribution of flexural deformation was dominant during the test. As the drift ratio increased, the contribution of sliding increased significantly under high loading rate.

In the PRDF1.0M (fig 3-14 (c)) with the maximum horizontal reinforcing bar ratio, the contribution of sliding was limited to 30 % of the overall deformation during the test because of the high vertical reinforcing bar ratio.

In the case of the other flexural yielding specimen PRDF0.5H (fig 3-14 (d)) with aspect ratio of 0.5, sliding did not significantly occurred, because of the use of a construction groove joint. Flexural deformation was dominant throughout the test.

In the shear-friction failure specimens PRSM0.5H and PRDM0.5H (figs 3-14 (e) and (f)) without the groove joint, the contribution of sliding was dominant.

In the shear failure specimens PRSS1.0H and PRDS1.0H (figs 3-14 (g) and (h)), the contributions of shear deformation were dominant throughout testing.

The effect of the loading rate on the deformation contributions were limited in all specimens.

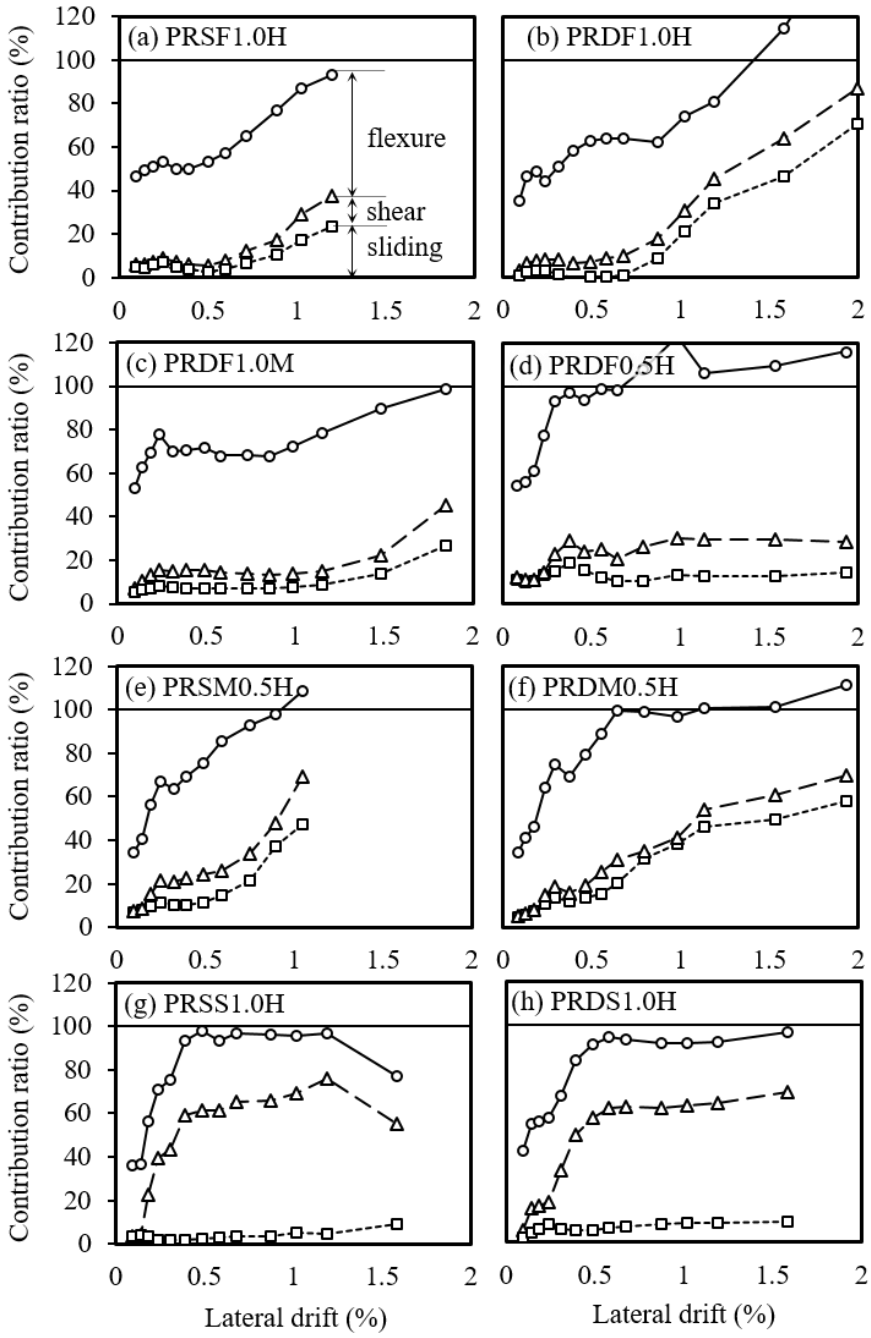

Figure 3-14 Contributions of components to overall lateral displacement

3.1.4 Effect of loading rate on reinforced concrete walls

To investigate the effect of loading rate on capacity of reinforced concrete walls in terms of flexural yielding, shear, and shear-friction, strength of the specimens under high and low loading rate were compared to each other (Table 3-4).

In the case of flexural yielding specimens, the yield stiffness was greater in the high loading rate specimens. In the case of flexural yielding specimens, the yield stiffness was 76 to 92 kN/mm and 61 to 80 kN /mm under high and low loading rate, respectively. The maximum test strengths were greater in the specimens with high loading rate. The ratio of maximum strength under high loading rate specimen to that of low loading rate was 9.9 to 12.2 % for the flexural yielding specimens.

In the case of shear failure specimens, the yield stiffness was 78 to 120 kN/mm and 75 to 93 kN/mm under high and low loading rate, respectively. Further, the maximum test strength were 4.0 to 17.5 % greater in the high loading rate species. The increases in strength are mainly attributed to the increased yield strength of reinforcing bars under high loading rate.

On the other hand, in the case of shear-friction failure specimens, the yield stiffness was smaller under the high loading rate: 119 to 171 kN/mm, and 126 to 183 kN/mm in high and low loading rate specimens, respectively. This result indicates that the stiffness and strength of shear-friction are affected by the greater crack width at the interface of wall-slab caused by high loading rate. On

the other hand, the maximum test strength of the shear-friction failure mode specimen was increased as the yield strengths of vertical reinforcing bars were increased due to high loading rate. Because of the negative (crack width) and positive (yielding strength of reinforcing bars) effects of high loading rate, the increment of maximum test strength was limited to 4.9 to 5.6 %, which is lower than the effect on the flexural, and shear strength.

3.1.5 Summary of experiment I

To investigate the effect of high loading rate on the structural capacity of low-rise reinforced concrete walls, five and three wall specimens with aspect ratios of 1.0 and 0.5, respectively, were tested under cyclic lateral loading. To directly compare the behavior of specimens, high and low loading rate were applied to identical pairs of specimens. The walls with shear, flexural, and shear-friction failure modes were tested. The major findings can be summarized as follows:

1.) The increase in reinforced concrete wall strength was observed because of increasing the loading rate. Although the crack pattern appeared different according to loading rate, the loading rate did not affect the behavior of the reinforced concrete wall. Therefore, the high-frequency earthquakes are not expected to have a negative effect on wall in-plane performance.

2.) In the specimens under high loading rate, cracks were occurred in low drift ratio. Further, the number of horizontal cracks in the wall boundary of high loading rate specimens was decreased by 20 % of that of low loading rate specimen.

3.) The strain rate affected regardless of the failure modes of reinforced concrete wall: flexural, shear-friction, and shear failure modes.

4.) In the case of specimens under high loading rate, the maximum strengths

were increased by 9.9 to 12.2 %, 4.0 to 17.5 %, and 4.9 to 5.6 % at flexural yielding, shear, and shear-friction failure mode specimens, respectively. The reason why the maximum test strengths were increased is mainly attributed to the increased yield strength of reinforcing bars under high loading rate.

3.2 Experiment II: Shaking table test

This chapter is about shaking table test for planar walls to investigate the effect of high-frequency contents of earthquakes. The difference in behavior of reinforced concrete under earthquakes with and without high-frequency contents was directly compared.

3.2.1 General

Since recent large earthquake, the earthquake acceleration demand had been increased even for seismic evaluation of existing nuclear power plant structures. Due to the Gyeong-Ju earthquake of magnitude 5.8, the Wol-sung nuclear power plant was shut down. In 2017, the Po-hang earthquake was occurred subsequently. These two large earthquakes were occurred near the nuclear power plant site. Based on the site investigate and the record of earthquakes, the characteristics of earthquake in Korea were verified. Especially, the high frequency contents beyond 10 Hz were included in the earthquakes occurred in Korea. This characteristic of earthquake is similar to those of earthquakes in the eastern United States. In general, the seismic evaluation of nuclear power plant has been conducted using earthquakes with low frequency contents. Therefore, a method of evaluating for an earthquake exceeding the design based earthquake (DBE).

The Electric Power Research Institute (EPRI, 2017) reported the

characteristics of high-frequency earthquakes. Because structural damage caused by earthquake is determined by relative displacement, the technical report indicates that since high-frequency earthquake generates relatively small displacements and the damage on structure is smaller than general earthquakes. However, in particular, since the natural frequency of nuclear power plant building is reported is in ranged 4 Hz to 8 Hz, the dynamic amplification is expected large under high-frequency earthquake. Thus, evaluation of the extreme capacity of reinforced concrete walls under high-frequency earthquake is important.

Various researches had been conducted on reinforced concrete walls. In particular, for the reinforced concrete wall with high reinforcing bar ratios used in nuclear power plants, various studies have been conducted such as shear failure (Baek et al. (2017)), shear friction failure (Baek et al. (2018)), failure modes (Farrar, et al. (1993) and fragility curve (Syed, (2012)). However, most studies had been conducted under static loading rate. In the quasi-static test, the effects of dynamic behavior and loading rate effect cannot be confirmed. In addition, to investigate the effect of high frequency contents, the shaking table test is essential.

In the chapter 3-1, the comparative tests of static and dynamic loadings were conducted. The maximum strength of major failure modes of reinforced concrete wall (flexural yielding, shear, and shear friction) was affected by the loading rate. In the case of high loading rate tests, the strength increments were 11 %, 5 %, and 4 ~ 17.5 % in the flexural yielding, shear-friction, and shear failure mode, respectively.

Carrillo and Alcocer (2008) conducted the shaking table and pseudo-dynamic tests using reduced specimens. The target building had 8 stories and the reduced scale was 1:1.25. As for the test parameters, four test specimens were compared with the compressive strength of concrete, the ratio of reinforced steel plates, and the reinforcing bar ratios. As the results of the test, in the shaking table test, the strength was higher than in the pseudo-dynamic test.

Ghorbanireenani, I. (2001) conducted a shaking table test with the wall specimens. The detail of specimen had two 8-layer walls reduced to a ratio of 1:0.429. The prototype structure is a commercial building in the northeastern United States, and shaking table tests were conducted by amplifying the actual recorded high-frequency earthquake observed under various conditions. As a result of the experiment, the high-frequency earthquake was amplified in the high-order mode, causing damage at the top of the structure.

Pinho, R. (2000) made a reinforced concrete specimen for the first floor wall of a four-story structure and conducted a shaking table tests. The analysis model, filtering, and experimental method used during the shaking table test were described. In addition, many researchers, including Ko (2006), Lee (2013), Lee (2013), and Woo (2007), have conducted shaking table test on buildings containing concrete walls. For RC walls, various experiments have been conducted, but the experiments under extreme seismic loads were limited. In particular, many studies have been conducted without considering the high frequency components.

In this chapter, to determine the effect of high frequency earthquakes on the

structure, shaking table tests were conducted using four reinforced concrete walls with aspect ratios of 1.0 and 2.0. The two input ground motions were used. On the basis of the test results, the maximum overturning moment, natural frequency, and strain distributions were measured. In particular, the analysis of shaking table test results was focused on the verification of the exact strength of reinforced concrete wall with the effect of strain rate.

3.2.2 Test Plan

3.2.2.1) Input ground motion

Two artificial earthquakes were used in the shaking table test. The information of used input ground motions is shown in Table 3-5 and fig 3-15. The response spectrum of Earthquake type 1, which was named EQ1 is a uniform hazard spectrum produced by Choi et al. (2009). Earthquake type 2, named EQ 2, is an artificial earthquake created using RG1.60 (USNRC (2014)) which is a design spectrum for nuclear power plants in Korea. UHS contains more high frequency contents than RG1.60 because of reflecting Uljin ground site characteristics. Figure 3-15 shows the elastic response spectrum of input ground accelerations with the peak ground acceleration (PGA) adjusted to 1.0 *g*. The elastic response spectrum shows a high response acceleration in a high frequency range of 10 Hz or more, while the dynamic amplification is expected less than that of RG1.60 in a section below 10 Hz. The strong motion duration of input earthquake was calculated as a 5% to 75 % section of arias intensity energy (Arias (1970)). The strong motion duration of earthquake was 8 and 16 seconds in EQ 1 and EQ 2, respectively.

Table 3-5 Input ground motion

No.	Name	High-frequency contents	Total duration (s)
1	EQ 1	Included	20
2	EQ 2		30

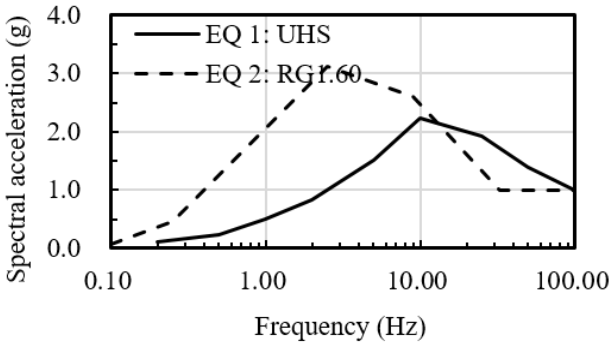

(a) Elastic response spectra of input ground accelerations

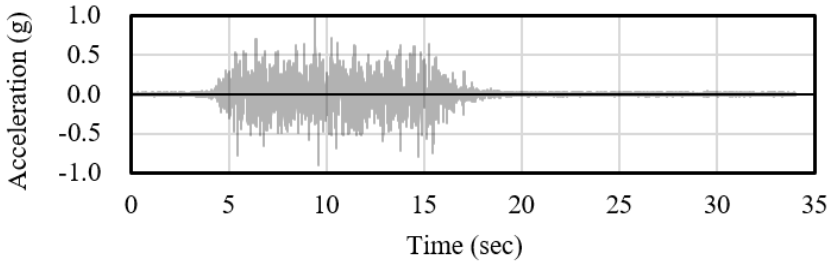

(b) Acceleration time history of EQ 1 (UHS)

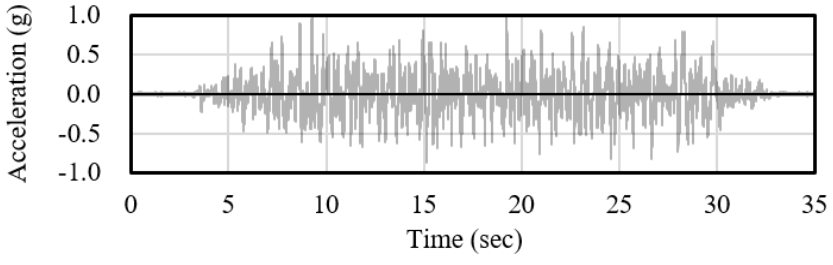

(c) Acceleration time history of EQ 2 (RG1.60)

Figure 3-15 Input ground motion

3.2.2.2) Major test parameters

Generally, nuclear power plant building walls are characterized by high reinforcing bar ratio due to high seismic demand. The test specimens were designed considering this requirement. Two pairs of reinforced concrete walls were prepared for testing (Table 3-6 and fig 3-16). The test parameters were input ground motion, peak ground acceleration, and aspect ratio. In the test specimens' name, the first and second letters P and R referred to the shape of planar wall and the reinforced concrete wall as mentioned in the Chapter 3.1. The third letter E, indicates the loading type: Earthquake (shaking table test). The nomenclature of the rest of the letters is the same as in Chapter 3.1. The last letters '1' and '2' refer the input ground motion types: EQ 1 and EQ 2, respectively.

Two pairs of identical twin specimens [PREF1.0H-1 and PREF1.0H-2] and [PREF2.0M-1 and PREF2.0M-2] were directly compared to investigate the effect of input ground motion type on flexural strength. For the flexural yielding failure mode specimens, an aspect ratio of 1.0 and 2.0 was used.

Table 3-6 Design parameters of test specimens of shaking table test

Specimens	Concrete f_{ck} (MPa)	Aspect ratio	Input EQ	Reinforcing bar ratio		Design strength				Increment of input PGA
				ρ_h (%)	ρ_v (%)	M_f (kN·m)	V_f (kN)	V_n (kN)	V_n / V_f	
PREF1.0H-1	40	1.0	EQ 1	0.59	0.55	577	312	983	3.15	0.3g
PREF1.0H-2		1.0	EQ 2	0.59	0.55	577	312	983	315	0.3g
PREF2.0M-1		2.0	EQ 1	1.06	0.79	307	165	577	3.50	0.1g
PREF2.0M-2		2.0	EQ 2	1.06	0.79	307	165	577	3.50	0.1g

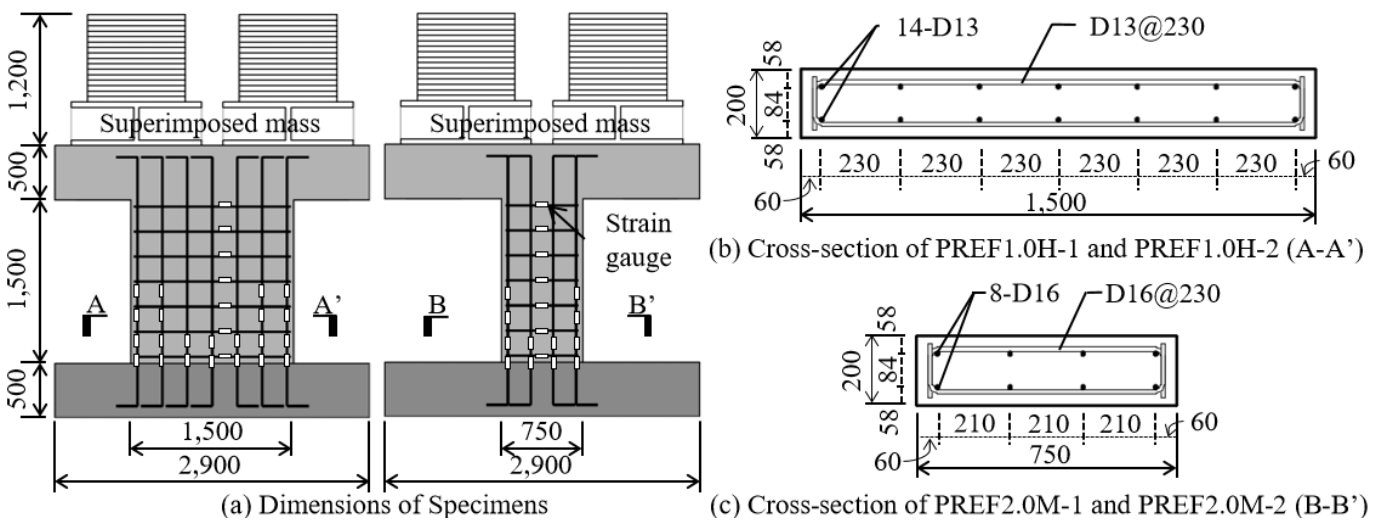

Figure 3-16 Dimensions and reinforcement details of specimens

3.2.2.3) Test specimens

The dimensions of the walls with an aspect ratio of 1.0 were 1500 (length) × 1500 (height) × 200 mm (thickness), whereas those of the walls with an aspect ratio of 2.0 were 750 (length) × 1500 (height) × 200 mm (thickness) (Table 3-6 and fig 3-16). For walls in nuclear power plants, due to the high seismic demand, the horizontal and vertical reinforcing bar ratios is close to 1.0 %. However, due to the limited capacity of shaking table, approximated half of the maximum shear reinforcement ratio (ρ_h = 0.51) was used for the specimens with aspect ratio of 1.0.

In the case of the specimens with aspect ratio 1.0, D13 reinforcing bars with a spacing of 230 mm were used for horizontal reinforcement; the horizontal reinforcing bar ratio ρ_h = 0.51, which is half of the maximum shear reinforcing bar ratio specified by ACI 349. The nominal flexural strength V_f = 312 kN estimated by sectional analysis and the nominal moment capacity M_n was 577 kN·m. The design shear strength V_n was 983 kN which was close to the nominal flexural strength V_f. In the case (V_f=V_n), due to conservative of the ACI design shear equation, flexural yielding was generally expected before shear failure. To prevent premature shear-friction failure, the interface of wall-slab was intentionally moved down 50 mm into the inside of the foundation.

In the case of the other specimens' pair with aspect ratio 2.0, D16 reinforcing bars with a spacing of 230 mm were used for horizontal reinforcement. The nominal flexural strength V_f was 165 kN. Because of low flexural capacity and high aspect ratio, the nominal overturning moment strength was low (M_n = 307

kN·m), which the flexural failure can be induced before shear failure occurs with the maximum horizontal reinforcing bar ratio. Thus, the horizontal reinforcing bar ratio was 1.06 %, and the nominal shear strength V_n was 577 kN. These specimens also installed pocket metals to prevent premature shear-friction failure.

The yield strengths of the reinforcing bars were 471 and 460 MPa for D13 and D16, respectively. The concrete compressive strength f_c' was 40 MPa for all specimens.

3.2.2.4) Test procedure and instrumentation

The amount of PGA increment was different depending on the aspect ratio of test specimens. In the cases of PREF1.0H-1 and -2 with aspect ratio of 1.0, the expected moment capacity was higher than that of PREF2.0H-1 and -2 with aspect ratio of 2.0. Due to the high overturning moment capacity, the increment of PGA was planned to be 0.3*g* for the specimens with aspect ratio of 1.0. On the other hand, in the cases of PREF2.0H-1 and -2, the increment of PGA was planned to 0.1 *g*. However, because the measured acceleration at the floor of the shaking table test was different from the input ground acceleration, it was expressed as the PGA values measured at the floor of shaking table when analyzing or displaying the experimental results. To apply a high seismic load to the wall, a superimposed mass of 21.68 tons was installed on the top slab.

In the figure 3-17, the shaking table, the location of the accelerometers, the LVDTs, and the load cells were shown. There are four accelerometers installed

in the lower part of the specimens: the floor of shaking table, the center of bottom slab, the center of the wall, and the center of the upper slab. To measure the displacement of the specimen during the test, the LVDTs was installed on the reference structure outside the shaking table. The installation locations were the bottom slab, the center of wall, the top slab, and the center of superimposed mass. To determine the degree of damage to the specimens, strain gauges were installed. Data was measured at 512 Hz using a dynamic data logger. After every tests, damage to the specimens was confirmed with the naked eyes.

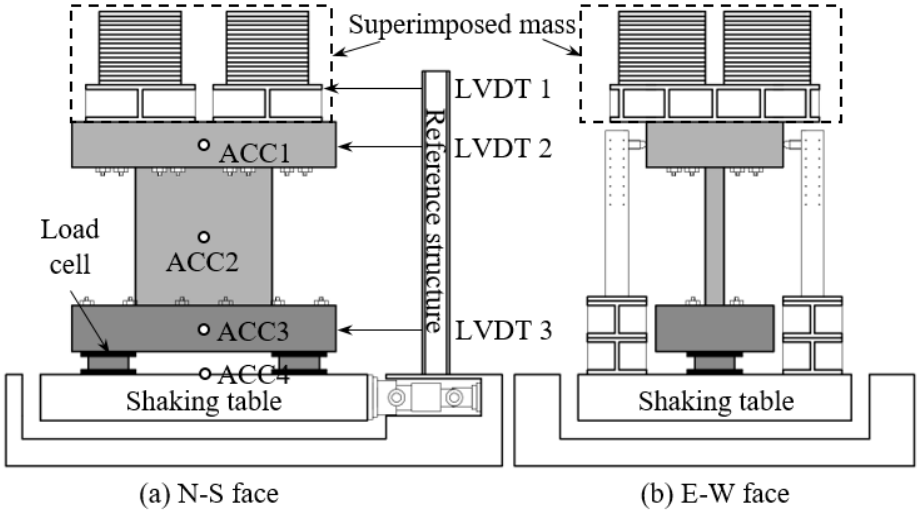

Figure 3-17 Test set up of shaking table test

3.2.3 Test results

3.2.3.1) Structural damages and eigenvalue analysis

Figure 3-18 shows the damages of specimens after the end of the test. In the case of specimen PREF1.0H-1, cracks were marked due to dry shrinkage and cracks due to seismic force were marked. All test specimens, except for the PREF1.0H-1, were painted again before the experiment to minimize the appearance of dry shrinkage.

In the cases of specimens PREF1.0H-1 and PREF1.0H-2 (figs 3-18 (a) and (b))with an aspect ratio of 1.0, cracks occurred in the horizontal direction about 400 mm from the end to the center in the test under PGA of 0.3 *g*. As the PGA increased, the diagonal cracks occurred at the bottom area of web, and horizontal cracks occurred on the upper part of the specimens. After that, the interface between wall and slab widened significantly, locking was occurred. Finally, the test was finished with concrete crushing at the boundary of walls.

In the cases of specimens PREF2.0M-1 and PREF2.0M-2 (figs 3-18 (c) and (d)) with an aspect ratio of 2.0, horizontal cracks occurred as same as that the initial cracks of the specimens with an aspect ratio of 1.0. However, the horizontal cracks did not progress to the web area of the walls. Unlike the specimens with an aspect ratio 1.0, locking deformation was not observed, which occurred in the lower part of wall. In the end of test, the concrete crushing was occurred in the boundary area.

(a) PREF1.0H-1 (b) PREF1.0H-2

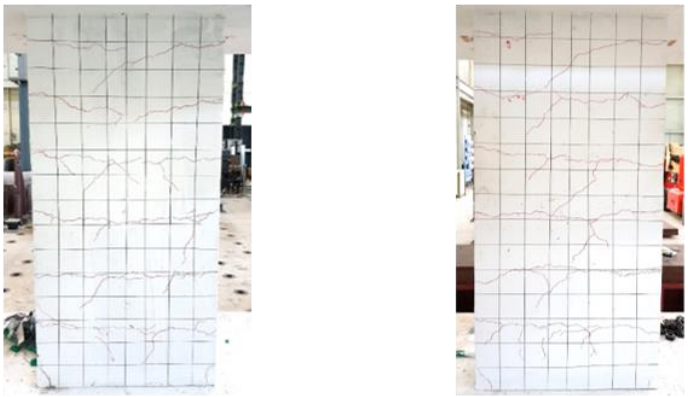

(c) PREF2.0M-1 (d) PREF2.0M-2

Figure 3-18 Damage modes of specimens at the end of shaking table test

Figure 3-19 shows the natural frequency and effective damping ratio of the specimens according to input PGAs. Because the nonlinear behavior was occurred during the test, the defining the damping ratio was difficult. Therefore, a resonance-searching test was additionally performed after the end of the every tests. The damping ratio was calculated based on the acceleration history at the lower and upper slab in the resonance-searching test.

In the cases of specimens (PREF1.0H-1 and -2) with an aspect ratio of 1.0 (fig 3-19 (a)), the natural frequencies were measured 8.6 Hz and 8.9 Hz for PREF1.0H-1 and PREF1.0H-2, respectively, before the test under PGA of 0.1 *g*. After the test under maximum PGA, the natural frequencies were decreased to 4.0 Hz and 4.1 Hz for PREF1.0H-1 and PREF1.0H-2, respectively.

In the cases of specimens (PREF2.0M-1 and -2) with an aspect ratio of 2.0 (gif 3-19 (b)), the natural frequencies were 4.1 Hz and 4.0 Hz for PREF2.0M-1 and PREF2.0M-2, respectively, before the test. The natural frequency and damping ratio measured after the final test were observed as (2.1 Hz and 1.8 Hz) and (14.4 % and 17.4 %) for PREF2.0M-1 and -2, respectively.

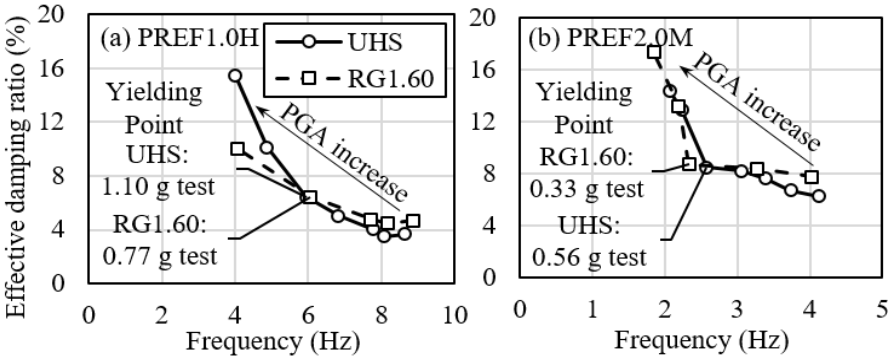

Figure 3-19 Frequency and effective damping ratio according to PGA.

3.2.3.2) Lateral displacement and overturning moment relationship

Figure 3-20 shows relationships of overturning moment and relative displacement during the tests. The overturning moment was calculated based on the measured axial force by the load cell installed in the bottom of specimens (fig 3-17). The relative displacement represents the difference of the measured displacement at the top and bottom slab. For comparison, the nominal flexural yielding strength M_f predicted by sectional analysis is shown together in figure 3-20. In the relationship graphs except for that of PREF2.0M-2 (fig 3-20 (d)), the results of the test under below PGA of 0.3 *g* were not displayed to the graph, because the overturning moment and the relative displacement were too small (fig 3-20 (a), (b) and (c)). On the other hand, in the case of PREF2.0M-1, although the total eight tests were conducted, the graph shows only five test results for clearance of the graph. In all specimens the overturning moment exceeding the nominal flexural yielding strength were measured. After flexural yielding, only the lateral relative displacement increased without increasing the overturning moment. This indicates that the capacity of ductility was maintained the load carrying capacity after the maximum flexural yielding strength.

The aspect ratio of 1.0 specimens PREF1.0H-1 under EQ 1input motion (fig 3-20 (a)), the maximum tested strength was +587 kN·m and -609 kN·m at the relative displacement of 5.99 mm and -9.23 mm (the drift ratio of 0.32 % and -0.50 %), respectively. At the relative lateral displacement greater than the displacement when maximum tested strength was occurred, the overturning

moment was decreased.

In the case of PREF1.0H-2 (fig 3-20 (b)) with an aspect ratio of 1.0 and under RG1.60 input ground motion, the maximum overturning moment strength was measured as +596 kN·m and -620 kN·m at relative lateral displacement of 7.96 mm and -15.04 mm (drift ratio of 0.43 % and -0.81 %), respectively. The maximum tested overturning moment strength was 2 % higher than that of PREF1.0H-1 under EQ 1 input ground motion. Although the relative lateral displacement which twice greater than that of PREF1.0H-1 was measured at the PREF1.0H-2 tests, the measured overturning moment was not significantly larger than that of PREF1.0H-1.

The test results of PREF2.0M-1 (fig 3-20 (c)) with an aspect ratio of 2.0 and under EQ 1 input ground motion were summarized as below: the maximum tested overturning moment: +370 kN·m and -372 kN·m at the relative lateral displacement of 17.07 mm and -10.30 mm (the drift ratio of 0.92 % and -0.56 %), respectively. After the maximum tested strength, the load-carrying capacities were not significantly decreased and the measured overturning moment was maintained up to the drift ratio of 1.0 %.

In the case of PREF2.0M-2 under RG1.60 input ground motion, the maximum measured overturning moments were +328 kN·m and -315 kN·m at the relative lateral displacement of 16.38 mm and -18.42 mm (drift ratio of 0.89 % and -1.00 %), respectively. These are 88.6 % and 84.7 % of the maximum measured overturning moments of PREF2.0M-1. A larger relative lateral displacement was measured in RG1.60 input ground motion. The load-carrying capacities of PREF2.0M-2 were measured up to the drift ratio of 1.85 %.

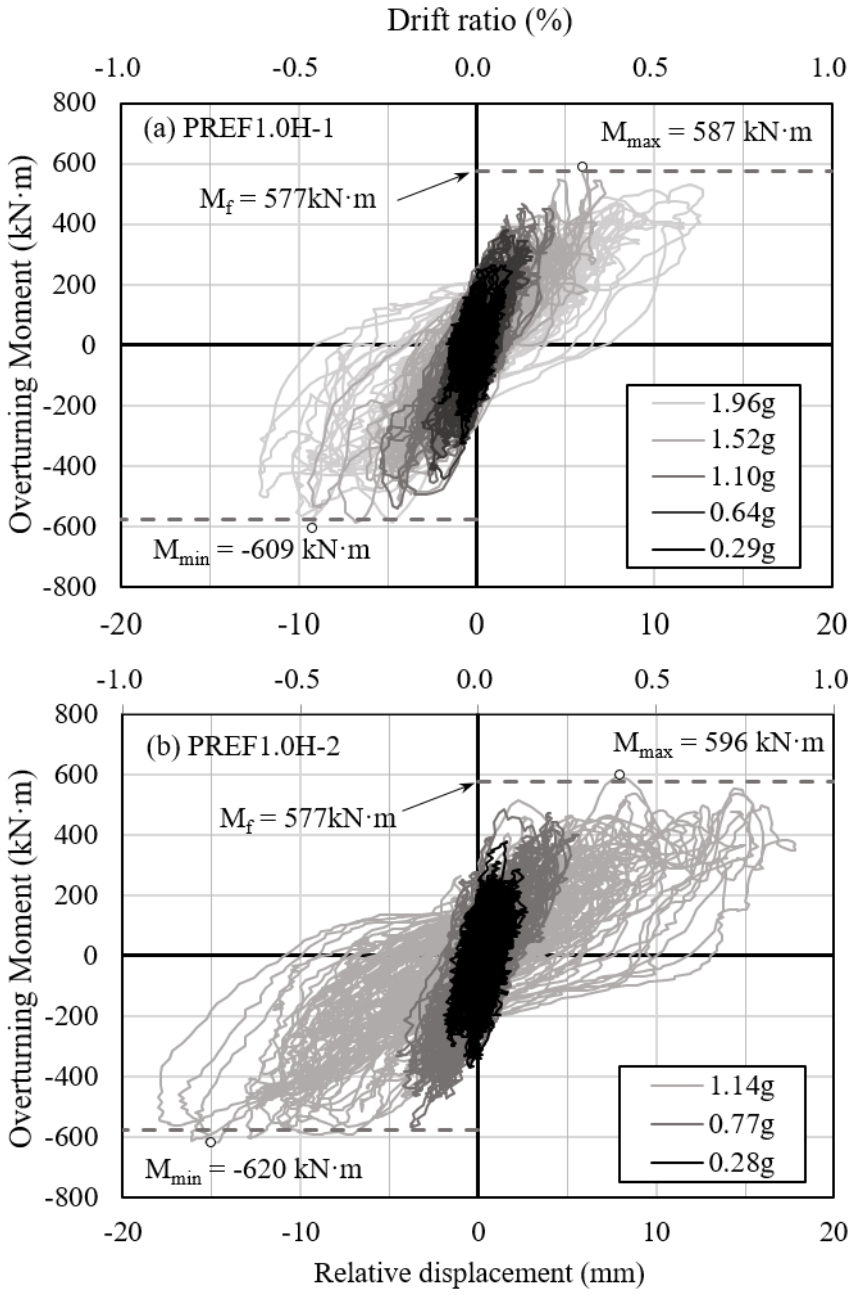

Figure 3-20 Relationships of overturning moment and relative displacement of shaking table tests

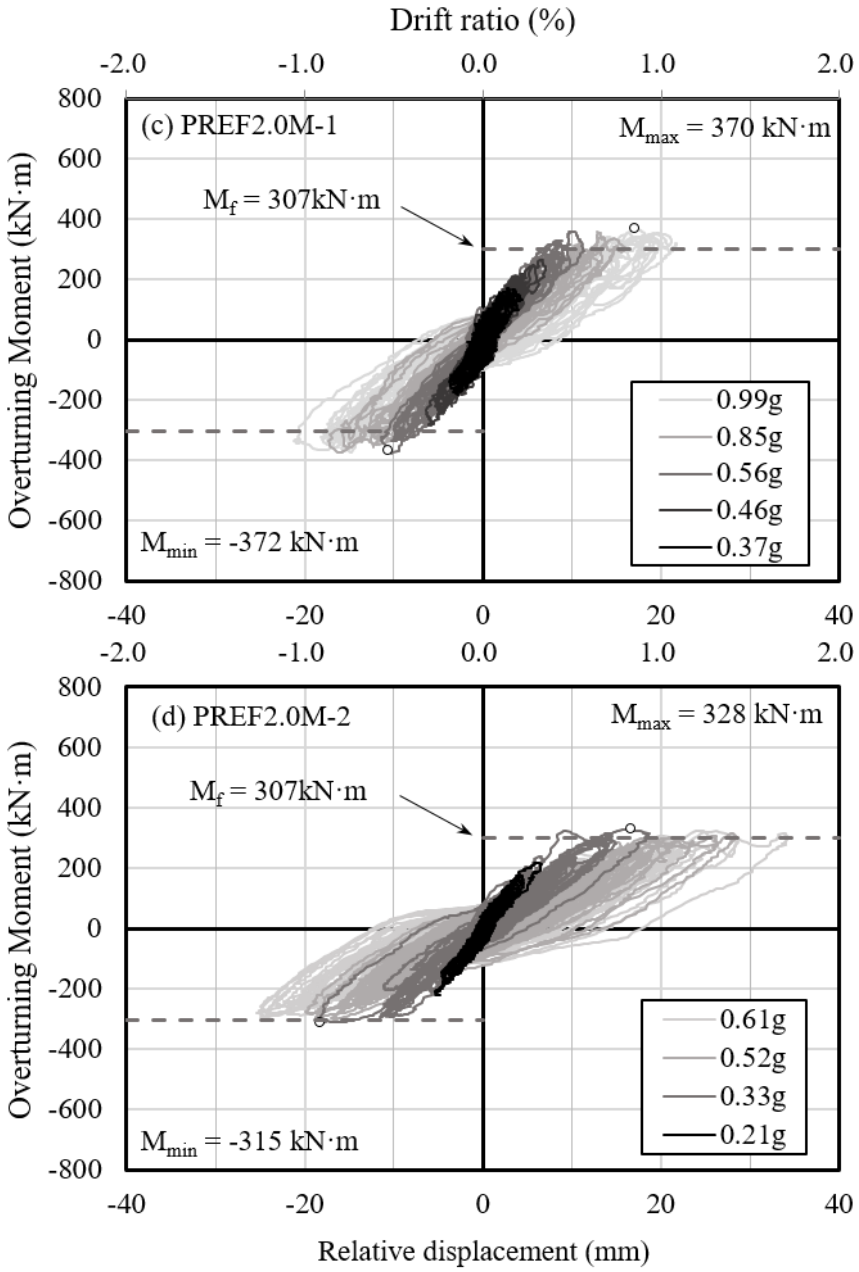

Figure 3-20 Relationships of overturning moment and relative displacement of shaking table tests

3.2.3.3) Strains reinforcing bars

Figure 3-21 shows the distributions of the strains of vertical reinforcing bars measured during the tests. The strains were marked at the same time of maximum overturning moment measured.

In the specimens PREF1.0H-1 and -2 (figs 3-21 (a) and (b)) with an aspect ratio of 1.0, the vertical reinforcing bars were yield for the first time in the test under PGA of 1.10 *g* and 0.77 *g* of the EQ 1 and EQ 2 input ground motions, respectively.

On the other hand, in the specimens PREF2.0M-1 and PREF2.0M-2 with an aspect ratio of 2.0, the tests when vertical reinforcing bars were yield were under PGA of 0.56 *g* and 0.33 *g* for the EQ 1 and EQ 2 input ground motions, respectively. The strain values of the vertical reinforcing bars at a position of 480 mm from the edge of tension stress area were measured larger in the test under the RG1.60 input ground motion.

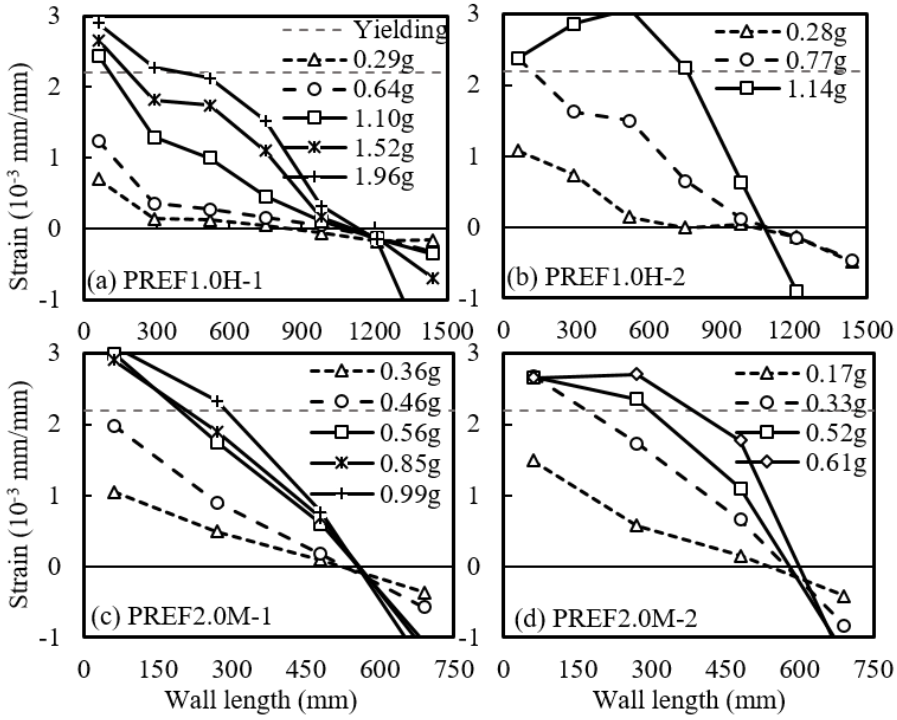

Figure 3-21 Measured strains of vertical bars in shaking table test specimens

3.2.4 Summary of experiment II

To evaluate the seismic capacity of reinforced concrete walls, shaking table tests were conducted. The four test specimens was prepared. Two different artificial earthquakes based on the Uljin site UHS and RG1.60 which are containing high-frequency components and the design spectrum of nuclear power plant, respectively, were applied to identical pairs of specimens to directly compare their behaviors. To increase the inertia force, the superimposed mass of 21.68 tons was installed on the upper of the specimens. The test results summarized as follows:

1) The maximum measured overturning moment were 1.08 and 1.13 times greater than the static analysis results for the specimens with aspect ratios of 1.0 and 2.0, respectively.

2) In the cases of the test with EQ 1 input ground motion with high-frequency components and short strong motion duration, the relative lateral displacement was 27 to 37 % lower than that of the test with RG1.60 input ground motion. In other words, the EQ 1 input ground motion required lower capacity of ductility than general earthquakes (RG1.60).

3) In addition, before reinforcing bars were yielding, the relative lateral displacement was 22.1 % lower than that of the tests with the EQ 1 input ground motion.

4) In the case of test with RG1.60, the acceleration amplification effect due to resonance occurred 1.5 times greater than that of the test with EQ 1. Thus, the yielding of vertical reinforcing bars were occurred at the 1.5 times lower PGA in the test with RG1.60.

5) In the cases of specimens with an aspect ratio of 2.0, the maximum measured overturning moment was 15 % higher in the test with EQ 1 input ground motion. However, in the cases of specimens with an aspect ratio of 1.0, the same maximum overturning moments were measured regardless of input ground motions.

6) The side effect of high-frequency earthquake was not observed in the results of shaking table test. The pseudo acceleration was measured similar to the value calculated based on the response spectrum as in general earthquakes.

Chapter 4. Structural Test for Cylindrical Walls

In Chapter 4, based on the results of cyclic axial loading test for cylindrical and semi-cylindrical wall specimens, the effect of loading rate and post-tensioning force on shear strength of cylindrical walls were investigated.

4.1 Experiment III: Cylindrical wall

4.1.1 General

After the great East Japan earthquake (2011), the seismic safety and evaluation of nuclear power plants has been concerned. Further, several earthquakes which were exceeding the design earthquake spectrum RG1.60 have occurred nearby the sites of nuclear power plant in moderate earthquake zones (i.e., North Anna EQ (2011), Kyung-Ju EQ (2016), and Po-Hang EQ (2017)). For this reason, the existing nuclear power plants was re-evaluated with advanced evaluation methods. In addition, in the case of nuclear power plants, generally the containment building has a post-tensioned cylindrical wall structure due to resist the internal pressure.

To investigate the shear strength of reinforced concrete walls, various experimental researches have been performed. However, the most of them were considered the planar walls with and without boundary elements and the case of the test with consideration of post-tensioning was rare. The researches of the shear strength of cylindrical walls are relatively rare. To verify the shear strength and ductility of cylindrical wall, structural tests using reinforced concrete cylindrical

vessel with internal pressure using water tank were conducted and reported by Uchida et al (1979). Ogaki et al. (1981) tested 16 prestressed cylindrical concrete vessels (PCCVs). The aspect ratios of specimens were 3.0 or 1.0 and the tests were conducted under torsional or lateral loading. The result of research was that the evaluated tangential shear strength of RCCV and PCCV was proposed based on the truss analogy or concrete failure envelope. On the other hand, flexural yielding occurred before shear failure in five specimens tested under horizontal loading. Thus, the proposed equation was based on the test data of test specimens with flexural yielding and shear failure modes. Katoh et al. (1987) and Wu et al. (2019) reported the seismic performance of prestressed cylindrical and reinforced walls using shaking table tests and cyclic tests.

Generally, to prevent leakage of radioactive material and withstand high internal pressure when the emergency accident occurs, the containment walls are designed using post-tensioning force. In this case, due to the cylindrical geometry of the containment wall, the detail of horizontal post-tensioning tendon is curved and the horizontal post-tensioning force causes tensile stress in the radial direction. The radial tensile stress can cause internal cracks along the post-tensioning tendon layer. The internal cracks induce the concrete delamination damage (Archarya and Menon 2003). Such concrete delamination cracks were found in the containment building of nuclear power plant while applying post-tensioning force (i.e. Turkey Point Nuclear Power Plant (Florida Power and Light Company, 1970), Crystal River Nuclear Power Plant (Florida Power and Light Company, 1976) and Kaiga Atomic Power Project (Basu et al. 2001)). In the Chapter 1, Figure 1-4 shows that the delamination failures occurred in Crystal River Nuclear Power Plant (Nuclear Regulatory Commission 2010).

In the test of curved concrete walls with horizontal post-tensioning ducts, Choi et al. (2017) and Choi (2018) investigated that concrete delamination cracks can occur due to horizontal post-tensioning. Two scales of test specimens with different sheath diameters were tested. The delamination failure was occurred under the design level of tensile stress of concrete. The internal cracks or concrete delamination may degrade the shear strength of cylindrical walls. However, in the previous researches, the effect of concrete delamination on the shear strength of cylindrical walls had not been investigated. Thus, the effect of early concrete delamination which is caused by horizontal post-tensioning is need to verify.

Recently, earthquakes with high-frequency contents had occurred nearby existing nuclear power. In addition, the earthquakes with high-frequency contents affects the resistance of containment building due to the high strain rate effect and the earthquake can cause high amplification in the response of equipment due to the high natural frequency of the equipment. Previous researches in the Chapter 3 on reinforced concrete planar walls and other researches (Hlralshi et al. 1984) reported that the maximum tested shear strengths of planar walls were increased by (5 – 10) % under strain rate of 10^{-1} s^{-1}. However, the effect of loading rate on cylindrical walls has not been reported.

In the present chapter, to investigate the shear strength of cylindrical wall, total six cylindrical reinforced and post-tensioned concrete wall specimens were tested under cyclic lateral loading: Two for without and four for with post-tensioning). The test parameters were the loading rate, post-tensioning force (with and without post-tensioning), and the magnitude of vertical and horizontal post-tensioning forces (vertical post-tensioning only; 100 % of vertical post-tensioning + 50 % of horizontal post-tensioning; and 100% of vertical post-tensioning + 100 % of horizontal post-

tensioning). The loading rate (low-rate (1mm /s [0.039 in/s] and high-rate 100mm /s [3.93 in/s]) was considered to investigate the loading rate effect on the shear strength. All test specimens were designed based on the reinforcing bar and tendon ratios of actual containment building of nuclear power plants in Korea.

4.1.2 Test plan

4.1.2.1) Major test parameters

In nuclear power plant containment buildings, due to high seismic demand, the horizontal reinforcement ratio approaches the maximum allowable reinforcement ratio of 1 % as specified in ACI 349. The post-tensioning bar ratios are 1.0% and 0.6% for horizontal and vertical direction, respectively (Lee and Song (1999)). Therefore, all specimens tested in these experiments were designed with the maximum reinforcing bar ratio.

Two RC and four PSC cylindrical walls were tested (see Table 4-1). The name of the specimens represents the test parameters. The first letter C represents the shape of specimens, which is cylindrical shape. The second letters, R and P, refer to the reinforced concrete with and without prestressing forces. The third letters, S and D, refer to low-and high-speed loadings of 1 and 100mm/s, respectively. The following letter S refers the failure mode: shear failure mode. The fifth letter 1.0 indicates the aspect ratio of specimens. The reinforcing bar ratio were 0.72 and 1.86 for horizontal and vertical directions, respectively. Thus, the sixth letter Q refers the 0.72 % of horizontal reinforcing bar ratio. The last letters V, and Vh represent only vertical and vertical and half of horizontal post-tensioning, respectively. The other last letters 31, and 43 indicate the compressive strength of concrete.

Table 4-1 Design parameters of cylindrical test specimens

Specimens	f_c', MPa	Aspect ratio	Design failure mode	Loading rate, (mm/s)	Reinforcing bar ratios			Prestressing bar ratios			Design strength prediction			
					ρ_h, %	ρ_v, %	ρ_f, %	ρ_{pv}, %	ρ_{ph}, %	F_{ph}, (MPa)	V_f, kN	$V_{n,ACI}$, kN	V_{sf}, kN	$V_{n,EPRI}$, kN
CRSS1.0Q	38	1.0	Shear	1	0.72	1.86	8.21	-	-	-	2,480	400	2,043	1,007
CRDS1.0Q	38			100	0.72	1.86	8.21	-	-	-	2,480	400	2,043	1,007
CPSS1.0Q-31	31			1	0.72	1.86	1.86	0.64	1.00	1300	2,781	859	2,043	1,518
CPDS1.0Q-43	43			100	0.72	1.86	1.86	0.64	1.00	1300	2,815	1,011	2,043	1,788
CPDS1.0Q-V	38			100	0.72	1.86	8.21	0.64	-	-	6,881	400	2,043	1,654
CPDS1.0Q-Vh	38			100	0.72	1.86	8.21	0.64	1.00	650	7,942	951	2,043	1,680

Note: f_c' is a concrete compressive strength; aspect ratio is h_w/l_w; ρ_h, ρ_v, and ρ_f, are horizontal, vertical reinforcing bar ratios in the web area, and vertical reinforcing bar ratio in the flange area, respectively; ; ρ_{ph}, ρ_h, and ρ_{pv}, are horizontal, vertical prestressing bar ratios in the web area, respectively; V_f is a flexural strength prediction; V_n is a shear strength predicted based on ACI 359; V_{sf} is a shear-friction strength prediction; and $V_{n,EPRI}$ is a shear strength prediction predicted based on EPRI report.

4.1.2.2) Test specimens

Six specimens were prepared for cyclic lateral loading test. Figure. 4-1 shows the dimensions and details of the specimens and Table 4-1 shows the design parameters. The dimensions of cylindrical wall specimens were 1400 mm (external diameter) × 1300 mm (height) × 90 mm (thickness). The aspect ratio of the specimen was designed to be the same ratio of the moment/shear (M/V) ratio of the prototype containment building under seismic loads. For anchorage of horizontal post-tensioning tendons, two flanges with a length of 900 mm were added. In the anchorage zone, exterior cover concrete of 30mm was provided inner face of the wall to prevent concrete spalling during applying horizontal post-tensioning (Fig. 4-1 (c) and (d)).

In specimens CRSS1.0Q and CRDS1.0Q, to investigate the effect of loading rate, the specimens were prepared. The reinforcing bar ratios of web ρ_{wv}, and flange ρ_{fv} were 1.86% and 8.21%, respectively (Table 4-1) and the horizontal reinforcing bar bar ratio was 0.72%. The vertical reinforcing bar ratio was increased to prevent flexural yielding failure before shear failure; Grade 420 MPa 12-D29 (No. 9) reinforcing bars were used (Fig. 4-1). The nominal flexural strength V_f = 2480 kN predicted by sectional analysis and the nominal shear-friction strength V_{sf} = 2043 kN were significantly greater than the design shear strength $V_{n,ACI}$ (=400 kN) predicted by ACI 359. For evaluation of nuclear power plant building, the evaluation strength based on EPRI $V_{n,EPRI}$ was 1007 kN.

In case of specimens with the post-tensioning force CPSS1.0Q-31 and CPDS1.0Q-43, Grade 420 MPa D19 (No. 6) reinforcing bars were used for vertical

reinforcement; the vertical reinforcing bar ratio ρ_v was 1.86%. For horizontal reinforcement, Grade 420 MPa D13 (No. 3) with a spacing of 110 mm were used (ρ_h = 0.72%). Because of the small wall thickness (90 mm), high-density polyethylene (HDPE) greased strands were used. The vertical and horizontal post-tensioning bar ratios were 0.64% and 1.00%, respectively. The post tensioning stress was 70% of yield stress of post-tensioning bar (= 1300 MPa). The applied compressive stresses to concrete due to post-tensioning force were 8.32 MPa and 13MPa according to vertical and horizontal direction, respectively. This post-tensioning force is similar to that of prototype containment structure. Using nonlinear finite element analysis (ATENA 5.6.0.15700 (Cervenka et al. 2002)) due to nonlinearity of post-tensioning behavior, The nominal flexural strength of CRSS1.0Q was predicted as V_f = 2781 kN. The nominal shear-friction strength of CPSS1.0Q-31 was V_{sf} = 2043 kN based on ACI 359. An equivalent axial load was used to apply the effect of vertical post-tensioning force. The design and evaluation shear strengths of CPDS1.0Q-31 according to ACI and EPRI were $V_{n,ACI}$ = 859 kN, and $V_{n,EPRI}$ = 1518 kN, respectively. To investigate the effect of concrete compressive strength, the specimen CPSS1.0Q-31 and CPDS1.0Q-43 had different compressive strength of concrete: 31 MPa and 43 MPa for CPSS1.0Q-31 and CPDS1.0Q-43, respectively. Reinforcing bar details and dimensions of CPDS1.0Q-43 were the same as CPSS1.0Q-31. The design strengths of CPDS1.0Q-43 were V_f = 2815 kN, V_{sf} = 2043 kN, $V_{n,ACI}$ = 1011 kN, and $V_{n,EPRI}$ = 1788 kN, respectively.

In the case of the other post-tensioned specimens CPDS1.0Q-V and CPDS1.0Q-Vh, the reinforcing bar details were the same as those of RC specimens (CRSS1.0Q and CRDS1.0Q). The details of horizontal and vertical post-tensioning tendons were the same as those of CPSS1.0Q-31 and CPDS1.0Q-43. The post-tensioning force for

vertical direction were the same as those of PSC specimens. However, the horizontal post-tensioning force were different. The horizontal post-tensioning forces of CPDS1.0Q-V and CPDS1.0Q-Vh were 0 MPa and 650 MPa, respectively. In the case of specimen CPDS1.0Q-Vh with half of horizontal post tensioning force, the compressive stress due to the horizontal prestressing forces were 6.5MPa to the concrete section. The shear strength predicted by ACI 359 of CPDS1.0Q-V without horizontal post-tensioning force was $V_{n,ACI}$ = 400 kN, and that predicted by EPRI was $V_{n,EPRI}$ = 1654 kN. The nominal flexural and shear-friction strengths were V_f = 6881 kN, and V_{sf} = 2043 kN. Because of high vertical reinforcing bar ratio of flange area, flexural strength (V_f = 6881 kN) and shear-friction strength (V_{sf} = 2043 kN) of CPDS1.0Q-V were much higher than the shear strength. Because of the higher horizontal post-tensioning force, in the case of CPDS1.0Q-Vh, the design shear strengths ($V_{n,ACI}$ = 951 kN, and $V_{n,EPRI}$ = 1680 kN) were higher than those of CPDS1.0Q-V. The nominal shear-friction strength of CPDS1.0Q-Vh (V_{sf} = 2043 kN) was the same as CPDS1.0Q-V due to identical reinforcing bar details of concrete cross-section. The nominal flexural strength was V_f = 7942 kN.

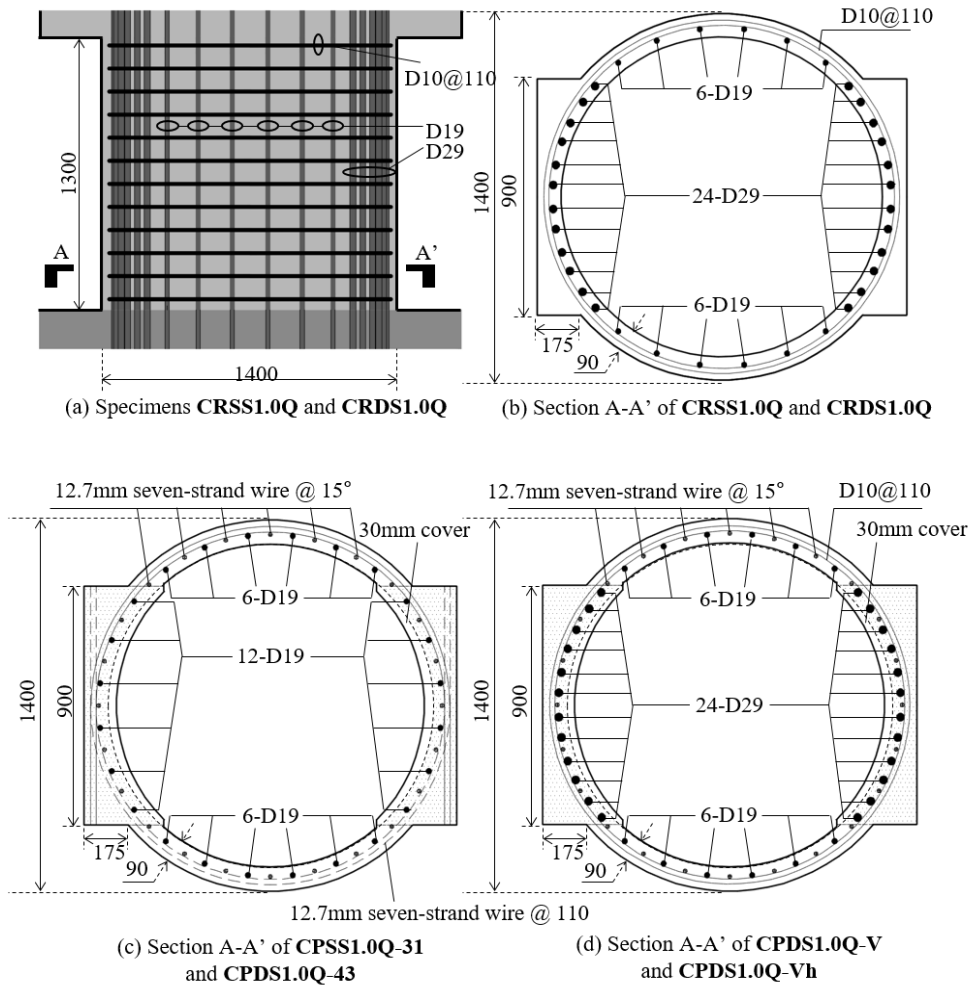

(a) Specimens **CRSS1.0Q** and **CRDS1.0Q**

(b) Section A-A' of **CRSS1.0Q** and **CRDS1.0Q**

(c) Section A-A' of **CPSS1.0Q-31** and **CPDS1.0Q-43**

(d) Section A-A' of **CPDS1.0Q-V** and **CPDS1.0Q-Vh**

Figure 4-1 Dimensions of cylindrical test specimens

4.1.2.3) Test procedure and application of post-tensioning

Two dynamic actuators were used to apply the cyclic loading. The test set-up is shown in Fig. 4-2. The loading protocol followed ACI 374.2: Three cyclic loads were applied at each load step, as the drift ratio is increased to 1.25 to 1.5 times the previous drift ratio. Fig. 4-2 shows the LVDTs for the measurement: L1 and L2 for lateral displacements, L3 and L4 for shear deformations, L5 - L10 for flexural deformations, and L11 for sliding at the wall base. Strain gauges were used to measure the strain of reinforcing bars and the location of strain gauges were in Fig 4-3.

In the use of tendon and prestressing, the major concern was the loss of load of the prestressing force due to seating of the wedges and measurement of prestressing force. Figures 4-4 (a) and (b) show the detail of anchor and load cells, which were for measuring the post-tensioning force. The load cells which were made of cylindrical iron and strain gauges was calibrated using UTM before measuring the post-tensioning forces. The load cell was installed at start and dead ends of the tendon. Figure 4-4 (c) shows the measured prestressing force. For applying the design force (128kN), at the first time, higher jacking force was applied. The measurements were continued during jacking and after wedge was settled

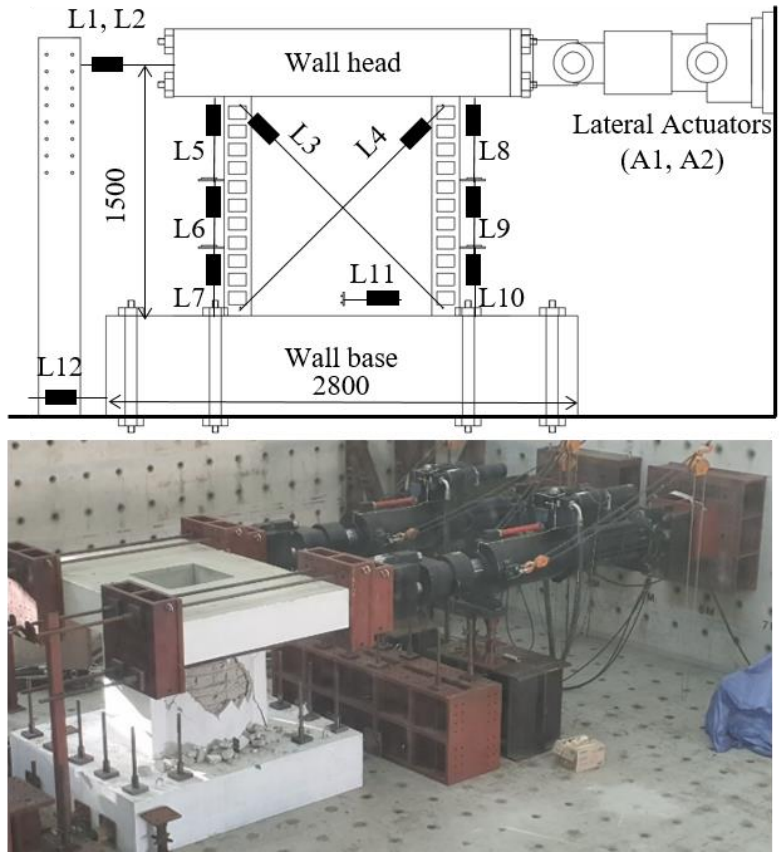

Figure 4-2 Test set up of cylindrical test specimens

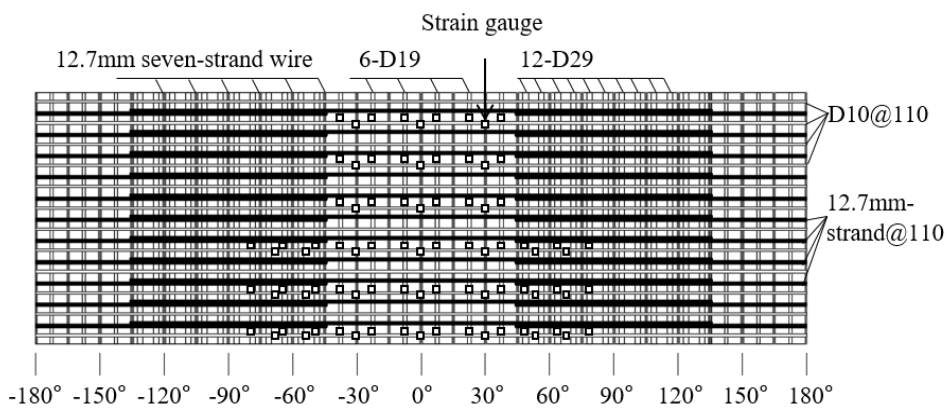

Figure 4-3 Location of strain gauges of cylindrical test specimens

(a) Anchorages of vertical and horizontal directions

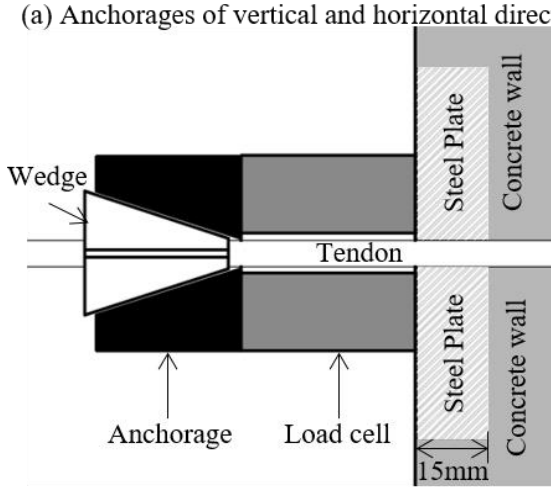

(b) Anchorage and load-cell details of live and dead ends

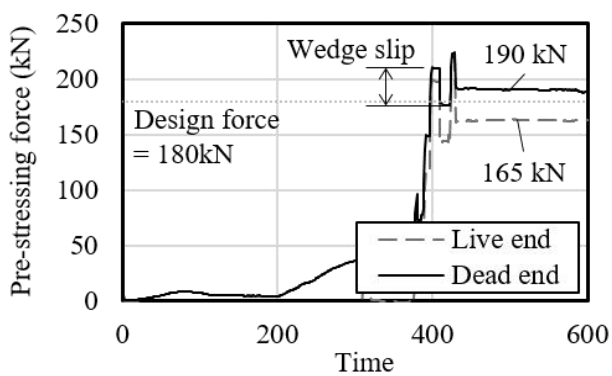

(c) Measured pre-stressing force at live and dead ends

Figure 4-4 Anchorage detail and prestressing force

4.1.3 Test results

4.1.3.1) Lateral load-displacement relationships

Table 4-2 shows the summary of test results. Figure 4-5 shows the relationships of lateral load-displacement of the test specimens. The lateral displacement indicates the measured average displacement from two LVDTs (L1 and L2) excluding slip displacement of the specimen measured at the bottom slab (L12). The lateral load refers the sum of reaction forces from actuators A1 and A2. Fig. 4-5 also includes the nominal shear strength $V_{n,ACI}$ and $V_{n,EPRI}$ predicted by ACI 359 and EPRI, and nominal flexural strength V_f to compare the test results. In all specimens, except CRDS1.0Q, the maximum strength in the positive direction (push) was greater than that in the negative direction (pull).

In the case of CRSS1.0Q (Fig 4-5(a)) without prestressing force and under low-loading rate, the maximum tested strengths were +1798 kN and -1491 kN at a drift ratio of +0.90% and -0.75%, respectively. These were 4.50 and 3.73 times the nominal shear strength predicted by ACI-359 $V_{n,ACI}$. Immediately after the peak load, the load carrying capacity decreased to 30% of the maximum tested strength.

In the counterpart reinforced concrete specimen CRDS1.0Q (Fig. 4-5(b)) with high loading rate, the maximum test strengths were +1935 kN and -1799 kN at drift ratio 14% and 1.07%, respectively. The maximum strengths of the specimen under high loading rate were 9% and 20% higher than those of CRSS1.0Q with low-loading rate.

In the case of post-tensioned specimen SPSS1.0Q-31 (Fig. 4-5(c)) under low

loading rate, the maximum tested strengths were +1375 kN and -1250 kN at the drift ratio of 0.6%. In this case, premature shear failure occurred before flexural yielding. Furthermore, the maximum tested strengths were 10% and 18% smaller than the nominal shear strength $V_{n,EPRI}$, respectively. In addition, in the case of CPDS1.0Q-43 (Fig. 4-5(d)) with prestressing force, under higher-loading rate and higher compressive strength of concrete, premature shear failure occurred. The maximum strengths were +1687 kN and -1470 kN at drift ratios of 0.6% and 0.5 %, respectively. In the case of high loading rate, the maximum tested strengths were 23%, and 18% higher than those of the specimens under low loading rate CPSS1.0Q-31 as the compressive strength of concrete was 28% higher. Nevertheless, in the case of CPDS1.0Q-43, the maximum tested strength in the negative direction was 18% lower the nominal shear strength $V_{n,EPRI}$.

In the case of CPDS1.0Q-V (fig 4-5(e)) without horizontal post-tensioning and CPDS1.0Q-Vh with 100 % of vertical and 50 % of horizontal post-tensioning stress, the maximum tested strengths in the positive direction were 2203 kN and 2222 kN, respectively. In the case of the negative direction, the maximum tested strengths of those were -1809 kN and -1844 kN. On the other hand, the drift ratio of the maximum tested strengths occurred were different (1.00% and 0.5%, CPDS1.0Q-V and CPDS1.0Q-Vh, respectively).

Table 4-2 Summary of cylindrical test results

Specimens	Loading rate, (mm/s)	Test results				
		$V_{test,+}$ (kN)	$V_{test,-}$ (kN)	$V_{test,}$ (kN)	Drift ratio at V_{test} (%)	Failure mode
CRSS1.0Q	1	1769	1491	1630	+0.90/-0.75	Shear
CRDS1.0Q	100	1935	1799	1868	+1.14/-1.07	Shear
CPSS1.0Q-31	1	1375	1250	1312	+0.61/-0.60	Shear
CPDS1.0Q-43	100	1687	1470	1578	+0.59/-0.54	Shear
CPDS1.0Q-V	100	2203	1809	2005	+1.00/-0.99	Shear
CPDS1.0Q-Vh	100	2222	1844	2033	+0.55/-0.45	Shear

Note: $V_{test,+}$, $V_{test,-}$, and V_{test} are the measured maximum loads in the positive, negative and average loading directions, respectively;

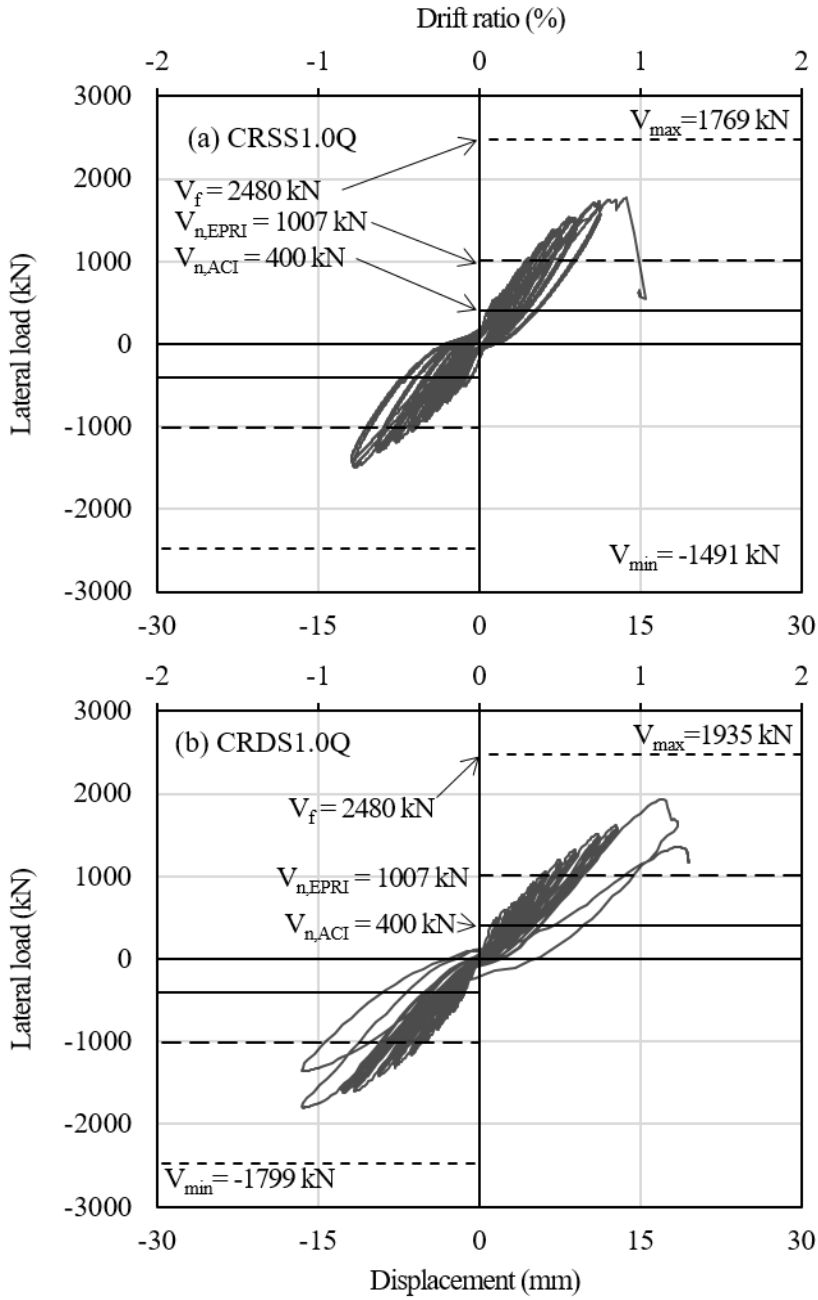

Figure 4-5 Relationships of load-displacement of cylindrical test specimens

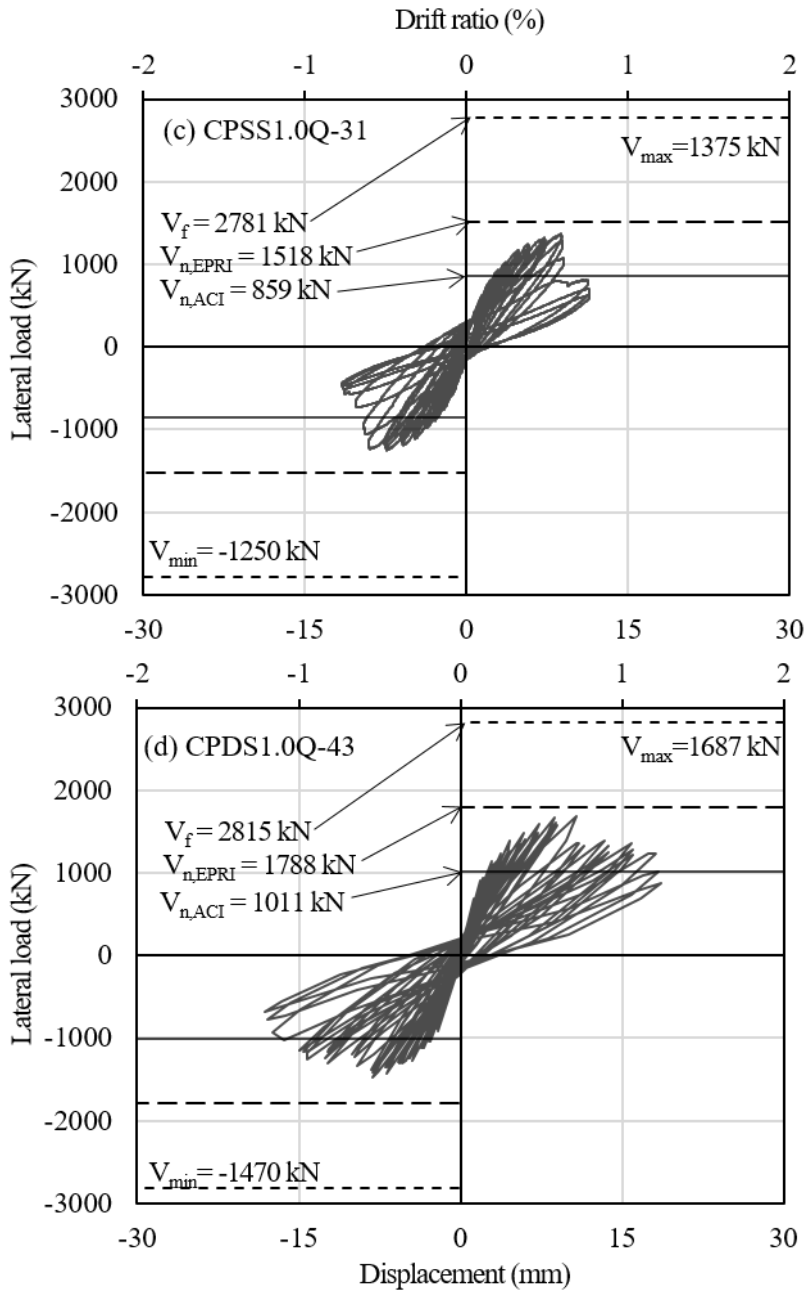

Figure 4-5 Relationships of load-displacement of cylindrical test specimens

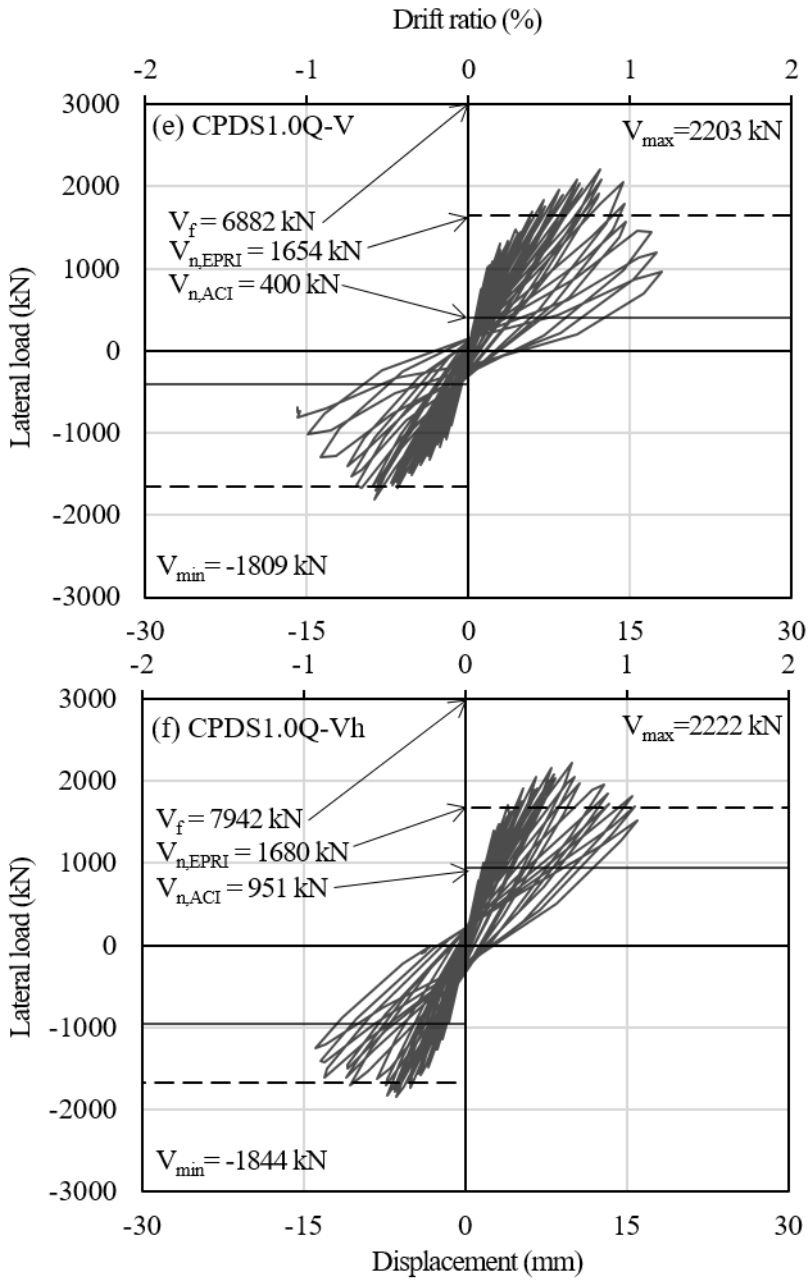

Figure 4-5 Relationships of load-displacement of cylindrical test specimens

4.1.3.2) Failure mode

Figure 4-6 shows failure modes of the cylindrical shape specimens at the end of the test. The macro cracks were occurred in the all specimens and the diagonal shear failure mode was occurred. In the case of reinforced concrete specimens CRSS1.0Q and CRDS1.0Q (figs 4-6 (a) and (b)), the large diagonal cracks were distributed in the web area of wall. The spacing of diagonal crack was similar to that of planar walls.

On the other hand, in the case of post-tensioned specimens CPSS1.0Q-31 and CPDS1.0Q-43 (figs 4-6(c) and (d)), macro diagonal cracks occurred in first step (the drift ratio of 0.1 %), and the spacing of cracks were large. After the test, cover concrete was easily removed. Figure 4-7 shows the side view of specimens with full horizontal post-tensioning specimens to show the cover concrete separated from the prestressed walls. This phenomenon was prominent in the specimens CPSS1.0Q-31 and CPDS1.0Q-43 with full horizontal prestressing force.

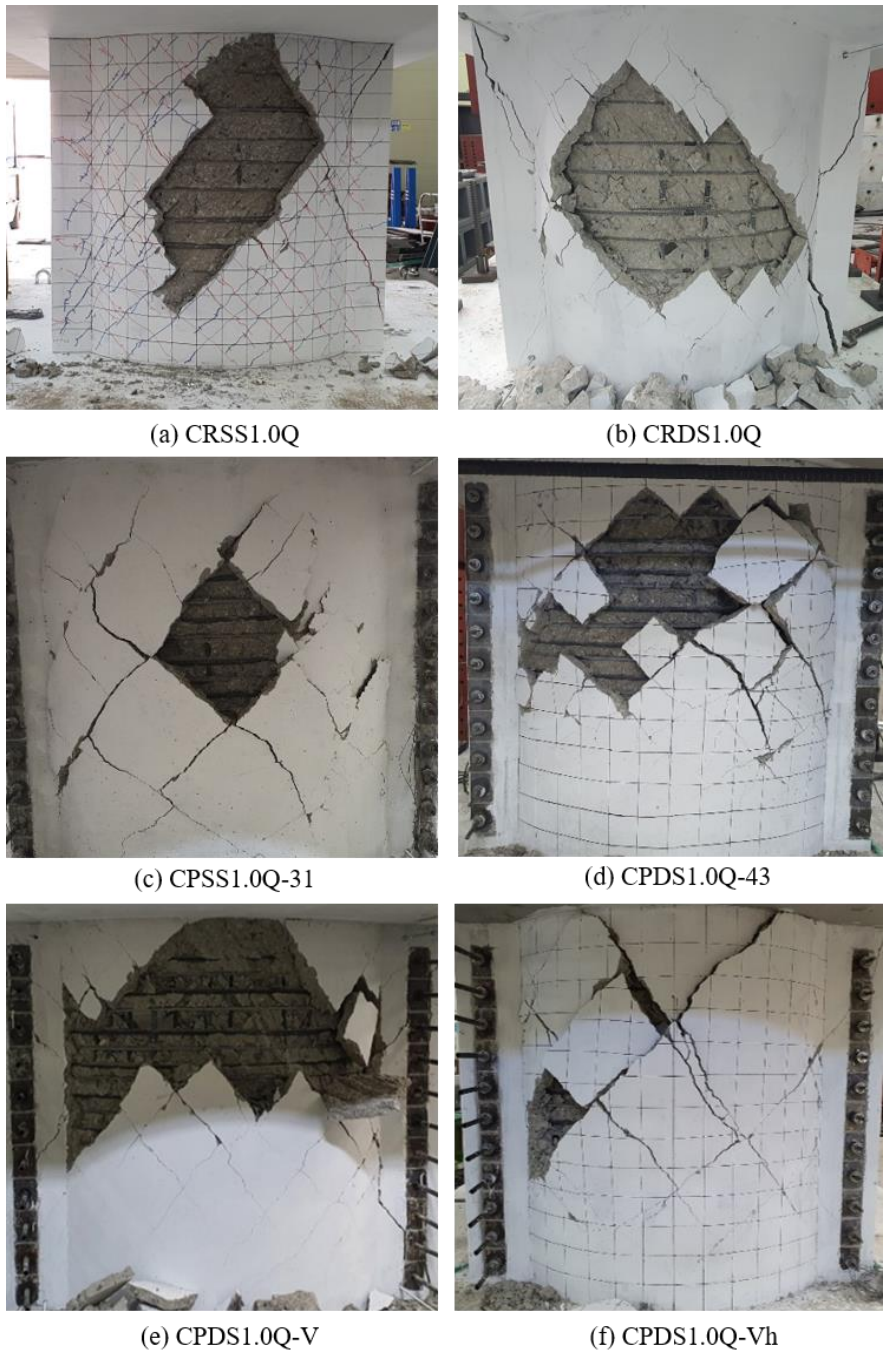

(a) CRSS1.0Q (b) CRDS1.0Q

(c) CPSS1.0Q-31 (d) CPDS1.0Q-43

(e) CPDS1.0Q-V (f) CPDS1.0Q-Vh

Figure 4-6 Failure modes of cylindrical shape specimens (front view)

(a) CPSS1.0Q-31 (b) CPDS1.0Q-43

Figure 4-7 Damage modes of specimens with horizontal post-tensioning at the end of test (side view)

4.1.3.3) Strains of reinforcing bars

Figure 4-8 shows measured strain distributions of the horizontal reinforcing bars along the wall height at 0.5 V_{max}, 0.75V_{max}, and 1.0V_{max}: where V_{max} indicates the maximum tested strength. The location of the strain gauges are shown in Fig. 4-3.

In the case of reinforced concrete specimens without post-tensioning force CRSS1.0Q and CRDS1.0Q (Figs. 4-8 (a) and (b)), at 0.75 V_{max}, the strains of horizontal reinforcing bars in the mid-height area exceeded the yield strain. The strains of horizontal reinforcing bars in the mid height were higher than those in the top and bottom area of the wall.

In the case of specimens CRSS1.0Q-31 and CRDS1.0Q-43 (figs 4-8 (c) and (d)) with vertical and horizontal prestressing force, the strains of all horizontal reinforcing bars were very low until the maximum tested strength.

On the other hand, in the case of specimens CPDS1.0Q-V with only vertical post-tensioning force specimen (fig 4-8 (e)), the strains of horizontal reinforcing bars were exceeded the yield strains of reinforcing bar at V_{max}.

In the case of the other specimen CPDS1.0Q-Vh with 100 % vertical and 50 % horizontal post-tensioning force (fig 4-8 (f)), the horizontal reinforcing bars were not yield after the test end.

These results indicate that in the case of cylindrical walls with the horizontal post-tensioning, due to premature loss of bond after concrete cover failure, the horizontal reinforcing bars did not provide shear resistance.

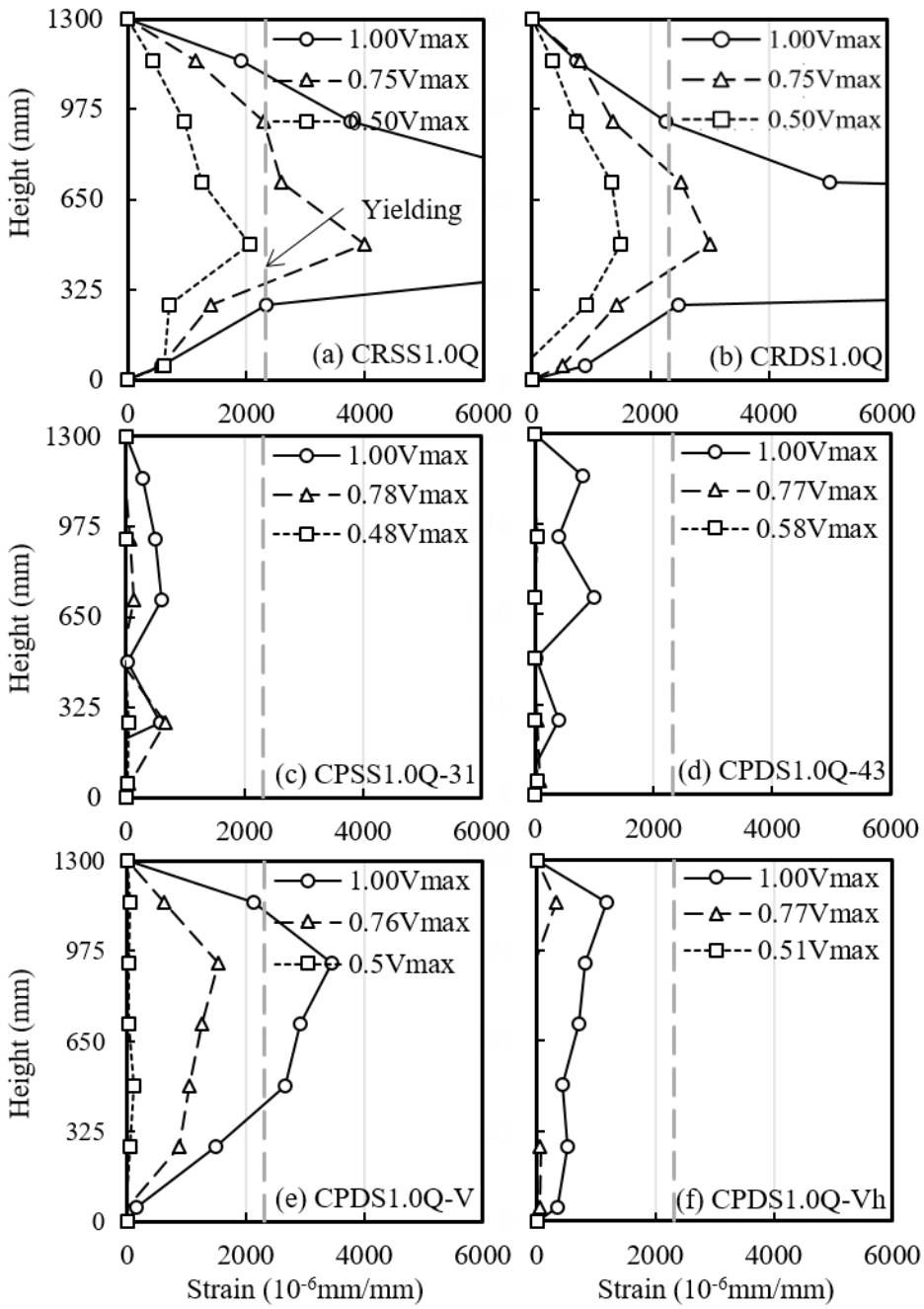

Figure 4-8 Measured strains of horizontal reinforcing bars of cylindrical specimens

Figure 4-9 shows strain distributions of the vertical reinforcing bars along the length of the wall at 0.5 V_{max}, 0.75V_{max}, and 1.0V_{max}. The gray area of Fig. 4-9 indicates the flange area where high reinforcing bar ratio was used. Some strain gauges were failed during or before the test. The results of the failed strain gauges were not displayed. Because of the flexural action, the strains of vertical reinforcing bars were linearly distributed along the wall angle in the all specimens. In all vertical reinforcing bars except CRSS1.0Q (Fig. 4-9 (a)), the values of vertical reinforcing bars were not yield. This result indicates that the failure mode of all specimens were shear failure before flexural yielding.

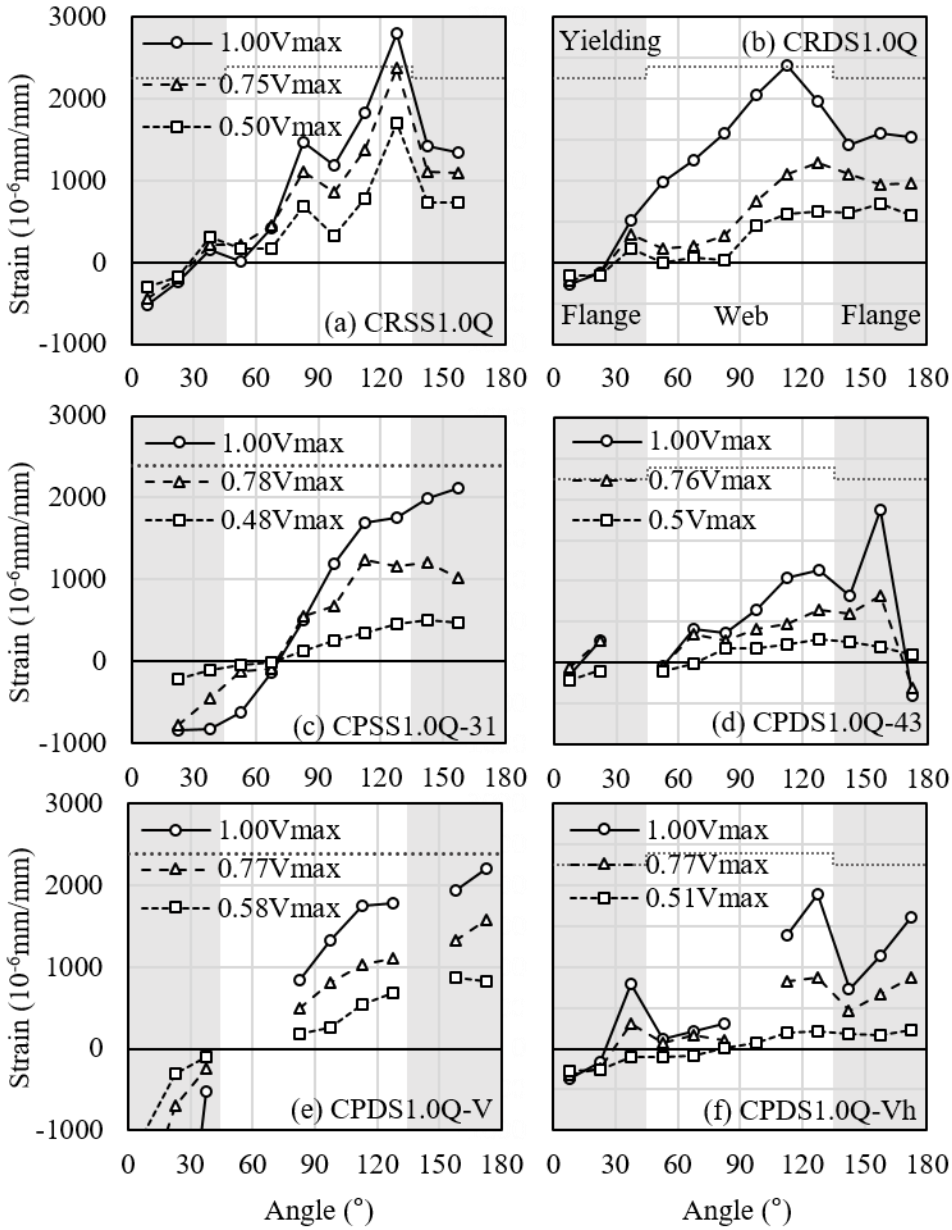

Figure 4-9 Measured strains of vertical reinforcing bars of cylindrical specimens

4.1.4 Summary of experiment III

To investigate the shear strength of cylindrical walls without and with post-tensioning, two reinforced concrete and four post-tensioning cylindrical shape specimens were tested under cyclic lateral loading. The major test parameters were loading rate, concrete strength and magnitude of horizontal post-tensioning. In the case of all test specimens, the shear failure mode with diagonal cracking was occurred. The major findings of this chapter are summarized as follows:

1) In the case of reinforced concrete specimen without post-tensioning force under higher loading rate, the maximum tested strengths were increased by 2% to 30%, when compared to the other reinforced concrete specimen with low loading rate. The failure mode of cylindrical shape wall with diagonal cracking was similar to that of planar reinforced concrete walls in **Chapter 3.1 Experiment I: Dynamic loading test**. The maximum tested strength exceeds the design shear strength predicted by ACI-359 which is current design code.

2) In the case of CRSS1.0Q-31 and CRDS1.0Q-43 with 100 % vertical and 100% horizontal post-tensioning, delamination cracks were occurred in along the horizontal post-tensioning tendons. Thus, due to delamination of cover concrete caused by horizontal prestressing, premature shear failure occurred. The maximum tested strengths were lower than the evaluation shear strength.

3) In the case of CPDS1.0Q-43 with higher concrete compressive strength and higher loading rate showed better performance than CPSS1.0Q-31. The

horizontal reinforcing bars did not resist shear force due to loss of bond strength (i.e. due to early delamination).

4) In the case of CPDS1.0Q-V without horizontal post-tensioning and only vertical post-tensioning and CPDS1.0Q-Vh with 50 % of horizontal prestressing, the maximum tested strength exceeded the design and evaluation shear strength ($V_{n,ACI}$ and $V_{n,EPRI}$).

5) The maximum tested strengths of CPDS1.0Q-Vh were similar as those of CPDS1.0Q-43 with full horizontal prestressing and high concrete strength. This result indicates that the advantage effect of horizontal prestressing on the shear strength of cylindrical PSC wall was occurred through maximum tested strength.

4.2 Experiment IV: Semi-Cylindrical wall

4.2.1 General

Containment building of nuclear power plants requires a high level of seismic safety and resistance capacity of internal pressure as a building that handles radioactive materials. In particular, containment buildings of nuclear power plant are the final safeguard against radioactive material leakage in case of an emergency accident such as earthquakes or airplane crashes. In the case of an emergency accident, the containment building withstands the internal pressure of about 0.4 MPa. Thus, post-tensioning is applied to the containment wall and is commonly used to resist membrane tensile stresses caused by internal pressure.

In general, due to the high requirements, containment walls of nuclear power plant are designed with high reinforcing bar ratios. In this case, the walls are susceptible to concrete crushing failure at the web. The behavior of web-crushing failure of reinforced concrete walls with high reinforcing bar ratio was reported by Eom et al. (2013), Oesterle et al. (1981), and Burgueño and Hines (2014) based on numerical and experimental results.

However, most existing researches about reinforced concrete walls were performed for a planar shape. The studies of cylindrical walls with prestressing are rare. Aoyagi et al. (1981), Ogaki et al. (1981), Uchida et al. (1979), Wu et al. (2019), and Katoh et al. (1987) studied cylindrical.

The post-tensioning is an effective method in restraining concrete cracking.

However, due to the cylindrical shape of containment building, tensile stress in the radial direction was occurred by the horizontal post-tensioning forces along the horizontal post-tensioning tendon. Due to the tensile stress in radial direction, internal cracking can occur. The internal cracks due to the horizontal post-tnesioning was reported in Archarya and Menon (2003), Choi (2018) and Choi et al. (2017). Such concrete delamination cracks were occurred in actual containment walls: Unit-3 containment of Turkey Point NPP (Florida Power and Light Company 1970), Unit-3 containment of Crystal River in Florida (Nuclear Regulatory Commission 2010 and Florida Power and Light Company 1976), and the Kaiga Atomic Power Project (Basu et al. (2001)). To prevent the delamination due to curved post-tensioning, ACI 359 requires radial cross-ties for dome and cylindrical walls. However, the effect of cross-tie on the shear strength of cylindrical wall was not experimentally verified.

In addition, in the Chapter 4-1, the cylindrical was also conducted the cyclic tests for cylindrical walls. In that case, because of the thickness of the wall, the reinforcing bars and post-tensioning tendons were arranged in a one layer. The area of the tendon sheath and reinforcing bars occupied a large area in the concrete section of the wall, which significantly reduced the net area of the concrete at the layer of the tendon and reinforcing bars. The net area of the concrete at the layer was reduced to 64 %. Due to the reduced concrete area and the curved shape, the tensile stress in the radial direction exceeded the tensile strength of the concrete and the delamination cracks were propagated significantly. In addition, the effect of internal delamination cracks on the shear strength of wall was increased. Thus, the test specimens with a thick cross-section for arranging reinforcing bars in double layers and separating the tendons and reinforcing bar layers should be considered.

In the this Chapter, the tangential shear strengths of cylindrical and I-shaped walls

were investigated focusing on the following considerations: 1) the effect of curved post-tensioning on concrete delamination in semi-cylindrical walls; 2) the effect of delamination on the shear strength of cylindrical walls with two reinforcing bar layers; 3) the effect of cross-ties on resistance of concrete delamination due to horizontal post-tensioning; and 4) the effect of horizontal and vertical post-tensioning on the shear strength and failure mode. For this purpose, semi-cylindrical and I-shaped RC & PSC wall specimens were prepared and tested under cyclic lateral loading. The test parameters were the post-tensioning (with and without post-tensioning), and the magnitude of vertical and horizontal post-tensioning forces (vertical post-tensioning only; 100% of vertical post-tensioning + 50% of horizontal p post-tensioning; and 100% of vertical post-tensioning + 100% of horizontal post-tensioning), shape of wall (cylindrical vs planar shape), and the use of cross-ties.

4.2.2 Test plan

4.2.2.1) Major test parameters

The target building of test specimens was the nuclear power plant containment building. Because of high seismic demand, the reinforcing bar ratio was closed to the maximum reinforcing bar ratio of ACI-349. However, due to the capacity limitation of actuators, the thickness of test specimen reduced. To investigate the shear capacity of thick-cylindrical reinforced concrete wall, the test specimens were designed as semi-cylindrical wall. Figure 4-10 shows the semi-cylindrical test specimen and location of actuators. Because of the asymmetric cross-section of test specimens, two actuators were used to apply lateral force without torsional force.

In this chapter, five semi-cylindrical walls and two I-shaped walls were prepared (Table 4-3). The name of the specimens represents the test parameters. The first letter S and I represents the shape of specimens: S is refers semi-cylindrical shaped walls and I is refers the I-shaped walls. The second letters, R and P, refer to the reinforced concrete with and without prestressing forces. The third letters, S refers to low-loading rate. The following the other letter, S refers the failure mode: shear failure mode. The fifth letter 1.0 indicates the aspect ratio of specimens. The sixth letter M refers the 0.93 % of horizontal reinforcing bar ratio which is the maximum reinforcing bar ratio of ACI 349. The last letters V, Vh, and VH represent (100 % of vertical), (100 % of vertical and 50 % of horizontal), (100 % of vertical and 100 % of horizontal) post-tensioning, respectively. The additional letter -C indicates the installation of cross-tie.

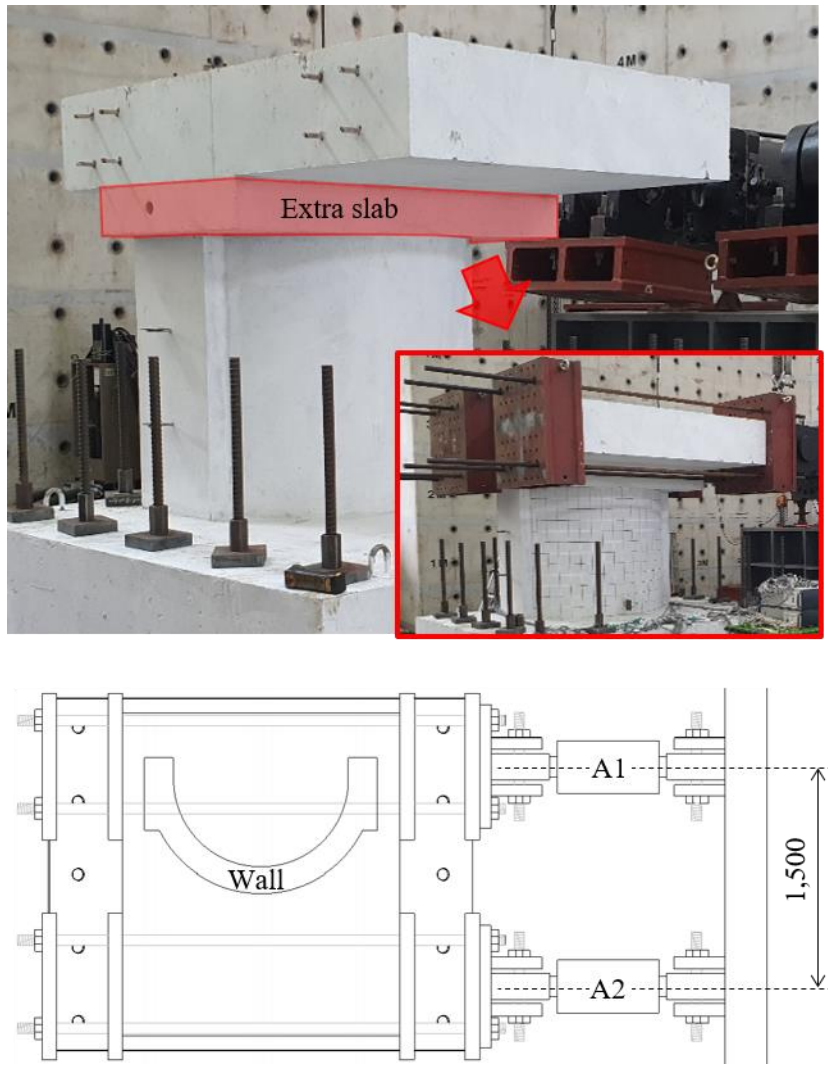

Figure 4-10 Test plan of semi-cylindrical wall

Table 4-3 Design parameters of semi-cylindrical test specimens

Specimens	f_c', MPa	Design failure mode	Shape	Reinforcing bar ratios			Prestressing bar ratios			Design strength prediction				Cross-tie
				ρ_h, %	ρ_v, %	ρ_f, %	ρ_{pv}, %	ρ_{ph}, %	F_{ph}, (MPa)	V_f, kN	$V_{n,ACI}$ kN	V_{sf}, kN	$V_{n,EPRI}$, kN	
SRSS1.0M	36	Shear	Semi-Cylindrical	0.93	1.86	5.71	-	-	-	3775	425	3121	1081	X
SPSS1.0M-V							0.64	-	-	4794	425	3121	1758	X
SPSS1.0M-Vh							0.64	1.00	650	4869	983	3121	1758	X
SPSS1.0M-VH							0.64	1.00	1300	4972	983	3121	1758	X
SPSS1.0M-VH-C							0.64	1.00	1300	4972	983	3121	1758	O
IRSS1.0M			I-shaped				-	-	-	2575	1434	2305	1380	X
IPSS1.0M							0.64	1.00	1300	3263	1434	2305	1981	X

Note: f_c' is a concrete compressive strength; aspect ratio is h_w/l_w; ρ_h, ρ_h, and ρ_h, are horizontal, vertical reinforcing bar ratios in the web area, and vertical reinforcing bar ratio in the flange area, respectively; ; ρ_{ph}, ρ_h, and ρ_{pv}, are horizontal, vertical prestressing bar ratios in the web area, respectively; V_f is a flexural strength prediction; V_n is a shear strength predicted based on ACI 359; V_{sf} is a shear-friction strength prediction; and $V_{n,EPRI}$ is a shear strength prediction predicted based on EPRI report.

4.2.2.2) Test specimens

Figures 4-11, 4-12, and 4-13 shows the dimensions and details of the specimens and Table 4-3 presents the design parameters. The aspect ratio of 1.0 was used, considering the lateral moment/shear (M/V) ratio of the containment building.

The dimensions of the semi-cylindrical wall specimen were 930 mm (external half diameter) × 1,200 mm (height) × 180 mm (thickness). The ratio of diameter and thickness was 0.1 which was 4.17 larger than the ratio of actual containment(R/t = 0.024). To prevent premature failure at the anchorage, the flanges area and vertical reinforcing bars were added at the anchorage area of horizontal prestressing. The dimensions of flanges were 500 mm (length) × 200 mm (thickness) and the total length of wall was 1,600 mm. In the case of I-shaped wall specimens, the dimensions of specimens were 1,600 mm (length) × 1,200 mm (height) × 180 mm (thickness). The length of the I-shaped wall was the same as that of the cylindrical wall, and the dimensions of flange area were the same (500 mm × 200 mm). The vertical and horizontal reinforcing bar ratios of web area were 1.86 % and 0.92 %, respectively (Table 4-3). The reinforcing bar ratios were the same as those of the prototype containment structure.

In the case of semi-cylindrical specimen without post-tensioning force SRSS1.0M, Grade 420 MPa [60 ksi] rebars were used for vertical and horizontal reinforcing bars. To induce the shear failure before flexural yielding, the vertical reinforcement ratio was intentionally increased in the area of flanges using 8-D-29 (No. 9) reinforcing bars. The nominal flexural strength V_f and shear-friction strength V_{sf} were 3,775 kN and 3,121 kN, respectively. Assuming the linear strain distribution, the nominal

flexural strength V_f was calculated by sectional analysis. The shear-friction strength V_{sf} was predicted based on ACI 359. The shear strengths predicted by ACI 359 $V_{n,ACI}$ and EPRI $V_{n,EPRI}$ were 425 kN and 1,018 kN, respectively. Since the shear strengths were smaller than the flexural and shear-friction strengths, the shear failure was expected before the flexural yielding failure.

To investigate the effect of vertical post-tensioning on the shear strength of cylindrical wall, the specimen SPSS1.0M-V was prepared. In the flange area, the vertical reinforcing bar was intentionally increased as the reinforced concrete specimen. The nominal flexural strength V_f was 4,794 kN and the nominal shear-friction strength V_{sf} was 3,121 kN. These nominal strengths were greater than the nominal shear strength of ACI ($V_{n,ACI}$ = 425 kN) and EPRI ($V_{n,EPRI}$ = 1,758 kN). The reason why the nominal shear strength predicted by ACI 359 is larger than $V_{n,EPRI}$ is that the contributions of concrete and vertical components of reinforcing bars were not considered.

To investigate the effect of magnitude of horizontal post-tensioning force on shear strength of cylindrical wall, the specimen SPSS1.0M-Vh with 100 % of vertical and 50 % of horizontal post-tensioning force was prepared. In addition, the effect of horizontal post-tensioning force on delamination was investigated.

In the cases of other post-tensioned specimens SPSS1.0M-VH and SPSS1.0M-VH-C with 100 % vertical and horizontal post-tensioning forces, the effects of magnitude of horizontal post-tensioning force on delamination and shear strength of cylindrical concrete wall was the major consideration.. The effect of cross-tie on delamination was investigated.

The vertical and horizontal post-tensioning tendon ratios were 0.64 % and 1.00 %,

respectively. The ASTM A416 Grade 270, 15.2 mm HDPE tendons without sheaths were used. The post-tensioning stress for 100 % post-tensioning force was 70 % of the yield stress of the tendon (= 1,300 MPa). The compressive stress of concrete due to the 100 % of vertical and horizontal post-tensioning force was 8.32 MPa and 13.0 MPa, respectively. The 50 % of horizontal post-tensioning force developed compressive stresses of and 6.5 MPa in the concrete section. The post-tensioning force were determined based on those of the prototype containment structure. The nominal strengths were V_f = 4,849 kN, V_{sf} = 3,121 kN, $V_{n,ACI}$ = 983 kN, and $V_{n,EPRI}$ = 1,758 kN for SPSS1.0M-Vh. In the case of SPSS1.0M-VH and SPSS1.0M-VH-C, the nominal strengths were V_f = 4,972 kN, V_{sf} = 3,121 kN, $V_{n,ACI}$ = 983 kN, and $V_{n,EPRI}$ = 1,758 kN. The nominal shear strength predicted by ACI and EPRI was limited by the web-crushing strength, due to the high reinforcement ratios and prestressing, the nominal shear strengths. Thus, the nominal shear strengths of the three specimens (SPSS1.0M-Vh, SPSS1.0M-VH, and SPSS1.0M-VH-C) predicted by ACI 359 and EPRI were the same.

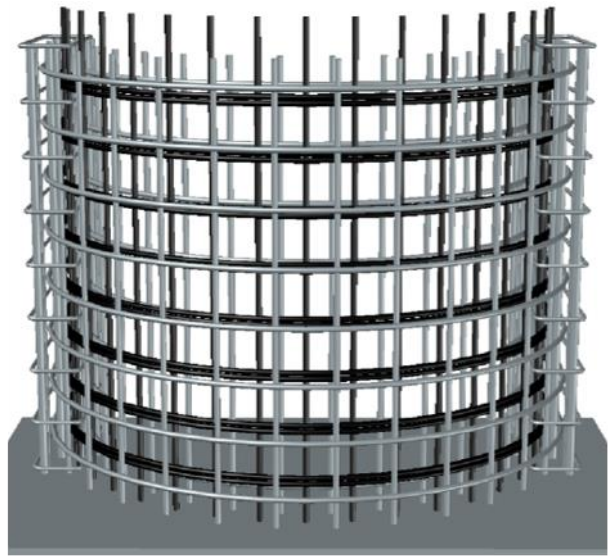

(a) Semi-cylindrical shape wall

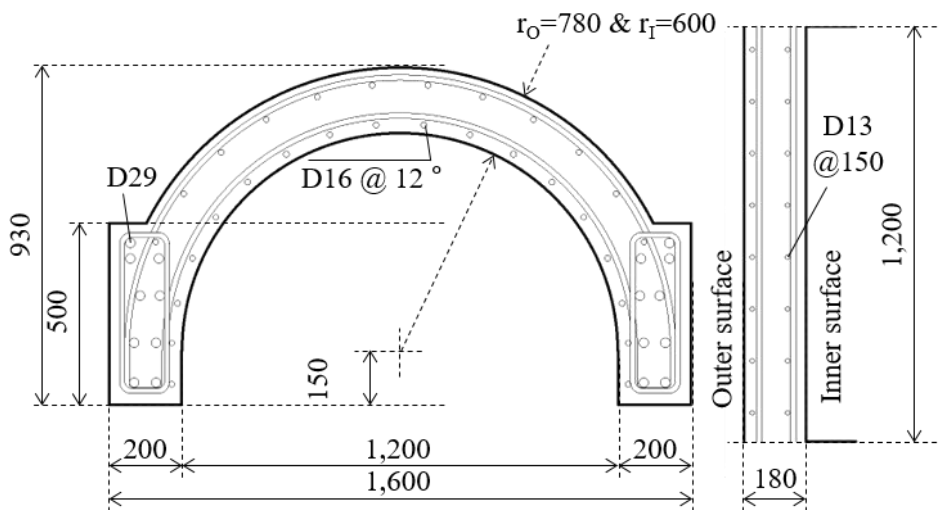

(b) Cross-section of CRSS1.0M

Figure 4-11 Dimensions of semi-cylindrical walls – 1

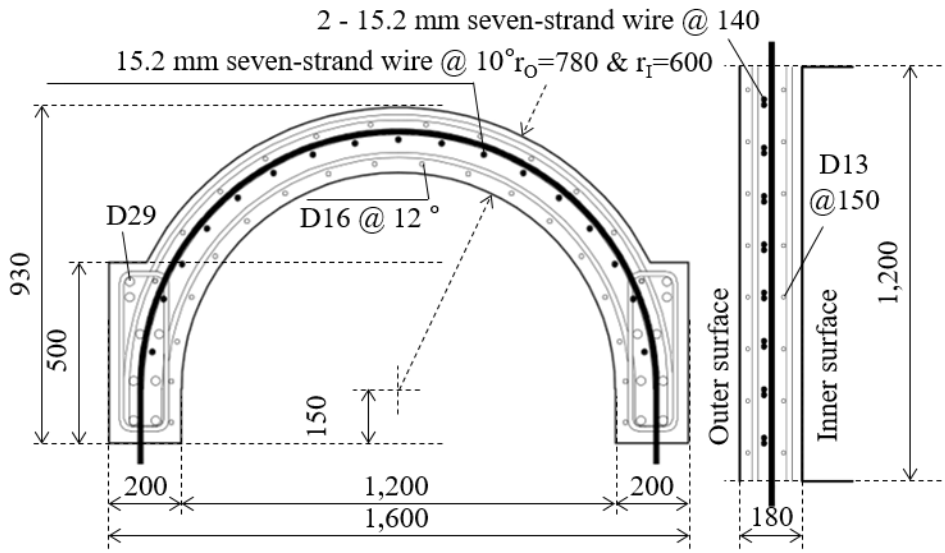

(a) Cross-section of CPSS1.0M-V, CPSS1.0M-Vh, and CPSS1.0M-VH

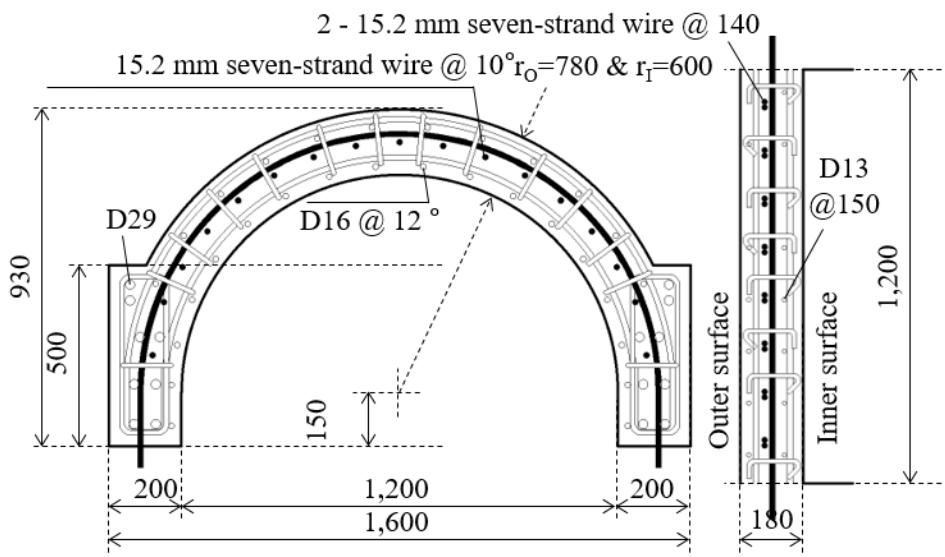

(b) Cross-section of CPSS1.0M-VH-C

Figure 4-12 Dimensions of semi-cylindrical walls – 2

In the case of I-shaped walls IRSS1.0M and IPSS1.0M with reinforced concrete and post-tensioned force, respectively (Fig. 4-12 and Table 4-3), to investigate the effect of post-tensioning forces on shear strength, the specimens were prepared. The reinforcing bar and post-tensioning tendon ratios were the same as those of SRSS1.0M and SPSS1.0M-VH. The nominal shear strengths predicted by ACI of IRSS1.0M without prestressing were $V_{n,ACI}$ = 1,434 kN and $V_{n,EPRI}$ = 1,380 kN. The nominal flexural and shear-friction strengths of IRSS1.0M were V_f = 2,575 kN, and V_{sf} = 2,305 kN. Those strengths of IPSS1.0M were $V_{n,ACI}$ = 1,434 kN, $V_{n,EPRI}$ = 1,981 kN, V_f = 3,263 kN, and V_{sf} = 2,305 kN. In the case of I-shaped specimens, the nominal shear strength $V_{n,ACI}$ was predicted by ACI-349 rather than ACI 359. In the nominal shear strength prediction, the vertical post-tensioning force was transformed to an equivalent axial force N_u.

The compressive strength of concrete was 36 MPa for all specimens. The measured tested yield strengths of reinforcing bars were 473, 473, and 458 MPa for D13, D16, and D29, respectively.

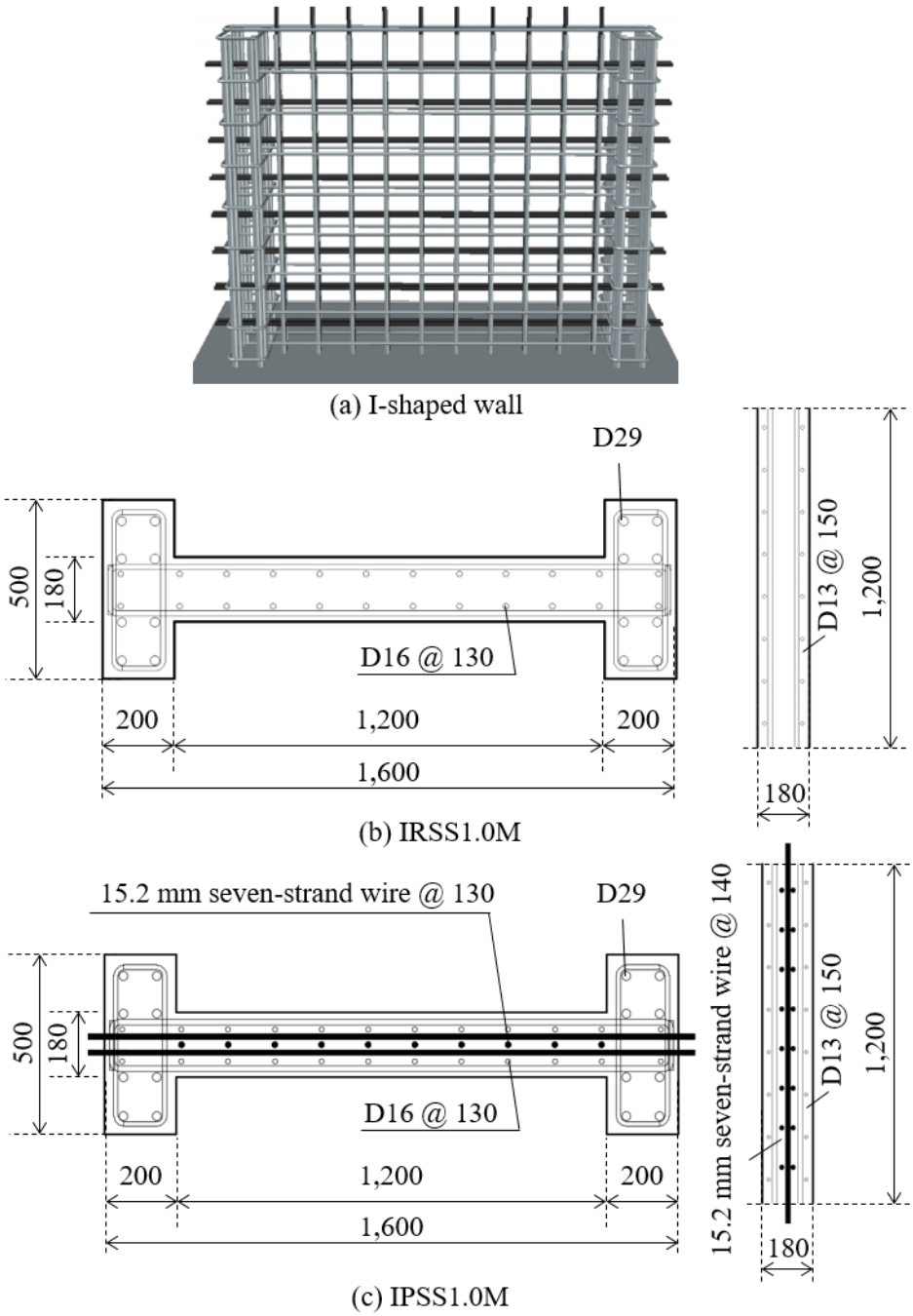

Figure 4-13 Dimensions of I-shaped walls

4.2.2.3) Test procedure and set up

Figure 4-14 shows the test set-up. Two dynamic actuators were used for applying lateral loading (fig 4-10). To restrain the torsional force, the lateral displacements of the two actuators were controlled to be the same. The lateral loading protocol followed ACI 374.2 (Fig. 3-4): Figure 4-5 shows the LVDTs for the measurement of lateral displacements: [L1 and L2], [L3 and L4]. [L5 – L10], L11 were for measuring total lateral, shear, flexural, sliding at the wall base deformations, respectively. To measuring the out-of-plane displacement, additional LVDT was installed at the top slab of specimens. The measuring the post-tensioning force was the same as that of **Chapter 4.1.**

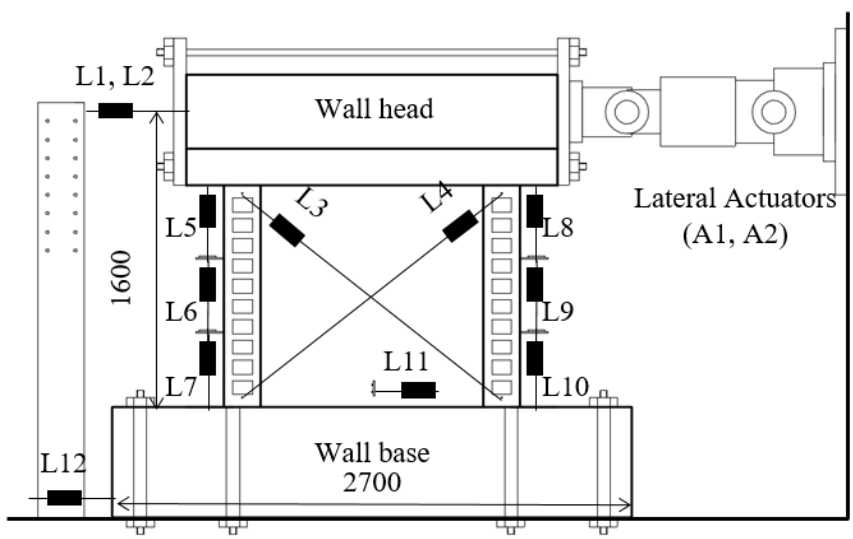

Figure 4-14 Test set-up of semi-cylindrical walls

4.2.3 Test results

4.2.3.1) Relationship of lateral displacement and load

Figures 4-15 and 4-16 show the lateral load-displacement relationships of the semi-cylindrical and I-shaped specimens, respectively. The actuators were controlled to follow the drift ratios of Fig 3-4 (a) using the displacement measured on LVDTs (L1 and L2 of fig 4-14). The lateral displacement refers the average of measured value of two LVDTs (L1 and L2) excluding slip at the base slab (L12 of fig 4-14). The lateral load indicates the sum of actuator forces A1 and A2. Figures 4-15 and 4-16 show the nominal shear strength $V_{n,ACI}$ and $V_{n,EPRI}$ predicted by ACI–ASME 359 and EPRI, respectively, and the nominal flexural strength V_f predicted by sectional analysis.

In the case of RC specimen, SRSS1.0M (Fig. 4-15(a)), the maximum tested strengths were observed at drift ratios of +1.02% and -1.00%: the maximum tested strengths were + 2,014 kN and –1,931 kN, respectively. The values were 4.74 and 4.54 times greater than the nominal shear strength of ACI 359. In the case of shear prediction based on EPRI, the ratios of test and prediction were 1.86 and 1.79. After the peak load, the load carrying capacity decreased immediately.

In the case of post-tensioned specimen SPSS1.0M-V with only vertical post-tensioning force (Fig. 4-15(b)), the maximum tested strengths were +1,853 kN and -1636 kN at drift ratio of 0.75 % and 0.68 in the positive and negative directions, respectively. The ratios of test and prediction were 0.99 and 4.10 for methods of the ACI and EPRI, respectively.

In the post-tensioned specimen SPSS1.0M-Vh (Fig. 4-15(c)) with 100 % vertical and + 50 % horizontal post-tensioning forces, the maximum tested strengths were +2,044 kN and -2,021 kN at 0.75 % and 0.73 %, respectively. These values were 3 % and 17 % greater than that of SRSS1.0M and SPSS1.0M-V. The peak tested strengths were exceeded the nominal shear strength ($V_{max} = 1.16V_{n,EPRI}$, and $V_{max} = 2.07V_{n,ACI}$).

In the case of CPSS1.0M-VH (Fig. 4-15(d)) with 100 % vertical and horizontal post-tensioning, the maximum tested strengths were measured at the drift ratio of 1.05 %. The values were +2,067 kN and -2,059 kN in the positive and negative directions, respectively. The maximum tested strengths were 1.17 % and 2.10 % greater than the nominal shear strength predicted by ACI 359 and EPRI. Comparing with the reinforced concrete specimen SRSS1.0M, the maximum strengths were 2%, and 6% greater in the case of CPSS1.0M-VH.

On the other hand, in the case of CPSS1.0M-VH-C with crossties, the peak strengths were +2,347 kN and -2,193 kN in the positive and negative directions, respectively (Fig. 4-15(e)). The maximum tested strengths were observed at the drift ratios of 1.03 % and 1.04 % in the positive and negative directions, respectively. The ratios of prediction by ACI and EPRI verse test were 1.29 and 2.31, respectively. The maximum tested strengths were 13 % and 6.5 % greater than those of CPSS1.0M-VH without cross-ties.

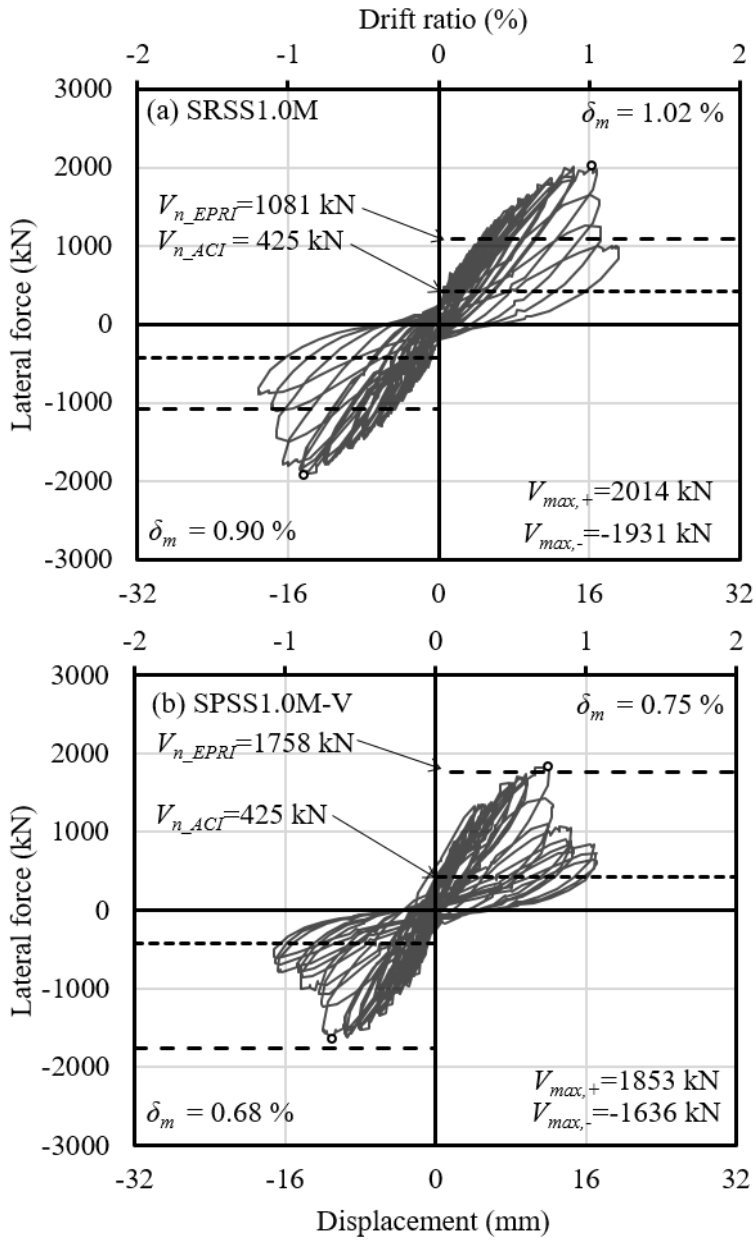

Figure 4-15 Relationships of lateral displacement and reactions of semi-cylindrical walls

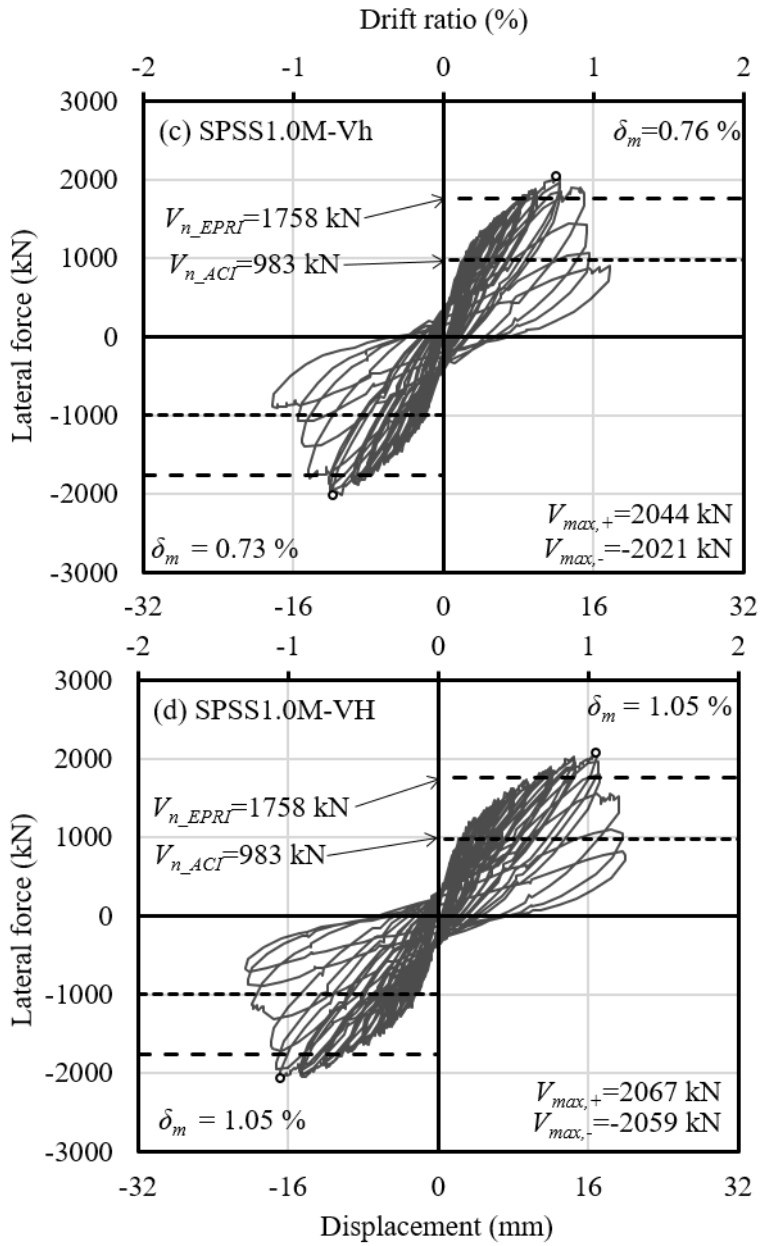

Figure 4-15 Relationships of lateral displacement and reactions of semi-cylindrical walls

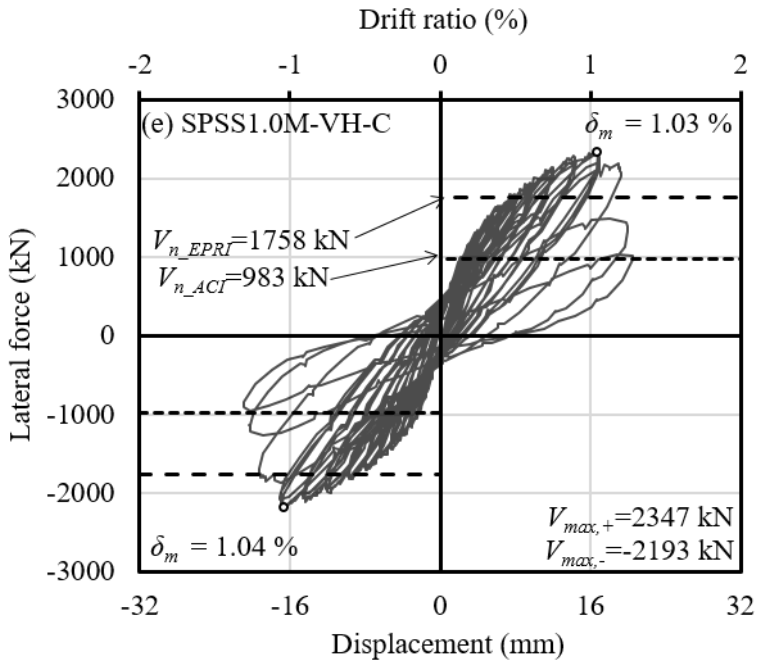

Figure 4-15 Relationships of lateral displacement and reactions of semi-cylindrical walls

In the case of I-shaped specimen IRSS1.0M, the maximum tested strengths were +2,154 kN and -2,202kN in the positive and negative directions, respectively (Fig. 4-16(a)). The peak strengths were observed at the drift ratios of 1.19 % and 1.17 % in the positive and negative directions, respectively. The average of maximum tested strength of I-shaped specimen was 10 % greater than that of semi-cylindrical specimen.

In the other case of I-shaped specimen SPSS1.0M (Fig. 4-16(b)) with post-tensioning forces, the maximum tested strengths were +2,200 kN and –2,198 kN at the drift ratio of 0.74 % and 0.72 % in the positive and negative directions, respectively. The peak strengths were close to those of the RC specimen IRSS1.0M.

The maximum strengths were 11 % and 53 % greater than the nominal shear strength predicted by ACI and EPRI. The average maximum strength of IPSS1.0M was 3 % less than that of the specimen with semi-cylindrical shape SPSS1.0-VH-C.

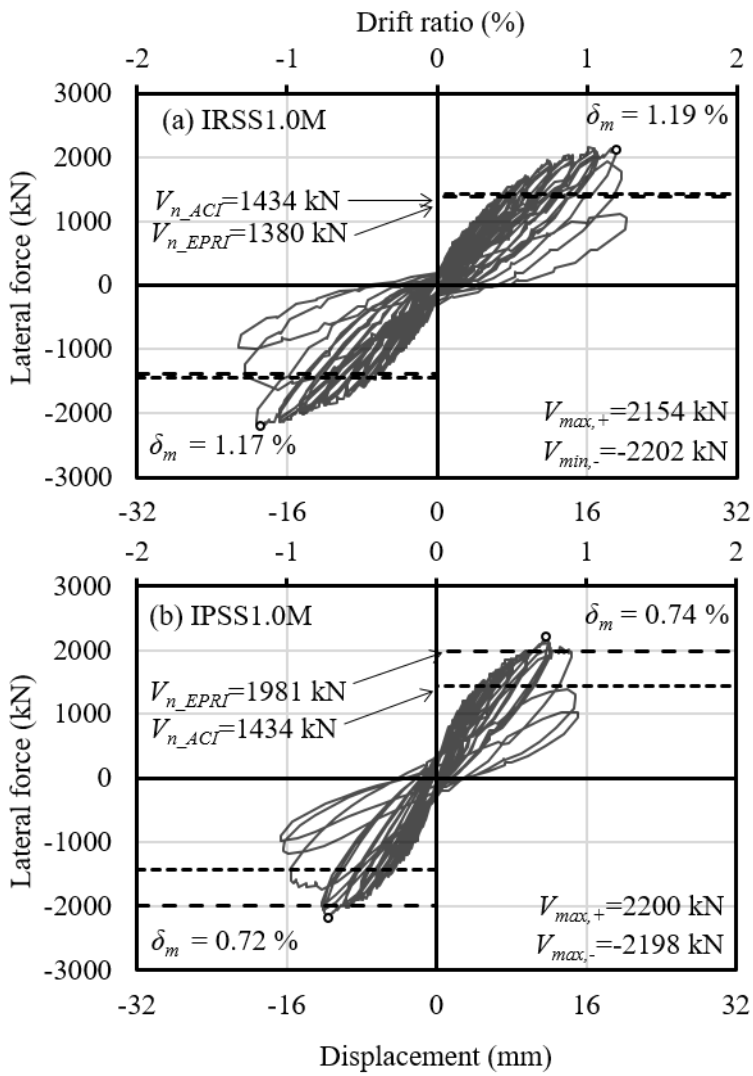

Figure 4-16 Relationships of lateral displacement and reaction of I-shaped walls

4.2.3.2) Damage modes of specimens

Figures 4-17 and 4-18 shows the damage modes of the semi-cylindrical specimens at the end of test. The figures show the failure mode of exterior surfaces and interior surfaces ((1) and (2) series of figs 4-17 and 4-18, respectively).

In the case of the specimen SRSS1.0M (fig 4-17 (a)) without post-tensioning, the failure mode of exterior surface was diagonal tension failure at the bottom of wall. On the other hand, in the case of interior surface, the failure mode was the web-crushing failure at 40 cm from the bottom. The diagonal cracking also occurred in the interior surface.

In the case of SPSS1.0M-V (fig 4-17 (b)) with only vertical post-tensioning force, the failure mode was similar with that of SRSS1.0M. In the post-tensioning case, the width of diagonal cracks were greater. The area where concrete cover failed was same as that of reinforced concrete specimen. In addition, the height of web-crushing failure was same.

In the case of specimens with horizontal post-tensioning specimens SPSS1.0M-Vh and SPSS1.0M-VH (fig 4-17 (c) and fig 4-18(a)), the diagonal tension and web-crushing failure was occurred in the exterior and interior surfaces, respectively. In the case of interior surface, the failure mode and locations were the same as the other semi-cylindrical specimens. However, in the failure mode of exterior surface, the location of cover concrete dropped was mid height of specimens with the macro diagonal cracks.

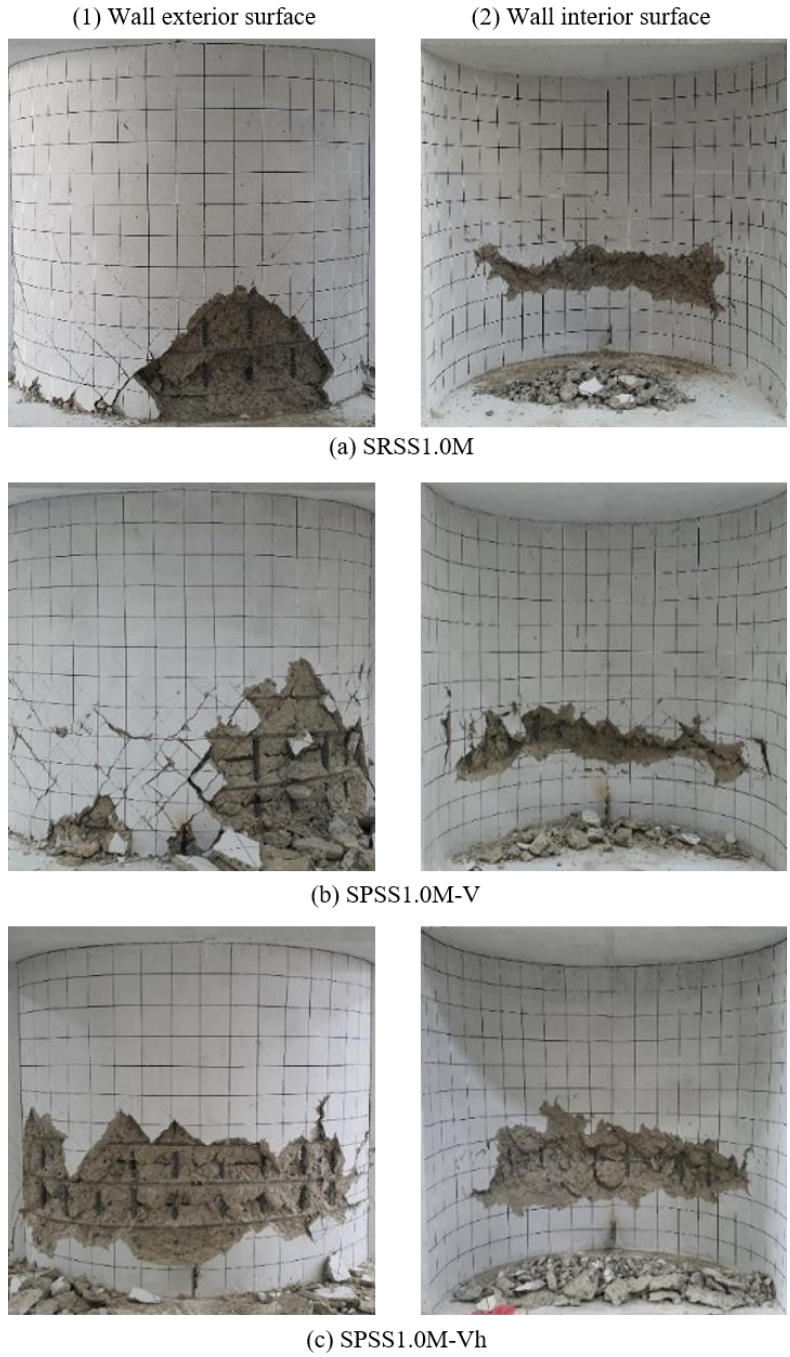

Figure 4-17 Damages on semi-cylindrical specimens at the end of test -1

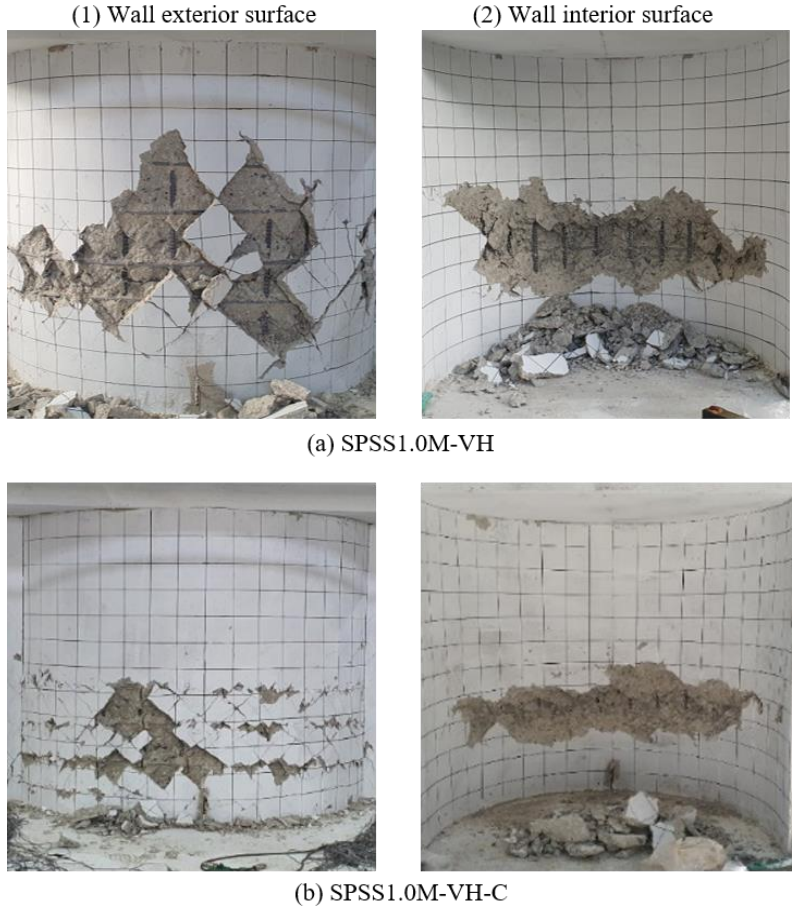

Figure 4-18 Damages on semi-cylindrical specimens at the end of test -2

On the other hand, in the case of SPSS1.0M-VH-C with crosstie (fig 4-18 (b)), large horizontal cracks occurred at the exterior and interior surfaces, which indicate web-crushing failure was occurred in both surfaces.

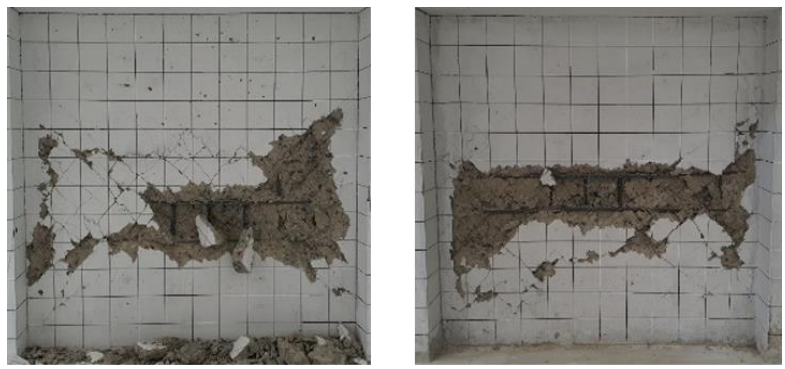

(a) IRSS1.0M (b) IPSS1.0M

Figure 4-19 Damages on I-shaped specimens at the end of test

Figure 4-19 shows damage of the I-shaped walls at the end of test. The concrete cracks and failure modes with large horizontal cracks were similar to those of the inner surface of semi-cylindrical specimens. The spacing of cracks was greater in the post-tensioning specimen SPSS1.0M (Fig. 4-19(b)).

After the end of tests, to check delamination cracks due to the horizontal post-tensioning, the concrete core boring was performed (Fig 4-20). The location of boring was at the top of wall, because the damage from lateral loading was minimized. Figures 4-20 (a) and (b) show that the internal cracks were occurred in the specimens with horizontal post-tensioning and without the crosstie (SPSS1.0M-Vh and SPSS1.0M-VH). The internal cracks occurred along the horizontal post-tension tendon layer. On the other hand, in the case of SPSS1.0M-VH-C with the crosstie, the internal cracks were not observed although the horizontal post-tensioning was applied.

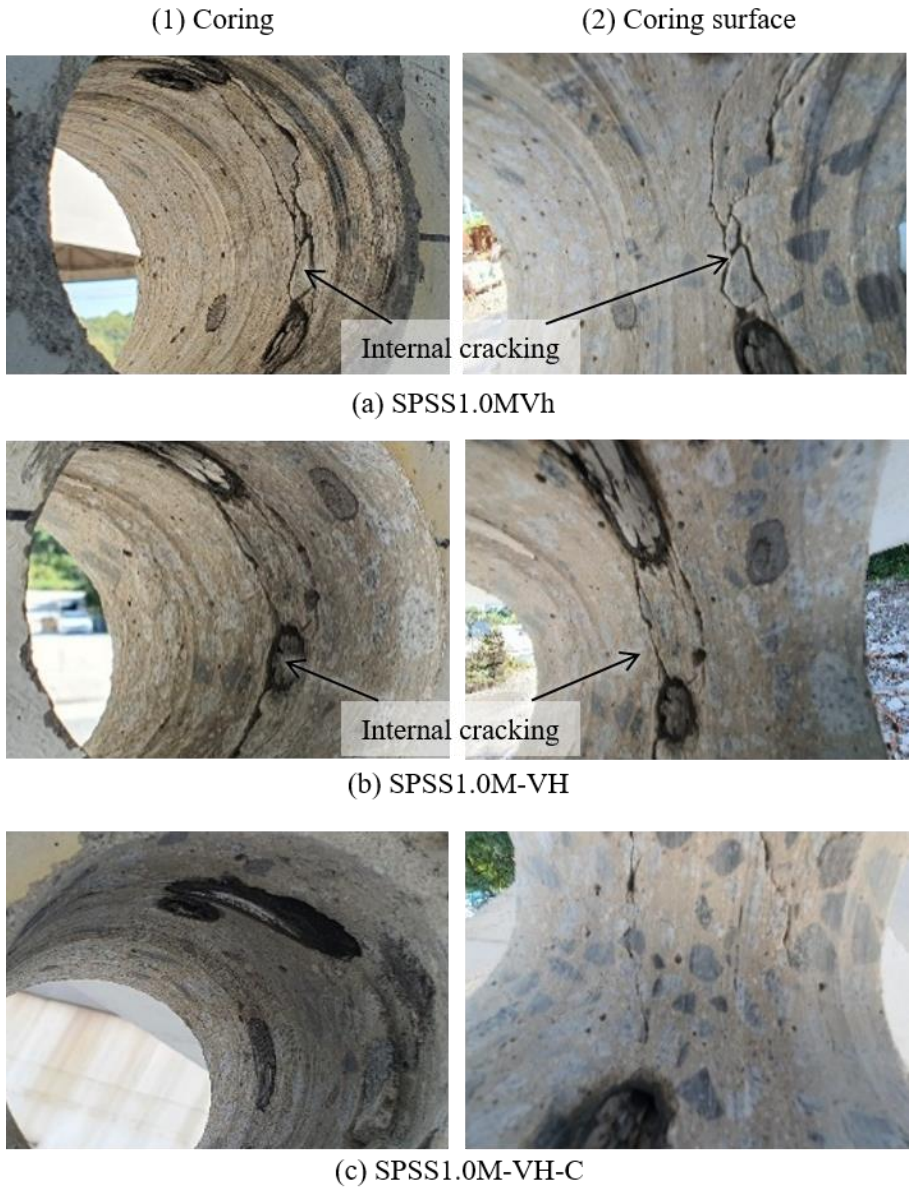

Figure 4-20 Internal cracks due to horizontal post-tensioning in semi-cylindrical specimens

4.2.3.3) Strain distributions

Figures [4-21 and 4-22] and [4-23 and 4-24] shows strain distributions of the horizontal and vertical reinforcing bars, respectively, in the semi-cylindrical and I-shaped walls along the wall height at 0.5 V_{max}, 0.75V_{max}, and 1.0V_{max}, where V_{max} indicates the maximum tested strength. Some strain gauges failed during or before the test and the values from failed gauges were not displayed in figs. The gray area in figs 4-23 and 4-24 indicates the area of flanges.

In the case of reinforced wall SRSS1.0M without prestressing (figs. 4-21(a) and (b)), the strains of all horizontal reinforcing bars were exceeded the yield strain at 0.75 V_{max} and V_{max} at the mid-height of wall.

In SPSS1.0M-V with only vertical prestressing (figs 4-21 (c) and (d)), only the strain of inner horizontal reinforcing bar at 400 mm from the bottom was exceeded the yield strain at V_{max}. The exterior horizontal reinforcing bar at 400 mm from the bottom was reached 98 % of yield strain at V_{max}.

In the case of specimen SPSS1.0M-Vh with 50 % of horizontal post-tensioning (figs. 2-22 (e) – (f)), the strain of the exterior horizontal reinforcing bar at 700 mm was greater than the yield strain at the V_{max}. In addition, the strains of the exterior horizontal reinforcing bars were greater than those of interiors. The maximum strains of interior horizontal reinforcing bars were less than those of specimens without horizontal post-tensioning (SRSS1.0M and SPSS1.0-V). On the other hand, the exterior strains was observed similar values as those of SPSS1.0-V with only vertical post-tensioning force.

In the case of specimens SPSS1.0M-VH and SPSS1.0M-VH-C with 100 % of post-tensioning, all strains of horizontal reinforcing bars were not exceeded the yield strain. The strains exterior horizontal reinforcing bars at mid-height section was greater than 90 % of yield strain. However, in the case of interior horizontal reinforcing bars, the strains were not exceed the 80 % of yield strain.

In the case of I-shaped specimen IRSS1.0M without post-tensioning (fig 2-22 (e)), the strain of horizontal reinforcing bar at 700 mm from the bottom slab was exceeded the yield strain at V_{max}. The others were not exceeded the yield strain. In the case of the other I-shaped specimen IPSS1.0M with post-tensioning force (fig 2-22 (f)), the all horizontal reinforcing bars were not yield during the test.

In the case of strains of vertical reinforcing bars, the specimen SRSS1.0M without post-tensioning (figs. 2-23(a) and (b)), only in the flange area, the strain of the exterior exceeded the yield strain. In the case of cylindrical walls with vertical post-tensioning and 50 % of horizontal post-tensioning (figs. 23(c) – (f)), the strains of vertical reinforcing bars did not exceed the yield strain until the maximum tested strengths were occurred. The only vertical reinforcing bar stains in SPSS1.0M-VH-C was yield at the V_{max}.

This result indicates that: 1) In the case of specimens with horizontal post-tensioning force, the strains of horizontal reinforcing bars were smaller than that of specimens without post-tensioning force at the maximum capacity. 2) the failure of specimens with horizontal post-tensioning occurred before the yield of horizontal reinforcing bars. 3) The vertical strain distributions showed that the similar distribution of wall with shear failure before flexural yielding.

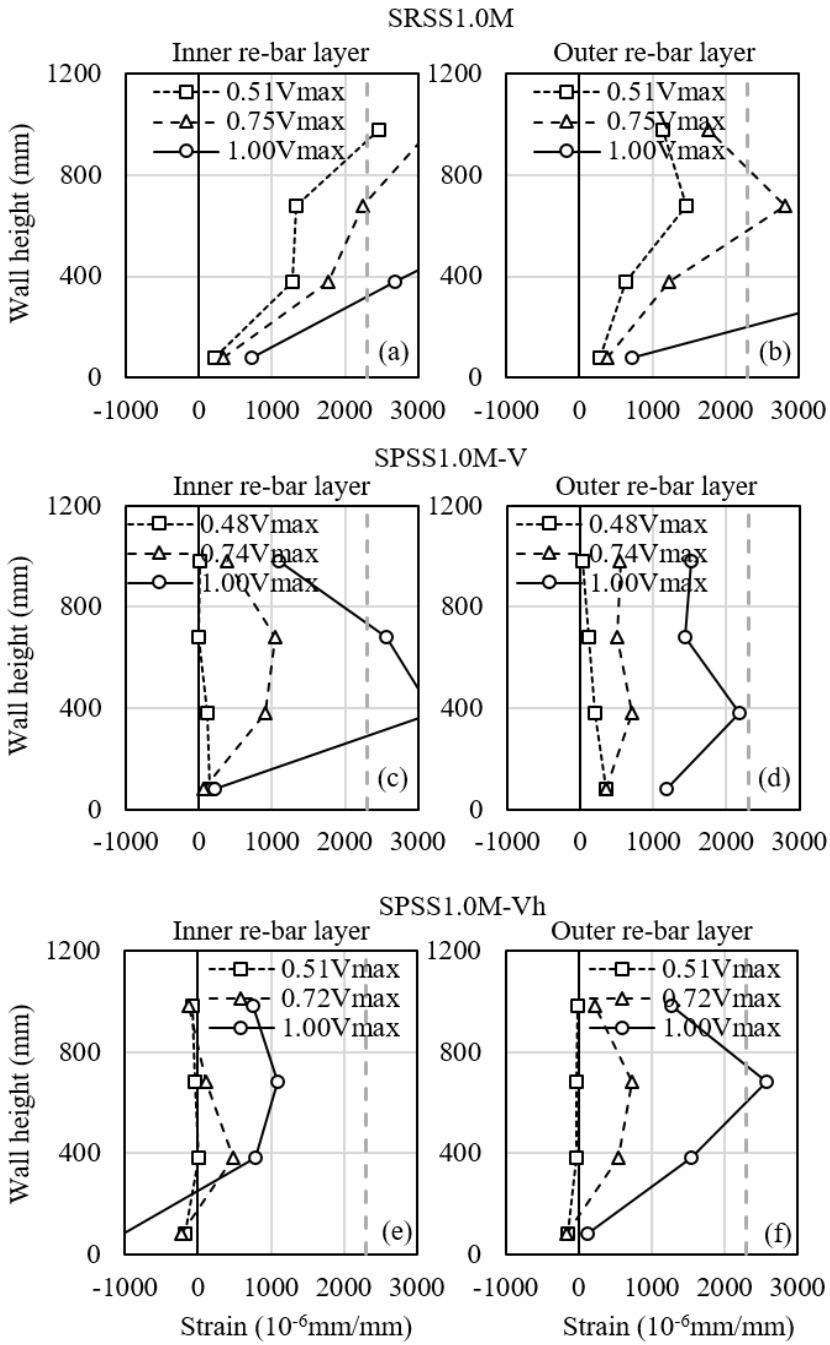

Figure 4-21 Strain distributions of horizontal reinforcing bars in semi-cylindrical specimens

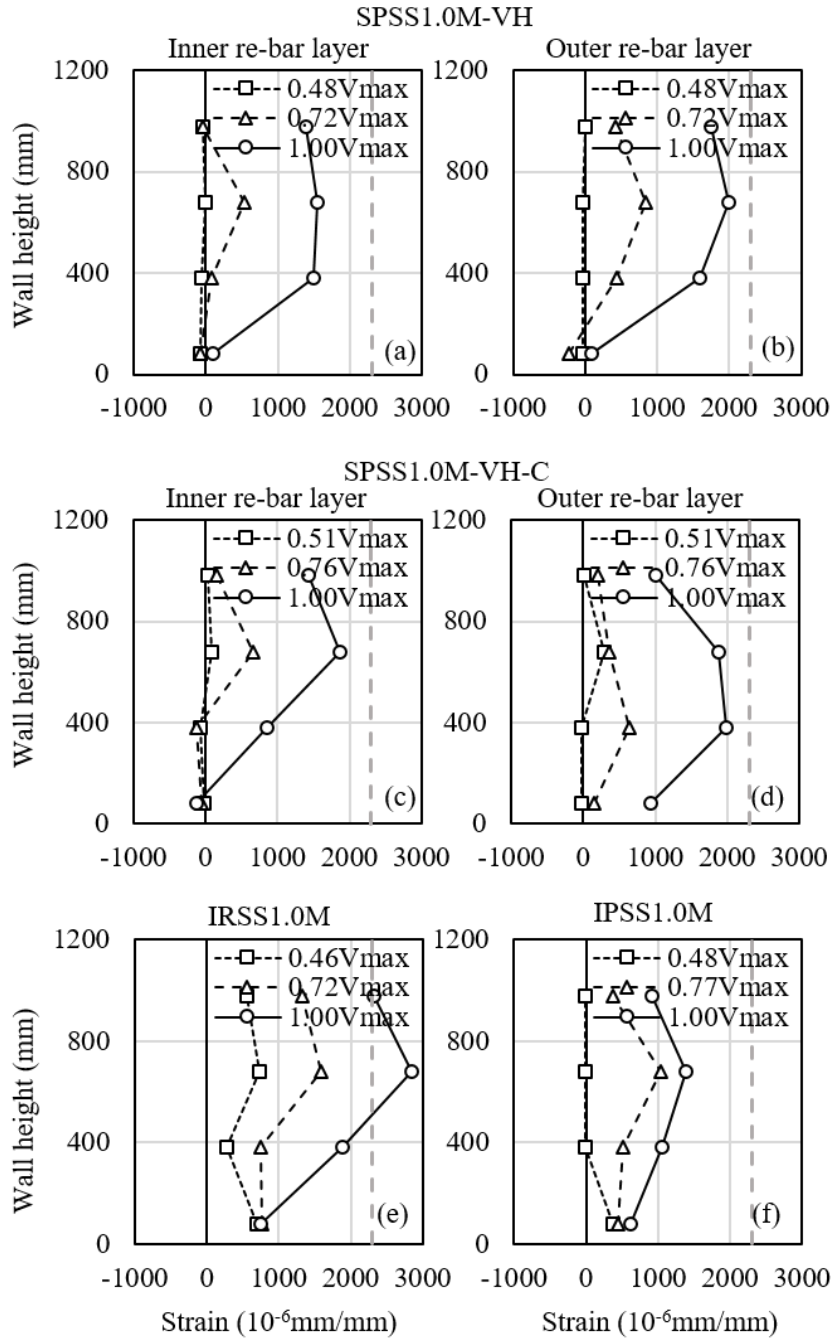

Figure 4-22 Strain distributions of horizontal reinforcing bars in semi-cylindrical and I-shaped specimens

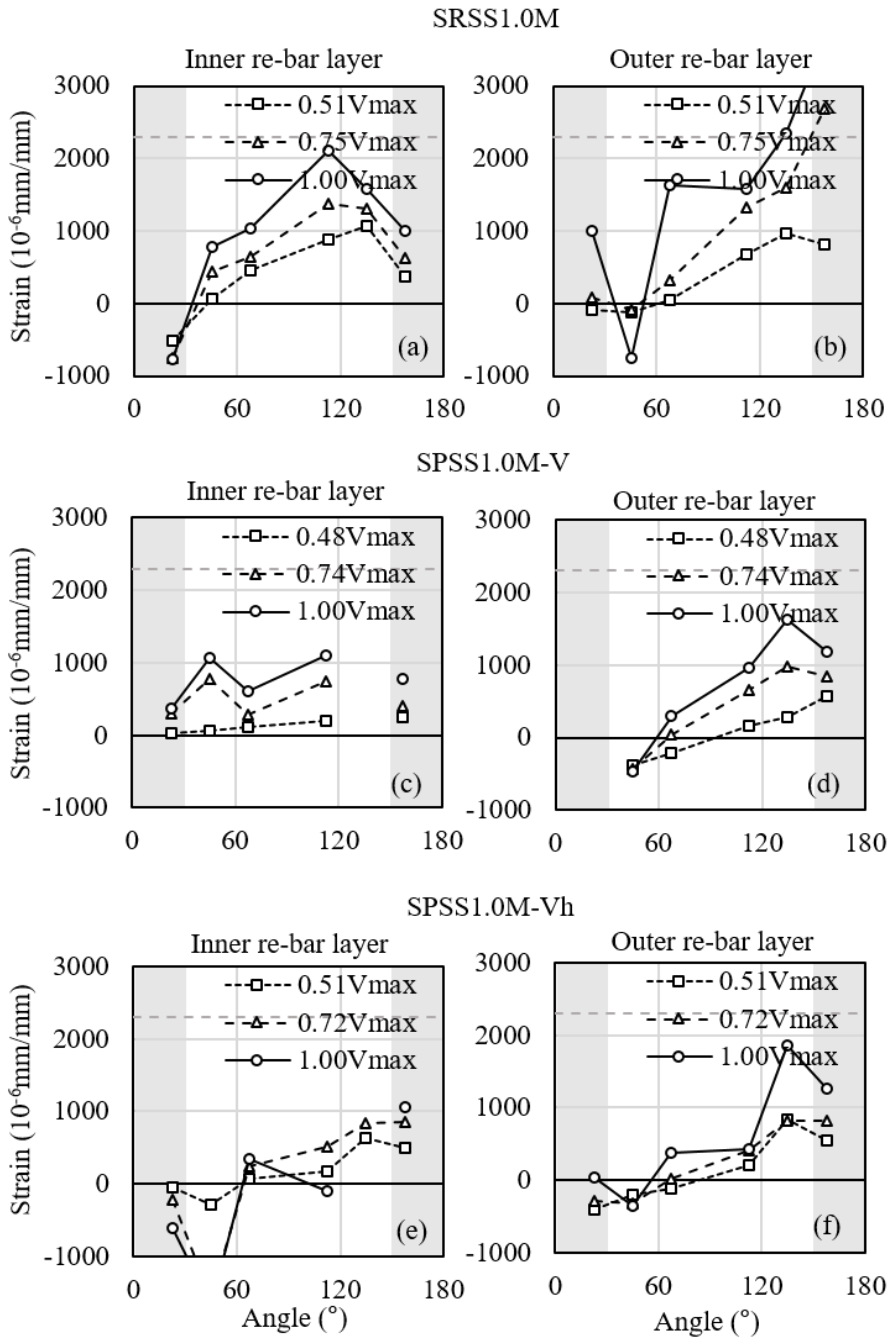

Figure 4-23 Strain distributions of vertical reinforcing bars in semi-cylindrical specimens

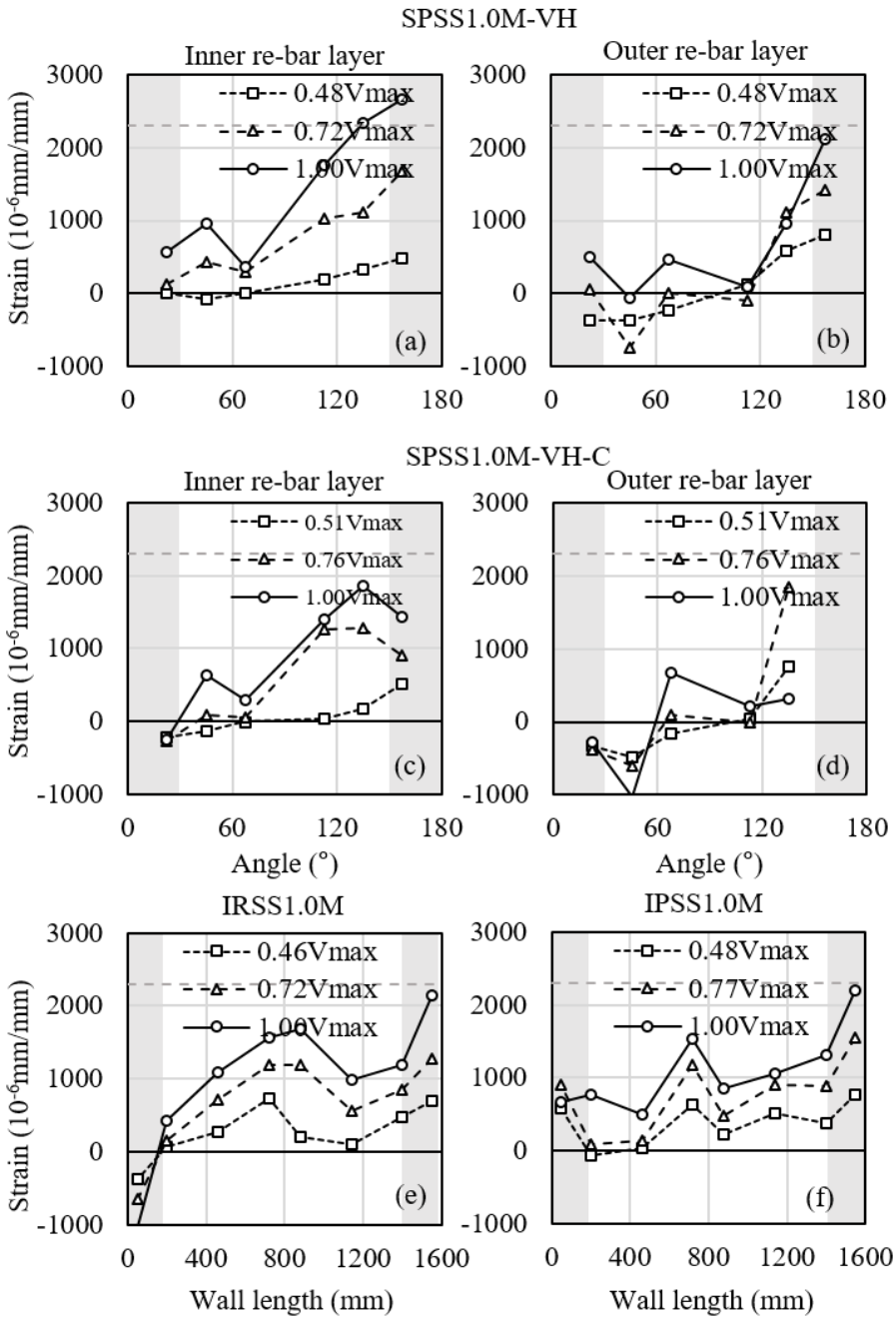

Figure 4-24 Strain distributions of vertical reinforcing bars in semi-cylindrical and I-shaped specimens

4.2.3.4) Effective frequency and energy dissipation

The load-displacement curve was analyzed to investigate the dynamic behavior characteristics of the cylindrical wall. The effective stiffness for identifying the natural frequency of wall is calculated. Figure 4-25 shows the idealized force deflection diagram and defines the elastic and effective stiffness (K and K_s). Table 4-4 shows the stiffness analysis results. The elastic stiffness of cylindrical wall was similar with or without post-tensioning. The reason is that the stiffness in the elastic region is predominantly determined by the concrete cross-sectional area. However, the effective stiffness including the capacity after the reinforcing bar yield was 3 % ~ 44 % greater in the wall with post-tensioning. Especially, in the case of two experiments with the same details (SPSS1.0M-VH and SPSS1.0M-VH-C), the effective stiffness was 12 % greater in the specimen with cross-tie.

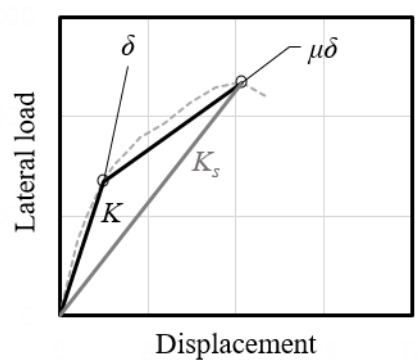

Figure 4-25 Idealized force deflection diagram

Table 4-4 Elastic and effective stiffness of semi-cylindrical wall

Specimen	K (kN/mm)	K_s (kN/mm)
SRSS1.0M	465.9	118.3
SPSS1.0M-V	456.4	152.8
SPSS1.0M-Vh	529.4	170.5
SPSS1.0M-VH	495.9	122.3
SPSS1.0M-VH-C	481.4	136.8

To investigate the damping ratio of cylindrical wall, the dissipated energy of wall during the lateral cyclic loading was calculated. Figure 4-26 shows the cumulative energy dissipation of the semi-cylindrical specimens according to the lateral drift. Figure 4-26 (f) shows the definition of cumulative dissipated energy. In the case of all specimens, the energy dissipation was significantly increased at the end of test. There was no decrease in energy dissipation according to the number of cyclic loading. At the drift ratio of 0.5 %, the average energy dissipation of RC and PSC wall were 5.45 kJ and 7.70 kJ, respectively. In the case of PSC wall, the values were 29 % ~ 40 % greater than that of RC.

In the case of I-shaped wall, Figure 4-27 shows the cumulative energy dissipation of them. When the lateral drift ratio was 0.5 %, the dissipated energy was 39 % greater in the PSC specimen than in the RC specimen. When compared according to the shape of wall, the energy dissipations were 2 % and 1 % greater than the RC and PSC cylindrical wall in the RC and PSC I-shaped wall, respectively.

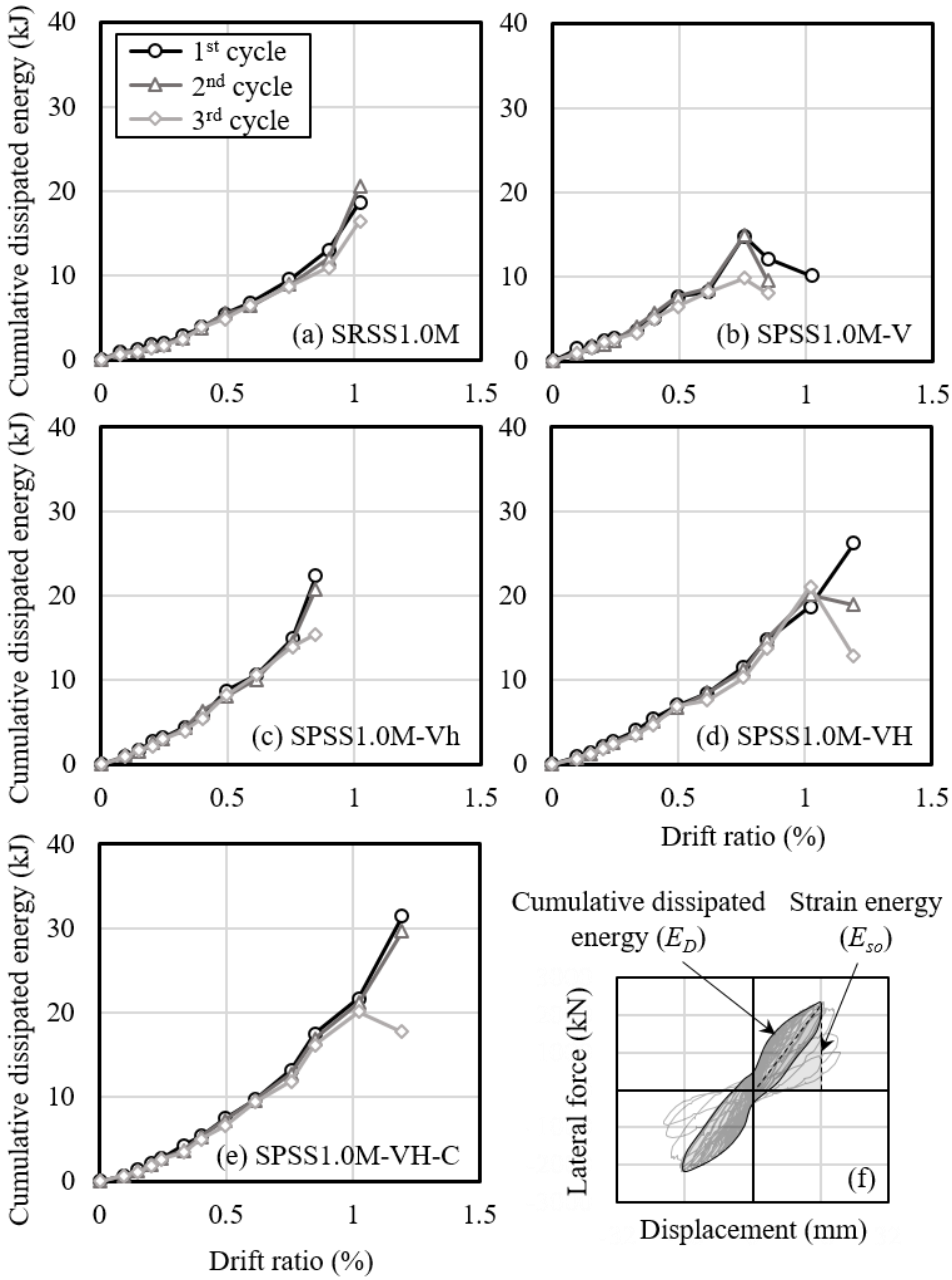

Figure 4-26 Cumulative dissipated energy of semi-cylindrical wall

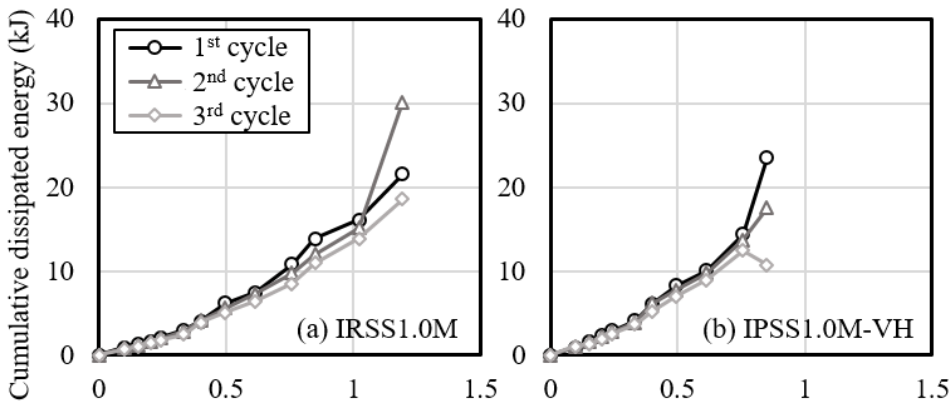

Figure 4-27 Cumulative dissipated energy of I-shaped wall

Based on the cumulative dissipated energy, the equivalent viscous damping ratio, ξ_{eq}, was calculated using EQ 4-1.

$$\xi_{eq} = \frac{1}{4\pi}\frac{E_D}{E_{SO}} \tag{4-1}$$

where E_D and E_{So} are cumulative dissipated energy and elastic strain energy, respectively, in Figure 4-26. Figure 4-28 shows the analysis results. In ASCE/SEI 4-16, the damping ratio are provided for two levels of structure seismic response: Response Level 1 (Not cracked significantly) and Response Level 2 (Cracked significantly). The damping ratio of 4% and 7% are for Response Level 1 and 2, respectively.

The equivalent viscous damping ratio was increased at the end of test. The equivalent viscous damping ratio of reinforced concrete wall without post-tensioning was close to 7 % during the test. On the other hand, the damping ratios of cylindrical walls with post-tensioning were 9%.

In general, the damping ratio of pre-stressed concrete structure is lower than that of reinforced concrete. On the other hand, in this research, the damping ratio of pre-stressed concrete was closed to 9 %, which was 28 % greater than that of reinforced concrete. Since the amount of steel (reinforcing bars and tendons) was greater in the case of pre-stressed concrete, the damping ratio was greater in the pre-stressed concrete wall.

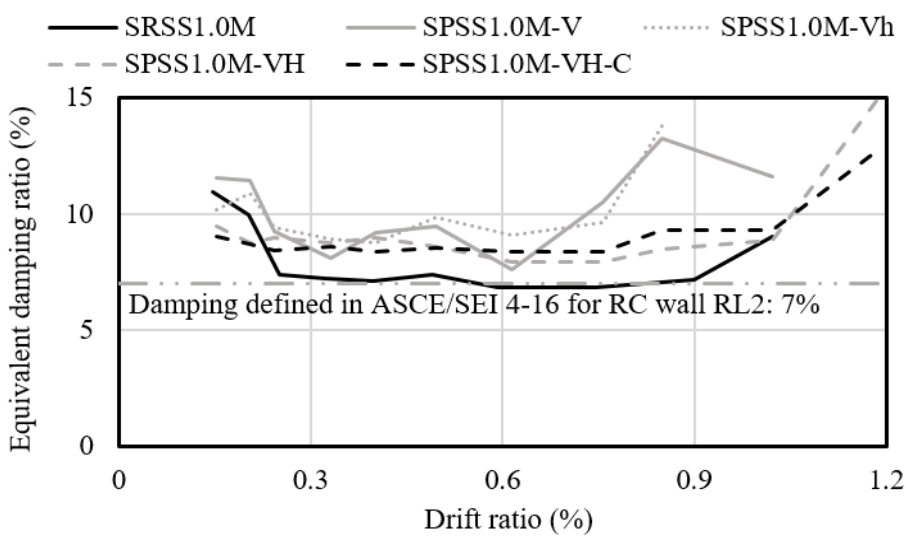

Figure 4-28 Equivalent damping ratio of semi-cylindrical wall

4.2.4 Summary of experiment IV

To investigate the effect of post-tensioning and cross-tie on shear strength of cylindrical and I-shaped walls, seven specimens were tested under cyclic lateral loading (five and two for semi-cylindrical and I-shaped, respectively). The major test parameters were the shape of wall, magnitude of horizontal post-tensioning, and the installation of crosstie. The major findings of this chapter are summarized as follows:

1) Due to high reinforcement ratio, web-crushing failure occurred in all specimens. Especially, in the case of semi-cylindrical specimens, the failure mode of interior and exterior surfaces were different. In the case of interior surface of all semi-cylindrical walls, the web-crushing failure was occurred. On the other hand, in the outer surface of semi-cylindrical walls, diagonal cracking occurred, except the specimens with the crosstie. In planar walls, diagonal cracking and web crushing occurred.

2) After testing, concrete core boring was performed at the top area of specimen. The results of boring was that concrete internal cracking occurred due to horizontal prestressing.

3) The maximum tested strength of SPSS1.0M-VH-C with crossties was 13 % and 6 % greater than that of SPSS1.0M-VH without crossties in the positive and negative directions, respectively. Because the crossties restrained concrete delamination, the maximum strength was increased.

4) In the case of I-shaped walls IRSS1.0M and IPSS1.0M, the shear strengths were similar, regardless of the presence of prestressing. This result indicates

that the effect of post-tensioning on strength of web-crushing failure of I-shaped walls was negligible. Further, the shear strengths of IRSS1.0M and IPSS1.0M were 10 % greater and 3 % less than that of SRSS1.0M and SPSS1.0M-VH-C, respectively. These results indicate that the shear strength of cylindrical wall can be predicted by using an equivalent planar wall (l_w = the diameter of cylindrical wall)

5) Since the semi-cylindrical wall had an asymmetrical cross-section, it is difficult to control eccentricities during the dynamic loading test; therefore, static experiments were performed on all subjects. Thus, the test results of semi-cylindrical wall show that the effect of loading rate is not reflected. When the effect of loading rate is applied, approximately 10% increase in the maximum strength is expected; such as cylindrical (Experiment III) and planar (Experiment I and II) walls that had been subjected to dynamic loading test.

6) In all specimens, the peak strengths of test were greater than the nominal shear strengths predicted by ACI and EPRI. In particular, the ACI 359 strengths underestimated the shear strength of cylindrical walls because of not considering the contributions of vertical component.

Chapter 5. Nonlinear Finite Element Analysis

5.1 Overview

In Chapters 3 and 4, the tests were conducted to investigate the shear strength of squat walls with high reinforcing bar ratios. Further, to improve the test results, the some test parameters was considered, such as loading rate (static and dynamic), post-tensioning force (vertical and horizontal directions, and delamination), and shape of wall (Cylindrical and I-shaped).

In this chapter, nonlinear finite element analysis was performed for cylindrical walls using ATENA program (Cervenka et al. (2002)), which is a commercial program designed for concrete structures especially containment structures. The main objectives of performing nonlinear finite element analysis is to investigate the effect of vertical and horizontal reinforcing bar ratio, aspect ratio, ratio of thickness to radius and vertical and horizontal post-tensioning force on shear strength of cylindrical wall.

Three dimensional finite element models were developed for parametric analysis based on the geometric of the test specimens and real containment building. Although the cyclic tests under dynamic and static loading rates were conducted, the monotonic analysis with static loading rate was performed in this chapter. Thus, the analysis was focused on the effect of shape of wall and post-tensioning. The analysis results were used to develop the proposed shear strength model of the cylindrical wall.

5.2 Modeling information

One of the advantage of ATENA program is that a material library and suggestion of default values for design of reinforced concrete structures. For 3-D solid concrete, a fracture-plastic model called "CC3DNonLinCemetitious2", which included constitutive law of tensile and compressive stress of concrete, was used to simulate various mechanical characteristic of concrete: concrete cracking; crushing under high confinement; and crack closure due to crushing in other material directions. The fixed crack model was used, assuming that the crack direction determined at the moment of the crack initiation is fixed. The Modified Compression Field Theory (MCFT, Vecchio and Collins (1986)) was used for the shear strength of a cracked concrete and compressive strength reduction in the cracked panel. Menetrey-Willam (1995) model was used for plasticity model for concrete crushing. The measured material strengths (yield strength of reinforcing bars, and compressive strength of concrete) were used for the constitutive stress-strain relationships of the materials. The tensile strength of the concrete was defined as (Zheng et al. (2001))

$$f_t = 0.47\sqrt{f_c'} \quad \text{(SI units)} \tag{5-1}$$

where f_t and f_c' are direct tensile strength and cylinder compressive strength of concrete, respectively.

ATENA provides the function of crack opening derived experimentally by Hordijk (1991). However, the crack-opening model differs from that of Vecchio and Collins (1986) model, which will be used in proposed model. Therefore, the fracture energy

coefficient, G_f, was adjusted as 0.0625 (N/mm) to generate the behavior most similar to the results of the Vecchio and Collins model. Figure 5-1 shows the adjust results. The concrete strength degradation model due to transverse strain was used Vecchio and Collins (1986). The maximal strength reduction factor under the large transverse strain, c, was used as 0. Although the factor was proposed by several researchers (Kollegger et al. (1990) and Dyngeland (1989)), the factor was decided as 0, because when developing model in chapter 7, the concrete strength degradation function was used without limited value. In the case of post-peak behavior of concrete, according to Van MIER (1986), the plastic strain of concrete, ε_d, for normal concrete was 0.0025 from the experiments and the value was used for FEA analysis.

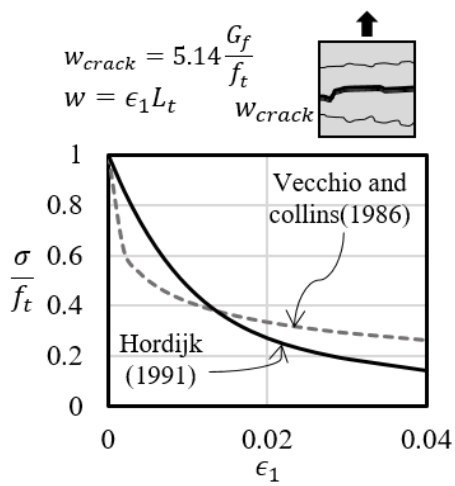

Figure 5-1 Material models and coefficients of each models

To simulate the behavior of reinforced concrete, the discrete model was used. For reinforcement or tendons, line element model was used. The multi linear stress-strain model was used to simulate strain hardening after yielding. For the detail of reinforcing bars, perfect bond was assumed between reinforcing bars and concrete. On the other hand, in the case of tendons, slip between tendon and concrete was allowed to address the effect of smooth surface of the tendon. The prestressing force was applied to the tendon using initial strain.

Tetrahedral elements with 24-DOF were used for concrete. In the interface between wall and top and bottom slabs, fixed contact element was used. The maximum size of finite element models controlled to be smaller than one-third of wall thickness. The meshed model and brief concepts of finite element analysis were shown in Figure 5-2.

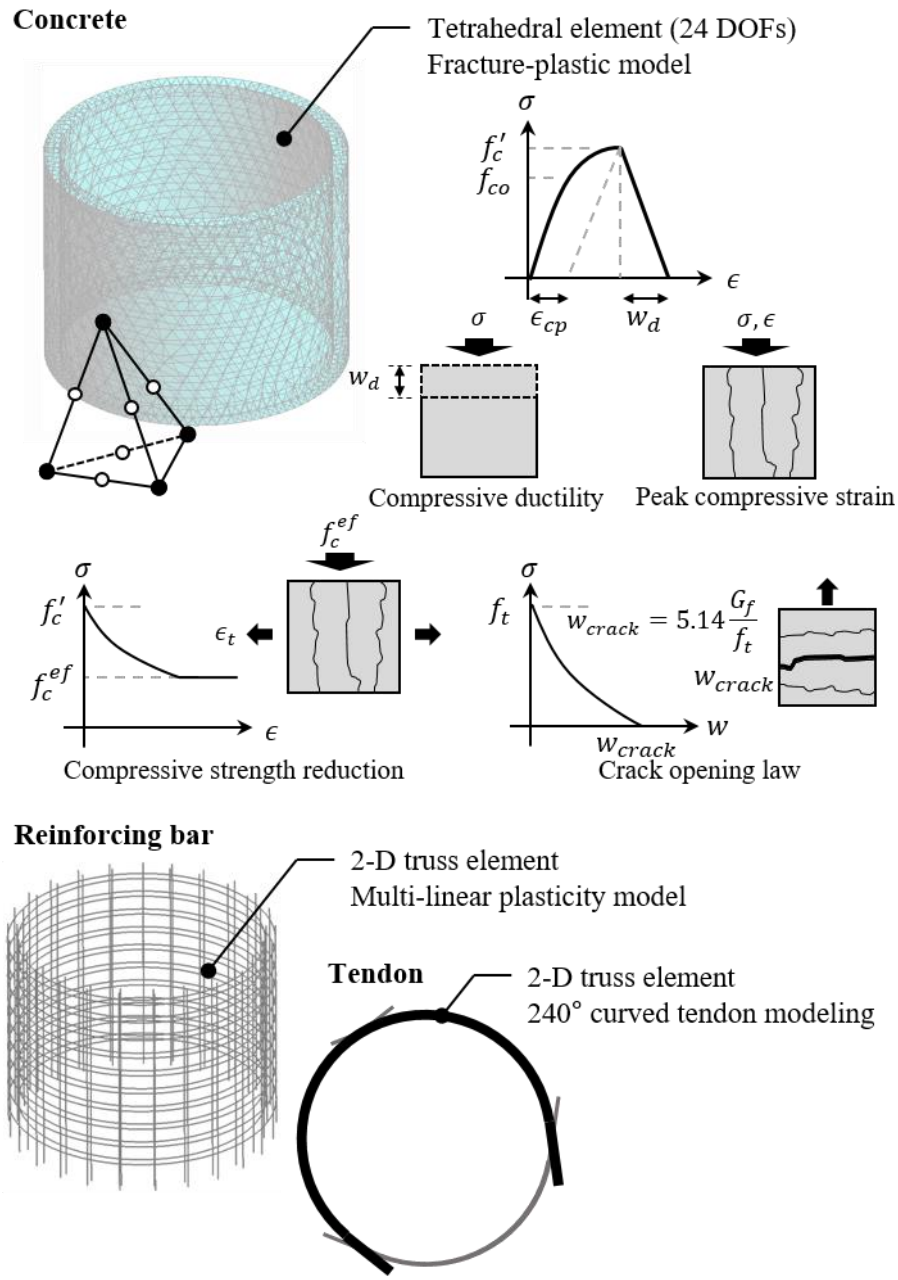

Figure 5-2 Finite element modeling using ATENA

5.3 Comparison with test results

5.3.1 Relationship of lateral displacement and force

Figure 5-3 and Figure 5-4 compare the results of the test and nonlinear FE analysis. Although the test was under cyclic loading, analysis was performed under monotonic loading to increase the convergence of interpretation. The finite element analysis results show reasonably prediction of the test results under cyclic loading. The ratio of test results to finite element analysis (V_{test}/V_{FEA}) is 0.94 on average. This result indicates that the strength of each structural components can also be determined with the adopted nonlinear finite element analysis method. However, the analysis under monotonic loading cannot reflect the effect of cyclic loading. Thus, the present finite element analysis was not intended to figure out all behavior of responses, but focused on the approximate trend the failure mechanism of the cylindrical wall.

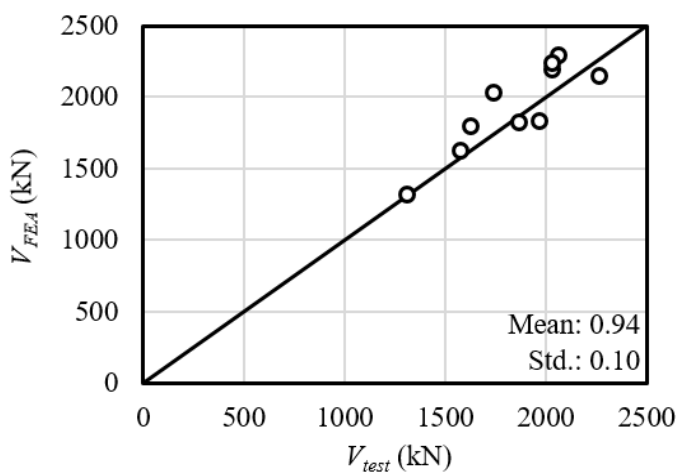

Figure 5-3 Comparison of maximum test strengths with FE analysis results

In the case of CRSS1.0Q and CRDS1.0Q without post-tensioning, the finite element analysis results agreed with the test results (Figure 5-4 (a) and (b)). However, after the maximum strength was occurred, the strength degradation of analysis results showed gradually unlike the test results showing brittle failure.

In the case of CPSS1.0Q-31 and CPDS1.0Q-43 with full vertical and horizontal post-tensioning, early delamination of cover concrete occurred due to horizontal prestressing, and due to loss of the bond, horizontal reinforcing bars did not provide shear resistance in the test results. To address the effect of early delamination, nonlinear finite element analysis was performed for net cross-section excluding the area of cover concrete and horizontal reinforcing bars. As shown in Figure 5-4 (c) and (d), the results of nonlinear finite element analysis using the net cross-section showed accurate prediction in the initial stiffness and the peak strength.

On the other hand, in the test results of CPDS1.0Q-V without horizontal prestressing and CPDS1.0Q-Vh with 50% horizontal prestressing, the horizontal reinforcing bars showed higher strain values. Thus, in the finite element analysis models, horizontal reinforcing bars were included while the area of cover concrete was excluded. In the case of CPDS1.0Q-Vh (Figure 5-4 (f)), the maximum strength of finite element analysis results agreed with that of test results. On the other hand, in the case of CPDS1.0Q-V, the results of finite element analysis with reduced section underestimated the test results. This result indicates that delamination of cover concrete was not severe in the specimen CPDS1.0Q-V without horizontal prestressing.

In the case of semi-cylindrical wall, due to the 180 mm thickness of wall and double layered reinforcing bar, the effect of delamination was not significant. All

finite element analysis models were used gross-section area. To simulate the effect of delamination on shear strength, the surface where the delamination crack occurred was modeled as an element that can transmit only in-plane compression. The crosstie details were replaced with fully bonded line elements for ease of interpretation. The results of nonlinear finite element analysis using the gross cross-section showed accurate prediction.

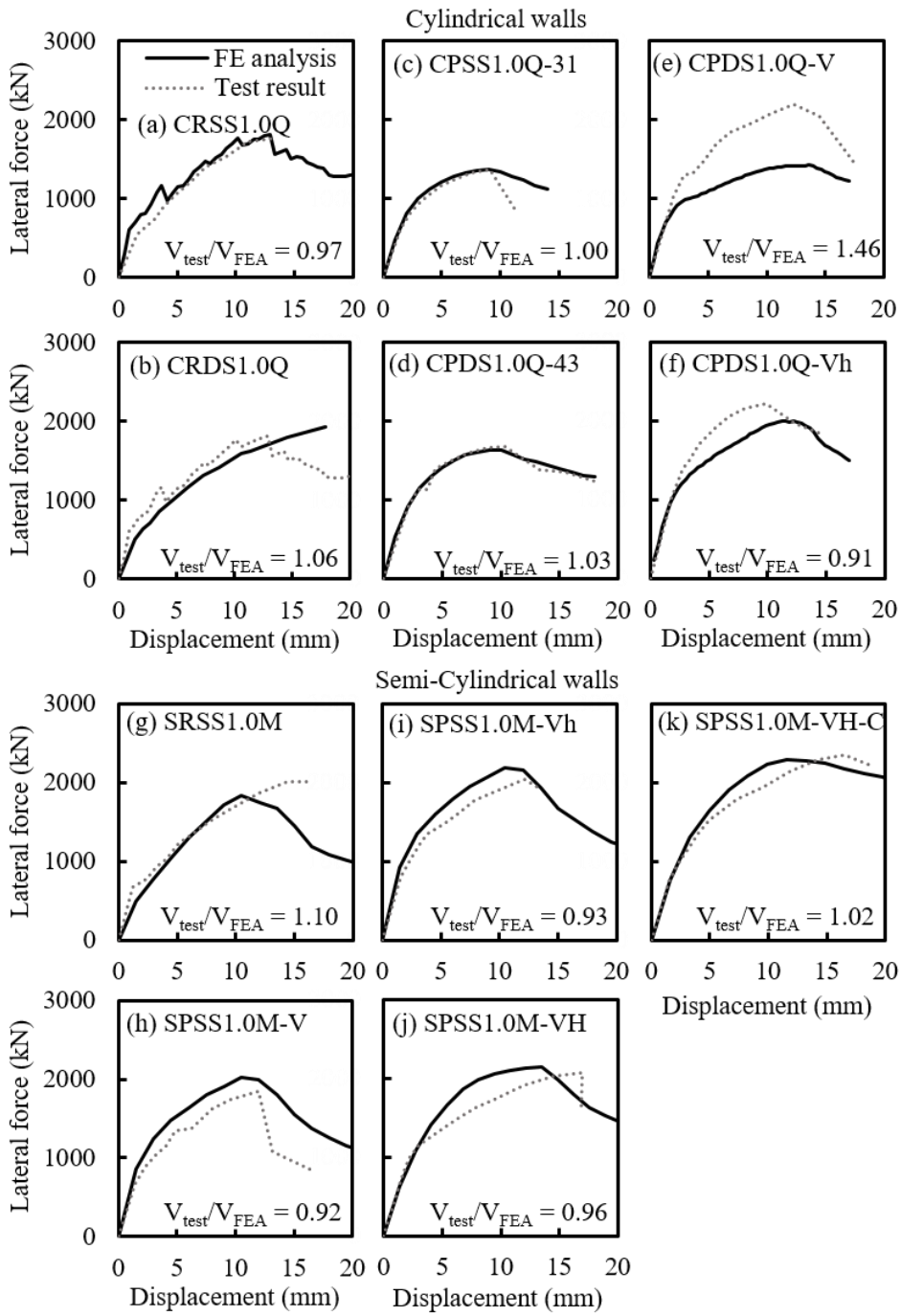

Figure 5-4 Comparison of test and FE analysis results

5.3.2 Concrete damage pattern

Figure 5-5 shows the analysis results on the damage pattern of concrete in CRSS1.0Q. In the figures, the distribution of principal stress in compressive and failure mode of specimen were captured at the maximum strength. The diagonal concrete strut was formed from the center area of upper height to the edge of bottom height. The maximum compressive stress was observed in compression zone at the bottom of wall. The inclined crack parallel to diagonal strut was occurred and the horizontal tensile stress was concentrated on along the diagonal cracks.

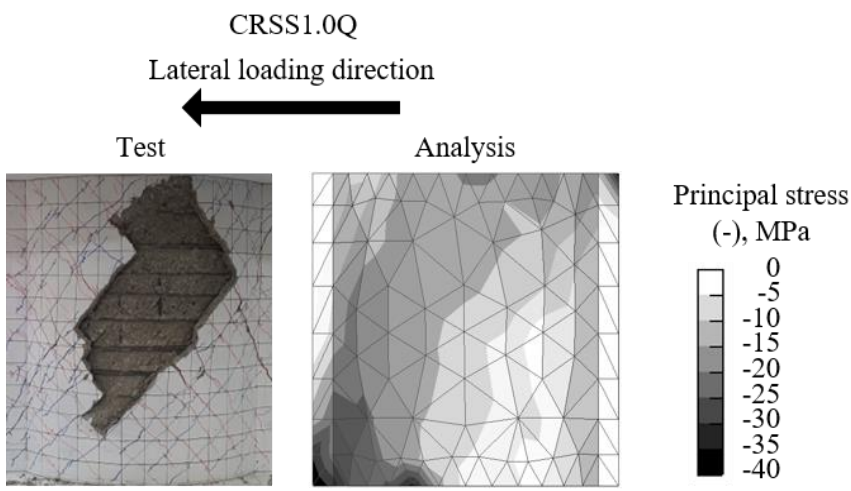

Figure 5-5 Damage pattern of concrete in CRSS1.0Q: test result, principal stress in positive and negative directions from finite element analysis result

Figure 5-6 and Figure 5-7 show the analysis results on the damage pattern of concrete in SPSS1.0M-VH and SPSS1.0M-VH-C. The difference between the two specimens is the installation of crosstie. In the figures, the distribution of principal stress in compressive and tensile direction were captured at the maximum strength. In the case of interior surface, the stress distributions were similar each other. The diagonal compressive field was formed in the compressive area. The maximum compressive stress was observed at the bottom of strut. In the ATENA program, after the peak strength, the concrete crushing was occurred in the local area, and the maximum compressive area was moved to the mid-height of the wall where concrete web crushing was observed in the test (Figure 6-12).

On the other hand, in the case of exterior surface, the compressive principal stress was higher in the specimen without crosstie (SPSS1.0M-VH). The concrete strut was also shown in the exterior surface. The compressive stress of SPSS-1.0-M-VH-C was less than that of SPSS1.0M-VH. The distributions of tensile stress were similar in the case of specimens with and without crosstie.

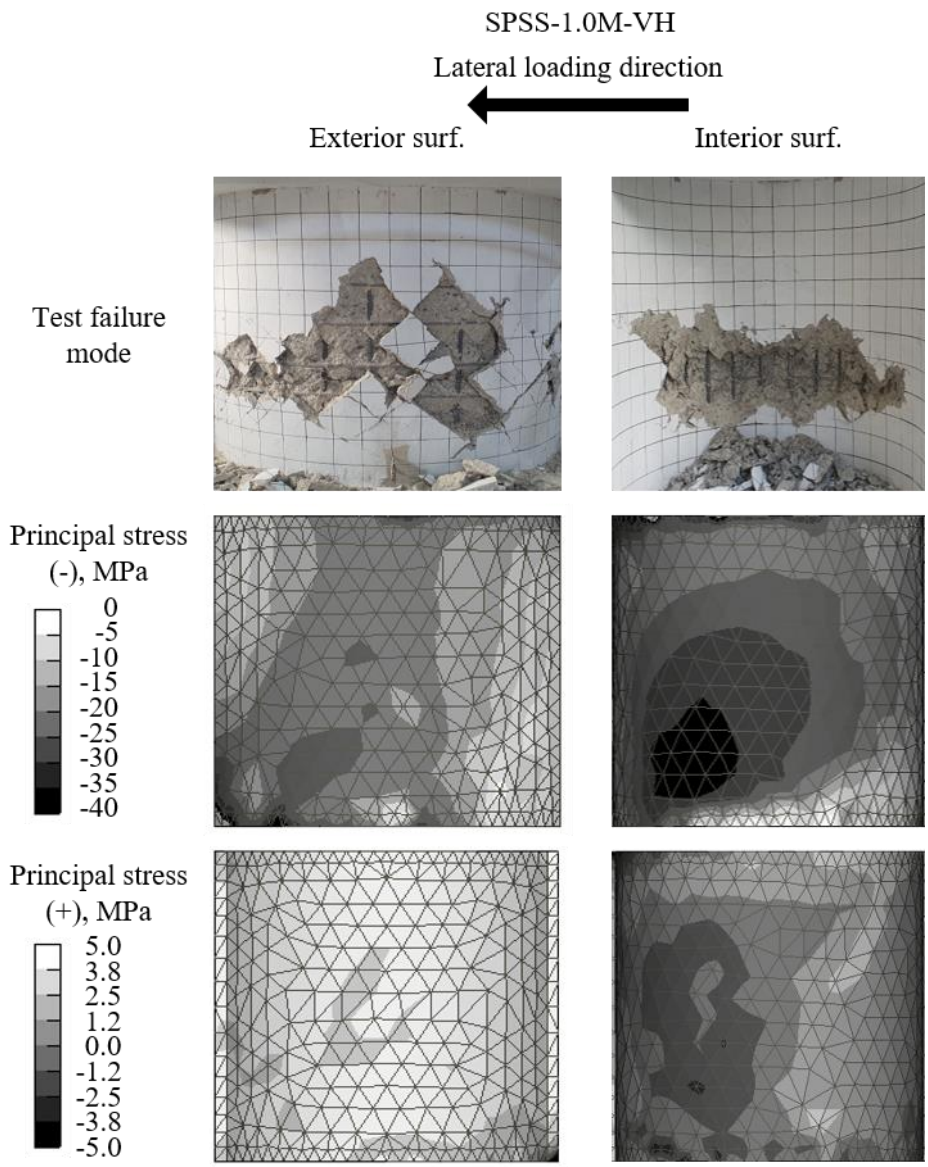

Figure 5-6 Damage pattern of concrete in SPSS-1.0M-VH: test result, principal stress in positive and negative directions from finite element analysis result

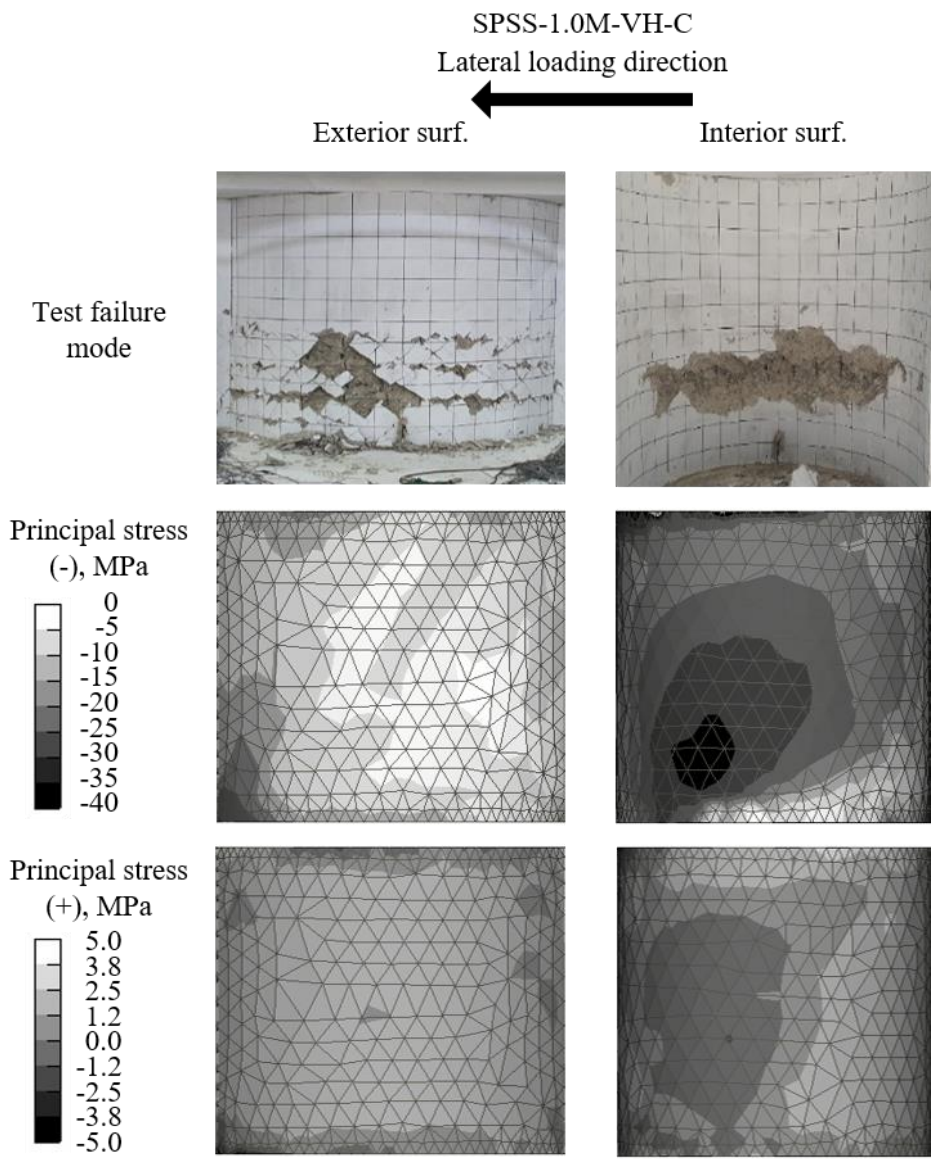

Figure 5-7 Damage pattern of concrete in SPSS-1.0M-VH-C: test result, principal stress in positive and negative directions from finite element analysis result

Figure 5-8 Principal stress of concrete in SPSS1.0M-VH-C according to the strength degradation.

5.4 Finite element analysis for parametric study

Since the number of test specimens was limited, to investigate the effect of reinforcing bar ratio, aspect ratio, and thickness on shear strength, the additional finite analysis was conducted. The analysis results were used to verify the proposed equation in Chapter 7. The analysis model was verified though previous chapters. Table 5-1 shows the list of variables. The considered variables were four cases for aspect ratio (h/R), five cases for ratio of thickness to radius (t/R), four cases for post-tensioning force and four cases for reinforcing bar ratio. The total number of analysis model was 320 (4 × 5 × 4 × 4). In all analysis model, additional vertical reinforcing bars were arranged at the flange area and bottom of wall to prevent premature flexural yielding. The values corresponding to the actual containment building are as follows: h/R = 2.0; t/R = 0.05; the post-tensioning force: 1300 MPa 0.64% and 1.0 % in vertical and horizontal directions, respectively; and 1.86 % and 0.92 % in vertical and horizontal directions, respectively. These values is colored in the Table 5-1.

Table 5-1 List of considered variables

Aspect ratio	Ratio of thickness/Radius	Post-tensioning force		Reinforcing bar ratio	
		Ver.	Hor.	Ver.	Hor.
1.0	0.05	0	0	0.93 %	0.46 %
1.5	0.1	1300 MPa 0.64 %	0	0.93 %	0.92 %
2.0	0.15	1300 MPa 0.64 %	1300 MPa 1.00 %	1.86 %	0.46 %
2.5	0.2	1300 MPa 0.64 %	1300 MPa 1.00 %	1.86 %	0.92 %
-	0.25	-	-	-	-

Figure 5-9 shows the comparison results of design (ACI 359), evaluation (EPRI) equation and maximum analysis strength. In the case of design strength, the ACI strength with considering concrete web crushing was underestimated the maximum analysis strength. The error increased when horizontal post-tensioning was applied. On the other hand, the design strength without considering web crushing is overestimated when the horizontal post-tensioning was applied and the ratio of thickness/radius was low. The reason why these overestimated was appeared is that the contribution of vertical component was ignored to determine the shear strength provided by ACI 359.

On the other hand, in the case of evaluation equation (EPRI), the prediction had low variation when the web crushing strength was ignored. The EPRI equation had almost twice times of the maximum strength of analysis and the standard deviation was 0.01. The reason why overestimation of EPRI is all analysis model expected the

web-crushing failure. When considering web crushing strength, the EPRI equation showed 1.07 times greater values than the analysis results with 0.07 of standard deviation. However, when the vertical or horizontal post-tensioning was applied, the web-crushing strength was not accurate. This result indicates that the web-crushing strength with consideration post-tensioning force should be improved.

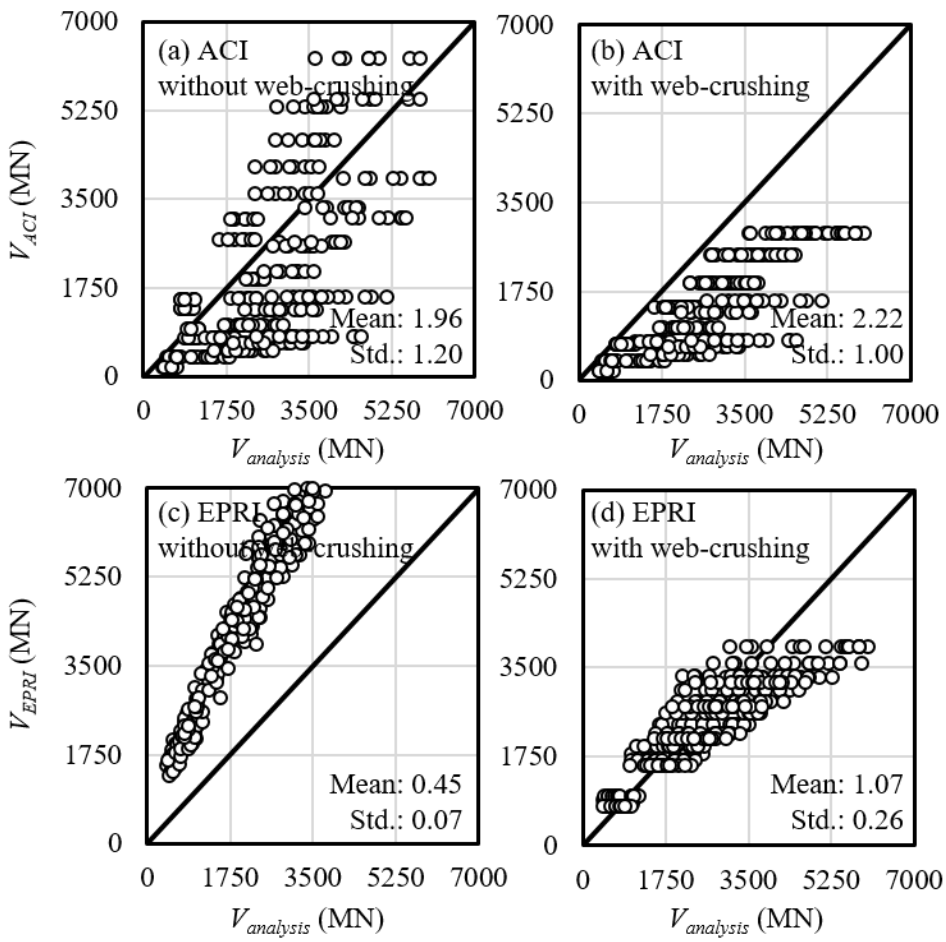

Figure 5-9 Comparison of shear strength by design or evaluation equation and FEA

5.5 Summary

In this chapter, nonlinear finite element analysis was performed to investigate the effect of variables on shear strength of cylindrical walls. The major findings was observed as follows:

1) The finite element analysis confirms that the web crushing before yielding is primary due to the horizontal strain in the cylindrical walls with high-reinforcing bar ratio. In the case of cylindrical walls with half of reinforcing bar ratios, the strains of vertical reinforcing bars were increased.

2) In the case of ACI prediction, the contribution of concrete and vertical component was not considered. In addition, the prediction of shear strength was dependent on the horizontal post-tensioning.

3) In the case of EPRI prediction, the diagonal tension strength ratio of analysis to evaluation equation was calculated with the low standard deviation. However, if the reinforcing bar ratio was high, web-crushing failure was observed before reinforcing bar yielding. Therefore, an upper limit of shear strength was existed and the evaluation equation without considering web crushing overestimated the capacity of concrete structure. However, the prediction of web crushing strength was not applied the effect of post-tensioning force.

Chapter 6. Effects of Design Parameters on Shear Strength of Concrete Wall

6.1 Overview

In Chapters 5, the finite analysis of the squat wall were conducted to investigate the shear strength of cylindrical walls with high reinforcing bar ratios. Further, to improve the test and analysis results, the some test parameters was considered, such as loading rate (static and dynamic), post-tensioning force (vertical and horizontal directions, and delamination), wall thickness, aspect ratio and shape of wall (Cylindrical and I-shaped).

In this chapter, the effect of these parameters on the shear strength were discussed based on the test and analysis results of the present study. The major subject of this chapter is the effect of loading rate, the post tensioning, and the shape of wall on shear strength of cylindrical wall.

In the section 6.3.4, the results of finite element analysis in the chapter 5 were used. Except for section 6.3.4, the effects of design parameters were verified only with the results of tests.

6.2 Loading rate effect

The loading rate effect is mainly due to two causes: the viscous effects and inertia confinement. For reinforced concrete structures under earthquake loading, the strain rate is less than 1 s^{-1}. In this case, the inertia force is negligible, only the viscous effect is considered. The effects of strain rate on steel were as follows: 1) the yield strength and ultimate strengths enhance as the strain rate increases, and 2) the elastic modulus is not influenced by the strain rate increases. On the other hand, the effects of strain rate on concrete were as follows: 1) the compressive and tensile strengths are increased as the strain rate increases, and 2) the elastic modulus is increased as the strain rate increases. In addition, the strain-rate effects are inversely proportional to the strengths of steel and concrete.

According to previous research (Chung et al (1989), Takeda and Tachikawa (1980), and Kulkami and Shah (1998)), the material capacity changes according to loading rate. In fib model code, to address the effect of loading rate, the dynamic increased factor (DIFs) for the yield and tensile strength of steels (f_{dy}/f_y, and f_{du}/f_u), and the ultimate compressive strength of concrete (f_{dc}'/f_c') were specified as a function of strain rate. In addition, in ACI 349 APPENDIX F “Special provisions for impulsive and impacted effects”, the DIFs were provided in the case of impulse and impact loading.

In previous researches, the wall test with high loading rate was not conducted. Thus, based on the Chapters 3 and 4-1, the effect of loading rate on wall was investigated. Figure 6-1 shows the comparison results of the load-displacement

envelop curve of dynamic and static test results of planar walls (Chapter 3-1). To investigate the effect of loading rate on the shear strength, three pairs of walls with the same detail were subjected under different loading condition [PRSF1.0H and PRDF1.0H, fig 6-1 (a)], [PRSM0.5H and PRDM0.5H, fig 6-1 (b)], and [PRSS1.0H and PRDS1.0H, fig 6-1 (c)].

In the case of high loading rate, the maximum average tested strengths were 11%, 10% and 5.2% greater than those of static loading specimen in flexural, shear and shear-friction failure mode, respectively.

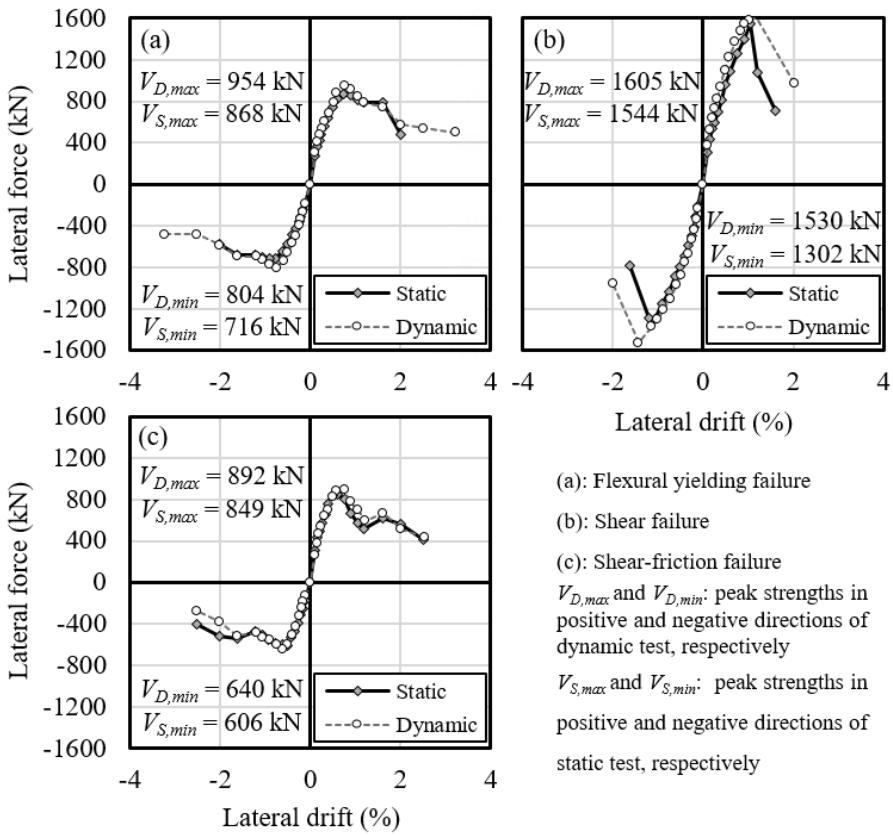

Figure 6-1 Comparison of envelop curves of planar walls according to loading rates

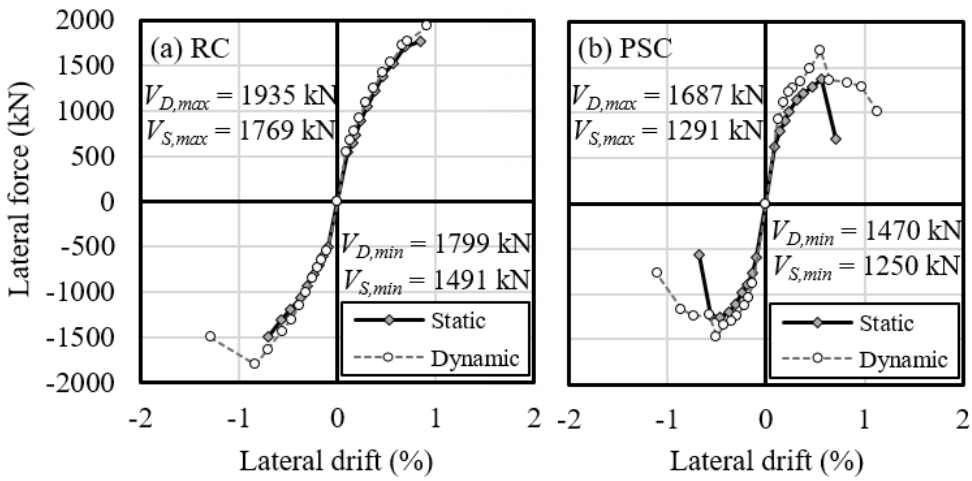

Figure 6-2 Comparison of envelop curves of cylindrical walls according to loading rates

Figure 6-2 shows the comparison results of cylindrical wall tests according to loading rate. To investigate the effect of loading rate on the shear strength, two reinforced concrete specimens (CRSS1.0Q and CRDS1.0Q) were prepared (Chapter 4-1). The specimens were subjected to different loading rates. In the case of high loading rate (CRDS1.0Q), the maximum strengths were 9.4%, 20.6%, and 14.6% greater than those of low loading rate specimen (CRSS1.0Q) in positive, negative directions, and average, respectively. On the other hand, the stiffness was similar to each other.

In the case of post-tensioned specimen, the direct comparison specimen was not prepared. However, the specimens with 100 % vertical and horizontal post-tensioning (CRSS1.0Q-31 and CRDS1.0Q-43) and different compressive strengths

were the same reinforcing bar details each other. The maximum tested strength was 24 % greater in CRDS1.0Q-43 high loading rate. Due to the greater compressive strength of concrete, the nominal shear strength of CRDS1.0Q-43 was 18 % greater than that of CRSS1.0Q-31. This result indicates that the effect of loading rate was about 5% indirectly if the effect of compressive strength is eliminated.

In all cases of the tests under a high loading rate, the maximum tested strengths were greater than those of the static loading test. This result indicates that the dynamic increased factor should be applied for strength evaluation under seismic loading. In the present dissertation, the number of material tests was limited. Therefore, the proposed models by Li and Li (2012), and Kulkami and Shah (1998) were used for a reinforcing bar and concrete, respectively, and Eqs. 6-1 and 6-2 represent the DIFs.

$$\frac{f_{dy}}{f_y} = 1 + c_u \log\left(\frac{\dot{\varepsilon}}{\dot{\varepsilon}_{so}}\right) \tag{6-1}$$

$$\frac{f_{dc}'}{f_c} = 0.022 \log\left(\frac{\dot{\varepsilon}_c}{\dot{\varepsilon}_{co}}\right) + 0.9973 \tag{6-2}$$

where f_{dy} and f_y are dynamic and quasi-static yield strengths of reinforcing bars, respectively; c_u is a factor ($0.1709 - 3.289 \times 10^{-4} f_y$); $\dot{\epsilon_s}$ and $\dot{\epsilon_{s0}}$ are actual and reference strain rates of reinforcing bars, respectively ($\dot{\epsilon_{s0}} = 3.0 \times 10^{-5}$); f_{dc}' and f_c' are dynamic and quasi-static compressive strengths of concrete, respectively; and $\dot{\epsilon_c}$ and $\dot{\epsilon_{c0}}$ are actual and reference strain rates of concrete, respectively ($\dot{\epsilon_{c0}} = 3.0 \times 10^{-4}$);

To determine the DIFs, the strain rate was calculated based on the test results. The

strain rates for concrete materials were estimated from the deformations measured by LVDTs for flexural, shear, and shear-friction strains. To obtain the proper DIFs, the strain rates corresponding to each failure mode were applied. The strain rates of reinforcing bars were estimated from the strain gauge of the vertical and horizontal reinforcing bars. For flexural and shear-friction failure mode, the strain rate of vertical reinforcing bar was used and for shear failure mode, the strain rate of horizontal reinforcing bar was used. The strain values and the modified design strengths with DIFs were summarized in table 6-1. In the case of shaking table tests, the strain rates for determining the DIFs were captured at the test of maximum input ground acceleration of each specimens.

Table 6-1 shows the predicted strength using DIFs. The predicted strengths were calculated based on ACI 349 and EPRI equation for the planar and cylindrical walls, respectively. The average ratios of maximum tested strength versus predicted strength with DIFs were 1.01, 1.50, and 0.88 in the case of specimens with flexural, shear, and shear friction failure modes. Due to the uncertainty of the predicted equation, the ratios of shear and shear-friction were with high uncertainty. However, the prediction of flexural strength was in +5 % to -4% of experimental results, except in the case of PREF2.0H-1. These results indicate that reflecting the effect of the loading rate should be considered under seismic loading conditions for the exact evaluation. The effect of loading rate according to shape of wall was not observed.

Table 6-1 Dynamic increased factors and predicted test strengths of test specimens

Specimen	Failure mode	Reinforcing bars				Concrete				V_{test} (kN)	V_{DIFs} (kN)	V_{test}/V_{DIFs}	V_{test}/V_p
		$\dot{\epsilon}_{s0}$	$\dot{\epsilon}_s$	DIF	f_{dy}	$\dot{\epsilon}_{c0}$	$\dot{\epsilon}_c$	DIF	f_{dc}'				
PRDF1.0H	Flexural	3.0×10^{-4}	3.5×10^{-2}	1.08	478	3.0×10^{-4}	3.3×10^{-2}	1.06	38	878	839	1.05	1.07
PRDF1.0M	Flexural		3.3×10^{-2}	1.03	499		3.0×10^{-2}	1.06	37	1301	1360	0.96	1.06
PRDF0.5H	Flexural		7.6×10^{-2}	1.04	502		7.3×10^{-2}	1.07	44	862	886	0.97	1.01
PRDM0.5H	Shear-fric.		7.6×10^{-2}	1.04	502		4.9×10^{-2}	1.07	44	766	866	0.88	0.92
PRDS1.0H	Shear		3.2×10^{-2}	1.04	497		2.2×10^{-2}	1.06	38	1568	857	1.83	1.88
PREF1.0H-1	Flexural		0.8×10^{-1}	1.06	497		0.8×10^{-1}	1.07	43	299	305	0.98	1.07
PREF1.0H-2	Flexural		1.0×10^{-1}	1.06	498		1.0×10^{-1}	1.07	43	304	306	0.99	1.09
PREF2.0H-1	Flexural		2.0×10^{-1}	1.06	500		2.0×10^{-1}	1.08	43	189	162	1.15	1.21
PREF2.0H-2	Flexural		1.7×10^{-1}	1.06	500		1.7×10^{-1}	1.08	43	161	162	1.00	1.05
CRDS1.0Q	Shear		3.3×10^{-2}	1.05	489		2.7×10^{-2}	1.06	40	1867	1037	1.80	1.86
CPDS1.0Q-43	Shear		3.3×10^{-2}	1.05	489		2.5×10^{-2}	1.06	46	1578	1841	0.86	0.88

Note: V_{test} is the maximum peak strengths of test; V_{DIFs} is a predicted strength with DIFs; and V_p is a predicted strength without DIFs.

6.3 Effect of post-tensioning force

Post-tensioning forces were widely used in nuclear power plant buildings, especially containment buildings to withstand internal pressure. In particular, a containment building is intended to contain the pressure of an accidental explosion. However, the researches on the effect of post-tensioning on shear strength of wall were rare. This chapter, based on structural test and nonlinear finite element analysis results, compares the shear strength of concrete walls with and without post-tensioning.

6.3.1 Vertical post-tensioning

Figure 6-3 shows the comparison results of envelop curves. In the case of cylindrical test results (Figure 6-3 (a)), the CPDS1.0Q-V with only vertical post-tensioning force, the maximum tested strength was 7 % greater than that of CRDS1.0Q without post-tensioning force, and the same reinforcing bar details with CPDS1.0Q-V. In the specimen with vertical post-tensioning force, the cover concrete failure occurred. The yield stiffness was twice larger as that of the specimen without post-tensioning. The yield stiffness was defined using the secant stiffness corresponding to 75 % of the maximum tested strength. This result indicates that vertical post-tensioning increases the stiffness of structures and diagonal tension strength.

In the case of semi-cylindrical test results (fig 6-3 (b)), the test results of

SRSS1.0M and SPSS1.0M-V show the effect of vertical post-tensioning on the shear strength. In the case of SPSS1.0M-V with only vertical post-tensioning force, the average maximum tested strength was 12 % lower than that of SRSS1.0M without post-tensioning force. In addition, the drift ratio at the maximum tested strength was decreased in the case of SPSS1.0M-V. The vertical post-tensioning force increases the principle compressive stress and can reduce the web-crushing strength of the wall with high reinforcing bar ratios.

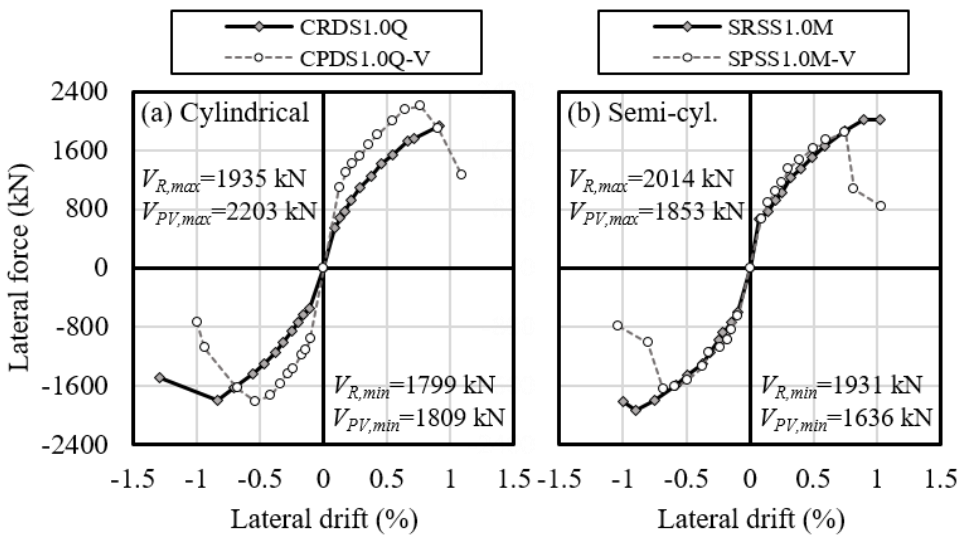

Figure 6-3 Comparison of envelop curves of cylindrical and semi-cylindrical walls according to vertical post-tensioning

6.3.2 Horizontal post-tensioning

Figure 6-4 shows the comparison results of envelop curves of cylindrical and semi-cylindrical walls according to horizontal post-tensioning. In the case of CPDS1.0Q-Vh with 100 % vertical and 50 % horizontal post-tensioning forces, the maximum tested strength was 3 % greater than that of the specimen without horizontal post-tensioning. On the other hand, in the case of CPDS1.0Q-43 with 100 % vertical and horizontal post-tensioning forces, the maximum tested strength was 20 % lower than that of CPDS1.0Q-Vh and CPDS1.0Q-V despite the compressive strength of concrete was 13 % greater (38 and 43 MPa).

The internal cracks occurred at very low lateral drift because the horizontal post-tensioning force causes tensile stress in the radial direction (Basu (2001) and choi (2017)). This is the reason why the maximum tested strength was less in the test results of the specimen with 100 % horizontal post-tensioning. The present test results also confirmed the delamination cracks in the walls. In addition, the maximum tested strength was significantly lower than the nominal shear strength.

However, in the case of semi-cylindrical specimens with thicker wall thickness, the strength decrement did not occur even if the delamination occurred. The reason why the effect of the delamination crack did not appear is as follows: 1) the thickness of the wall (90 mm → 180 mm) 2) the double reinforcing bar layer. Because of the double reinforcing bar layer, the cover concrete resisted shear deformation after the delamination cracks were propagated.

In the case of specimens with horizontal post-tensioning force, the maximum strength was 18 % greater than the result of specimen without horizontal post-tensioning. On the other hand, there was no difference between the test results of 50 % and 100 % horizontal post-tensioning.

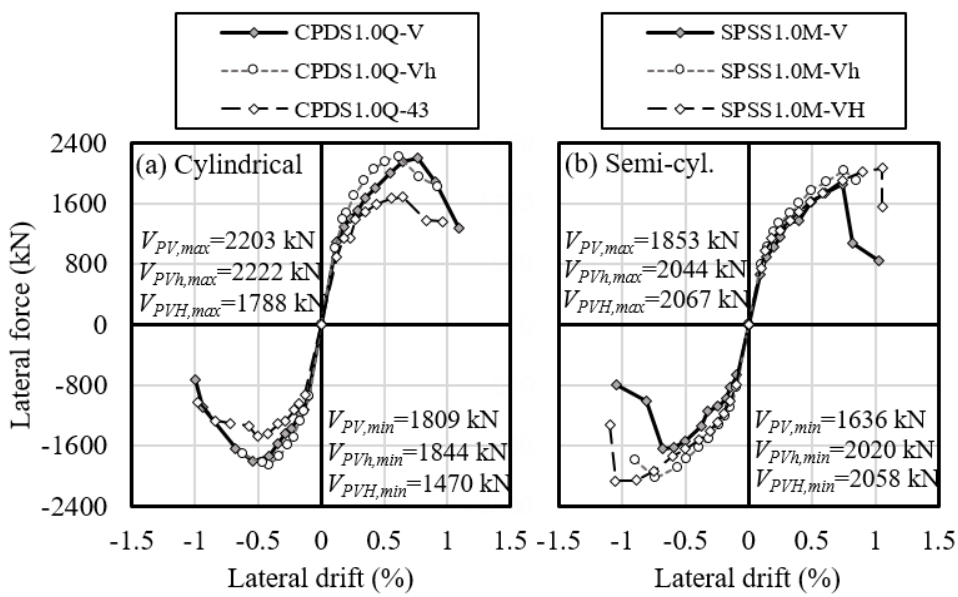

Figure 6-4 Comparison of envelop curves of cylindrical and semi-cylindrical walls according to horizontal post-tensioning

6.3.3 Delamination on walls and effect of cross-tie

Due to the horizontal post-tensioning, radial stress occurred and internal cracks were observed. To investigate the effect of crossties on the resistance of delamination cracks, the crossties between the exterior and interior horizontal reinforcing bars were installed in the SPSS1.0M-VH-C.

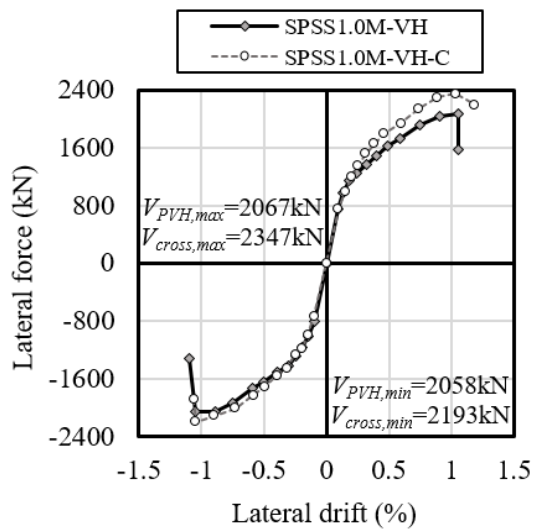

Figure 6-5 Comparison of envelop curves of semi-cylindrical walls with and without crosstie

Figure 6-5 shows the comparison of envelop curves of the specimens with and without crossties. In the case of specimen with crosstie, the maximum tested strengths were 14 %, 7 %, and 10 % greater than those of specimen without crosstie in the positive and negative directions and average, respectively. Due to the internal cracks that occurred in SPSS1.0-VH, the concrete section to resist the shear force

was decreased. The decrement in strength was close to the ratio of concrete cover area to total thickness (11.1 %). In addition, from the boring test results, the delamination cracks were not observed in the specimens with crosstie. This result indicates that the crosstie resists generating internal cracks due to horizontal post-tensioning. In addition, after the diagonal cracks occurred, the stiffness was greater than that of SPSS1.0M-VH.

The failure mode of interior surface was concrete crushing with large horizontal cracks at both specimens. However, the failure mode of exterior surface was different according to the installation of crosstie. In figs 6-6 (b), the distributions of horizontal reinforcing bar strain were concentrated to the mid-height in the range of 1500 to 2000 μm. On the other hand, in the case of SPSS1.0M-VH-C, the strains were distributed in the range of 1000 to 2000 μm. This result indicates that the in-plane shear is spread in the case of specimen with crosstie.

The crosstie did not directly affect the shear capacity of cylindrical wall. However, the delamination cracks were prevented due to crosstie. Therefore, the crosstie effects on the increase in shear capacity.

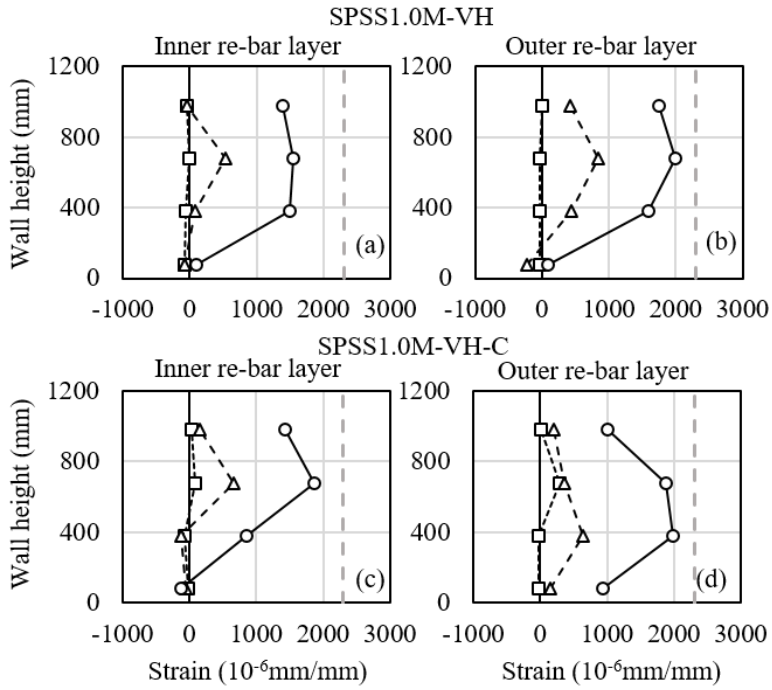

Figure 6-6 Strain distribution of horizontal reinforcing bars with and without crosstie

6.3.4 Bending moment due to horizontal post-tensioning

In the case of a containment building, to prevent leakage of radioactive material, horizontal and vertical post-tensioning is applied. However, in the case of horizontal post-tensioning, radial stress is occurred due to curved geometry. The previously known effect of radial stress is delamination which was mentioned in the previous section. In addition, the finding from the finite element analysis was an additional bending moment at the lower part of containment. According to Timoshenko (1970), an additional moment occurs at the boundary of the cylindrical wall under a load uniformly distributed radial pressure. Figure 6-7 shows the conceptual diagram of the above theory.

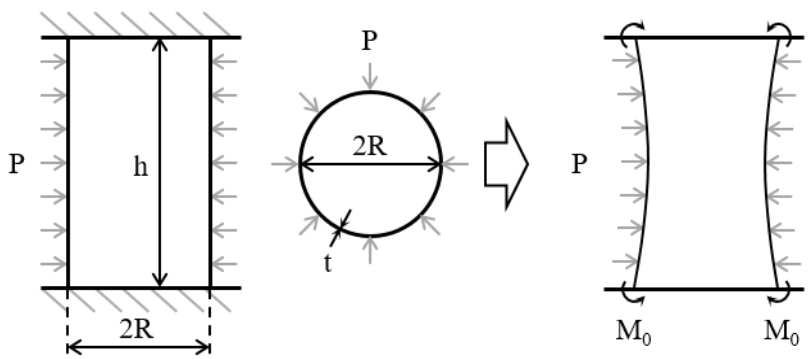

Figure 6-7 Concept diagram of moment due to radial pressure

The additional moment does not cause structural failure in the static state. However, under lateral loading (i.e. seismic, wind), the moment capacity of the structure is decreased due to the initial stress of reinforcing bar. The additional moment can be obtained as Eqs 6-3 to 6-5.

$$M_0 = \frac{p}{2\beta^2}\chi_2(2\alpha) \tag{6-3}$$

$$\chi_2(2\alpha) = \frac{\sinh(2\alpha) - \sin(2\alpha)}{\sinh(2\alpha) + \sin(2\alpha)} \tag{6-4}$$

$$\beta = \frac{1}{\sqrt{Rt}}\sqrt[4]{3(1-\nu^2)} \tag{6-5}$$

where p is an external pressure (MPa·mm), h is a thickness of wall (mm), and $2\alpha = \beta h$.

The radial pressure 'p' caused by horizontal post-tensioning can be calculated Eq 2-27. Using these two equations, the moment caused by horizontal post-tensioning can be derived below Eq 6-6.

$$M_0 = \left(\sigma_{ph}\rho_{ph}\frac{tw}{R}\right)\frac{Rt}{2\sqrt{3\left(1-\nu^2\right)}}(2\alpha) \tag{6-6}$$

In the case of the actual containment building, the $\chi_2(2\alpha)$ is close to 1.0. In addition, substituting a known value for Poisson's ratio of concrete $\upsilon = 0.2$, the unit length b = 1. Therefore, Eq 6-7 can be derived as Eq 6-6.

$$M_0 = \frac{\left(\sigma_{ph}\rho_{ph}t^2 w\right)}{3.4} \tag{6-7}$$

To verify that the theory can be applicable to the actual cylindrical wall, using the results of finite element analysis, the theoretical value and analysis value were compared. Table 6-2 shows the comparison result. The ratio of M_{FEA}/M_{Theory} was decreased with an increment of thickness. Because, as the thickness increases, the greater difference between the theoretical and finite element analysis value according to the shell theory. Likewise, in the case of finite element analysis, the decrement of radius at the mid-height was lower than that of theoretical results.

Table 6-2 Additional bending moment comparison of theoretical and finite element analysis

Case No.	Thickens (mm)	M_{FEA} (N·mm)	M_{Theory} (N·mm)	M_{FEA}/M_{Theory}	δ_{FEA} (mm)	δ_{Theory} (mm)
1	1200	1.61×10^9	1.42×10^9	1.03	10.5	10.76
2	2500	5.37×10^9	5.54×10^9	0.92	9.70	10.76
3	3400	9.80×10^9	11.10×10^9	0.88	9.31	10.76
4	4500	15.78×10^9	19.48×10^9	0.81	8.54	10.76
5	5400	21.89×10^9	28.21×10^9	0.76	8.19	10.76

To investigate the effect of bending moment at the bottom, finite element analysis was performed using the model in chapter 5. The information of analysis model is summarized in Table 6-3. The target of analysis model was a bottom area of the APR1400 containment building. In this analysis model, the additional vertical reinforcing bars to prevent flexural yielding were not included.

Table 6-3 Information of analysis model to verify the bending moment due to horizontal post-tensioning

H (mm)	R (mm)	t (mm)	f_c' (MPa)	f_y (MPa)	Reinforcing bar		Tendon	
					Ver.	Hor.	Ver.	Hor.
50,000	25,000	1,200	40	470	0.65 %	0.92 %	0.6 %	1.0 %

Figure 6-8 shows the distribution of vertical reinforcing bar stress after post-tensioning force was applied. The percentage shown above each figures are the change rate of the post-tensioning force from the model in Table 6-3. The maximum tensile stress occurred in the case of analysis results with only horizontal post-tensioning force. In the case of target model in the rectangular box, although the tensile stress was reduced due to vertical post-tensioning, the tensile stress remained from 12 to -91 MPa (Positive in tensile direction).

Figure 6-9 shows the stress distribution of the vertical reinforcing bar at the maximum strength occurred. The tensile stress was concentrated on the bottom area due to horizontal post-tensioning.

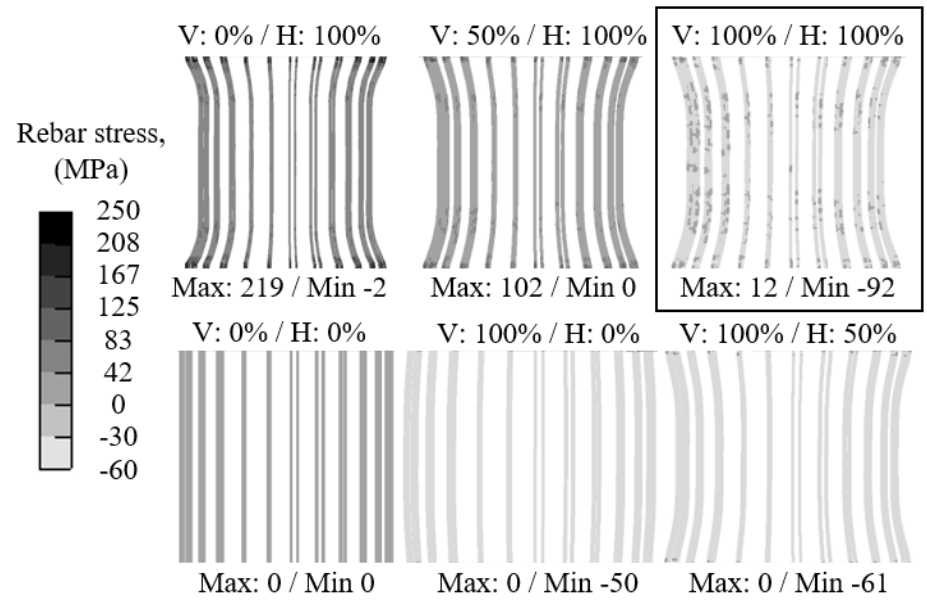

Figure 6-8 Stress distribution of vertical reinforcing bars after applying post-tensioning

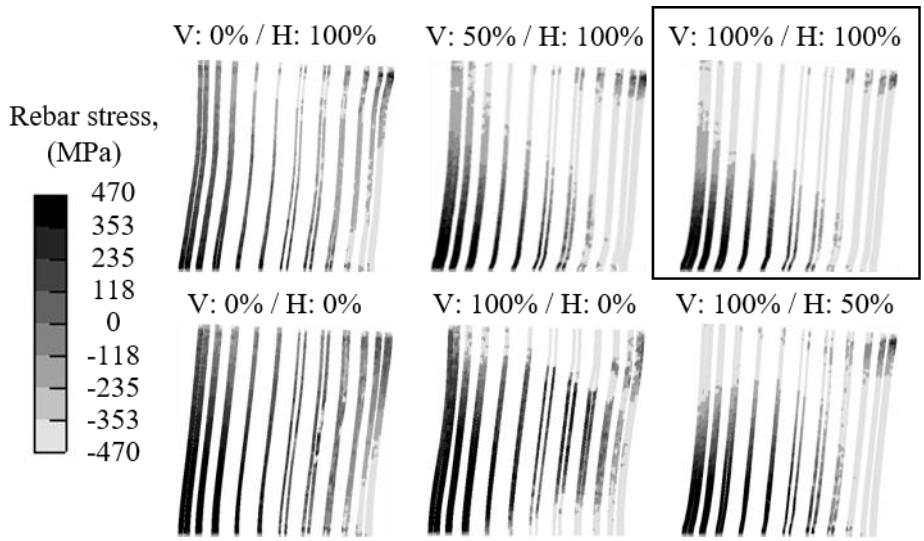

Figure 6-9 Stress distribution of vertical reinforcing bars at maximum load

To verify the effect of initial bending force on the maximum overturning capacity of the cylindrical wall, the lateral displacement was applied to the analysis model. Figure 6-10 (a) and (b) show the relationship between lateral displacement and force according to horizontal and vertical post-tensioning force, respectively. The maximum strength occurred at the "V100H50" with 100 % vertical and 50 % horizontal post-tensioning cylindrical wall. This result indicates that a certain level of horizontal post-tensioning force increases seismic performance. However, in the case of larger horizontal post-tensioning force, due to radial stress generated by the curved tendon, a moment was generated at the bottom and seismic performance was reduced. On the other hand, vertical post-tensioning had a direct effect on the improvement of seismic performance (Figure 6-10 (b)). Especially, in the case of "V0H100" with only horizontal post-tensioning force, the maximum strength was 28 % lower than that of the reinforced wall without post-tensioning. This result indicates that the horizontal post-tensioning generated an additional moment at the bottom area, and the maximum moment capacity was decreased.

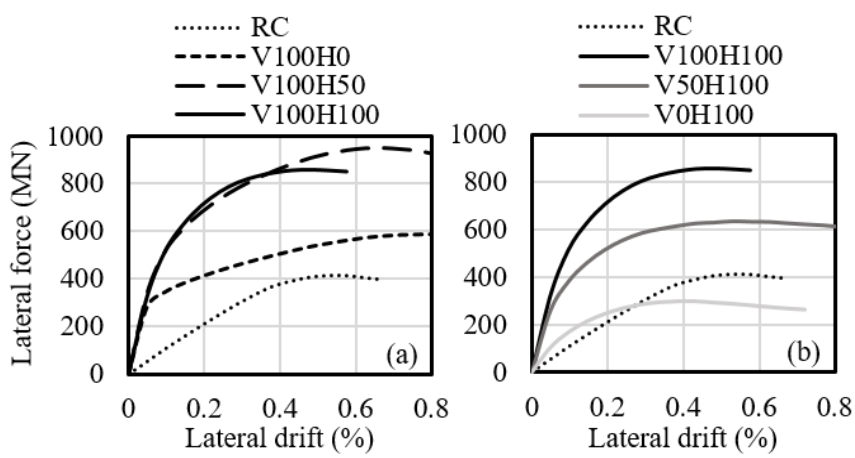

Figure 6-10 Relationship of lateral force and displacement according to (a) horizontal and (b) vertical post-tensioning force

6.4 Effect of wall shape

6.4.1 Cylindrical and planar wall

To investigate the effect of structural shape of wall on shear strength, the test results of I-shaped and semi-cylindrical walls were compared. The details of specimens were summarized in Chapter 4-2. The thickness of wall, detail of boundary element vertical and horizontal reinforcing bar ratios and post-tensioning force were the same for I-shaped and semi-cylindrical specimens.

In the case of specimens without post-tensioning force, the test results of semi-cylindrical specimen SRSS1.0M were compared to those of IRSS1.0M. On the other hand, in the case of post-tensioning specimens, the I-shaped specimen IPSS1.0M was compared to SPSS1.0M-VH-C. All details of SPSS1.0M-VH were the same as SPSS1.0M-VH-C or IPSS1.0M, however, the crosstie was not installed. Thus, the test result was different from SPSS1.0M-VH-C with delamination cracks.

Figure 6-11shows the comparison results of envelop curves of reinforced and post-tensioning concrete specimens. The difference of stiffness from two comparison results was small. Because the contribution of stiffness was mainly from the contribution of in-plane shear stiffness, and that was determined from the cross-section detail of web area. The maximum tested strengths of specimens without post-tensioning forces were 6 %, 12 % and 9 % less at the semi-cylindrical specimen in positive and negative directions and average, respectively (Figure 6-11 (a)). The failure mode of interior surface of semi-cylindrical wall was similar to the failure mode of I-shaped. However, the failure mode of exterior surface with large diagonal

tension was different. The reason for this will be explained in the last of this section.

In the case of semi-cylindrical shape specimen with post-tensioning forces (SPSS1.0M-VH-C, Figure 6-11 (b)), the average maximum tested strength was 3 % greater than that of I-shaped specimen. The failure modes of two specimens were same with huge horizontal cracks at the middle height. The failure mode of exterior surface was slightly different with that of interior surface, but the main failure mode with horizontal cracks was same.

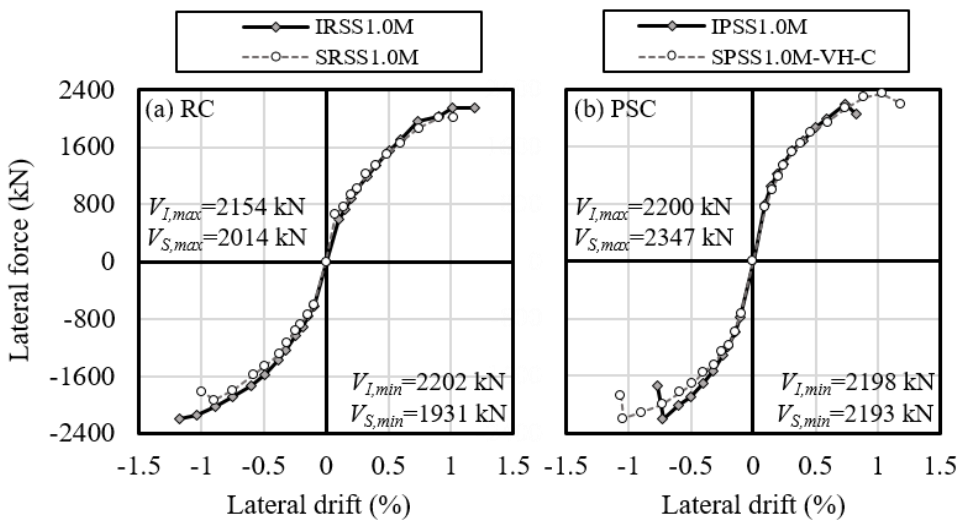

Figure 6-11 Comparison of envelop curves of I-shaped and semi-cylindrical walls

In the Figure 6-12, the comparison results of strain distributions of horizontal reinforcing bars were presented. In the case of reinforced concrete walls (Figure 6-12 (a)), the strain of horizontal reinforcing bars of semi-cylindrical specimen when the maximum strength was occurred were 46 % greater than those of I-shaped specimen. Especially, the strain of horizontal reinforcing bar in the middle height was 192 %

greater in the semi-cylindrical specimen.

In the case of specimens with post-tensioning force (Figure 6-12 (b)), the strains at the maximum tested strength of horizontal reinforcing bars of semi-cylindrical specimen were 46 % greater than those of I-shaped specimen. The difference ratio of strains was 1.10 to 1.87.

However, in the case of the vertical reinforcing bars, the strain distributions were similar to each other according to the wall length (figs 4-24 and 4-25).

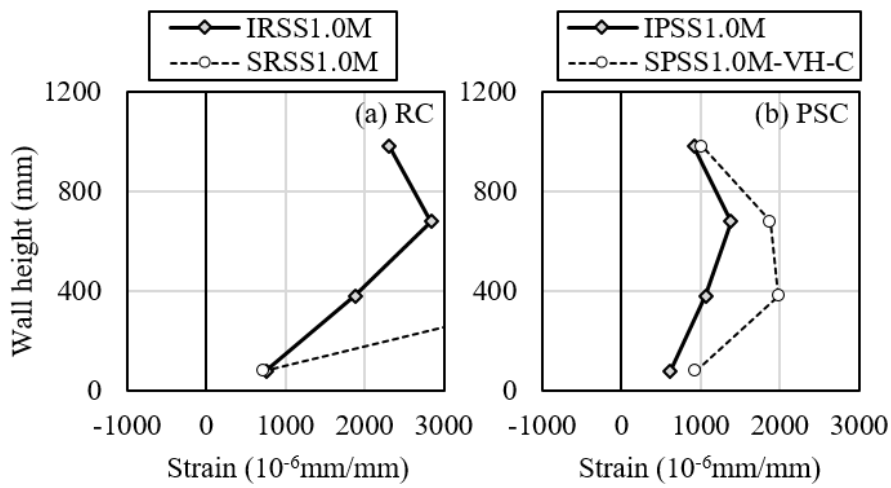

Figure 6-12 Strain distribution of horizontal reinforcing bars according to wall shapes.

The hollow cylindrical wall cannot transfer the lateral force (i.e. seismic load, or wind load) through the center of the cross section unlike planar, I-shaped, or circular walls. Thus, the stress due to the lateral load is transferred along the cross section. In this case, the direction of the load must be continuously changed along the cross section. Therefore, the confining force for lateral force is required.

The confining force occurs indirectly through the tensile stress of the vertical and horizontal reinforcing bars. The confining force by vertical reinforcing bar was calculated to be very smaller than that by horizontal reinforcing bar. On the other hand, in the case of horizontal reinforcing bars, as shown in Figure 6-12, a higher additional strain appeared in the cylindrical section for the same strength.

In the case of the I-shaped reinforced concrete specimens without post-tensioning test, the maximum tested strength was greater than that of a cylindrical wall. However, the strains of horizontal reinforcing bars were smaller in the case of I-shaped wall as shown in Figure 6-12 (a). This result indicates that additional strain to generate confining forces was appeared. Due to extra strain of horizontal reinforcing bars to generate this confining force, in the case of cylindrical wall, the structural failure was occurred at the lower drift ratio or strength.

On the other hand, in the case of the specimens with horizontal post-tensioning force, the tendencies of maximum strength and strains were different with the results of specimen without post-tensioning. The horizontal post-tensioning force applied to the cylindrical wall generated a radial stress as if to cause delamination. The radial stress was generated the compressive radial stress inside of horizontal tendon layer, and the stress contributes as a confining force on the cylindrical wall. Thus, in the case of cylindrical wall with horizontal post-tensioning like SPSS1.0M-VH-C, the confining force is determined by the sum of effect of horizontal reinforcing bars and radial compressive stress due to horizontal post-tensioning force. Therefore, in the case of specimens with horizontal post-tensioning, the difference of strain distributions at the maximum tested strength was 54 % smaller than that of without horizontal post-tensioning.

In the case of I-shaped wall, the maximum tested strength was similar regardless the post-tensioning force ($V_{I,PSC}/V_{I,RC}$ = 1.01). However, in the case of semi-cylindrical test, due to the additional confining force from horizontal post-tensioning, the maximum tested strength ratio of RC and PSC ($V_{S,PSC}/V_{S,RC}$) was increased to 1.15.

In the present test results of specimens with cylindrical section, the failure mode interior surface was huge concrete crushing. According to Timoshenko (1970), in a hollow circular section under radial stress, the in-plane stress increased toward the center of the cross section. Due to characteristics of the stress distribution of cylindrical section, the concrete crushing was occurred at the interior surface. This is why internal and external failure modes were different each other.

6.4.2 Horizontal strain due to increment of radius

To investigate the effect of radius on shear strength, the horizontal strain was measured at the FEA results. Figure 6-13 shows the concept of horizontal strain of cylindrical wall. Due to the deviation force caused by the radius effect, the radius of wall increases. The horizontal strain of the wall increases due to the increase in radius. Therefore, the horizontal strain of cylindrical wall under lateral loading is summation of strain due to shear deformation and effect of radius.

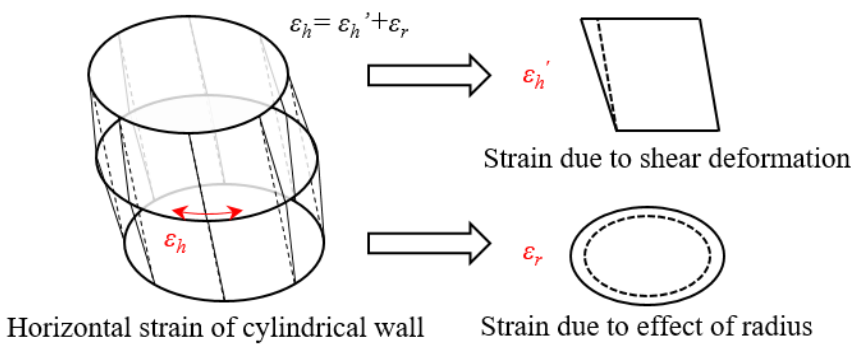

Figure 6-13 Component of horizontal strain of cylindrical wall

Due to the increase in radius of cross section, the horizontal strain of the reinforcement in the cylindrical wall is greater than that in the planar wall. It is believed that the radius effect will affect the degradation of the shear performance of the wall. In particular, the increment of strain of horizontal reinforcing bar is critical to the diagonal tension strength, which is determined by the yield of reinforcing bars. On the other hand, the strength of web crushing failure is affected by the principal tensile stress. However, since the web crushing strength is dominated by the

compressive strength of concrete, the effect of the radius is less. In addition, in the previous section, the test results also showed differences in the strain of horizontal reinforcing bars, but the maximum strengths of cylindrical and planar wall were similar each other.

Figure 6-14 shows the contribution of radius effect on the average horizontal strain based on FEA and test results. The contribution increased as the thickness of the cylindrical wall decreased. The expected contribution based on the analysis results is indicated by a dotted line. The contribution by the radius effect is expected to have significant results from when the thickness of the cylindrical wall becomes half the radius (r_i/r_o = 0.5).

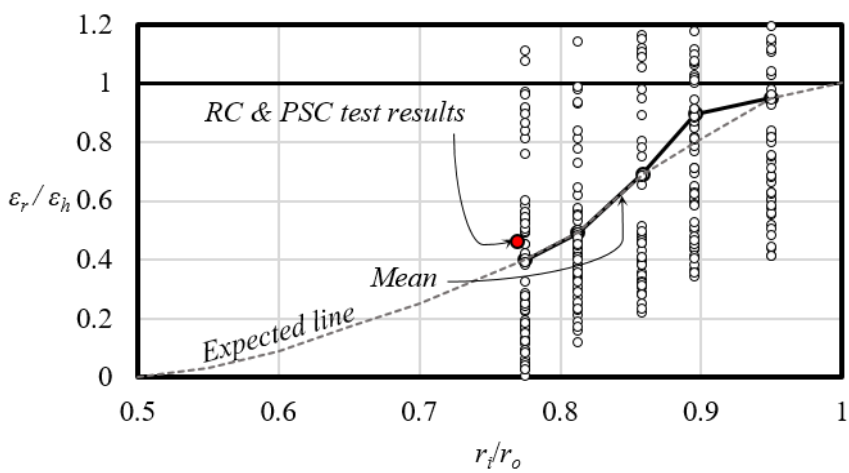

Figure 6-14 Contribution of effect of radius ($\varepsilon_r/\varepsilon_h$) according to internal and external radius ratio (r_i/r_o)

The thrust line was assumed to investigate the radius effect according to the wall thickness. Figure 6-15 shows the expected load path in the cylindrical section according to wall thickness. The load path was assumed to have the minimum curvature among the line from the external loading point to the opposite end. The load path determined under above assumption does not have a curvature when the wall thickness is greater than half the radius.

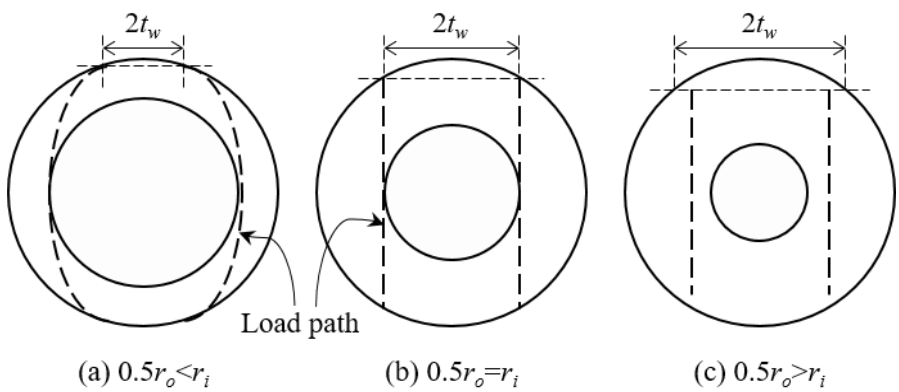

Figure 6-15 Expected load path in cylindrical section according to internal and external radius ratio (r_i/r_o)

In addition, the load path is affected by the aspect ratio and the cracked angle. Therefore, the loading path does not reach the end of the wall opposite the loading point when the aspect ratio is low. However, in the case of walls with low aspect ratio, the curvature of load path is greater than that of in Figure 6-15. Thus, when the aspect ratio is low, the radius effect disappear at a lower ratio of t_w/r_o.

If the load path is shown in Figure 6-15, the curvature can be obtained through the following EQ 6-8.

$$\kappa_T = \kappa_{R_o}\left[\frac{-1+2\left(\frac{r_i}{r_o}\right)}{1-2\left(\frac{r_i}{r_o}\right)+2\left(\frac{r_i}{r_o}\right)^2}\right] \tag{6-8}$$

Figure 6-16 shows the curvature of expected load path according to the ratio of internal and external radius.

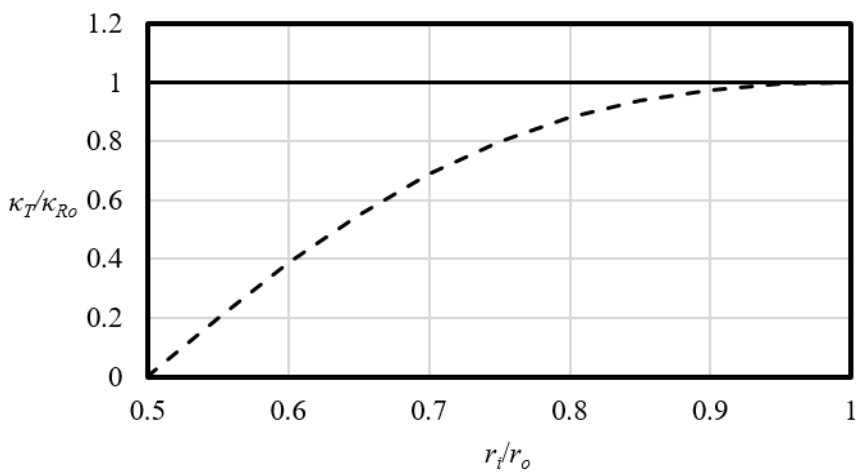

Figure 6-16 Curvature ratio of cylindrical wall and expected thrust line (κ_R/κ_T) according to internal and external radius ratio (r_i/r_o)

The load path is also affected by the aspect ratio, and the crack angle. Therefore, further research is required on when the radius effect disappears or the ratio of the radius effect in the shear deformation.

6.5 Summary

In the present Chapter, to develop the shear strength model of cylindrical wall, the effect of design parameters on the containment building were discussed based on the wall test and analysis results. The major design parameters affecting the shear strength are the loading rate and post-tensioning force. In addition, due to the shape of cylindrical wall, extra strain increment was observed on horizontal reinforcing bars. The major findings are summarized as follows:

1) The loading rate effect on shear strength was verified. Based on the results of direct and indirect comparison specimens, the maximum tested strength was increased as much as DIFs. The crack width was increased and the number of cracks was decreased. On the other hand, the effect of loading rate according to shape of wall was not observed.

2) The effect of vertical post-tensioning on shear strength was different according to failure mode. If the diagonal tension failure is expected due to the wall thickness is thin or the reinforcing bar ratio is low, the vertical post-tensioning was increased the shear strength. However, in the case of web-crushing strength, the effect of vertical post-tensioning was not significant.

3) In case of the cylindrical wall with horizontal post-tensioning, the shear strength was increased. The magnitude of horizontal post-tensioning force caused the internal cracks (delamination) and the internal cracks degraded the shear capacity. Installation of crosstie can resist the propagation of delamination cracks due to horizontal post-tensioning. However, in the case

I-shaped wall, the maximum shear strength was not affected by post-tensioning forces.

4) The additional moment in the lower section of cylindrical wall caused by the horizontal post-tensioning force was observed. The additional moment caused the vertical reinforcing bars at the lower part to be in tension. This tensile stress has no effect in normal condition; however, it causes premature reinforcing bar yielding when a lateral force such as seismic, hurricane forces is applied.

5) The shape of cross-section affects the shear strength of wall. In the case of cylindrical wall, the confining force is needed to resist the lateral forces. The confining force was from the tensile stress of horizontal reinforcing bars mainly. In addition, the radial compressive stress due to horizontal reinforcing bars was contributed to the confining force. Thus, the increment strain of horizontal reinforcing bars due to deviation force should be considered.

6) Due to the characteristic of stress distribution in cylindrical section under radial stress, the failure mode of interior and exterior surface was different.

Chapter 7. Shear Strength Model for Cylindrical Walls

7.1 Overview

In the present dissertation, the shear strength model for the cylindrical wall was developed by modifying the traditional truss analogy. Since, the failure modes of specimens were determined from the crushing of web concrete or diagonal tension cracking, rather than the damage of the boundary zone. For failure criteria, two failure modes were considered: 1) Diagonal tension failure after horizontal reinforcing bar yielding and 2) Elastic web crushing failure.

For diagonal tension failure, the strains of horizontal reinforcing bars included the additional strains due to deviation force. In addition, the effect of horizontal post-tensioning forces, such as delamination and confining force, was adopted in the proposed equation. For the failure mechanism, the compressive strength of diagonal struts was defined based on the existing model (Luna (2015)). For the web-crushing mechanism, the model improvement was achieved by considering the effect of the deviation force due to the cylindrical shape. For the verification, the shear strength predicted by the proposed model was compared with the test and analysis results.

Figure 7-1 shows the relationships between Chapter 7 and the previous chapters. Based on the experimental results (Chapter 4), the data was used to define the failure mode of cylindrical wall and the failure procedure of the wall with delamination cracks. In addition, the test data was used to determine the strain of vertical

reinforcing bars in the simplification process. The proposed equation in this chapter was verified by the maximum tested strength. Using the FEA results of Chapter 5, the crack angle was assumed during the simplification process, and the maximum strength was used in the verification of the proposed equation. Based on the results in Chapter 6, the confining force generated by horizontal post-tensioning and the deviation force due to shape of cylindrical wall were calculated.

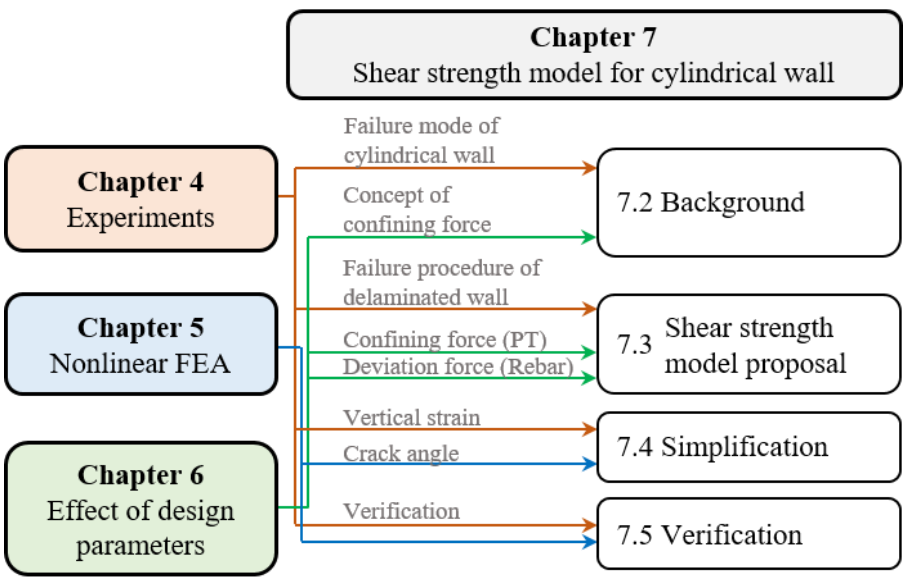

Figure 7-1 Overview of Chapter 7

7.2 Background

7.2.1 Web-crushing and observed failure mode of cylindrical walls

The parallel cracks in the diagonal direction are shown in a reinforced concrete member subject to shear loading. Due to the cracks, diagonal concrete struts between shear cracks are formed. For squat reinforced concrete walls, the shear force is transferred through the truss action of the diagonal struts and horizontal reinforcing bars. In the case of reinforced concrete walls with high reinforcing bar ratios, web-crushing failure occurs due to the shear demand that exceeds the compressive strength of concrete. On the other hand, in the case of that low reinforcing bar ratios, diagonal tension failure occurs with reinforcing bars yielding or subsequent sliding at the diagonal cracks before web crushing occurs.

In the case of cylindrical walls, web-crushing failure may occur before flexural bar yielding. In chapter 4 of this dissertation, such failure modes were appeared in the test results. In the case of the reinforced concrete member with web-crushing failure and without flexural bar yielding, the deformation capacity is limited. Thus, current design criteria restrict the web-crushing failure by limitation of reinforcing bar ratios. The design provisions of ACI 349 and 359 provide the maximum shear strength corresponding to web crushing failure, based on such assumptions. Web-crushing strength is independent of deformation demand, proportional to concrete tensile strength, and depends on average shear stress.

Figure 7-2 shows the diagonal cracks and concrete struts of the cylindrical wall during the test. The main failure modes were 1) web-crushing failure in the web (Figure 7-2 (a)) and 2) diagonal tension failure with out-of-plane displacement (Figure 7-2 (b)). In the case of a cylindrical wall with crosstie, the concrete strut appeared clearly and the concrete crushing was observed in the middle-bottom area. On the other hand, the failure mode of all specimens except the cylindrical wall with crosstie was the first failure mode with out-of-plane displacement. After the out-of-plane displacement occurred, the width of diagonal cracks significantly increased and the load-carry capacity decreased rapidly.

This failure mode did not appear in the case of planar wall. This result indicates that the additional mechanism to the shear resistance of cylindrical walls is necessary. Thus, for better prediction or evaluation of the shear strength of cylindrical walls, the additional concept should be considered.

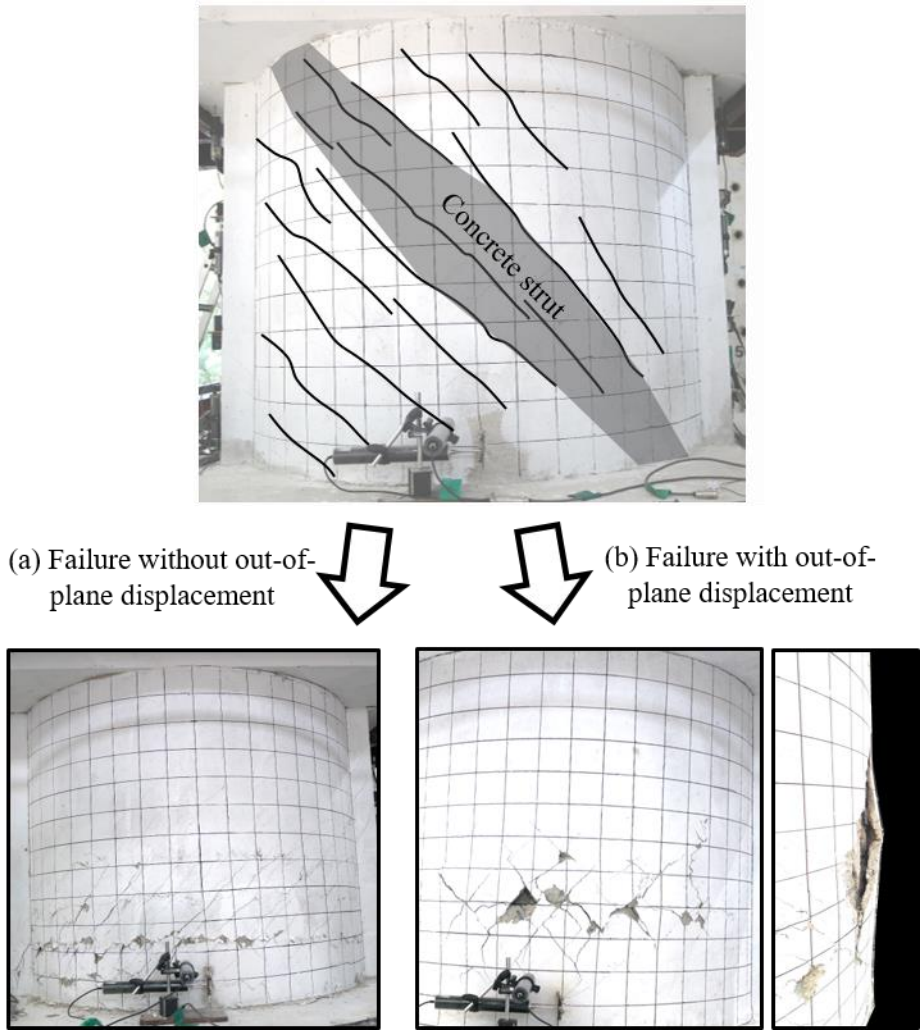

Figure 7-2 Diagonal cracks and compressive strut and failure mode

7.2.2 Confining force (or deviation force)

To explain the concrete cover failure with out-of-plane deformation in the web area, the confining force to maintain the cylindrical shape is used. In addition, the strains of horizontal reinforcing bars of cylindrical specimens were greater than those of I-shaped specimens in the previous chapter. Therefore, for maintaining the cylindrical shape of cross section, confining force is required. Figure 7-3 shows the concept of confining force. The shape of cylindrical wall cannot be maintained without the confining force.

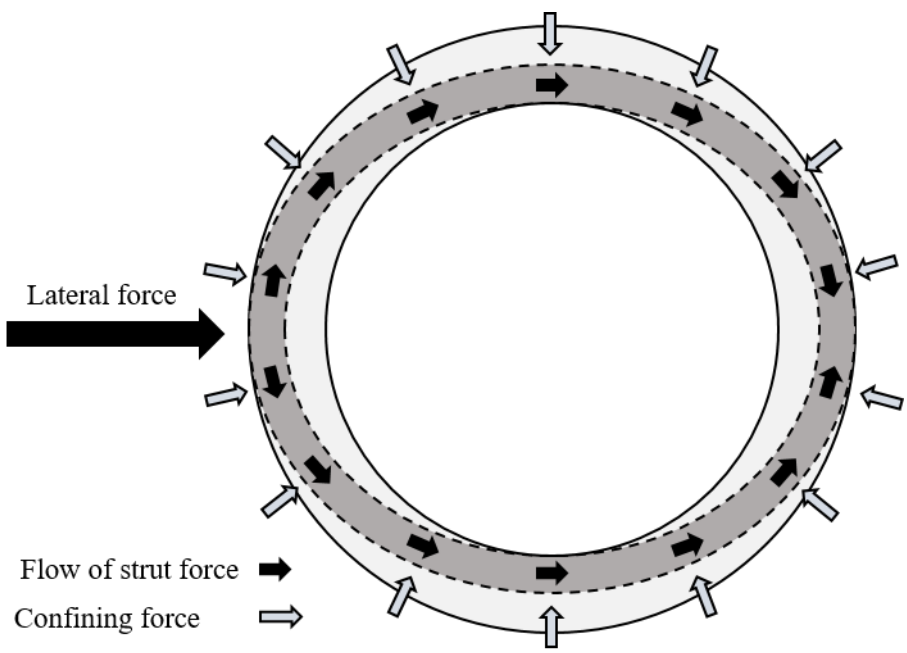

Figure 7-3 Concept of confining force

The confining force of cylindrical wall is caused by tensile force of horizontal reinforcing bars and post-tensioning tendons. The compressive radial stress due to curved post-tensioning force is applied to the additional confining force. The confining stress from horizontal members is calculated based on equation 7-1 (Acharya and Menon, (2003))

$$p_c = \frac{F_x}{Rw} \tag{7-1}$$

where p_c is a confining pressure, F_x is a tensile force of reinforcing bar or tendon for confining force, R is a radius of cylindrical wall, and w is a width of cross-section.

The requirement of confining force of cylindrical wall is also calculated using the equation 7-1. Based on the force equilibrium, the additional strain of horizontal reinforcing bar ε_R can be obtained as equation 7-2.

$$\varepsilon_R = \frac{T_b}{\rho_h \left(wt_w \right) E_s} = \frac{1}{\rho_s E_s} \sigma_c \tag{7-2}$$

where ρ_h is a ratio of horizontal reinforcing bar, E_s is an elastic modulus of reinforcing bar and σ_c is a compressive stress of concrete strut. Due to the tensile stress on reinforcing bars for maintaining the cylindrical shape, the additional strain of horizontal reinforcing bars occurs. Thus, the width of diagonal cracks was greater than that of a planar wall. In addition, the expected diagonal tension failure strength decreased.

In this dissertation, the shear equation for cylindrical wall considering the confining force is proposed.

7.2.3 Elastic analysis of cylindrical squat wall

To investigate the stress distribution of cylindrical wall, the elastic analyses were conducted using a commercial program MIDAS GEN. The analysis purpose was the behavior of cylindrical wall under lateral loading. The analysis model was used a beam element with a single layer and used a rigid frame for top slab. The lateral force was applied at the top of the analysis model. Because of the high reinforcing bar ratios of containment building, most nonlinear behaviors were expected to appear at the bottom of wall. Indeed, the strains of reinforcing bars in the web area of test specimens did not exceed the yield strain until the test end.

To compare the stress distribution of planar and cylindrical wall, truss analysis was conducted. The diagonal, vertical and horizontal truss members indicate the concrete strut, vertical and horizontal reinforcing bars, respectively. Figure 7-4 shows the contour result graph of truss analysis. The major differences between planar and cylindrical walls based on truss analysis are summarized as follows:

1) Compressive forces of diagonal struts in the web area were greater in the cylindrical wall. However, in the case of planar wall, the compressive force was concentrated on the bottom of wall boundary (compression zone).

2) Diagonal strut, and horizontal member forces were equal regardless of wall height (cylindrical wall). However, in the case of planar wall, the forces of horizontal and diagonal members were increased at the lower part of wall.

3) In the case of a cylindrical wall, the force distribution of vertical member was similar to that of planar wall. As the aspect ratio increased, the forces of vertical

member increased due to overturning moment. In the case of planar wall, the force distribution of vertical member was linear to the wall length. However, in the case of cylindrical wall, the force of vertical member at the boundary was 12 % less than the maximum tensile force of vertical element.

4) Because of cylindrical shape, the out-of-plane force occurred. The out-of-plane forces were balanced by the upper slab (Figure 7-5). The lateral force was redistributed in the top slab, and only in-plane load was transmitted to the wall area.

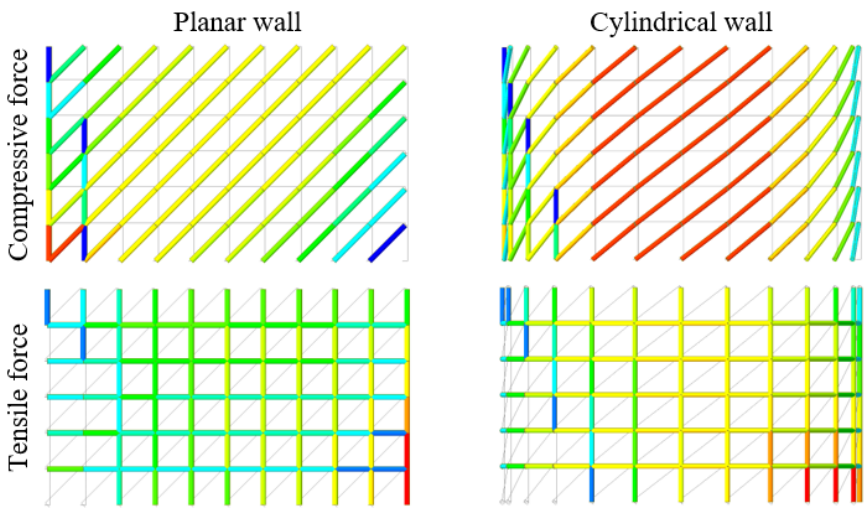

Figure 7-4 Comparison truss analysis of planar and cylindrical walls

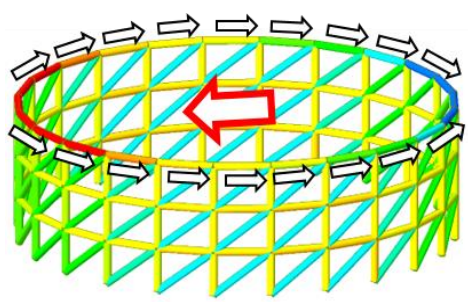

Figure 7-5 Force flow at top area

However, the truss model can only be performed in the elastic range. Thus, truss analysis cannot apply the yield stress of reinforcing bars. According to the above considerations, the nonlinear boundary condition was used. Figure 7-6 shows the boundary condition of analysis model. The stiffness and maximum strength of spring element in boundary condition were modified as follows.

1) In the case of compressive force, the elastic modulus was used that of concrete and the maximum strength was $A_{cb} \times f_c'$. A_{ch} is an equivalent area of beam member and f_c' is a compressive strength of concrete. The boundary condition cannot resist deformation beyond maximum strength.

2) In the case of tensile force, the elastic modulus was used that of reinforcing bars and the yield strength was $\rho_v \times A_{cb} \times f_y$. ρ_v is a ratio of vertical reinforcing bar and f_y is a yield strength of reinforcing bar. The multi-linear force-displacement relationship was used.

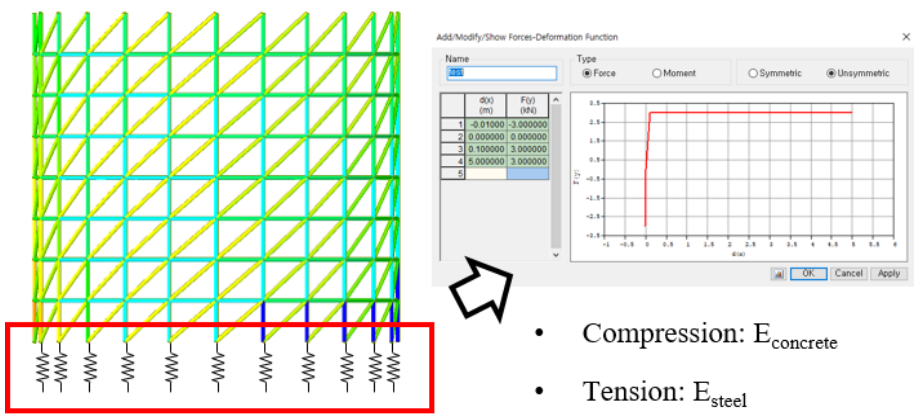

Figure 7-6 Nonlinear boundary condition

Figure 7-7 shows the stress distribution of cylindrical wall according to aspect ratios. Figure 7-7 (a) and (b) show the results as absolute and normalized to the minimum and maximum value, respectively. As the aspect ratio increased, because the moment force is governed, the forces vertical member at the bottom of wall was increased. The force distributions at the top area were similar to that of aspect ratio of 0.4 when confirmed by the result indicated by the absolute value (Figure 7-7 (a)).

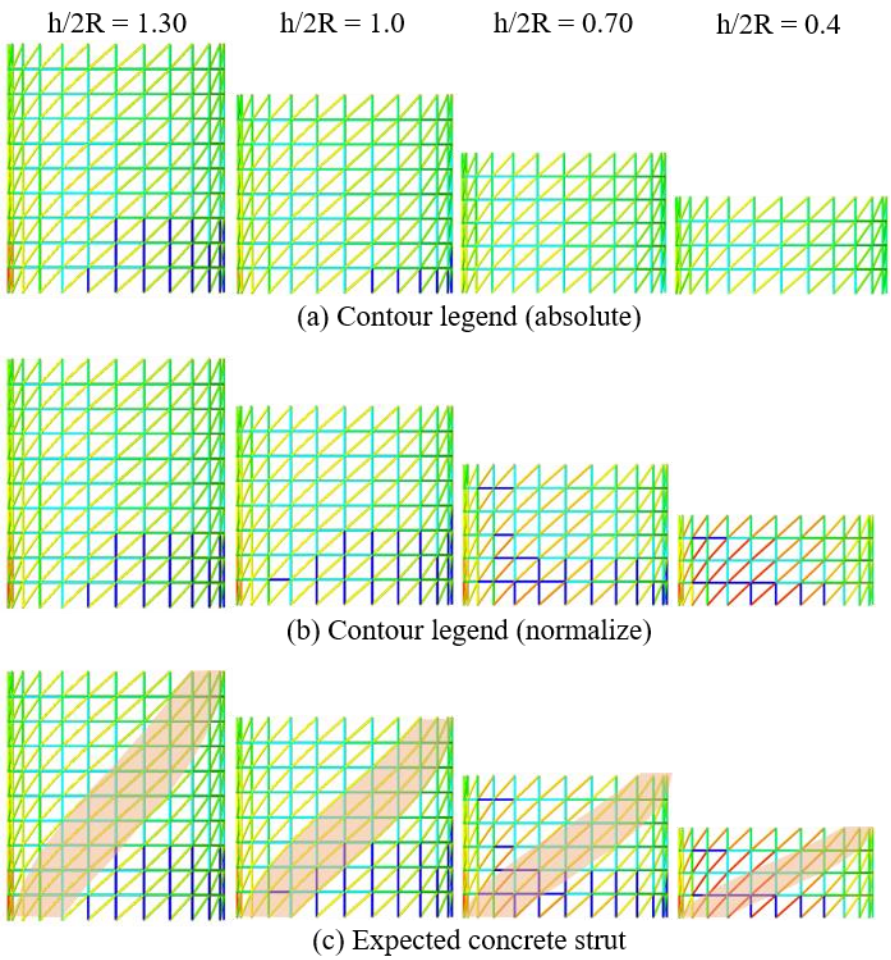

Figure 7-7 Stress distribution according to aspect ratios and expected concrete strut

On the other hand, in the case of normalized results, the forces of horizontal and diagonal members were relatively increased as the aspect ratio decreased. The forces of horizontal members near the tension zone were less than those in web and compression zone. This result indicates that the shear force is transferred by the truss mechanism in the case of cylindrical wall with a low aspect ratio. In addition, the strut angle depends on the aspect ratios. (Figure 7-7 (c)).

7.3 Shear strength of cylindrical wall

7.3.1 Concept of shear strength model

7.3.1.1 Assumptions

In the results of analysis, the shear stress on concrete is concentrated along the macro diagonal strut across the cross-section. In this dissertation, the web crushing strength is defined in terms of compressive stress of concrete struts. For the shear strength model determined by web crushing, the following assumptions are used:

1) Parallel shear cracking appears in the entire web with constant crack angle: θ_c

2) The strut strength is determined by the capacity of confinement. The cylindrical shape cannot be maintained after horizontal reinforcing bar yield (Diagonal tension failure).

3) The web crushing strength is independent of lateral drift.

4) The capacity of boundary elements is enough to maintain the shape of wall.

5) The force equilibrium at the top area of cylindrical wall is maintained by top slab and only in-plane force transferred to wall area.

From the experimental test and analysis results, the first assumptions are obvious. The second assumption reflects the deviation force explained in the Section 7.2.2. In the case of the third assumption, it is assumed that when large deformation demand is required due to horizontal reinforcing bar yield with the second assumption or

vertical reinforcing bar yield due to flexural deformation. Therefore, under large deformation, the failure mechanism is not under elastic range. In the inelastic range, the shear strength is degraded. Related to the fourth assumption, the web crushing failure is only valid when the damage of boundary element is limited.

When lateral force applied on cylindrical wall, the out of plane force must occur. In this dissertation, the out-of-plane force is canceled by top slab and only in-plane stress is transferred to wall area. This assumption is related to the last result of elastic analysis at chapter 7.2.3. In addition, the actual containment building has a thick slab on the top area to install a polar crane (Figure 7-8).

Figure 7-8 A polar crane of containment building

7.3.1.2 Model concept

Based on the elastic analysis and test results, the concept of a shear strength model is proposed. In Figure 7-9, to investigate the shear strength of cylindrical squat wall, the wall element is divided into three segments based on the observed cracking pattern. The characteristics of each segments are as follows:

1) Segment A: Compression area

The bottom area of segment A can resist compression and shear forces because the diagonal cracks do not propagate in the test results. The main shear resistance mechanism is shear friction.

2) Segment B : Strut area

In the case of segment B, the concrete struts resist the shear forces. The failure mode and strength are determined in this segment. As mentioned, to maintain the cylindrical shape of wall, the confining force is necessary. If the strain of horizontal reinforcing bars exceeds the yield strain, the diagonal tension failure is expected with failure of maintaining shape. On the other hand, if the confining force is sufficient and the shape of wall is maintained, the web crushing failure with concrete crushing is expected at the maximum compressive strength of concrete.

3) Segment C: Tension area

In the area of segment C with flexural and diagonal cracks, the tensile force of the horizontal reinforcing bars is caused by the lateral force

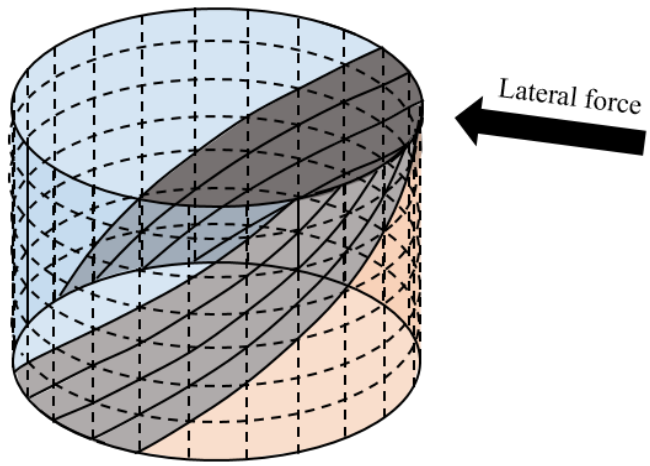

Figure 7-9 Concept of shear strength model

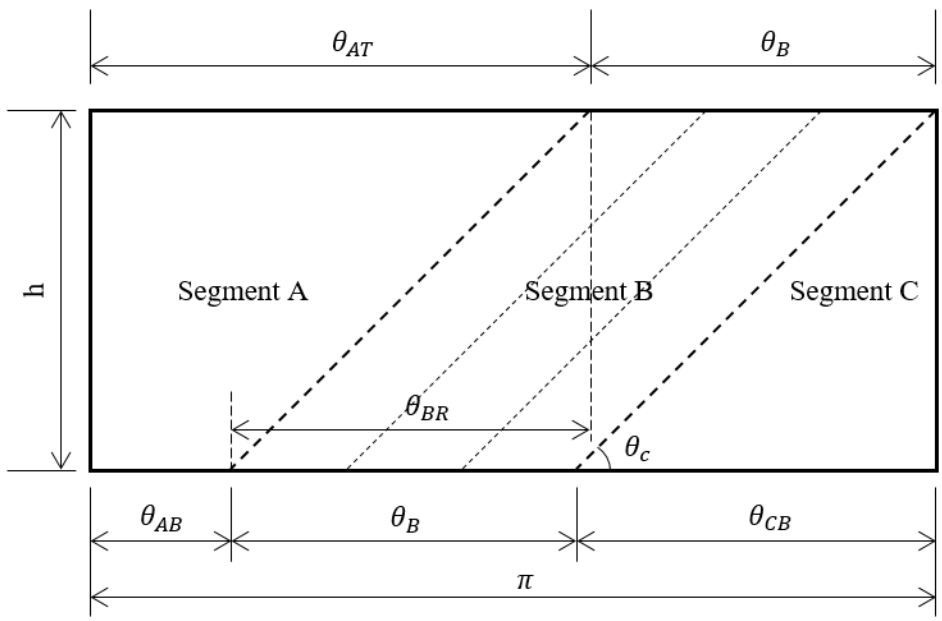

Figure 7-10 Development figure of cylindrical wall

To increase readability, Figure 7-10 shows the development figure of half side surface of cylindrical wall: [θ_{AT} and θ_{AB}] and [θ_{CT} and θ_{CB}] are top and bottom central angles of segment A and C, respectively; θ_C is a cracked angle; θ_B is a central angle of segment B; θ_{BR} is a rotational angle of segment B; and h_w is a height of wall. The relationships of the angles according to the cracked angle θ_C are as follows:

$$\theta_{BR} = \frac{1}{\tan\theta_c}\frac{h_w}{R} \tag{7-3}$$

$$\theta_{BR} = \theta_{CB} \le \pi \tag{7-4}$$

$$\theta_{AT} = \theta_{AB} + \theta_{BR} \le \pi \tag{7-5}$$

$$\theta_{AT} + \theta_B = \pi \text{ or } \theta_{AB} + \theta_B + \theta_{CB} = \pi \tag{7-6}$$

Based on the force equilibrium, the free body diagrams of each segment are shown in Figure 7-11. The boundary of each segment was made at observed typical diagonal cracks based on test results.

The forces on the free-body diagram include below terms: 1) Lateral force at the top of the wall; 2) Forces carried by the vertical and horizontal reinforcing bars of each segment; 3) Reaction forces of each segment at the bottom; 4) Forces from concrete struts; and 5) The confining forces are included in the strains of horizontal reinforcing bars. The functional force caused by aggregate interlock between cracks was ignored because due to the large crack width of cylindrical shape of wall. The shear resistance of cylindrical wall is calculated as the sum of horizontal force vectors of each segment (Eq 7-7).

$$\vec{V} = 2\left(\overrightarrow{F_{Ax}} + \overrightarrow{F_{Bx}} + \overrightarrow{F_{Cx}}\right) \tag{7-7}$$

The forces of each segment F_{Ax}, F_{Bx}, and F_{Cx} are calculated in the next chapter.

In this dissertation, the evaluation of the top element is considered sufficient to withstand the lateral load. In addition, in the top area of containment building, because of a buttress for crane installation and a greater reinforcing bar ratio, the seismic capacity is greater in the top area.

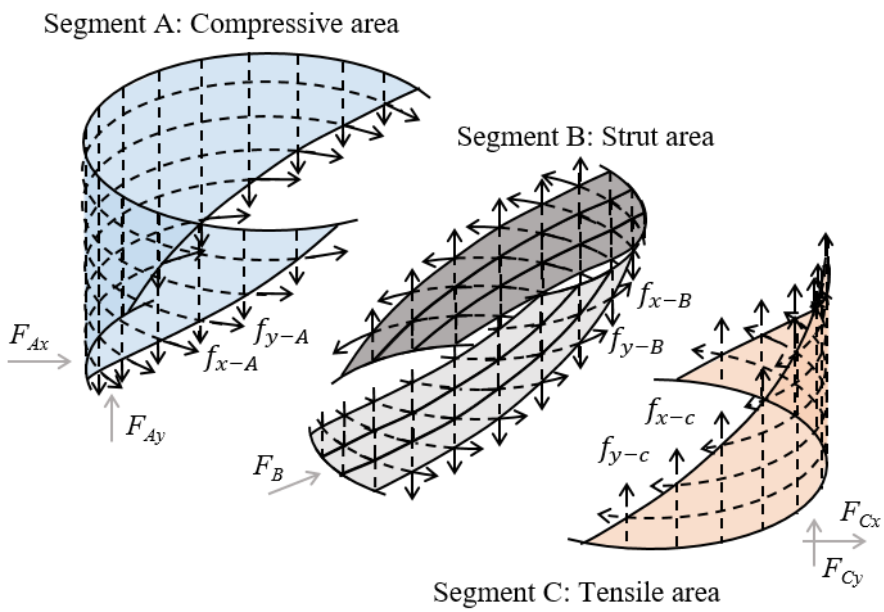

Figure 7-11 Free-body diagram of each segments

7.3.2 Define the forces and prediction of shear strength

7.3.2.1 Strut area (Segment B)

1) Force equilibrium and strain of horizontal reinforcing bars

To calculate the squat cylindrical wall, due to the cylindrical shape, the curved strut is considered. The curved strut is assumed as that only axial force is considered without tangential shear or moment. Figure 7-11 (b) and Figure 7-12 show the free body diagram of segment B.

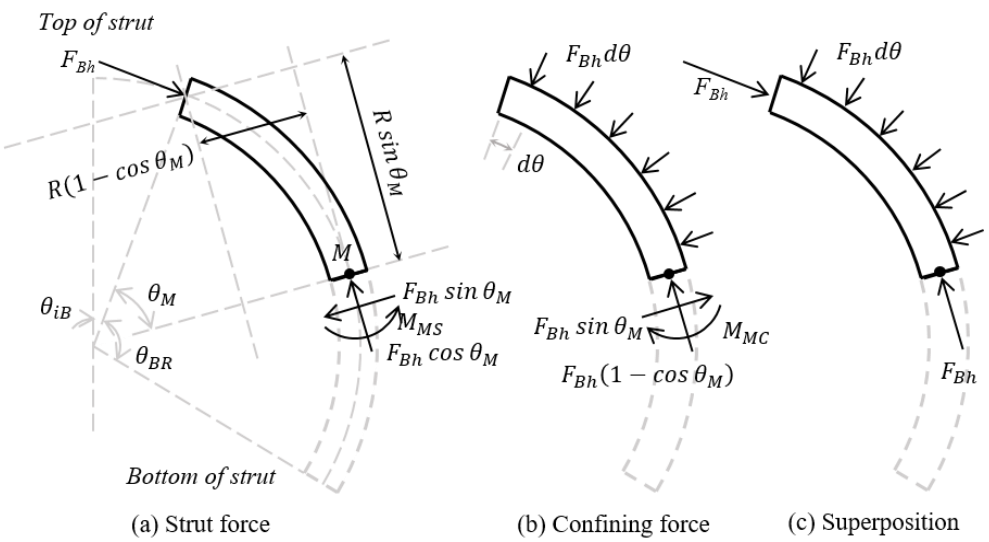

Figure 7-12 Free body diagram of segment B (In-plane)

The F_{Bh} is the horizontal component of the compressive force of segment B (F_B, EQ 7-8). The moment at the point M is obtained according to the central angle of

strut (Equation 7-9).

$$F_{Bh} = F_B \cos\theta_c \tag{7-8}$$

$$M_{MS} = F_{Bh} \sin\theta_M R \sin\theta_M - F_{Bh} \cos\theta_M R(1-\cos\theta_M) \tag{7-9}$$

$$M_{MS} = F_{Bh} R(1-\cos\theta_M) \tag{7-9'}$$

Due to maintain the cylindrical shape, the binding force is applied. The moment at the point M_{MC} is derived as Eq 7-10.

$$M_{MC} = \int_0^{\theta_M} \left(F_{Bh} \cos\theta R \sin\theta + F_{Bh} \sin\theta R\left(1-\cos\theta\right)\right) d\theta \tag{7-10}$$

$$M_{MC} = F_{Bh} R\left(1-\cos\theta_M\right) \tag{7-10'}$$

Thus, the total moment at the point M is calculated as zero (Eq 7-11) and according to equations, the assumption was established.

$$M_M = M_{MC} + M_{MS} = 0 \tag{7-11}$$

The horizontal confining force is calculated by force equilibrium between confining and deviation forces. The deviation force caused by compressive force of strut can be obtained. Based on that, the strain of horizontal reinforcing bar is obtained as follow:

$$\varepsilon_{h-B} = \frac{1}{\rho_h E_S} \frac{t_c}{t_w} \frac{R_T}{R_C} f_B \cos\theta_c \sin\theta_c \tag{7-12}$$

In the test results, the specimens without delamination cracks, the cross-section except the cover concrete showed the same shear performance. In this case, the radius of concrete strut and wall is similar and the thickness of strut can be expressed with t_c and t_{cover} ($R_c \approx R_w$ and $t_c = t_w - t_{cover,}$ Eq 7-12').

$$\varepsilon_{h-B} = \frac{1}{\rho_h E_S}\left(1 - \frac{t_{cover}}{t_w}\right) f_B \cos\theta_c \sin\theta_c \qquad (7\text{-}12')$$

Considering the thickness of concrete cover is a very small compared to the entire wall thickness, t_{cover}/t_w can be as zero. Thus, the equation 7-12' can be expressed as simple equation.

$$\varepsilon_{h-B} = \frac{1}{\rho_h E_S} f_B \cos\theta_c \sin\theta_c \qquad (7\text{-}12'')$$

In the case of cylindrical wall with horizontal post-tensioning, the radial compressive stress due to curved post-tensioning resists the deviation force. Therefore, the horizontal reinforcing bars are not subjected to tensile force due to deviation force until radial compressive stress is offset by the deviation force and the stress is represented below.

$$f_{ph\_deviation} = \rho_{ph}\sigma_{ph}\frac{t_w}{R} \qquad (7\text{-}13)$$

However, in the case of delamination failure, it is considered that the horizontal reinforcing bars that are outside of the horizontal tendons or delamination cracks are not affected by post-tensioning (Figure 7-13). Thus, the thickness of strut is determined by the presence of delamination. For cylindrical RC walls, or cylindrical

PSC walls with cross ties, the entire wall thickness is considered as the strut thickness. On the other hand, when the delamination occurs, the stress conditions inside and outside the tendon occur differently, thus, the concrete struts inside and outside the tendon should be considered separately.

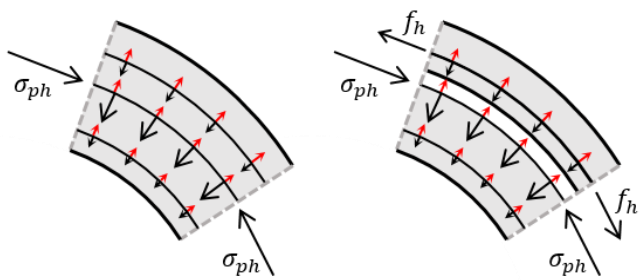

Figure 7-13 Force equilibrium of radial direction with and without delamination cracks

In this case, the compressive stress of exterior concrete strut does not increase after the exterior horizontal reinforcing bars yield. However, in the case of strut which is located interior of the horizontal tendon, due to the confining force of horizontal post-tensioning, the strength of diagonal tensile failure is increased. Then, the diagonal tensile failure mode of cylindrical wall with delamination cracks can be as follow procedure. 1) The strain of external and internal horizontal reinforcing bars increases until the external reinforcing bar yields. 2) After the external reinforcing bar yield, the compressive stress of external strut cannot be increased. Only compressive stress of the internal strut is increased. 3) If the external and internal horizontal reinforcing bars both yield, diagonal tension failure occurs. Figure 7-14 shows the procedure of internal and external horizontal reinforcing bars yielding in the cylindrical wall with delamination cracks.

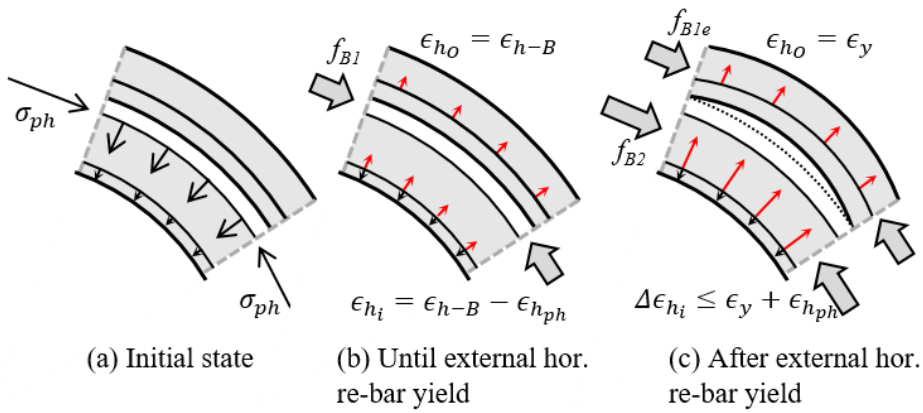

Figure 7-14 Failure procedure of cylindrical wall with delamination cracks

2) Strength degradation of concrete

The maximum principal compressive stress in the concrete was found to be a function of the strains of principal compressive and tensile directions (Eq 7-14, Vecchio and Collins 1986).

$$f_{c,\max} = f_c' \frac{1}{0.8 + 0.34\frac{\varepsilon_1}{\varepsilon_c'}} \leq f_c' \tag{7-14}$$

where $f_{c,max}$ is the maximum compressive strength considered principal tensile strain, ε_1 is a strain of principal tensile direction, and ε_c is a concrete cylinder strain corresponding to the cylinder strength f_c'. The value of ε_c can be determined approximately as Eq 7-15 (Foster and Gilbert 1996).

$$\varepsilon_c = 0.002 + 0.001\frac{f_c' - 20}{80} \quad \text{for } 20 \leq f_c' \leq 100\text{MPa} \tag{7-15}$$

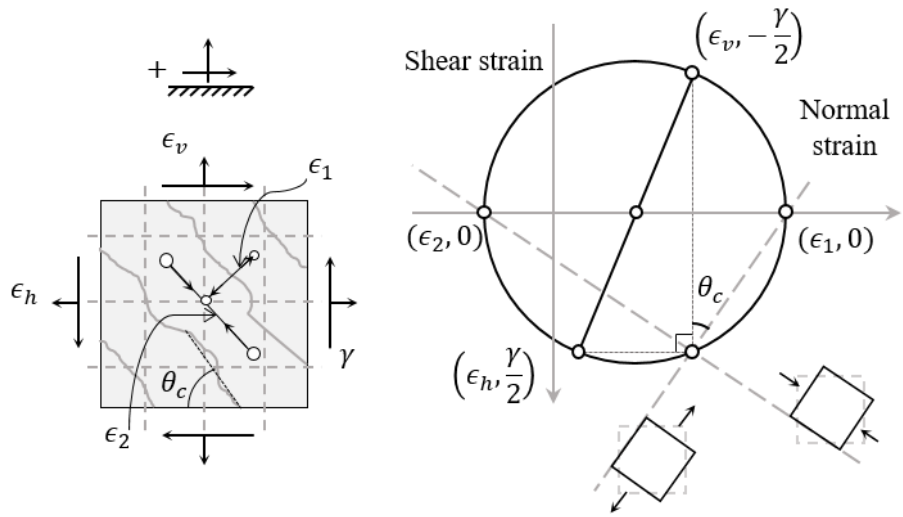

Figure 7-15 Mohr circle for strain in strut

Figure 7-15 shows Mohr circle of segment B. From the Mohr circle for strain, the relationships between strains are defined as follow Eq 7-16.

$$\varepsilon_v + \varepsilon_h = \varepsilon_1 + \varepsilon_2 \tag{7-16}$$

where ε_v and ε_h are the average strains in the vertical and horizontal directions, respectively (Positive for tension). Flexural yielding did not occur until the cylindrical wall failure occurred in the test results. Based on the measured strain of vertical reinforcing bars, the average vertical strain is assumed to be $\varepsilon_v = 0.0015 - \rho_{pv}\sigma_{pv}/E_c$. The vertical compressive stress due to vertical post-tensioning σ_{pv} affects the average vertical strain by $\rho_{pv}\sigma_{pv}/E_c$. When web-crushing occurs, the principal compressive strain ε_2 is equal to the ε_c. The average of horizontal strain ε_h can be obtained from the deviation force from the previous chapter. Thus, the maximum compressive strength can be determined by modifying equation 7-13. Figure 7-16

shows the normalized maximum concrete strength with f_c' = 40 MPa according to average horizontal strain using Eq 7-16.

$$f_{c,\max} = f_c' \frac{1}{0.8 + 0.34\left(\frac{0.0015 - \rho_{pv}\sigma_{pv}/E_c + \varepsilon_h}{\varepsilon_c'} + 1\right)} \le f_c' \qquad (7\text{-}17)$$

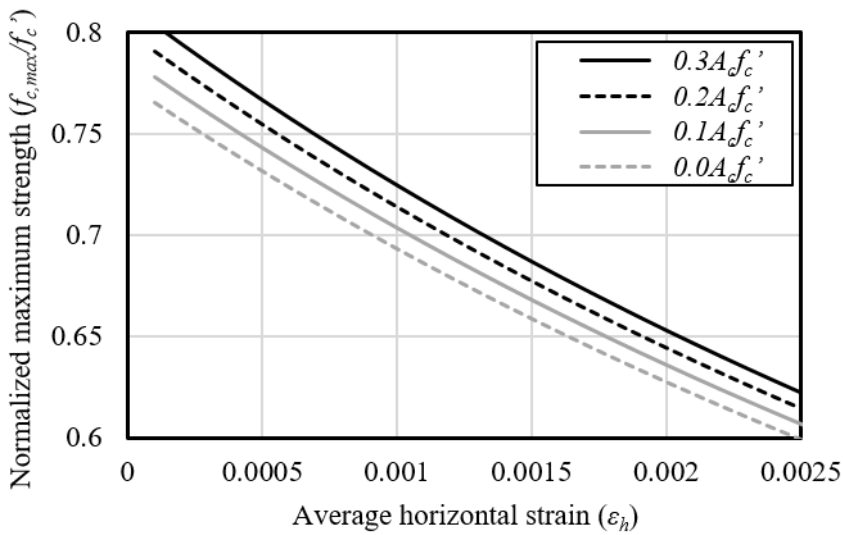

Figure 7-16 Normalized maximum concrete strength according to average horizontal strain and axial force.

3) Strength equation of strut area

Based on the strain of horizontal reinforcing bars and maximum concrete strength, the failure criteria is considered.

$$\varepsilon_{h-B} \leq \frac{f_y}{E_s} \quad \text{(Eq 7-18)}$$

$$f_B \leq f_{c,\max} \quad \text{(Eq 7-19)}$$

Due to the shape of cylindrical wall, if the strain of horizontal reinforcing bar exceeds the yield strain, the structure failure is expected because the cylindrical wall cannot maintain the shape of wall. Based on this assumption, the strength of diagonal tension failure is determined by the lateral force of horizontal reinforcing bar to yield (Eq 7-18). On the other hand, if the compressive stress of strut exceeds the maximum concrete strength, the web-crushing failure is expected (Eq 7-19). Because this strength model considers the only in-plane shear stress in cylindrical section, the process of summation is calculated by summation of shear stress vector (Figure 7-17).

The central angle at the bottom of Segment A θ_{AB} is calculated in the next chapter. The central angle of strut length θ_{BR} is obtained from Eq 7-3.

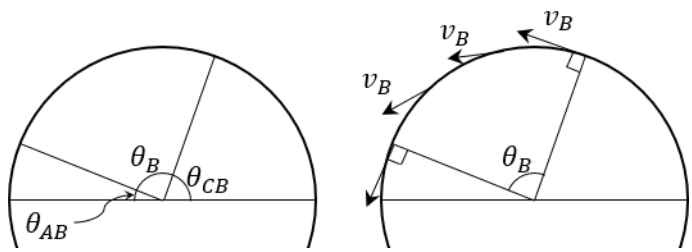

Figure 7-17 In-plane force of cylindrical wall

Equation 7-20 shows the total strength of segment B and equation 7-21 represents the shear strength using θ_{AB} and θ_{BR}.

$$F_{Bx} = 2F_{Bh} = 2t_w R \int_{\theta_{AB}}^{\theta_{AB}+\theta_B} \left(\sin\theta f_B \cos\theta_c \sin\theta_c\right) d\theta$$

$$= 2t_w R f_B \cos\theta_c \sin\theta_c \left(\cos\theta_{AB} - \cos\left(\theta_{AB} + \theta_B\right)\right) \tag{7-20}$$

$$F_{Bx} = 2t_w R f_B \cos\theta_c \sin\theta_c \left(\cos\theta_{AB} + \cos\theta_{BR}\right) \tag{7-21}$$

Figure 7-18 shows the total procedure of calculating the capacity of segment B. The segment B determined the failure of cylindrical wall under lateral loading.

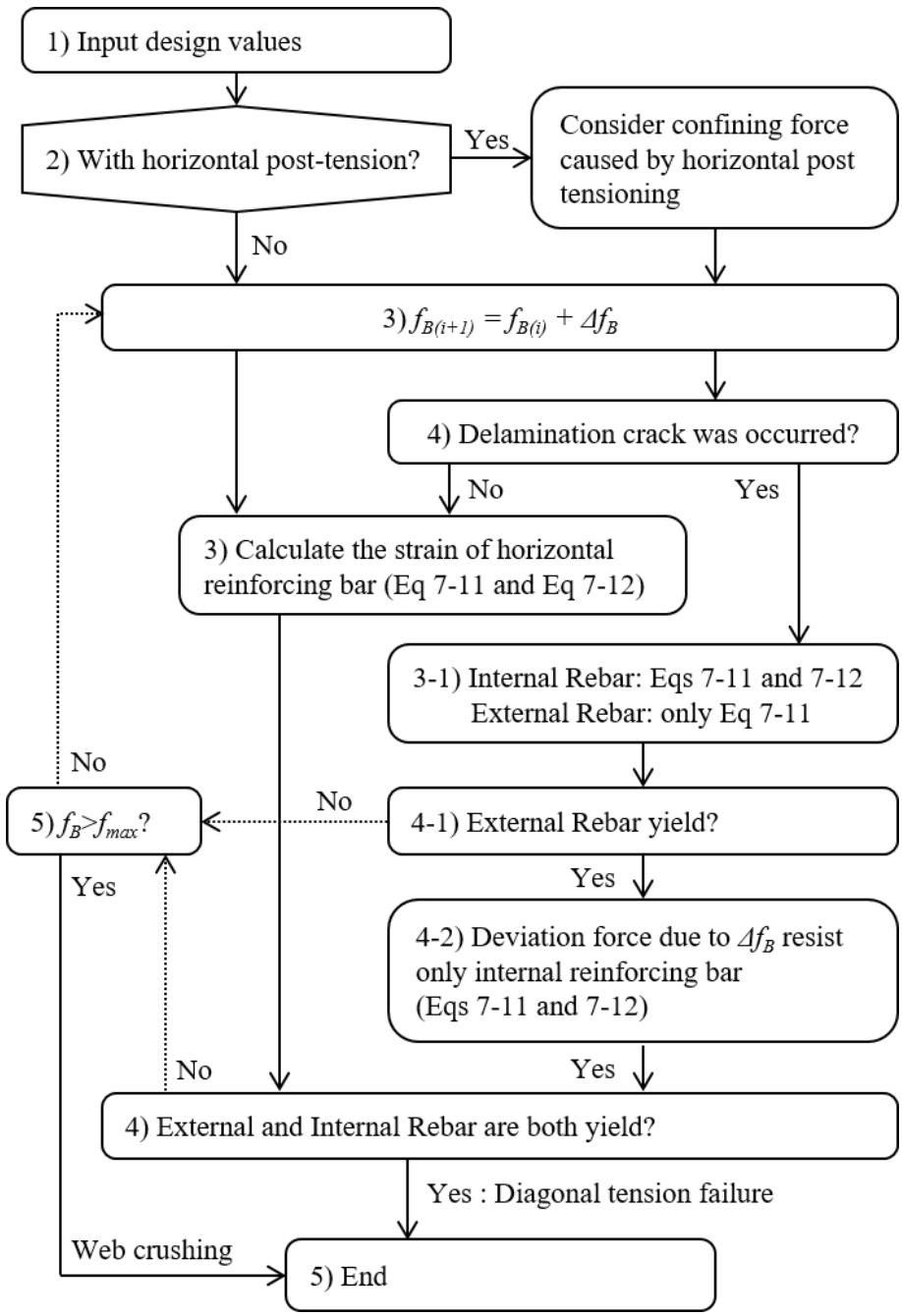

Figure 7-18 Calculating procedure of segment B

7.3.2.2 Compression area (Segment A)

The stress of vertical reinforcing bars was assumed in the previous step and the stress is applied as external loads to compression zone. Based on the vertical force equilibrium, the central angle of bottom of segment A θ_{AB} is obtained.

$$\sum F_{Ay} = \rho_v f_{v-A} t_w R\theta_{BR} - f_{Av} t_w R\theta_{AB} = 0 \tag{7-22}$$

$$\theta_{AB} = \rho_v \frac{f_{v-A}}{f_{Av}} \theta_{BR} \tag{7-23}$$

where f_{Ay} is an axial stress in the concrete at the bottom of segment A.

According to Eqs 7-4, and 7-23, the limitation of aspect ratio (h/R) that this strength model can be applied can be suggested (Eq 7-24).

$$\frac{h_w}{R} \le \pi \tan\theta_c \frac{1}{\rho_v} \frac{f_{Av}}{f_{v-A}} \tag{7-24}$$

The axial stress f_{Ay} is assumed as f_c' which is compressive strength of concrete. The stress of vertical reinforcing bar $f_{x\text{-}A}$ is equal to that of segment B $f_{x\text{-}B}$. The shear force carried by the Segment A can be estimated by multiplying F_{Ay} by a coefficient of friction μ.

$$F_{Ax} = 2\mu F_{Av} = 2\rho_v \mu t_w R\theta_{BR} f_{v-B} \tag{7-25}$$

7.3.2.3 Tension zone (Segment C)

Consider the third diagram in Figure 7-11 that represents a free body diagram of segment C. The sum of forces in the horizontal reinforcing bars in segment C is obtained based on the $f_{y\text{-}B}$. The shear resistance of the segment C (F_{Cx}) is calculated as:

$$v_c = \frac{\rho_h t_w R d\theta}{\tan\theta_c} f_{h-B} \sin\theta \tag{7-26}$$

$$F_{Cx} = \frac{\rho_h t_w R}{\tan\theta_c} f_{h-B} \int_0^{\theta_{CB}} \sin\theta d\theta = \frac{\rho_h t_w R}{\tan\theta_c} f_{h-B} \left(1-\cos\theta_{BR}\right) \tag{7-27}$$

7.3.2.4 Total shear strength

Based on Eq 7-21, 25 and 27, the maximum shear strength predicted by proposed model is as:

$$V = 2\rho_v \mu t_w R\theta_{BR} f_{v-B} + 2t_w R f_B \sin\theta_c \cos\theta_c (\cos\theta_{AB} + \cos\theta_{BR}) + 2\frac{\rho_h t_w R}{\tan\theta_c} f_{h-B}(1-\cos\theta_{BR}) \tag{7-28}$$

where θ_{BR} is $h_w/(R\times\tan\theta_C)$.

7.4 Simplified shear strength equation and application

7.4.1 Simplified shear strength

In this chapter, the proposed equation is modified according to the specific cases of actual containment and failure mode. In the case of nuclear power plant, the post-tensioning force is applied to withstand the internal pressure. In addition, the dimensions of containment are about 25 m (radius) × 50 m (height) × 1.2 m (thickness), respectively. In the simplified procedure, the delamination was not considered. In other words, the proposed model represents the shear strength of cylindrical wall with cross-tie.

The proposed equation Eq 7-28 can be modified as below with follow assumptions: 1) the cover concrete thickness can be ignored $t_c = t_w = t$; and 2) Cross-tie is installed or delamination crack is not occurs. According to these assumptions, the proposed shear strength of cylindrical squat wall (Eq 7-28) is modified as below Eq 7-29.

$$V = 2t_w R\left[\rho_v \mu\theta_{BR} f_{v-B} + f_B \sin\theta_c \cos\theta_c (\cos\theta_{AB} + \cos\theta_{BR}) + 2\frac{\rho_h}{\tan\theta_c} f_{h-B}(1-\cos\theta_{BR})\right] \tag{7-29}$$

Based on the test results, the cracked angle was 45° regardless the location in the case of cylindrical wall with aspect ratio of 1.5. In addition, based on the nonlinear finite element, the cracked angle according to aspect ratio was calculated. Figure 7-19 shows the cracked angle according to aspect ratio when concrete crushing occurred at the web area. The horizontal and vertical strains ε_h and ε_v is defined as

the average tensile deformation within the web region, and the maximum of ε_h and ε_v is obtained at web crushing failure. The cracked angle is defined based on the direction of principal tensile stress.

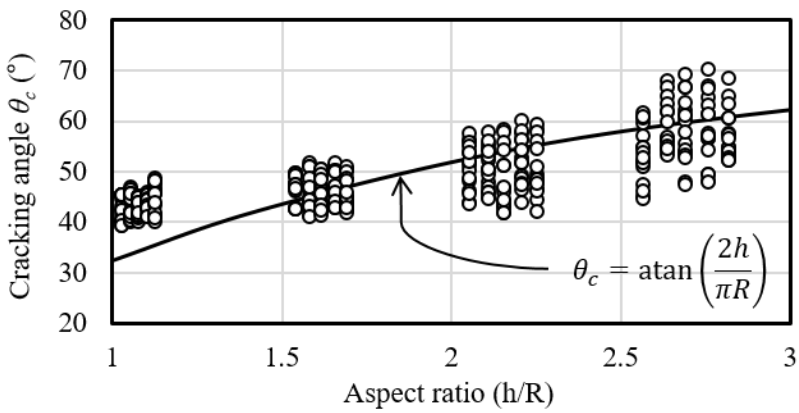

Figure 7-19 Cracking angle according to aspect ratio (h/R)

Based on the analysis results, the crack angle θ_c is assumed according to the aspect ratio. The assumed crack angle is as follows:

$$\tan\theta_c = \frac{2h_w}{\pi R} \tag{7-30}$$

This crack angle is that the strut starting from the loading point reaches the center of web. The white dashed line in the Figure 7-20 shows the assumed crack angle.

The shear strength equation 7-29 can be simplified substituting Eq 7-30 to the θ_c.

$$\frac{V}{A_{cv}} = \frac{1}{2}\rho_v \mu f_{v-B} + \frac{1}{\pi} f_B \sin\theta_c \cos\theta_c \cos\theta_{AB} + \rho_h \frac{R}{2h} f_{h-B} \tag{7-31}$$

The cracked line appeared to be greater at the end of wall when viewed from the

front.

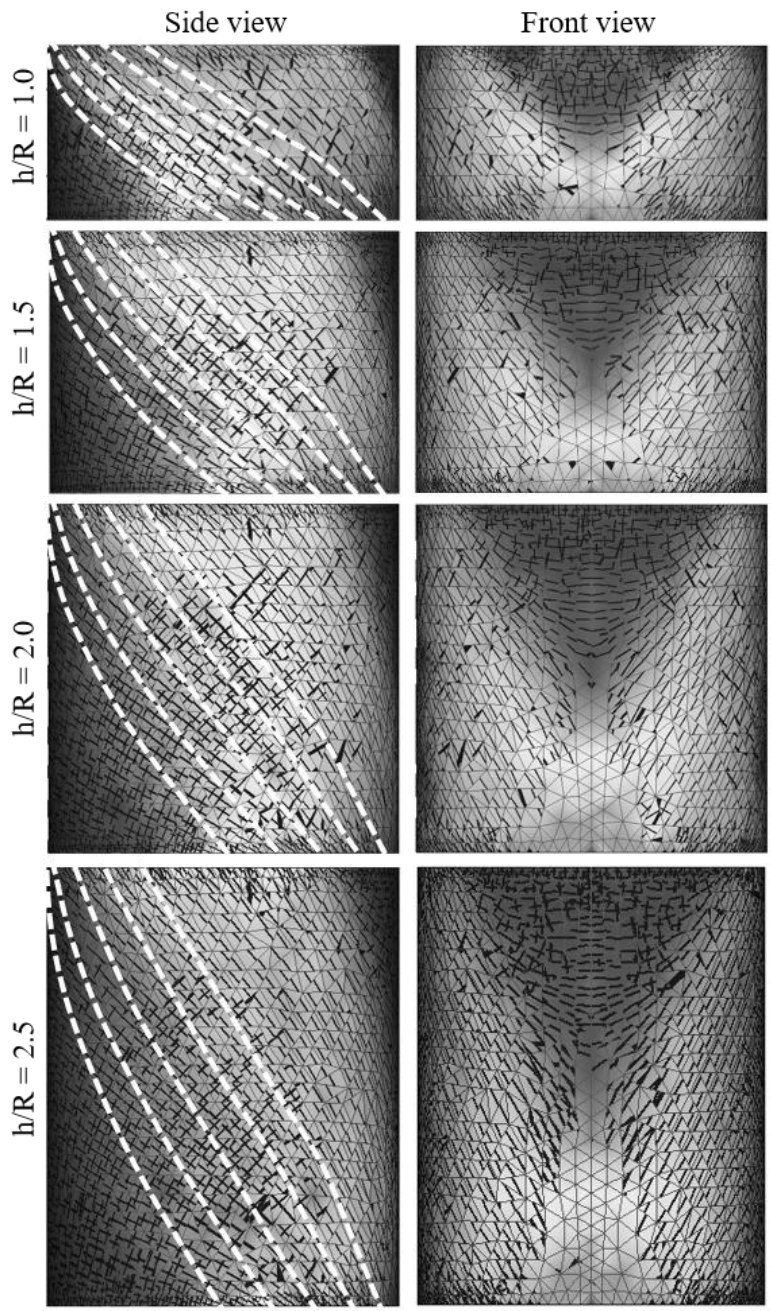

Figure 7-20 Crack propagation according to aspect ratio and assumed cracked angle (Finite element analysis)

1) Web crushing

Using the maximum compressive strength degradation of concrete (Eq 7-14), the horizontal strain (Eq 7-12) and assumed vertical strain, the maximum compressive strength with considering principal tensile stress can be derived as below equation.

$$f_{c,\max}=\frac{-\left(\frac{1.14}{0.34}\varepsilon_c+0.0015-\frac{\rho_{ph}}{E_s\rho_h}\sigma_{ph}-\frac{\rho_{pv}}{E_c}\sigma_{pv}\right)+\sqrt{\left(\frac{1.14}{0.34}\varepsilon_c+0.0015-\frac{\rho_{ph}}{E_s\rho_h}\sigma_{ph}-\frac{\rho_{pv}}{E_c}\sigma_{pv}\right)^2+2\frac{\varepsilon_c f_c'}{0.34}\frac{1}{E_s\rho_h}}}{\frac{1}{E_s\rho_h}}\le f_c' \tag{7-32}$$

By substituting the determined constant values (ε_c = 0.00225, E_s = 205000, and E_c = 29000), the Eq 7-32 can be modified with κ, ρ_h and f_c':

$$f_{c,\max}=-\kappa+\sqrt{\kappa^2+2713.235\rho_h f_c'} \tag{7-32'}$$

where, $\kappa=(1851.544-7.069\rho_{pv}\sigma_{pv})\rho_h-\rho_{ph}\sigma_{ph}$.

In the case of reinforced concrete without post-tensioning, κ is $1751\rho_h$ and $f_{c,max}$ can be simplified as the Eq 7-33. The simplified equation focused on the range $0.0001\le\rho_h/f_c'\le0.0005$. Figure 7-21 shows the comparison results of actual and simplified maximum concrete strengths according to the ratio of horizontal reinforcing bar ratio to concrete compressive strength. The simplified equation was obtained empirically.

$$\frac{f_{c,\max}}{f_c'} = 0.2 + 17.5\sqrt{\frac{\rho_h}{f_c'}} \le 1 \tag{7-33}$$

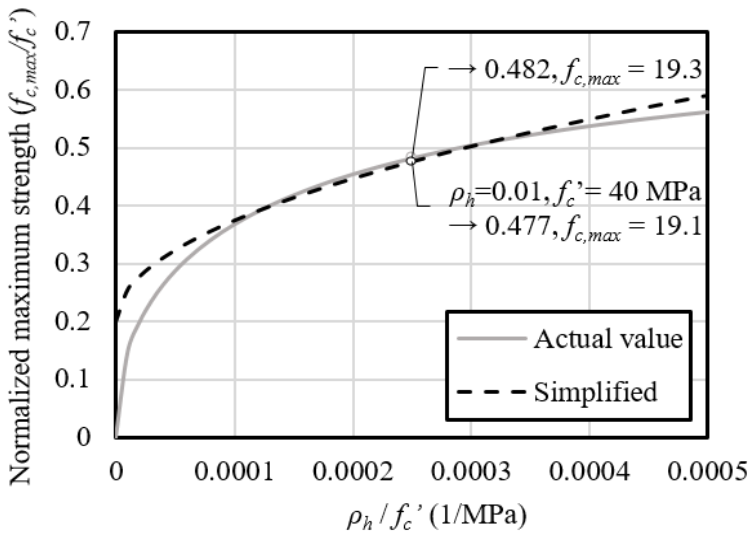

Figure 7-21 Maximum compressive strength of reinforced concrete without post-tensioning

In the case of cylindrical wall with post-tensioning, the variable κ is determined according to vertical and horizontal post-tensioning and horizontal reinforcing bar ratio. Figure 7-22 (a) shows the relationship between κ and vertical and horizontal post-tensioning according to ratio of horizontal reinforcing bars. Figure 7-22 (b) shows the example of maximum compressive strength considering the tensile principal strain with f_c' = 40 MPa.

According to the figure, the vertical post-tensioning force (Dashed or Bold) did not significantly affect the maximum compressive strength. Therefore, based on equation 7-33 for the cylindrical wall without post-tensioning, the modified equation

(7-33') for post-tensioning structures is derived with a term of horizontal post-tension.

$$\frac{f_{c,\max}}{f_c'} = 0.2 + 17.5\sqrt{\frac{\rho_h}{f_c'}} + \left(\frac{\rho_{ph}\sigma_{ph}}{f_c'}\right)\left(1.4 - 45\sqrt{\frac{\rho_h}{f_c'}}\right) \le 1 \qquad (7\text{-}33')$$

Figure 7-23 shows the comparison results of exact and simplified maximum compressive strength with considering tensile principal strain.

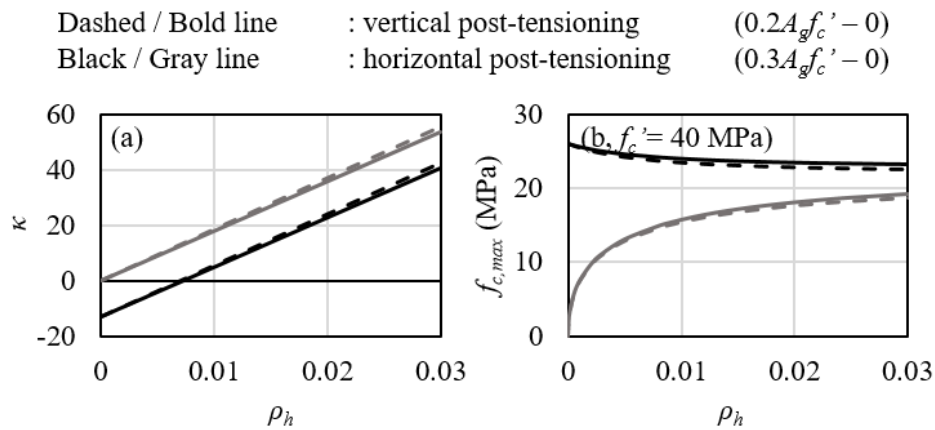

Figure 7-22 Maximum compressive strength and horizontal reinforcing bar ratio relationships of cylindrical wall with various post-tensioning forces

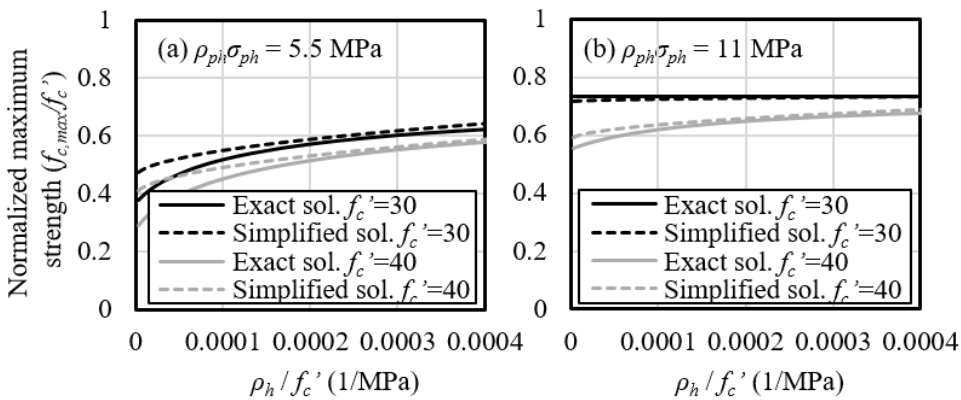

Figure 7-23 Maximum compressive strength of reinforced concrete with post-tensioning

The web-crushing failure occurs when the compressive strength of concrete strut reach to the Eq 7-33'. In addition, the $f_{h\text{-}B}$ is derived as Eq 7-34 using the Eqs 7-12 and 7-13.

$$\rho_h f_{h-B} = f_B \cos\theta_c \sin\theta_c - \rho_{ph}\sigma_{ph} \tag{7-34}$$

The equation 7-35 can be derived by combining Eqs 7-31, and 7-34, and the cosine function "$cos\,\theta_{AB}$" in Eq 7-31 is closed to 1.

$$V = A_{cv}\left[\rho_v \mu \frac{1}{2}\beta f_y + f_B \sin\theta_c \cos\theta_c\left(\frac{1}{\pi}+\frac{R}{2h_w}\right) - \frac{R}{2h_w}\rho_{ph}\sigma_{ph}\right] \tag{7-35}$$

where A_{cv} is a gross section of cylindrical wall ($A_{cv} = 2\pi rt$), and β is a factor of the ratio of tensile stress to yield stress of vertical reinforcing bar ($f_{v\text{-}B}/f_y$). In the case of squat cylindrical wall in this dissertation, the factor β is assumed as (0.0015-$\rho_{pv}\sigma_{pv}/E_c$)/0.0023.

According to Eq 7-35, the concrete crushing strength considering tensile strain can be calculated. Based on that, the web crushing strength of cylindrical wall Eq 7-36 can be derived by substituting Eq 7-33' to Eq 7-35.

$$V_{wc} = \frac{A_{cv}}{\gamma}\left[0.2 f_c' + 17.5\sqrt{\rho_h f_c'} + \rho_{ph}\sigma_{ph}\left(1.4 - 45\sqrt{\rho_h / f_c'}\right)\right] + A_{cv}\left(\rho_v \mu \frac{1}{2}\beta f_y - \frac{R}{2h_w}\rho_{ph}\sigma_{ph}\right) \tag{7-36}$$

where γ is a factor $= \sin\theta_c \cos\theta_c\left(\frac{1}{\pi}+\frac{R}{2h_w}\right)$ and Figure 7-24 shows the value of γ according to aspect ratio ($h/2R$). This shear strength model is not suitable for

cylindrical walls with high aspect ratio (*h/2R*), thus, this equation is limited to the aspect ratio of 2 (*h/2R* < 2). In addition, the factor γ related to aspect ratio can be simplified as follow.

$$\gamma = 3\left(\frac{h_w}{2R}\right) + 0.6 \qquad \text{for} \quad 0.7 \le \frac{h_w}{2R} \le 2.0$$

$$\gamma = 2.7 \qquad \text{for} \quad \frac{h_w}{2R} \le 0.7$$

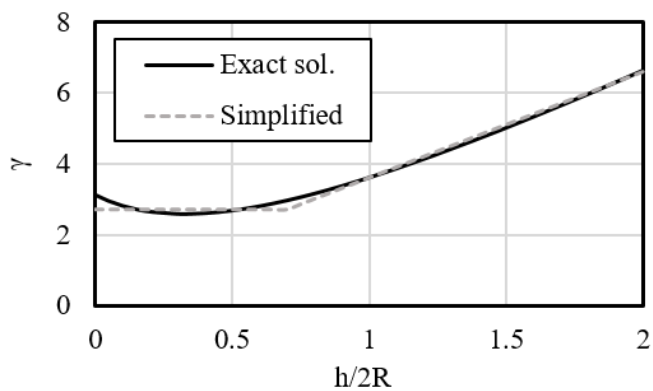

Figure 7-24 Relation of γ and aspect ratio (h/R)

2) Diagonal tension failure

On the other hand, in the case of diagonal tension failure, when the strain of horizontal reinforcing bars is exceeded the yield strain, the shear failure is occurred without maintaining the cylindrical shape. In that case, the $f_{y\text{-}B}$ is equal to the yield stress of reinforcing bar f_y. At that time, the strut force f_B is as $(\rho_h f_y + \rho_{ph}\sigma_{ph})/cos\theta_c sin\theta_c$.

The diagonal tension strength of squat cylindrical wall is derived as Eq 7-37.

$$V_{DT} = A_{cv}\left[\rho_v \mu \frac{1}{2}\beta f_y + \rho_h f_y \left(\frac{1}{\pi} + \frac{R}{2h_w}\right) + \rho_{ph}\sigma_{ph}\frac{1}{\pi}\right] \quad (7\text{-}37)$$

From the assumption, the strain of vertical reinforcing bar was determined as the factor β = (0.0015-$\sigma_{pv}\rho_{pv}/E_c$)/0.0023 without considering the flexural or shear deformation, which is related to the aspect ratio or reinforcing, bar ratio. Thus, the proposed equation has a lower accuracy at the cylindrical wall with a high aspect ratio or low reinforcing bar ratios.

In addition, for cylindrical walls with a high aspect ratio, the factor of tensile stress of the vertical reinforcing bar at failure β can be assumed as 1.0. The diagonal tensile strength equation can be simplified as follow:

$$V_{DT} \approx 2t_w R\left[\left(0.5\rho_v \mu + \rho_h\right) f_y + \rho_{ph}\sigma_{ph}\right] + A_{cv}\rho_h f_y \frac{R}{2h_w} \quad (7\text{-}38)$$

In this case, the additional effect due to low aspect ratio is only due to the horizontal reinforcing bar, and the effect is decreased as aspect ratio is increased.

The horizontal post-tensioning ($\rho_{ph}\sigma_{ph}$) increased the web-crushing and diagonal tension strength of cylindrical walls. The radial stress generated by horizontal post-tensioning acted as an additional confining force. Therefore, the strain of horizontal reinforcing bar was decreased. As a result, the shear capacity of cylindrical wall with horizontal post-tensioning was increased.

7.4.2 Application to current code

In the case of containment building, various load cases are used and opening or hatches are located in the wall. However, the proposed model is a method based on an ideal cylindrical wall. Thus, to apply the confining force, there should be a method to reflect the confining force in the current design or evaluation codes. In this section, based on the proposed and simplified equation, the method to apply existing evaluation or design code is introduced.

On the other hand, in the evaluation code of EPRI, the seismic safety of cylindrical wall is evaluated based on average shear stress. The basic equation is as follows:

$$V_{n-EPRI} = v_{n-EPRI} \frac{A_{cv}}{\alpha}$$

where α is a factor according to aspect ratio.

$$\alpha = \frac{2}{3}\frac{h_w}{2R} + \frac{5}{3} \qquad \text{for} \quad 0.5 \le \frac{h_w}{2R} \le 1.25$$

$$\alpha = 2 \text{ or } 2.5 \qquad \text{for} \quad \frac{h_w}{2R} = 0.5 \text{ or } 1.25 \text{, respectively}$$

The form of effective area factor α is similar to γ in the proposed equation. On the other hand, the mechanism of EPRI evaluation is not considered the compressive area or tensile area (Segment A or B in the proposed shear strength model). Therefore, the terms related to segments A and C in the Eq 7-36 should be ignored. To be applied to the EPRI equation form, the proposed shear strength equation in the previous

chapter can be modified as Eq 7-39.

$$V_{wc}' = \frac{A_c}{\gamma}\left[0.2 f_c' + 17.5\sqrt{\rho_h f_c'} + \rho_{ph}\sigma_{ph}\left(1.4 - 45\sqrt{\rho_h f_c'}\right)\right]$$

$$\approx \frac{A_c}{\alpha}\varphi\left[0.2 f_c' + 17.5\sqrt{\rho_h f_c'} + \rho_{ph}\sigma_{ph}\left(1.4 - 45\sqrt{\rho_h f_c'}\right)\right] \quad (7\text{-}39)$$

$$\varphi = \min\left(0.75, -0.24\frac{h_w}{2R} + 0.87\right) \qquad \text{for } \frac{h_w}{2R} \le 2$$

In the above equation, φ replaced with the effective cross-section coefficient α and γ. Therefore, the proposed web-crushing equation for EPRI method is modified with φ. Figure 7-25 shows the comparison results of φ and α/γ according to aspect ratio (h/R).

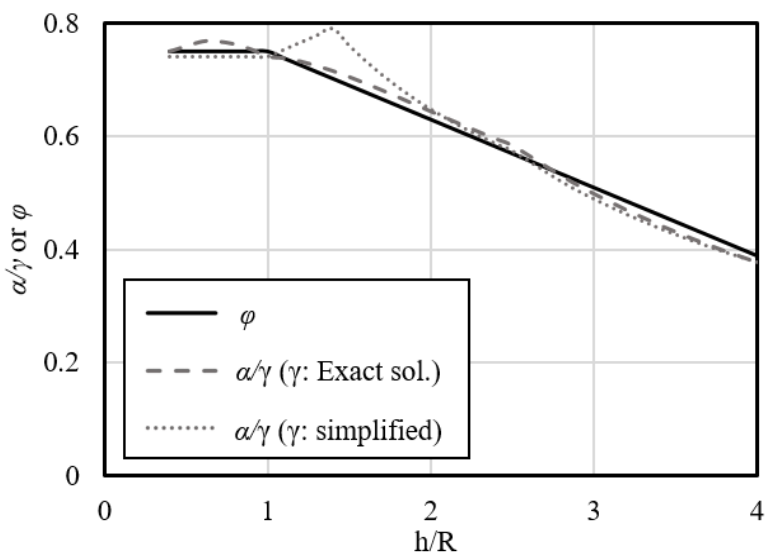

Figure 7-25 Comparison of φ and α/γ

Based on above procedure, the web-crushing strength can be proposed for EPRI.

$$v_{wc,EPRI} \approx \varphi\left[0.2 f_c' + 17.5\sqrt{\rho_h f_c'} + \rho_{ph}\sigma_{ph}\left(1.4 - 45\sqrt{\rho_h f_c'}\right)\right] \quad (7\text{-}40)$$

7.5 Verification

1) Proposed equation

To verify the proposed equation in the chapter 7-3, the maximum tested strength was compared. The comparison result was presented in Figure 7-26. In the figure, the y-axis and x-axis represent the predicted strength using proposed equation and the maximum strength from test or finite element analysis, respectively. The mean values of V_{pre}/V_{test} and $V_{pre}/V_{anaylsis}$ were 1.01 and 0.99, respectively. The standard deviations were 0.11 and 0.22 for the ratio of V_{pre}/V_{test} and $V_{pre}/V_{anaylsis}$, respectively. The ratio of prediction and test was ranged from 0.84 to 1.20 and that of prediction and finite element analysis was from 1.88 to 0.55. The FE analysis model was included the low reinforcing bar ratio and high aspect ratio, which was not suitable for proposed strength model. This is why the variation was greater in the case of analysis.

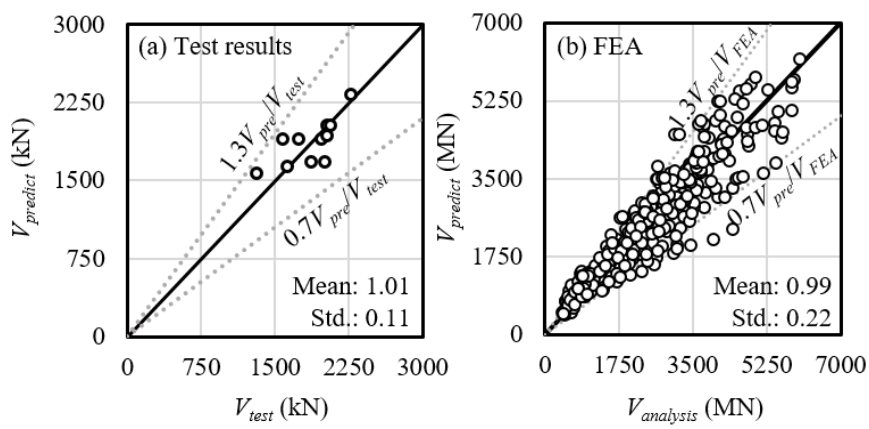

Figure 7-26 Comparison of shear strength by proposed equation and test or FEA.

In addition, the simplified equation was proposed in Chapter 7.4.1. The comparison results using the simplified equation was shown in Figure 7-27.

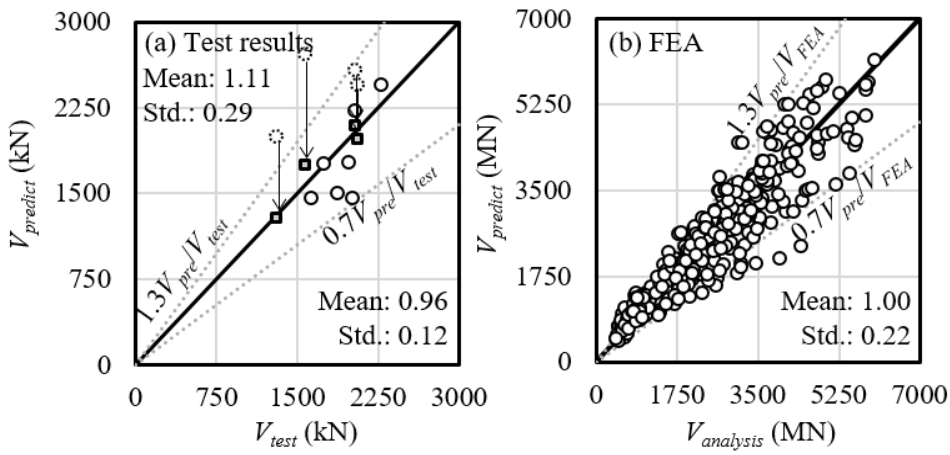

Figure 7-27 Comparison of shear strength by simplified equation and test or FEA.

The simplified model predicted the test strength to be 4 % lower with large standard deviation of 0.23. However, in the case of simplified model, the strength degradation due to delamination crack was not considered. Therefore, the simplified model overestimated in such case (dotted circular marks). Because the delamination crack caused premature concrete cover failure, to reflect the strength degradation, the cross-sectional information excluding the concrete cover was used. The rectangular marks were represented the improved strength prediction considering delamination cracks. On the other hand, in the case of the finite element analysis results without delamination cracks, the simplified equation predicted the results as an average of 1.0 and standard deviation of 0.22.

2) The current design or evaluation codes with binding force

In Chapter 7.4.2, the proposed web-crushing strength was modified to apply to the cylindrical wall seismic strength evaluation using the method of EPRI. The test and analysis results were compared original and proposed equation and Figure 7-28 shows the results. The EPRI evaluation equation predicted the finite element analysis strength as an average of 1.07 and a standard deviation of 0.26. However, the web-crushing strength cannot reflect the effect of post-tensioning forces and characteristic of cylindrical shape. To improve these problems, the proposed web-crushing strength was applied. Figure 7-28 (b) shows the results of with simplified proposed web-crushing strength. The proposed equation predicted the finite analysis as an average of 0.9 and a standard deviation of 0.2. The average accuracy of the proposed equation was lower than the original equation; however, the standard deviation was 25 % less than that of the original equation.

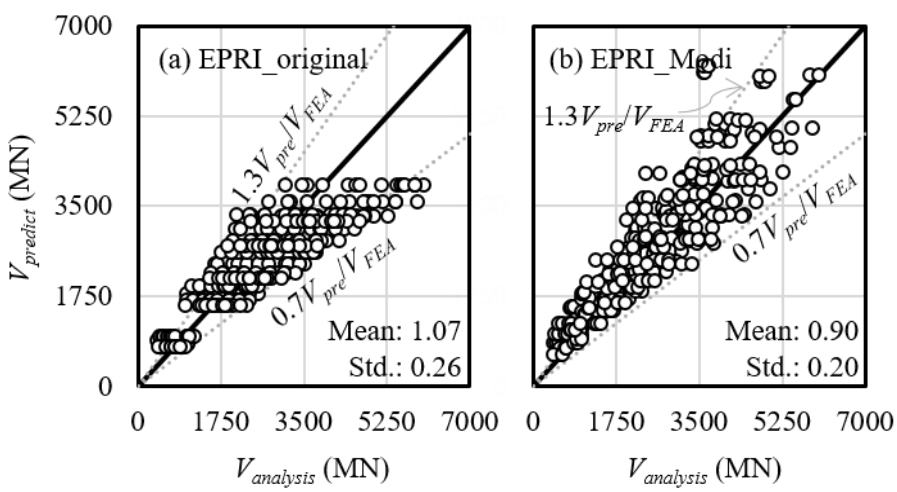

Figure 7-28 Comparison of shear strength by original and proposed EPRI equation and test or FEA.

3) Parameter study

To investigate the effect of parameters on shear strength, additional analysis was conducted using FEA results. Figure 7-29 and Figure 7-30 show the comparison results. The effect of aspect ratio (h_w/R) and horizontal post-tensioning was shown in Figure 7-29. In the proposed equation, the maximum shear strength decreased as the aspect ratio increased. The effect of aspect ratio is expressed by the γ of the proposed equation and the effect acts more critically to web-crushing than the diagonal tensile strength. Therefore, as the aspect ratio increased, the expected failure mode changed from diagonal tensile to web crushing. The change in the failure mode appeared at a low aspect ratio when the vertical and horizontal reinforcing bar ratios were high.

The horizontal post-tensioning increased the maximum shear strength of cylindrical wall (Figure 7-29). The effect of horizontal post-tensioning increased the confining force and reduced the average strain of horizontal direction. Thus, the expected strengths of web-crushing and diagonal tension were improved due to the decrease in the strain of horizontal reinforcing bars.

Figure 7-30 shows the effect of horizontal reinforcing bar ratios on the shear strength of cylindrical wall. The x-axis represents the horizontal reinforcing bar ratio. The solid and dashed line represent the predicted shear strength of cylindrical walls with the vertical reinforcing bar ratio of 1.86 % and 0.93 %, respectively. When the aspect ratio was low, the error was greater than when the aspect ratio was high. The reason is that the error in the case of aspect ratio in the process of simplifying the equation about γ. In addition, the assumed cracked angle did not accurately predict the case with very low aspect ratio.

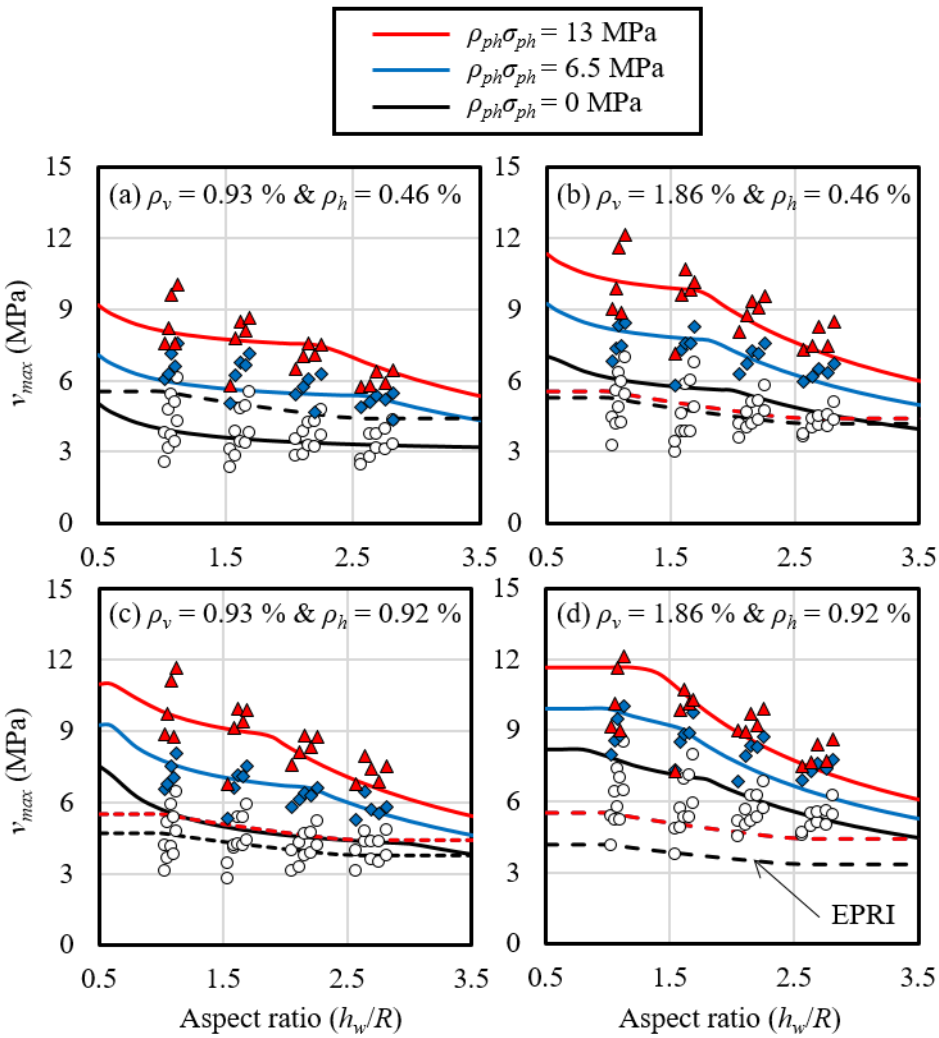

Figure 7-29 Predicted and FEA strength according to aspect ratio (h_w/R)

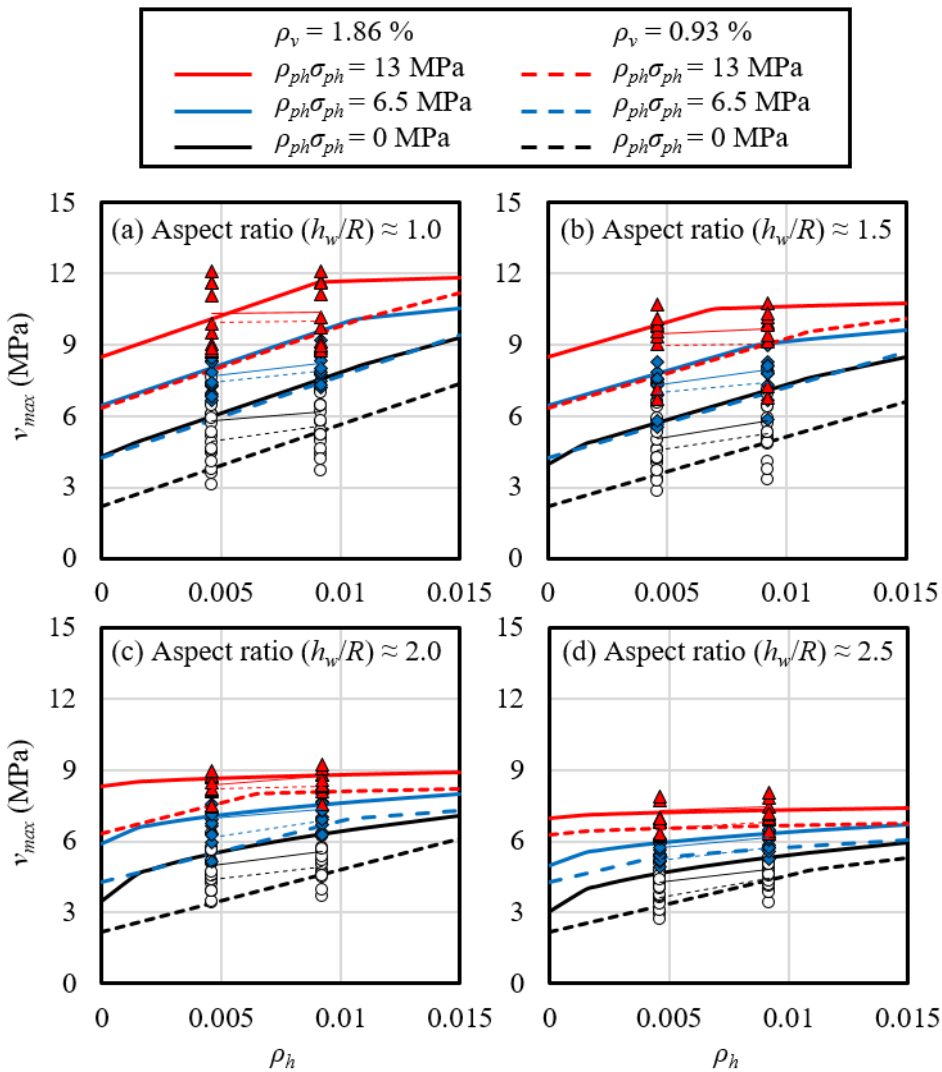

Figure 7-30 Predicted and FEA strength according to horizontal reinforcing bar ratio (ρ_h)

4) Verification with previous test results

To verify the proposed equation, the results of previous cylindrical wall test were compared. The database is summarized in Appendix A. Figure 7-31 shows the comparison results. Since the number of cylindrical wall test under horizontal loading was few, the results of shaking table, torsional loading were included. To calculate the torsional strength of wall, the cylindrical wall was assumed to be consist of only segment B, and the total torsional strength of cylindrical wall was calculated as $A_g f_B$.

The average and standard deviation values of $V_{test}/V_{predict}$ were 1.03 and 0.62, respectively. Except for the test results with flexural yield of vertical reinforcing bars and high aspect ratio, the values were 0.95 and 0.17 for average and standard deviation, respectively.

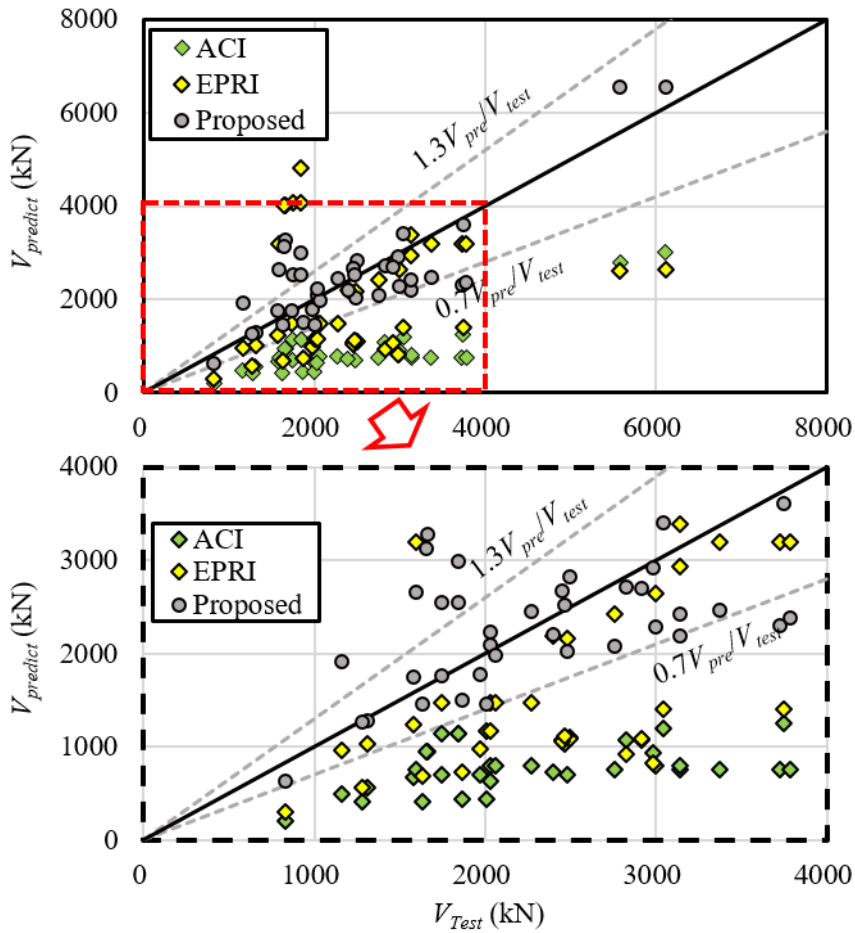

Figure 7-31 Comparison of shear strength by proposed equation and previous test

7.6 Summary

In this chapter, the equation for shear strength prediction of cylindrical post-tensioning wall was proposed based on force equilibrium. Based on the equation, the simplified model and the method to apply the proposed equation to EPRI strength equation was presented. Lastly, for the verification of the model, the test results and finite element analysis results were compared with proposed equations. The major conclusion drawn are summarized as follows:

1) The shear strength model for post-tensioning cylindrical wall was proposed using the force equilibrium and the deviation concept. To reflect the characteristic of cylindrical wall, the confining force to maintain the shape was applied. Based on that, the prediction of cylindrical wall was conducted.

2) The web crushing strength considering the cylindrical shape and post-tensioning force was proposed. To derived the web crushing strength of cylindrical wall, the principal tensile strength was calculated and using the strength degradation equation. The basic equation of concrete strength degradation was used previous research. In addition, the modified web crushing equation for EPRI was proposed.

The proposed model was compared with test and finite analysis results. The verification was conducted FEA analysis, own experimental results in this dissertation, however only few database performed by previous researchers was used to verify the proposed strength.

Chapter 8. Conclusion

8.1 Summary

In this dissertation, to develop the seismic evaluation of nuclear power plant, experimental, theoretical and analytical researches were conducted. The shear equation for reinforced or post-tensioned cylindrical squat wall and design recommendations were proposed. The researches was conducted to investigate the effect of wall shapes and post-tensioning on shear strength. Based on the test results, the shear strength model were developed. The conclusions of this dissertation were summarized as follows:

1. Loading rate

To investigate the effect of loading rate on reinforced concrete wall, dynamic and shaking table test were conducted. The major findings are summarized as below:

1) In the reinforced concrete wall under high loading rate, initial cracks were occurred in lower drift ratio and the maximum strengths were increased by 9.9 to 12.2 %, 4.0 to 17.5 %, and 4.9 to 5.6 % in flexural yielding, shear, and shear-friction failure mode specimens, respectively.

2) In the case of shaking table test, the maximum measured overturning moment were 1.08 and 1.13 times greater than the static analysis results for the

specimens with aspect ratios of 1.0 and 2.0, respectively.

3) In the case of cylindrical wall, the maximum tested strengths were increased by from 2% to 30% compared to the other reinforced concrete specimen with low loading rate.

4) The loading rate effect was verified based on test results. To applying the effect of loading rate on evaluation of reinforced concrete, the DIFs were suggested even if the effect of loading rate is low and the prediction using DIFs improved the accuracy of strength prediction of reinforced concrete wall.

2. Characteristic of cylindrical wall

To investigate the shear strength of cylindrical wall, cylindrical and semi-cylindrical reinforced concrete wall was prepared and cyclic loading test were conducted. In addition, the finite element analysis of cylindrical wall was conducted. The major findings are summarized as below:

1) The failure mode of interior and exterior surfaces were different in the cylindrical wall. In the case of interior surface, the concrete crushing was occurred with horizontal cracks. On the other hand, in the outer surface, diagonal cracks with great crack width were occurred, except the specimens with the crosstie.

2) In case of the cylindrical wall with horizontal post-tensioning, the shear strength was increased. However, the 100 % of horizontal post-tensioning force can cause the internal cracks. Through concrete core boring of tested

specimens, the internal crack due to horizontal post-tensioning was observed. To prevent to occur this internal crack, crosstie was installed, and the effect of crosstie was confirmed.

3) The additional moment at the boundary of cylindrical wall caused by the horizontal post-tensioning force was investigated using theoretical and analytical studies. The vertical reinforcing bars at the lower part were applied tensile stress without vertical post-tensioning. The initial local moment caused the premature reinforcing bar yielding under lateral loading, such as seismic, hurricane forces.

4) In the case of cylindrical wall, the deviation force was occurred under lateral loading. To resist the deviation force, the confining force was required, and the tensile strain of horizontal reinforcing bar was increased. In addition, the radial compressive stress due to horizontal reinforcing bars can contribute to the confining force.

3. Shear strength model for cylindrical wall

Based on the test and analysis results, the effect of cylindrical shape on the shear strength were investigated. The shear strength model was developed considering the shear failure mechanisms, binding forces, and web crushing. The major findings are as follows:

1) When the deviation force was exceeded the capacity of confining force of cylindrical wall, the diagonal tensile failure was expected. If the confining

force was sufficiently to maintain the cylindrical shape, the concrete crushing was expected.

2) Based on the failure mode, the shear strength prediction model for cylindrical squat wall was proposed. The cylindrical wall was categorized as three parts: compressive, strut, and tensile zone. The strut area was determined the strength of cylindrical wall. The tensile strain of horizontal reinforcing bars was calculated based on the concept of confining force. Based on this model, shear strength equation for web crushing and diagonal tension of cylindrical wall was proposed.

3) To application of the proposed model, the simplified equation was derived and web-crushing strength for EPRI was proposed. For verification, the proposed model was compared to the test and analysis results. As a result, the proposed prediction shows low covariance with the test and analysis results.

8.2 Recommendations for design and evaluation of NPP wall structures

In this chapter, based on the experimental and theoretical study of cylindrical wall, the design or evaluation recommendations for nuclear power plant buildings, especially containment building is proposed.

8.2.1 Loading rate effect

The current evaluation codes were derived based on the results of structural experiment under static loading rate. However, when an earthquake with high-frequency contents occurs, the loading rate on the structure is expected as high. The DIFs can be used to eliminate conservatism when evaluating seismic performance. Therefore, it is important to evaluate the structure using the expected loading rate in the event of an earthquake. According to previous researches and Chapter 3, the effect of loading rate effect was verified in the seismic load.

Based on the experiment results, the loading rate caused by earthquakes did not change the failure mode of the concrete structure, but the number of cracks were decreased and the width of cracks were increased. The width of cracks can effect on the intensity capacity of containment building. In addition, the maximum strengths were increased. Thus, the flow chart of applying the loading rate effect to the structure is shown in Figure 8-1 and the details of each step is as below.

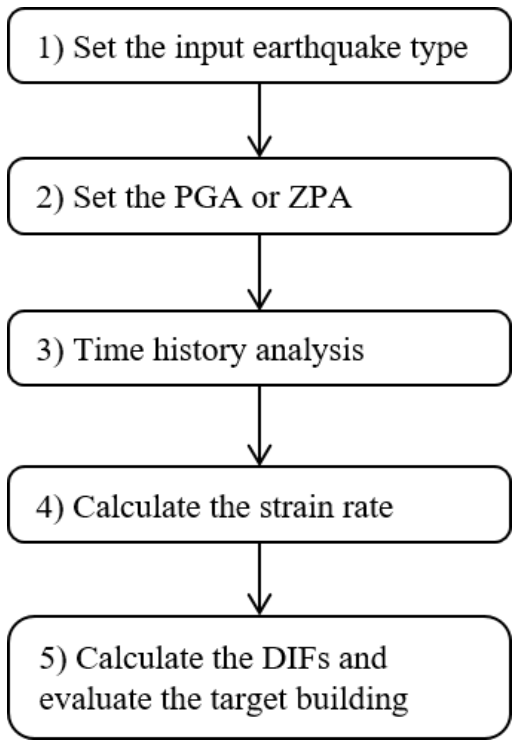

Figure 8-1 Flow chart for applying the effect of loading rate

1) Set the input earthquake type

According to the site of the nuclear power plant or purpose of evaluation, the input earthquake is selected. The characteristics of earthquake (i.e. high-frequency contents, strong motion duration) are reflected in this process. Because the dynamic amplification depends on the type of input ground motion, and the characteristics of the structure (the natural frequency), the velocity of deformation for calculating the DIFs are determined according to the input earthquake type.

2) Set the PGA or ZPA

For seismic evaluation of nuclear power plant building, the seismic probabilistic risk assessment is conducted. The seismic probabilistic risk assessment is a method of calculating the probability of core damage frequency (CDF) of a nuclear power plant according to PGA of input ground acceleration. Various magnitudes of input earthquakes are required for evaluation. Therefore, the magnitude of input ground motion should be considered.

3) Time history analysis

The elastic time history analysis should be performed. In the strain rate level of earthquakes, the effect of loading rate on stiffness is small. The stiffness in the criteria can be used. Based on the results of time history analysis, the velocity of deformation of each component of the structure can be derived.

4) Calculate the strain rate

The expected loading rate in an earthquake is calculated through the results of time history analysis. The loading rate is obtained by differentiating the strain history graph. The strain records for calculating strain rate or DIFs should be used as the value from the measured area that affects the expected failure mode of the member. For example, the strain rate of vertical reinforcing bars is considered for flexural yielding. Although the loading rate continues to change during the seismic load, the maximum value during the total time history should be considered. Generally, the effect of the strain rate at the maximum deformation is expected large, however, the rate of strain at the maximum drift ratio is close to zero, and that at the point of zero displacements is calculated as maximum. According the Chen et al (2020), the

loading rate effect was determined by the maximum value. Thus, the maximum strain rate is determined the DIFs.

5) Calculate the DIFs and evaluate the target building

The effect of loading rate on maximums strength can be reflected using DIFs. In the Chapter 6-2, the DIF models proposed by Li and Li (2012), and Kulkami and Shah (1998) for reinforcing bars and concrete, respectively were used. However, in this dissertation, the proposal of DIF model was not within the scope.

Because the effect of loading rate depends on the PGA, response spectrum of earthquake and locations of member, the loading rate effect should be considered during the evaluation. In addition, for conservative design, the effect of loading rate should only be considered during the evaluation.

In addition, the other simple method for determining the loading rate is based on eigenvalue analysis. The process is as follows: 1) Eigenvalue analysis of cracked and un-cracked models. 2) Identification of fundamental frequencies. 3) Calculate pseudo-velocity based on the spectral acceleration. In this case, the pseudo-velocity can represent the loading rate.

8.2.2 Delamination due to horizontal post-tensioning

Due to the curved shape of the horizontal post-tensioning, the tensile stress in radial direction occur in the cross section of the concrete. In the current researches, the internal cracks due to the post-tensioning forces with single curvature was observed (Florida Power and Light Company (1970), Florida Power and Light Company (1976), and Basu et al. (2001)). In addition, Choi (2018) reported that radial stress occurred when horizontal post-tensioning was applied to a cylindrical wall such as a containment and the internal cracks were initiated at the 0.13 to 0.23 f_c' of tensile radial stress which was lower than the design tensile stress (0.35 f_c').

If the internal cracks were not occurred, the effective thickness of wall can be set to the overall thickness. However, when the internal cracks were occurred, the external cover concrete cannot resist even a small deformation. Therefore, if there is no radial reinforcement in the cylindrical wall, the concrete cover should be excluded when calculating the strength of cross-section. On the outside of the tendon layer, if the crosstie is not existed, the effect of horizontal post-tensioning is transferred to external cross-section of the horizontal tendon.

If the crossties are installed, even if the internal cracks occurred, the crosstie transfers the binding force to the exterior horizontal reinforcing bars. Overall thickness of containment wall can be used if crossties are installed according to ACI 359 (The spacing of the radial reinforcement as defined in ACI 359 CC3545 is half of the wall thickness or 600 mm.).

8.2.3 Bending moment due to horizontal post-tensioning

In the case of horizontal post-tensioning force with curved section, radial stress was expected. If the boundary condition of cylindrical wall is restricted or fixed, the moment can be generated in the bottom of wall and that can be calculated using Eq 6-1.

A cross-sectional analysis of the bottom area of the cylindrical wall with the horizontal post-tensioning should be performed with considering the additional moment.

On the other hand, the effect of vertical post-tensioning was ignored in this procedure. The additional moment was calculated based on the central deformation (reduction of radius) of cylindrical wall. Because the vertical post-tensioning had lower effect on the decrement of radius than horizontal post-tensioning, the effect of vertical post-tensioning was not considered.

8.2.4 Effective wall length

In the evaluation code (EPRI, 2018) of nuclear power plant structure, the shear strength of cylindrical wall should be calculated by the strength equations for low-rise shear walls with boundary elements in ASCE 43-05 (Barda et al. (1977)) or Gulec and Whittaker (2011). For applying these equations, the effective wall length of cylindrical wall l_{eff} is required. In the current code, the effective wall length is conservatively evaluated and the effective cross-section is calculated as the area of an arc having a central angel of 45° to 40°. The effective wall length calculated by the above method is 1.26R to 1.57R.

Based on the test results in the chapter 4-2, the effective wall length was proposed. The maximum tested strengths ratios of cylindrical and planar walls were 0.91 and 1.03 in the case of RC and PSC, respectively. The length of planar wall was twice the radius of the cylindrical wall and the details of flange area were the same in the cylindrical and planar wall. The effective length of the cylindrical wall depends on the aspect ratio. However, considering that the aspect ratio of the test specimens is used in the actual containment buildings, it is believed that the effective wall length can be used from 1.8R to 2.0R. In addition, when calculated as an equivalent wall, the thickness of effective wall is $2t_w$.

8.2.5 Finite element analysis modeling

Finite element analysis or analysis using commercial programs is performed for nuclear power plant evaluation in the event of a high frequency earthquake. This section proposes recommendations to consider when creating an analytical model.

1) Elastic analysis

1-1) For high-frequency earthquakes, it is possible to consider an increase in strength according to the deformation rate of the structure.

- Most of the currently used design and evaluation equations are derived based on the results of static experiments. However, when an earthquake occurs, the structure deforms at a high loading rate. In this case, not only the extreme strength but also the failure mode may be changed. Therefore, it is important to evaluate the structure with respect to the expected load speed in the event of an earthquake. According to Bischoff and Perry (1991) and Grote (1991), the strain rate in previous static experiments is 10-5 (mm/mm), and the strain rate in structures under seismic loads ranges from 10^{-3} to 10^{-2} (sec^{-1}).

1-2) Structural evaluation can be performed using the maximum value of the strain rate generated during the total time history analysis as the representative strain rate.

The expected rate of strain in the event of an earthquake can be obtained through time history analysis. The strain rate value may be obtained from a value obtained by differentiating the strain graph obtained through the

time history analysis result.

2-1) Elastic finite element analysis is used to evaluate stress or required strength by load action. Heavy equipment mass and load affecting structural behavior inside nuclear power plants shall be reflected in the modeling.

1-3) Table 8-1 is used for effective stiffness.

Table 8-1 Effective stiffness

Structural member	Flexural rigidity	Shear rigidity	Axial rigidity
Flexural member, beam, and slab	0.5 E_cI_g	G_cA_w	-
Prestressed bending element	E_cI_g	G_cA_w	-
Columns in compression	0.7 E_cI_g	G_cA_w	E_cA_g
Columns in tension	0.5 E_cI_g	G_cA_w	E_cA_{gs}
In-plane bending and shear of walls and diaphragms			
Uncracked	E_cI_g	G_cA_w	E_cA_g
Cracked	0.5 E_cI_g	$0.5G_cA_w$	E_cA_g

- Table 8-1 is used in ASCE/SEI 4-10 and EPRI (2018). It is interpreted that there is a crack when a load exceeding $3\sqrt{f_c'}$ (psi) is applied to a shear wall having a shape ratio (h_w/l_w) of 1.5 or less. $2\sqrt{f_c'}$ (psi) is used for walls with a shape ratio of 2.0 or higher, and linear interpolation is used for a shape ratio between 1.5 and 2.0. This cracking load criterion is in accordance with ACI 349-13.

1-4) The wall is modeled as a shell-element or a three-dimensional solid-element. Wall reinforcement is not modeled separately and the material properties of the wall follow concrete. The prestressed tendon is modeled

as a line-element in consideration of non-attachment, and the tension is applied using the initial strain.

1-5) Slabs are modeled using shell-element or plate bending element. Rigid diagram assumptions can be used for simplified modeling.
For a brief interpretation, the slab can be assumed as a rigid diagram. However, it is necessary to consider the flexural rigidity of the slab for precise evaluation of the device response affected by the local response.

2) Nonlinear analysis

2-2) Several criteria deal with strength calculation equations or methods according to the shape and use of the wall. However, for the verification or precise identification of the design, it can be verified through the strength evaluation results through nonlinear finite element analysis. Basic modeling methods and element settings follow previous elastic modeling.

2-3) Concrete

- As for the compressive strength of concrete, the result of the compressive strength of the specimen obtained through the specimen or the coring operation may be used.
- When concrete is subjected to shear stress (tension-compression), the reduction in compressive strength due to tensile cracking should be considered.
- Concrete element models use solid-element or shell-element.

2-4) Reinforcing bars

The rebar material strain-stress curve uses the bi-linear model based on the results obtained from the material experiment. Reinforcement element models are modeled using line-element. It is modeled in a fully attached state, except when destruction by adhesion is expected.

2-5) Tendons

The strain-stress curve of the steel wire can be the same as the rebar using the bi-linear model and the element model uses a line-element. The tension introduced to the wire introduces tensile stress as the initial strain. However, this should be considered in the case of large friction due to curvature.

2-6) Considerations for creating a finite element analysis model for evaluating the performance of cylindrical walls used in containment buildings are as follows.

1. When the prestressing applied to the cylindrical wall, tensile stress may occur in the wall thickness direction, and cracks may occur. This crack should be considered because it may reduce the in-plane load capacity of the wall.

2. It is modeled to have nodes at the location of the steel line and horizontal reinforcement in the cross section of the concrete wall.

→ The horizontal post-tensioning applied to the containment of the nuclear power plant generates out-of-plane stress due to the shape of the

containment. For the simulation of cracks generated inside concrete by tensile stress in the out-of-plane direction, the elements shall be modeled separately.

3. When cracks in the concrete are generated by tensile stress in the wall thickness direction, the tensile and shear stresses between the concrete at the interface where the cracks occurred are modeled so that they can be ignored.

→ When delamination by a lecture wire occurs, cracks occur on the surface where the lecture wire is arranged, and only compression and friction stress must be transmitted on the surface.

4. Alternatively, when cracks in the thickness direction occur, modeling may be performed except for an area corresponding to the outer covering concrete.

→ Circular concrete walls have a curved shape. Confining force is required for shear stress resistance in shear reinforcement and concrete cross section. However, if an internal crack occurs, the cross section corresponding to the concrete sheath is lost when in-plane shear stress is applied.

5. If the shear reinforcement is appropriately arranged in the thickness direction, the cracks in the thickness direction is prevented.

References

[1] Arias, A. (1970). Measure of earthquake intensity, Massachusetts Inst. of Tech. *Cambridge. Univ. of Chile,* Santiago *de Chile*.

[2] Acharya, S., & Menon, D. (2003). Prediction of radial stresses due to prestressing in PSC shells. *Nuclear engineering and design*, *225*(1), 109-125.

[3] AL.Katoh, M., Tamura, S., Watanabe, Y., Takeda, T., & Yamaguchi, T. (1987). Dynamic and static loading tests using 1/30 scale model of PCCV. *Puresutoresuto*

[4] American Concrete Institute, ACI, (2013), *Code Requirements for Nuclear Safety-Related Concrete Structures (ACI 349-13) and Commentary*, Farmington Hills, Michigan, USA.

[5] ACI-ASME Joint Technical Committee. (2015). 2015 *ASME BPVC Section III-Rules for Construction of Nuclear Facility Components-Division 2-Code for Concrete Containments (ACI-359-15).* The American Society of Mechanical Engineers, New York, NY.

[6] Aoyagi, Y., Ohmori, S., & Yamada, K. (1981). Strength and deformational characteristics of orthogonally reinforced concrete containment models subjected to lateral forces. *Structural mechanics in reactor technology. Vol. J (a)*.

[7] Bae, S. (2013). Radial tension induced by prestressing forces and moments. *SMiRT-22, San Francisco, California*.

[8] Baek, J. W., Park, H. G., Lee, J. H., & Bang, C. J. (2017). Cyclic

loading test for walls of aspect ratio 1.0 and 0.5 with grade 550 MPa (80 ksi) shear reinforcing bars. *ACI Structural Journal*, *114*(4), 969.

[9] Baek, J. W., Park, H. G., Lee, B. S., & Shin, H. M. (2018). Shear-friction strength of low-rise walls with 550 MPa (80 ksi) reinforcing bars under cyclic loading. *ACI Structural Journal*, *115*(1), 65-78.

[10] Baek, J. W., Yang, H. K., & Park, H. G. (2020). Loading Rate Effect on Reinforced Concrete Walls with Low Aspect Ratios under High-Frequency Earthquake. *ACI Structural Journal, 117(6).*

[11] Barda, F.; Hanson, J. M.; and Corley, W. G., (1977) Shear Strength of LowRise Walls with Boundary Elements, *Reinforced Concrete Structures in Seismic Zones*, SP-53, American Concrete Institute, Farmington Hills, MI, 1977, pp. 149-202.

[12] Basu, P. C., Gupchup, V. N., & Bishnoi, L. R. (2001). Containment dome delamination. *SMiRT-16, Washington DC*.

[13] Bischoff, P. H. and Perry, S. H. (1991). Compressive behavior of concrete at high strain rate. *Material and structures*, 24 (6), 425-450.

[14] Burgueño, R., Liu, X., & Hines, E. M. (2014). Web crushing capacity of high-strength concrete structural walls: experimental study. *ACI Structural Journal*, *111*(2), 235.

[15] Carrillo, J., & Alcocer, S. (2008). Shaking table test of low-rise concrete walls for housing. *14th World Conference on Earthquake Engineering, Beijing, China, Artículo* (pp. 12-01).

[16] Cervenka, V., Cervenka, J., & Pukl, R. (2002). ATENA—A tool for engineering analysis of fracture in concrete. *Sadhana*, 27(4), 485-492.

[17] Chen, H., Xu, B., Wang, J., Zhou, T., Nie, X., & Mo, Y. L. (2020). Parametric analysis on compressive strain rate effect of concrete using mesoscale modeling approach. *Construction and Building Materials*, *246*, 118375.

[18] Cho, N. S., Jeong, W., Kim, K. W., Kim, H. T., & Lee, S. H. (2005). *Experimental evaluations for failure behavior of PCCV wall-base juncture* (KAERI/CM-948/2006).

[19] Choi, I. K., Nakajima, M., Choun, Y. S., & Ohtori, Y. (2009). Development of the site-specific uniform hazard spectra for Korean nuclear power plant sites. Nuclear Engineering and Design, 239(4), 790-799.

[20] Choi, J. (2018). *Investigating delamination behavior of curved post-tensioned concrete structures* (Doctoral dissertation).

[21] Choi, J., Woods, C. R., Hrynyk, T. D., & Bayrak, O. (2017). Behavior of curved post-tensioned concrete structures without through-thickness reinforcement. *ACI Structural Journal*, 114(4), 983.

[22] Chopra, A.K. (2012) *Dynamics of Structures, 4th ed.*" Pearson Prentice Hall: Hoboken, NJ, USA.

[23] Chung, L., & Shah, S. P. (1989). Effect of loading rate on anchorage bond and beam-column joints. *Structural Journal*, *86*(2), 132-142.

[24] Dyngeland, T. (1989). *Behavior of reinforced concrete panels.* Doktor Ingenierafhandling (Ph. D. thesis, Institute for Betongkonstruksjoner, Trondheim.

[25] EPRI (Electric Power Research Institute) (2017) *Advanced Nuclear*

Technology: High-frequency Seismic Loading Evaluation for Standard Nuclear Power Plants, Palo Alto, CA, USA: Electric Power Research Institute (EPRI), p 170.

[26] EPRI (Electric Power Research Institute) (2018) *Seismic fragility and seismic margin guidance for seismic probabilistic risk assessments.* Palo Alto, CA: EPRI

[27] Eom, T. S., Park, H. G., Kim, J. Y., & Lee, H. S. (2013). Web crushing and deformation capacity of low-rise walls subjected to cyclic loading. *ACI Structural Journal*, *110*(4), 575.

[28] Farrar, C. R., Reed, J. W., & Salmon, M. W. (1993). Failure modes of low-rise shear walls. *Journal of energy engineering*, *119*(2), 119-138.

[29] Florida Power and Light Company (1970), *Containment Dome Report: Turkey Point Unit 3,* Florida Power and Light Company, Miami, FL, Dec. 1970.

[30] Florida Power and Light Company (1976), *Reactor Building Dome Delamination Report: Crystal River Unit 3*, Florida Power and Light Company, Miami, FL, 1976

[31] Foster, S. J., & Gilbert, R. I. (1996). The design of nonflexural members with normal and high-strength concretes. *Structural Journal*, *93*(1), 3-10.

[32] Ghannoum, W.; Saouma, V.; Haussmann, G.; Polkinghorne, K.; Eck, M.; and Kang, D.-H., Experimental Investigations of Loading Rate Effects in Reinforced Concrete Columns, *Journal of Structural Engineering*, ASCE, V. 138, No. 8, 2012, pp. 1032-1041. doi:

10.1061/(ASCE)ST.1943-541X.0000540

[33] Grote, D., Park, S, and Zhou, M., (1991) Dynamic behavior of concrete at high strain rates, *Materials and Structures*.

[34] Gulec, C. K. (2009). *Performance-based assessment and design of squat reinforced concrete shear walls.* State University of New York at Buffalo. (Doctoral dissertation).

[35] Hwang, S. J., Fang, W. H., Lee, H. J., & Yu, H. W. (2001). Analytical model for predicting shear strength of squat walls. *Journal of Structural Engineering*, 127(1), 43-50.

[36] Hordijk, D. A., & Reinhardt, H. W. (1991). Growth of discrete cracks in concrete under fatigue loading. In Toughening mechanisms in quasi-brittle materials (pp. 541-554). Springer, Dordrecht.

[37] fib MC2010.*Model Code for Concrete Structures 2010. Fédération Interna-tionale du Béton (fib),* Lausanne, Switzerland. Berlin: Wilhelm Ernst & Sohn.

[38] Ko, D. W., & Lee, H. S. (2006). Shaking table tests on a high-rise RC building model having torsional eccentricity in soft lower story. *Earthquake engineering & structural dynamics*, *35*(11), 1425-1451.

[39] Kollegger, J., & Mehlhorn, G. (1990). Material model for the analysis of reinforced concrete surface structures. *Computational Mechanics*, *6*(5), 341-357.

[40] Kulkarni, S. M., and Shah, S. P., Response of Reinforced Concrete Beams at High Strain Rates, *ACI Structural Journal*, V. 95, No. 6, Nov.-Dec. 1998, pp. 705-715.

[41] Kupfer, H., Hilsdorf, H. K., & Rusch, H. (1969, August). Behavior of concrete under biaxial stresses. *Journal proceedings* (Vol. 66, No. 8, pp. 656-666).

[42] Limberger, E.; Brandes, K.; and Herter, J. (1982), Influence of Mechanical Properties of Reinforcing Steel on the Ductility of reinforced Concrete Beams with Respect to High Strain Rates, *Symposium on Concrete Structures under Impact and Impulsive Loading,* Berlin, Germany, 1982, 656 pp.

[43] Lee, N. H., & Song, K. B. (1999). Seismic capability evaluation of the prestressed/reinforced concrete containment, Yonggwang nuclear power plant Units 5 and 6. *Nuclear engineering and design*, 192(2-3), 189-203.

[44] Lee, H. S., Hwang, S. J., Lee, K. B., Kang, C. B., Lee, S. H., & Oh, S. H. (2011). Earthquake simulation tests on a 1: 5 scale 10-story RC residential building model. *Journal of the Earthquake Engineering Society of Korea*, *15*(6), 67-80.

[45] Lee, H. S., Lee, K. B., Hwang, K. R., & Cho, C. S. (2013). Shake table responses of an RC low-rise building model strengthened with buckling restrained braces at ground story. *Earthquake and Structures*, *5*(6), 703-731.

[46] Li, M, and Li, H., (2012) Effects of strain rate on reinforced concrete structure under seismic loading, *Advances in Structural Engineering*, V. 15, No. 3.

[47] MacGregor, J. G., Wight, J. K., Teng, S., & Irawan, P. (1997). *Reinforced concrete: Mechanics and design* (Vol. 3). New Jersey:

Prentice Hall.

[48] Mahin, S. A.; Bertero, V. V.; Atalay, M. B.; and Rea, D. (1972), Rate of Loading Effects on Uncracked and Repaired Reinforced Concrete Members, *Earthquake Engineering Research Center*, University of California, Berkeley, Berkeley, CA, 1972, pp. 1461-1470.

[49] Menetrey, P., & Willam, K. J. (1995). Triaxial failure criterion for concrete and its generalization. *ACI Structural Journal*, *92*(3), 311-318.

[50] Mutsuyoshi, H., and Machida, A. (1984), Properties and Failure of Reinforced Concrete Members Subjected to Dynamic Loading, *Transactions of the Japan Concrete Institute*, V. 6, 1984, pp. 521-528.

[51] Oesterle, R. G., Aristizabal-Ochoa, J. D., Shiu, K. N., & Corley, W. G. (1984, May). Web crushing of reinforced concrete structural walls. *Journal Proceedings* (Vol. 81, No. 3, pp. 231-241).

[52] Ogaki, Y., Kobayaski, M., Takeda, T., Yamaguchi, T., Yoshizaki, S., & Sugano, S. (1981). Shear strength tests of prestressed concrete containment vessels. *Structural mechanics in reactor technology.* Vol. J (a).

[53] Park, H. S., and Lee, T. H. (2017) Effect of high-frequency ground motions on the response of NPP components: A state-of-the-art review. *Journal of the Korean Society of Hazard Mitigation 17*, no. 6 (2017): 285-294.

[54] Pinho, R. (2000). Shaking table testing of RC walls. *ISET Journal of Earthquake Technology*, *37*(4), 119-142.

[55] *Seismic Analysis of Safety Related Nuclear Structures and*

Commentary, American Society of Civil Engineers, Reston, VA: 2017. ASCE/SEI standard 4-16.

[56] Syed, S. Q. (2013). *Seismic Probabilistic Fragility Assessment of Reinforced Concrete Shear Wall Structures in Nuclear Power Plants.* (Doctoral dissertation).

[57] Takeda, J., and Tachikawa, H. (1972), Deformation and Fracture of Concrete Subjected to Dynamic Load, *Proceedings of the Conference on Mechanical Behavior of Materials*, 1972, Transport and Road Research Laboratory (TRRL), Crowthorne, UK, pp. 267-277.

[58] Timoshenko, S. P., & Goodier, J. N. (1970). *Theory of Elasticity 3rd ed*., 567.

[59] Uchida, T., Ohmori, N., Takahashi, T., Watanabe, S., Abe, H., & Aoyagi, Y. (1979). Behavior of Reinforced Concrete Containment Models under the Combined Action of Internal Pressure and Lateral Force. *SMiRT-5.*

[60] USNRC (1984), *Engineering Characterization of Ground Motion-Task I, Effects of Characteristics of Free-Field Motion on Structural Response,* Washington, D.C. NUREG/CR-3805.

[61] USNRC (2001), *Safety-Related Concrete Structures for Nuclear Power Plants (Other than Reactor Vessels and Containment)*, Revision 2. Washington, DC. US Nuclear Regulatory Guide 1.142.

[62] USNRC, (2007). *A performance-based approach to define the site-specific earthquake ground motion.,* US Nuclear Regulatory Commission, Washington, DC. Regulatory Guide 1.208

[63] USNRC, (2014). *Design response spectra for seismic design of nuclear power plants*, Washington, DC. Regulatory Guide RG 1.60

[64] USNRC, (2020). *Safety-related concrete structure for nuclear power plants.* US Nuclear Regulatory Commission, Washington, DC. , Regulatory Guide 1.142.

[65] Van Mier, J. G. (1986). Multiaxial strain softening of concrete. *Materials and structures*, 19(3), 190-200.

[66] Vecchio, F. J. and M. P. Collins (1986). The modified compression-field theory for reinforced concrete elements subjected to shear. *ACI Structural Journal*. 83(2): 219-231.

[67] Völgyi, I., Windisch, A., & Farkas, G. (2014). Resistance of reinforced concrete members with hollow circular cross-sections under combined bending and shear–Part I: experimental investigation. *Structural Concrete*, 15(1), 13-20.

[68] Völgyi, I., & Windisch, A. (2014). Resistance of reinforced concrete members with hollow circular cross-section under combined bending and shear–Part II: New calculation model. *Structural Concrete*, 15(1), 21-29.

[69] Wakabayashi, M.; Nakamura, T.; Yoshida, N.; Iwai, S.; and Watanabe, Y. (1980), Dynamic Loading Effects on the Structural Performance of Concrete and Steel Materials and Beams, *Proceedings, 7th World Conference on Earthquake Engineering,* 1980, Turkish National Committee on Earthquake Engineering, V. 6, pp. 271-278.

[70] Woo, S. S., Lee, S. H., & Chung, L. (2007). Shaking table test of small-scale 5-story RC structure with tuned liquid damper. *The*

Architectural Institute of Korea, *23*(2), 3-8.

[71] Yang, H. C., Wu, C. L., & Hsu, T. T. (2017) Reversed Cyclic Tests of Cylindrical Concrete Containment Structures, *16th World Conference on Earthquake Engineering,* Santiago Chile.

[72] Zhang, L. X. B., & Hsu, T. T. (1998). Behavior and analysis of 100 MPa concrete membrane elements. *Journal of Structural Engineering*, 124(1), 24-34.

[73] Zheng, W., Kwan, A. K. H., & Lee, P. K. K. (2001). Direct tension test of concrete. *Materials Journal*, *98*(1), 63-71.

APPENDIX A
: Summary of Existing Cylindrical Squat Wall Specimens

In this appendix, the database of cylindrical squat wall specimens were summarized.

Table A Summary of existing cylindrical squat wall specimens

No.	*Failure mode*	External radius (mm)	Internal radius (mm)	Height (mm)	Reinforcing bar ratios (%)		Prestressing stress for concrete section ($\rho_{p\_}\sigma_{p\_}$ MPa)		f_y (MPa)	f_{ck} (MPa)	Test strength (kN)	Predicted strength (kN)	$V_{test}/V_{predict}$	Ref.
					ρ_h	ρ_v	ρ_{pv}, %	ρ_{ph}, %						
1	Shear	750	600	1200	0.0093	0.0186	0	0	470.0	36.0	1,973	1,777	1.11	Yang
2	Shear	750	600	1200	0.0093	0.0186	0	8.32	470.0	36.0	1,745	1,766	0.99	
3	Shear	750	600	1200	0.0093	0.0186	6.5	8.32	470.0	36.0	2,033	2,089	0.97	
4	Shear	750	600	1200	0.0093	0.0186	13	8.32	470.0	36.0	2,063	1,978	1.04	
5	Shear	750	600	1200	0.0093	0.0186	13	8.32	470.0	36.0	2,270	2,451	0.93	
6	Shear	670	610	1200	0.0072	0.0186	0	0	480.0	38.0	1,630	1,463	1.11	
7	Shear	670	610	1200	0.0072	0.0186	0	0	506.4	40.1	1,868	1,505	1.24	
8	Shear	670	610	1200	0.0072	0.0186	13	8.32	480.0	31.0	1,312	1,286	1.02	
9	Shear	670	610	1200	0.0072	0.0186	13	8.32	506.4	45.4	1,578	1,745	0.90	
10	Shear	670	610	1200	0.0072	0.0186	0	8.32	506.4	40.1	2,005	1,463	1.37	
11	Shear	670	610	1200	0.0072	0.0186	6.5	8.32	506.4	40.1	2,033	2,229	0.91	

APPENDIX A: Summary of Existing Cylindrical Squat Wall Specimens

Table A Summary of existing cylindrical squat wall specimens

No.	*Failure mode*	External radius (mm)	Internal radius (mm)	Height (mm)	Reinforcing bar ratios (%)		Prestressing stress for concrete section ($\rho_{p\_}\sigma_{p\_}$ MPa)		f_y (MPa)	f_{ck} (MPa)	Test strength (kN)	Predicted strength (kN)	$V_{test}/V_{predict}$	Ref.
					ρ_h	ρ_v	ρ_{pv}, %	ρ_{ph}, %						
12	Shear	1250	1100	2250	0.02	0.02	0	0	270.0	37.0	5,580	5,242	1.06	Wu et al.
13	Shear	1250	1100	2250	0.02	0.02	0	0	270.0	43.0	6,113	5,319	1.15	
14	Torsion	580	500	3000	0.01	0.01	3.136	1.568	400.0	45.3	2,482	1,948	1.27	Ogaki et al.
15	Torsion	580	500	3000	0.01	0.01	4.312	3.92	400.0	45.3	2,756	2,587	1.07	
16	Torsion	580	500	3000	0.02	0.02	4.312	3.92	400.0	45.3	3,370	2,833	1.19	
17	Torsion	580	500	3000	0.01	0.01	6.664	8.624	400.0	45.3	3,139	3,864	0.81	
18	Torsion	580	500	3000	0.01	0.01	0	0	400.0	45.3	1,162	246	4.73	
19	Torsion	580	500	3000	0.01	0.01	6.664	7.84	400.0	45.3	3,727	3,864	0.96	
20	Torsion	580	500	3000	0.01	0.01	6.272	7.84	400.0	45.3	3,783	3,651	1.04	
21	Torsion	580	500	3000	0.02	0.02	6.272	7.84	400.0	45.3	1,593	1,897	0.84	
22	Torsion	580	500	1000	0.01	0.01	4.312	3.92	400.0	50.6	2,397	2,616	0.92	
23	Torsion	580	500	1000	0.01	0.01	6.664	7.84	400.0	50.6	3,139	3,892	0.81	
24	Torsion	580	500	1000	0.01	0.01	6.664	8.624	400.0	50.6	2,995	3,892	0.77	
25	Shear	820	750	1500	0.0167	0.0167	6.272	7.84	400.0	63.7	1,844	2,081	0.89	
26	Shear	820	750	1500	0.0167	0.0167	3.136	1.568	400.0	63.7	1,746	1,786	0.98	

Table A Summary of existing cylindrical squat wall specimens

No.	*Failure mode*	External radius (mm)	Internal radius (mm)	Height (mm)	Reinforcing bar ratios (%)		Prestressing stress for concrete section ($\rho_{p\_}\sigma_{p\_}$ MPa)		f_y (MPa)	f_{ck} (MPa)	Test strength (kN)	Predicted strength (kN)	$V_{test}/V_{predict}$	Ref.
					ρ_h	ρ_v	ρ_{pv}, %	ρ_{ph}, %						
28	Flexural	820	750	2250	0.025	0.025	6.272	7.84	400.0	44.0	1,665	2,622	0.63	Ogaki et al.
29	Flexural	820	750	2250	0.025	0.025	3.136	1.568	400.0	44.0	1,655	2,354	0.70	
30	Shear	600	540	1150	0.006	0.012	0	0	324.0	23.0	414	413	1.00	Naohiro et al.
31	Shear	600	540	1150	0.012	0.024	0	0	324.0	25.2	639	830	0.77	
32	Torsion	850	750	2000	0.012	0.012	0	0	370.0	29.1	283	336	0.84	Aoyagi
33	Torsion	850	750	2000	0.01	0.01	0	0	370.0	34.5	299	347	0.86	
34	Torsion	850	750	2000	0.018	0.018	0	0	370.0	36.0	374	647	0.58	
35	Torsion	850	750	2000	0.014	0.013	0	0	370.0	28.1	250	396	0.63	
36	Torsion	850	750	2000	0.018	0.018	0	0	370.0	32.9	304	393	0.78	
37	Torsion	850	750	2000	0.012	0.015	0	0	370.0	28.4	245	329	0.75	
38	Torsion	850	750	2000	0.014	0.013	0	0	370.0	26.2	292	368	0.79	
39	Shear	1015	940	1000	0.012	0.012	0	0	375.0	34.3	1,233	1,342	0.92	Hiroshi et al.

초 록

지진하중에서 변형률 속도 및 프리스트레싱이 원형 저형 벽체 전단 강도에 미치는 영향

양 현 근

서울대학교 건축학과 대학원

최근 몇 년간 경주와 포항에서 두 차례 지진이 발생하였다. 원자력 발전소 부지 인근에서 발생한 지진으로 원전의 내진 안전성에 대한 우려가 증가하였다. 또한 지진 발생 횟수와 위험성이 증가함에 따라 원자력발전소의 정확한 내진성능을 파악하는 것이 중요하다고 강조되어 왔다. 또한, 한국 지진의 특징에는 고주파 성분이 포함되어 있는 것으로 확인되었다.

원전은 방사성 물질을 통제하는 건물로 사고 발생 시 방사성 물질 누출을 최소화하기 위해 높은 내진 성능이 요구된다. 따라서 보조 및 격납건물의 두께는 약 1.2m로 높게 설계된다. 또한 현재 설계 기준을 초과하는 높은 철근비가 사용된다. 특히 격납건물은 비상사고 발생 시 발생할 수 있는 내부 압력을 견디기 위해 포스트 텐션이 적용된다. 그러나, 격납건물의 포스트텐션과 거대한 크기로 인해, 구조 실험은 거의

수행되지 않았다. 기존 실험의 경우 상세가 같은 패널 실험을 위주로 수행되었고, 포스트 텐션을 갖는 원통형 벽의 실험은 거의 수행되지 않았다.

평면 벽과 달리 원통형 벽은 전단력을 직접 전달하지 않는다. 전단력은 단면 형상을 따라 전달되므로, 이러한 원통형 단면의 특성 때문에 추가 구속력이 요구된다. 그러나 기존 평면벽 실험을 통한 제안식을 이용할 경우 수평보강근의 구속력을 적용할 수 없다. 따라서 원통형 벽체의 전단강도 모델 개발이 필요하며, 특히 고주파 성분의 지진에 대한 구조물의 구조 거동 특성에 대한 연구가 필요하다.

본 연구에서는 동적하중시험과 진동대 시험을 통해 고주파 지진의 영향을 확인하였다. 실험결과 고진동수 지진에서 파괴 모드 변화는 발생하지 않았고, 지진하중에서 철근콘크리트 벽체의 내진성능을 확인하였다. 또한, 빠른 가력속도에서 구조물의 강도 증가 현상을 확인하였다. 또한, 격납 건물의 내진성능을 조사하기 위해 원통형 벽체를 작성하고 주기적 하중 시험을 실시하였다.

원통형 벽체와 평면형 벽체의 비교 실험 결과, 포스트텐셔닝이 최대 전단 강도에 미치는 영향은 평면형 벽체의 경우 낮은 것으로 나타났다. 그러나 포스트 텐션과 크로스 타이를 적용한 원통형 벽의 경우 최대 강도가 증가하였다. 반면, 크로스타이가 없는 포스트텐셔닝 원통형 벽의 경우, delamination 균열이 관찰되었다. 내부 균열로 인해 최대 전단 강도가 감소하였고, 실험 결과를 바탕으로 원통형 벽체의 전단강도

방정식을 제안하였다.

본 논문의 결론에서는 시험 및 분석 결과를 바탕으로 원통형 벽체에 대한 전단강도 방정식을 제안하여 벽체의 내진 성능을 예측하였다. 또한 구조물의 조기 파괴를 방지하고 지진 하중에 의한 원자력발전소의 구조안전성을 향상시키기 위한 설계 권고사항이 제시되었다.

주요어 : 고진동수 지진, 프리스트레스트 콘크리트, 구속력, 원형 전단 벽체, 원자력 발전소 내진 성능 평가

학 번 : 2017-23892